UNIVERSITY OF CANTERBURY

Development and validation of a CFD-based approach towards analysing Pentane vaporizers

A thesis submitted for the degree of Doctor of Philosophy

in Mechanical Engineering,

by Sandeep Siwach

at University of Canterbury,

Christchurch, New Zealand - 2016

Acknowledgments

Foremost, I would like to acknowledge the support of my supervisors during the course of this study. Special thanks goes to my senior supervisors, Associate Professors Dr. Mark Jermy and Dr. Mathieu Sellier, for the valued opportunity to undertake this PhD study, expertise, guidance and proofreading of this thesis. They were a constant source of encouragement and guidance on various issues faced during the course of this project. I would like to acknowledge the deep expertise and detailed guidance provided by Dr. David Fletcher regarding ANSYS™ CFX™ module and also for the significant help in the form of a customization routine without which this work would not achieved the scope that it has achieved. I would also like to thank Dr. Natalia Kabaliuk for the permission to use a MATLAB™ code developed by her that was used for droplet trajectory analysis in this project. I thank the Ministry of Business, Innovation and Employment, New Zealand for funding the project that this thesis is a part of. I would also like to thank Alex Stefan, James Hewett and Dr. Choon Seng Wong for valuable discussions regarding the project. I would like to especially thank Dr. Pradeep Siwach for financial support when I was coming to New Zealand and that is what started my second phase of pursuit of higher education which has benefited me in more ways than purely academic progression. I would like to thank my mother Kamlesh Siwach for constant emotional support throughout the project.

Abstract

Geothermal heat-energy based power-generation has been an area of intense focus and development in New Zealand for more than five decades now. There are immense benefits of geothermal power generation in terms of environmental conservation. Other benefits include constant base load capability, lower foot print etc. The geothermal heat energy resource can be classified as high-enthalpy and low-enthalpy heat source based on the temperature and whether geothermal brine comes out in liquid or vapor phase. New Zealand geothermal resources are largely under the low-enthalpy category which makes it necessary to use Organic Rankine Cycle (ORC) as the plant thermodynamic cycle.

ORC-based power plants use fluids with boiling point lower than water. ORC power plants are complicated systems with a significant influence of components on each other and performance of the entire system. Heat exchangers form a crucial part of geothermal power plants at all stages of the plant – starting with claiming a major portion of the capital cost for commissioning the plant right up to governing the working (and hence profitability) of the plant in terms of deciding the plant downtime (for maintenance) and plant performance (preheaters/vaporizers/superheaters should be able to provide a minimum degree of superheating to working fluid and this minimum value decides the maximum value of working fluid mass flow rate through the plant which translates into plant's net electric power output). Although heat exchangers have such a critical influence on the life-time profitability of power plants, their designs are still based on empirical/semi-empirical models, developed over the years through extensive experimentation, which form a constraint towards predicting their performance if the unit is operating in off-design conditions or is different in some geometrical aspects from the units that were used in experiments generating the empirical/semi-empirical models.

The vaporizer is a critical component in a power generation system. It is where the motive/working fluid undergoes change of phase to power the prime rotor (expander)

and generate electrical or shaft power. Figure 1 shows a schematic of an organic Rankine cycle power plant of the type of interest for the present work. It has been estimated that more than half of the heat exchangers employed in process industries involve two-phase flow on the shell-side [50], and yet two-phase flow patterns in cross-flow have received much less attention than in-pipe two-phase flow patterns. There have been a number of experimental studies on various single and multi-tube geometries [44, 50, 51, 73, 95, 106, 116, 153] with main focus on areas such as void-fraction prediction correlations and frictional pressure drop prediction correlations. The void fraction and pressure drop measurements obtained by these investigators produced bundle average or pitch average values that were used in the formulation of various correlations.

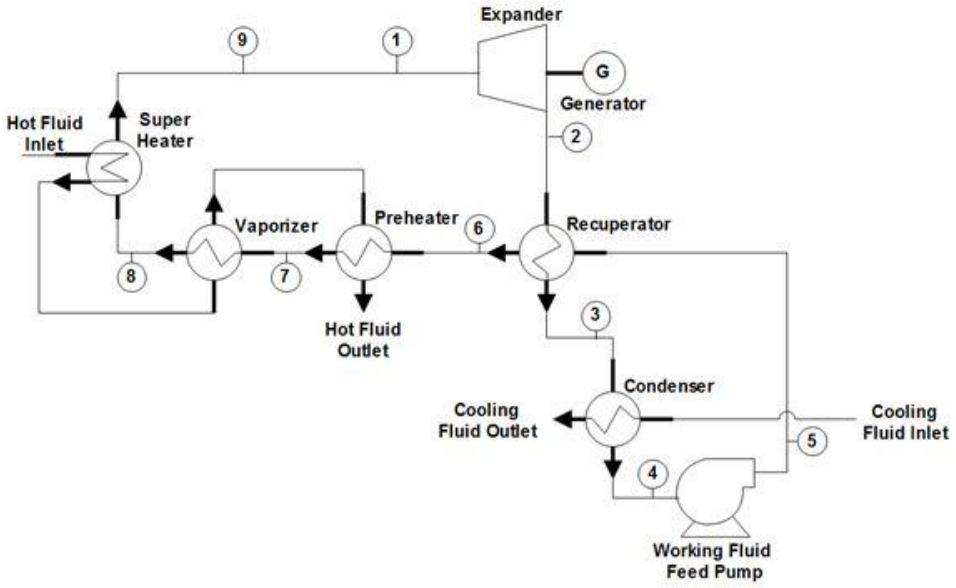

Figure 1 - General schematic representation of an Organic Rankine Cycle based power plant

In this thesis, the aim is to develop a Computational Fluid Dynamics (CFD) approach towards simulation of a full-scale pentane vaporizer with the aim of building capability for troubleshooting installed vaporizer units. CFD analysis of single-phase heat exchangers (e.g. preheaters, superheaters) was also carried out to present a comprehensive CFD approach towards troubleshooting the heating side of a power-

plant. Heat exchangers are also used on the condensing side but that was excluded from the CFD scope of the project although MATLAB™ codes were written for analysing condensers as well.

In order to achieve the target the project was divided into different stages – a) CFD simulation and validation of preheaters, b) MATLAB™ code development for preheaters and vaporizers, c) CFD simulation and validation for single- and multi-tube geometries, d) selection of a substitute fluid to ascertain CFD set-up tuning factors in view of the absence of pentane boiling experimental data. This is done by – i) comparing thermophysical properties of three fluids – water, R113 and Pentane, ii) analysis of dimensionless numbers characterizing bubble dynamics (Bubble Reynolds number, Eötvös number, Morton number) and boiling process (Weber number, Jakob number, Boiling number) , e) parametric CFD analysis of a Shell-and-Tube Heat Exchanger (STHE) slice geometry to obtain relationship between liquid level and heat transfer performance of the unit, f) CAD modeling of a full scale vaporizer unit, g) CFD simulation on a scaled down representative geometry of repeating unit within the full scale vaporizer to verify the CFD set-up, h) droplet carryover analysis with the help of MATLAB™ code and CFD simulation. The project was originally aimed at getting the simulation for the full-scale vaporizer's repeating unit done at its end, but the time requirement estimation for multi-phase simulations proved to be an under-prediction. In the tasks completed, validation is carried out at each step and constraints/assumptions of the set-up clearly outlined and explained in the respective sections.

The validation for single-phase CFD analysis has been done against well-established theoretical models along with a mesh-dependence study. CFD analysis is also conducted on novel heat exchanger geometries to demonstrate capabilities of thermal and flow field visualization. A MATLAB™ code has been developed for PHEs with validation against experimental data. Phase-change (boiling) CFD analysis of single- and multi- tube geometries has been validated against experimental data. A substitute fluid has been selected for tuning of pentane vaporization CFD studies on the basis of

dimensionless numbers that characterize bubble dynamics and boiling. CFD studies have also been conducted on a STHE slice geometry with five different inflow rates to obtain information about the impact of inflow rate on heat transfer performance and vapor volume fraction escaping the vaporizer unit. A CAD model for a generic industrial scale kettle-type vaporizer has also been developed. Based on the representative structure within the full scale geometry a scaled down representative geometry is used for CFD analysis. The CFD-Post™ data of the vapor velocity field of this representative geometry is used as an input to a MATLAB™ code to plot droplet trajectories. The MATLAB™ code is unable to factor in droplet vaporization. Droplet vaporization is simulated by CFD analysis imagining a worst case scenario where the droplet is traveling straight up a vapor outflow channel.

The main tasks for future work on this project would be – a) do CFD analysis of the full scale vaporizer and benchmark computational requirements, investigate any potential optimizations with regards to computational time and hardware resources, and b) integrate droplet vaporization code into the droplet trajectory plotting code. A preliminary design for a lab has also been presented that can be used to conduct experiments providing detailed information about parameters required to tune CFD model set-up.

In conclusion, it can be said that the project has demonstrated a validated CFD analysis approach towards understanding and troubleshooting heat exchangers used in geothermal power plants and in general this approach can be extended to any process industry that uses heat exchangers.

Deputy Vice-Chancellor's Office
Postgraduate Office

UNIVERSITY OF CANTERBURY
Te Whare Wānanga o Waitaha
CHRISTCHURCH NEW ZEALAND

Co-Authorship Form

This form is to accompany the submission of any thesis that contains research reported in co-authored work that has been published, accepted for publication, or submitted for publication. A copy of this form should be included for each co-authored work that is included in the thesis. Completed forms should be included at the front (after the thesis abstract) of each copy of the thesis submitted for examination and library deposit.

Please indicate the chapter/section/pages of this thesis that are extracted from co-authored work and provide details of the publication or submission from the extract comes:

*An earlier version of the MATLAB code for kettle vaporizer analysis used in Chapter 3 has been used in conference paper – "*Impact Of Organic Rankine Cycle Working Fluid Selection On Heat Exchanger Design And Cost*" published in proceedings of 36th New Zealand Geothermal Workshop held in Auckland (Nov 2014).*

Please detail the nature and extent (%) of contribution by the candidate:

I worked on the MATLAB code that calculates tube arrangement based on specific inputs and calculates various thermal performance parameters of the heat exchanger. The %age extent would be 25%.

Certification by Co-authors:

If there is more than one co-author then a single co-author can sign on behalf of all

The undersigned certifies that:

- The above statement correctly reflects the nature and extent of the PhD candidate's contribution to this co-authored work
- In cases where the candidate was the lead author of the co-authored work he or she wrote the text

Name: *Leighton Taylor* Signature:  Date: *21-7-15*

Publications from Research

Journal Papers

1. S. Siwach, M.C. Jermy, M. Sellier – A CFD methodology for single-phase heat exchangers and pentane vaporizers validated against single-tube experimental data, International Journal of Heat and Mass Transfer 2016 (***Current***)

Conference Proceedings

S. No.	Description	Conference	Paper/ Presentation
1	Design of Pentane Vaporizers - A CFD Approach	Fluids in New Zealand – 2016 (University of Auckland, NZ)	Presentation
2	Design of Pentane Vaporizers: A CFD Approach	New Zealand Geothermal Workshop – 2015 (Taupo, NZ)	Paper & Presentation
3	Heat Exchanger Design – A CFD Approach	Fluids in New Zealand – 2015 (University of Canterbury, NZ)	Presentation
4	Design of a Test Rig to Improve Thermal Design Approach for Evaporators for Organic Rankine Cycle Power Plant	Australian Fluid Mechanics Conference – 2014 (Melbourne, Australia)	Paper & Presentation
5	Impact of Organic Rankine Cycle Working Fluid Selection on Heat Exchanger Design and Cost	New Zealand Geothermal Workshop – 2014 (Auckland, NZ)	Paper (Co-author)

Supervisors

Dr. Mark Jermy	Senior Thesis Supervisor, University of Canterbury, New Zealand
Dr. Mathieu Sellier	Senior Thesis Supervisor, University of Canterbury, New Zealand
Dr. Sid Becker	Thesis Supervisor, University of Canterbury, New Zealand

Special acknowledgement to the following people in supporting the research project and development of this thesis:

Dr. David Fletcher	Adjunct Professor and Computational Fluid Dynamics Specialist, School of Chemical and Biomolecular Engineering, University of Sydney, Australia
Dr. Natalia Kabaliuk	Post-doctorate Fellow, Department of Mechanical Engineering, University of Canterbury, New Zealand

This author is funded by "**MBIE Grant E6049**" in supporting this research project.

Contents

Table of Symbols

Symbol	Description	Page No.
α_H	Void fraction measured with homogeneous flow model	40
x	Quality	40
ρ_g & ρ_l	Density of vapor and liquid phases	40
q	Heat flux	47
D_{inf} & D_b	Diameter of bubble influence and Diameter of bubble	48
δ	Micro-region thickness	51
T_{sat}	Saturation temperature	51
T_i	Interfacial temperature	51
Nu	Nusselt number	54
A & $F(p)$	Correlation factors	54
P_{red}	Reduced pressure (= Operating pressure / Critical pressure)	54
Re	Reynolds number	54
Pr	Prandtl number	54
P_{crit}	Critical pressure	54
h_{bundle}	Bundle heat transfer coefficient	73
h_{nb}	Nucleate boiling heat transfer coefficient	73
h_{cb}	Convective heat transfer coefficient	73
Q_{flux}	Heat flux	89

μ_{WF}	Dynamic viscosity of working fluid	89
g	Gravitational acceleration	89
ρ_{liq} & ρ_{vap}	Density of liquid and vapor phases	89
Cp_{WF}	Specific heat capacity of working fluid	89
ΔT_{excess}	Temperature of hot surface – Saturation temperature of boiling fluid	89
H_{latent}	Latent heat of vaporization	89
σ	Surface tension value	89
$L_{char,nb}$	Characteristic length	90
k_{WF}	Thermal conductivity of working fluid	91
α_{WF}	Heat transfer coefficient of working fluid	91
ν_{WF}	Kinematic viscosity of working fluid	92
M	Molecular mass of boiling fluid	93
T_{wall}	Heated wall temperature	94
Δi_{vap}	Latent heat of vaporization	94
R_p & $R_{p,ref}$	Roughness of surface and reference roughness	95
h_{ref}	Reference heat transfer coefficient for boiling fluid	95
$R_{gas\ constt}$	Universal gas constant, R	96
T_{crit}	Critical temperature of boiling fluid	96
Ra	Surface roughness	98
$\mathcal{E}$	Void fraction	101
h_{ST}	Single-tube nucleate boiling heat transfer coefficient	103

h_{nc}	Heat transfer coefficient by natural convection	103
V_l	Liquid phase velocity	135
L	Pipe length	135
V_{rel}	Liquid and vapor phase relative velocity	135
V_g	Vapor phase velocity	136
V_b	Bubble velocity	136
d	Bulk bubble diameter	141
d_b & d_B	Bulk bubble diameter	142, 143
ϵ	Effectiveness (in $\epsilon - NTU$ method for HE design)	148

List of Tables

List of Figures

1.0 Introduction

Traditional power-generation methods (e.g. steam power plants) are generally dependent upon non-renewable sources of energy such as petroleum, natural gas and coal. These are burned to vaporize the working fluid which is used to power the prime-mover in order to run the electricity generators. There are two major drawbacks of using these sources for power generation: a) limited supply, b) burning of fossil fuels is detrimental to environment. This has necessitated exploration of alternate methods of electricity generation that can be powered by renewable sources. This includes hydro-power, wind-power, solar power, marine (tidal energy) and geothermal energy sources. Out of all these methods, geothermal has a number of advantages:

- Small footprint for plant
- Proven technology
- Least effect on surrounding environment
- Independent of weather conditions
- Base load provider, i.e. power is generated continuously unlike wind and solar

Geothermal power plants can be divided into two main groups: steam (single-flash, double-flash and dry steam) cycle power plants & binary cycle power plant. The steam cycle based plants are used with geothermal wells producing high-enthalpy brine and binary cycle based plants are used where the geothermal well produces low enthalpy brine. When the geothermal wells produce a mixture of steam and liquid, the flash plants offer a relatively simple way to convert the geothermal energy into electricity. First the mixture is separated into distinct steam and liquid phases with minimum loss of pressure.

This is done in a cylindrical cyclonic pressure vessel, usually oriented with its axis vertical, where the two phases separate owing to their inherently large density difference. The steam is used to power the turbine. The liquid phase is re-injected back into the ground to minimize the environmental impact of the power plant. Before re-injection into the ground, the liquid phase, if it is at a sufficiently high temperature, may be used to run a binary cycle unit attached to main plant.

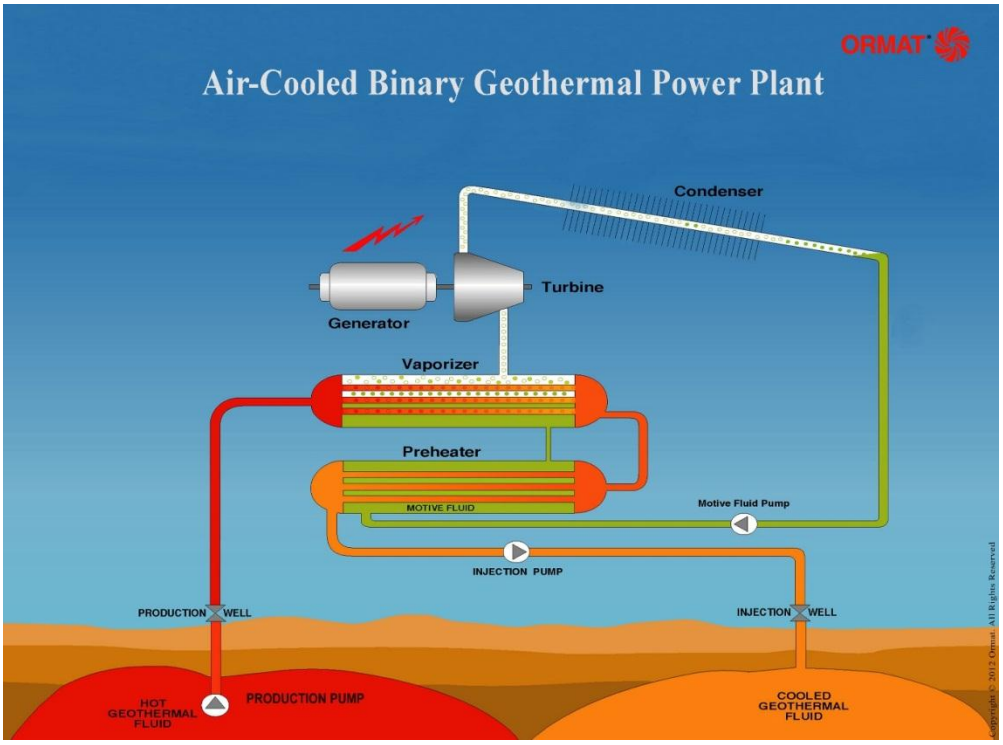

Figure 2: Schematic of air-cooled binary geothermal power plant

Binary cycle geothermal power plants are the closest in thermodynamic principle to conventional nuclear or fossil power plants in the sense that the working fluid undergoes an actual closed cycle [35]. The working fluid is chosen based on its thermodynamic properties. During the cycle it receives heat from the geothermal brine, gets evaporated, expands and powers a prime-

mover which is coupled with electricity generator. After having spent its energy in the expander it is passed through condenser(s) and is returned to the evaporator by means of feed pump(s). The geothermal brine is re-injected back into the ground. A simplified schematic of a basic binary geothermal power plant is shown in Figure 2[110].

Geothermal power plants can also be classified as subcritical and supercritical based on the position of thermodynamic cycle w.r.t. vapor curve of the working fluid, Figure 3 [124].

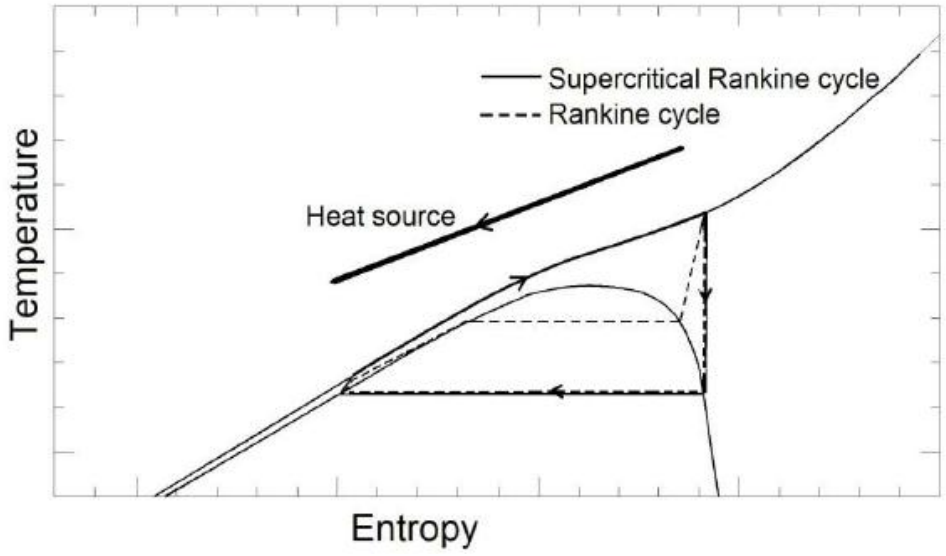

Figure 3: T-S diagram for Supercritical Rankine Cycle (SRC) and Organic Rankine Cycle (ORC)

The status of geothermal power generation across the world as of 2015 [14] is shown in Figure 4. Figure 5 [35] shows a detailed break-up of geothermal power generation in New Zealand as of August 2011 and in Figure 6 [14] for plants commissioned post 2011. The focus post-2011 has been on binary units due the economic benefits of extracting maximum energy from the geothermal brine coupled with wider availability of the technology.

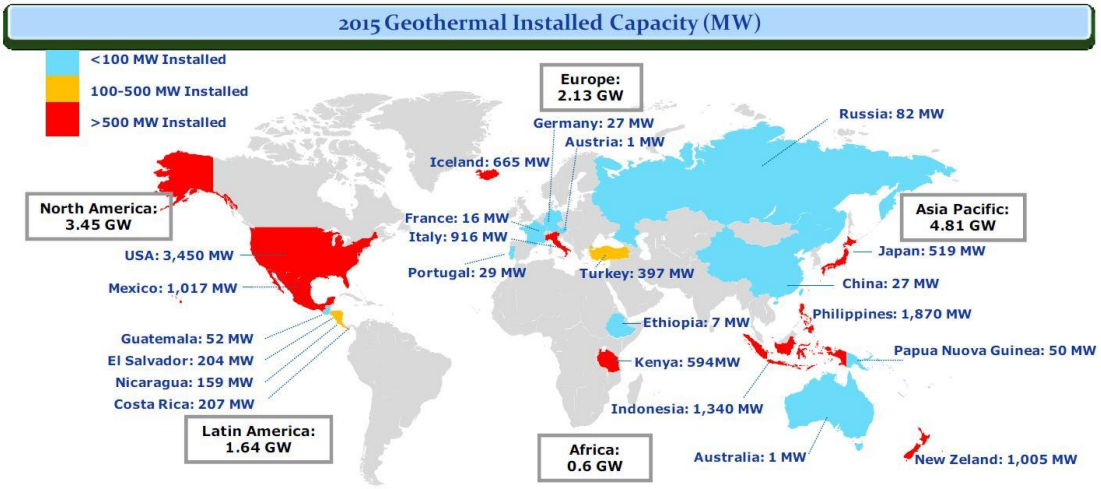

Figure 4: Installed capacity in 2015 worldwide (12.6 GWe)

Plant	Year	Type	MW-rated	No. units	MW-total	Comments
WAIRAKEI						
Unit 1	1959	2-Flash	11.2	1	11.2	
Unit 2	1958	1-Flash	6.5	1	6.5	Retired
Unit 3	1959	1-Flash	6.5	1	6.5	Retired
Unit 4	1959	2-Flash	11.2	1	11.2	
Unit 5 & 6	1962	1-Flash	11.2	2	22.4	Moved
Unit 7 & 8	1959	3-Flash	11.2	2	22.4	
Unit 9 & 10	1960	3-Flash	11.2	2	22.4	
Unit 11	1962	2-Flash	30	1	30	
Unit 12 & 13	1963	2-Flash	30	2	60	
Unit 14	NA	1-Flash	5	1	5	
Poihipi	1996	Dry Steam	55	1	55	
Bottoming Unit	2005	Binary	5	3	15	
KAWERAU						
Unit 1	1961	1-Flash	10	1	10	Retired
TG 1	1989	Binary	1.2	2	2.4	
TG 2	1993	Binary	3.5	1	3.5	
KA 24	2008	Binary	8.3	1	8.3	
Mighty River Power	2008	2-Flash	100	1	100	
TAUHARA	2010	Binary	23	1	23	aka Te Huka
OHAAKI						
Unit 1 & 2	1988	2-Flash	11.2	2	22.4	From Wairakei
Unit 3 & 4	1988	2-Flash	46	2	92	
MOKAI						

Mokai I	1999	Flash-binary	25, 5	1, 6	55
Mokai II	2005	Flash-binary	33, 6	1, 1	39
Mokai IA	2007	Binary	17	1	17
NGAWHA					
Unit 1	1998	Flash-binary	4.5	2	9
Unit 2	2008	Binary	15	1	15
ROTOKAWA					
Combined Cycle	1997	Flash-binary	13, 4.5	1, 3	26.5
Extension	2003	Flash-binary	6	1	6
Nga Awa Purua	2010	3-Flash	132	1	132
TOTALS				48	828.7
ACTIVE				43	783.3

Figure 5: Detailed break-up of geothermal power development in New Zealand (August 2011)

Plant	**Unit**	**COD**	**Type**	**Manufacturer**	**Capacity (MWe)**	**Operator**
Te Mihi	1	2014	Double Flash	Toshiba	83	Contact Energy
Te Mihi	2	2014	Double Flash	Toshiba	83	Contact Energy
Ngatamariki	1	2013	Binary	ORMAT	20.5	Mighty River Power
Ngatamariki	2	2013	Binary	ORMAT	20.5	Mighty River Power
Ngatamariki	3	2013	Binary	ORMAT	20.5	Mighty River Power
Ngatamariki	4	2013	Binary	ORMAT	20.5	Mighty River Power
Te Huka	1	2013	Binary	ORMAT	12	Contact Energy
Te Huka	2	2013	Binary	ORMAT	12	Contact Energy
Kawerau-Topp	1	2012	Binary	ORMAT	23	Norske Skog Tasman

Figure 6: New additions to geothermal power in New Zealand post 2011

1.1 The Problem

The ORC power plants are complicated systems with a significant influence of components on each other and performance of the entire system. Heat exchangers form a crucial part of geothermal power plants at all stages of the plant – starting with claiming a major portion of the capital cost for commissioning the plant right up to governing the working (and hence profitability) of the plant in terms of deciding the plant downtime (for maintenance) and plant performance (preheaters/vaporizers/superheaters should be able to provide a minimum degree of superheating to working fluid and this minimum value decides the maximum value of working fluid mass flow rate through the plant which translates into plant's net electric power output). Although heat exchangers have such a critical influence on the life-time profitability of power plants, their designs are still based on empirical/semi-empirical models which form a constraint towards predicting their performance if the unit is operating in off-design conditions or is different in some geometrical aspects from the units that were used in experiments generating the empirical/semi-empirical models.

This project endeavours to develop a CFD approach towards understanding the – a) boiling process within a vaporizer, and also b) single phase heat exchangers (preheaters/superheaters) with the potential to extend this approach towards troubleshooting and possibly designing vaporizers in future.

In discussions with plant managers within New Zealand, it was found that some vaporizer units are unable to provide the stated degree of superheating. It is necessary to understand the boiling process within a vaporizer if we hope to progress to troubleshooting. This project is focused towards this objective and has two approaches to simulating a vaporizer – a) empirical/semi-empirical approach using MATLAB™, b) a combination of mechanistic modeling

(CFD, Computational Fluid Dynamics) and empirical/semi-empirical models using ANSYS™ CFX™ and Fluent™ modules. There are advantages and disadvantages to both these approaches. While the MATLAB™ approach is faster but it depends on existence of correlations/methods in literature for the vaporizer geometry and operating conditions to be analyzed. The CFD approach gives a more intuitive and visual understanding of the actual boiling process but it is intensely demanding of computational power if we want to study multi-tube industrial scale geometries. It also requires validation and tuning which requires availability of suitable experimental data in existing literature. In the case of geometry and working fluid being analyzed in this study, both of the aspects were found lacking. In view of dearth of existing models/data to build up on, the project started with developing CFD models for single-tube geometries as there is vast and detailed experimental data available for such cases. These set-ups and analyses will be validated against experimental values. Subsequent to CFD of single-tube boiling, multi-tube geometry will be analyzed and validated against available experimental data. To fine tune CFD set-up parameters for pentane boiling simulation, a suitable substitute fluid will be selected based on dimensionless numbers that characterize bubble dynamics and boiling process. A CAD model of full scale pentane vaporizer will be developed which will be used in the final stages of the project for CFD analysis. This CFD analysis will provide vapor velocity field data above the tube bank which will be used in conjunction with MATLAB™ code(s) for predicting droplet trajectory.

Degree of fidelity of the solution achieved by the Thesis

The envisioned goal of the project is to gain a deeper understanding of the boiling process inside a kettle vaporizer with two main objectives:

a) Analysing the relationship between liquid level and heat transfer performance in a vaporizer
b) Analysing the probability of droplet carryover from the vaporizer

The project is able to deliver satisfactorily on a number of crucial aspects while simultaneously not being able to thoroughly analyse some other aspects of the problem:

- The validation of the CFD analysis of single-phase heating in preheaters is complete – quantitatively and qualitatively. There are no case- dependent parameters in the CFD set-up of such simulations which gives them high credibility and wide spread applicability.
- The validation of CFD analysis of single-tube geometries is complete – quantitatively and qualitatively. There are a number of user-modifiable case- dependent parameters in the set-up for phase-change applications, but the existence of vast literature on single-tube boiling experiments is able to provide the project with all the required data/parameters. This gives high credibility to these results.
- The validation of CFD analysis of multi-tube geometries is complete – qualitatively/semi-quantitatively. There was not found much literature for detailed experiments on boiling of hydrocarbons under high pressure in multi-tube geometries. The validation is credibile in light of the available data (which was not as detailed as single-tube boiling data) as no differences with the recorded data in the literature were observed

- The MATLAB™ code for analysing the vaporizer gives values within 5% of real-world data with only one "tuning" factor. The factor mentioned as "tuning" factor here is actually the effectiveness (ϵ) in the ϵ-NTU method of heat exchanger analysis.
- The validation of multi-tube geometries has been completed qualitatively and semi-quantitatively.
- The selection of substitute fluid has been done on the basis of – a) behavior of thermophysical properties against pressure, b) dimensionless numbers characterizing bubble dynamics and boiling process.
- A parametric study has been carried out on a STHE slice geometry with different inflow rates and the results match predictions based on real world data. This needs to be validated quantitatively to the same detailed extent in future as is currently possible for single-tube geometries. No suitable reported values were found in the literature to complete this quantitative validation.
- The droplet trajectory prediction is based on a MATLAB™ code that has been developed by a previous PhD candidate. This code has been enhanced to be able to factor in varying velocity of surrounding medium at different coordinates. The droplet vaporization has been analyzed using ANSYS™ CFX™ for the worst case scenario (vertical ejection with vapor pushing it upwards).
- A preliminary CFD analysis has been done on the scaled down representative geometry based on a full-scale CAD model of a pentane vaporizer that was also developed as part of the project.
- A preliminary design for a lab is also presented that could be set-up and used to fine-tune multi-tube CFD analysis set-ups.

1.2 Thesis Layout

Background Study and Literature Review

Chapter 2 presents the literature review for the project. This includes detailed study of thermal-modelling approaches for heat exchangers with emphasis on Shell-and-Tube Heat Exchangers (STHEs) and Plate Heat Exchangers (PHEs). Nucleate boiling has been studied with various modelling approaches, which have been developed over the years, outlined along with correlations used. The models used for Bundle Boiling are reviewed and the differences between single-tube and multi-tube boiling are studied and presented. Bubble dynamics has been studied and analyzed with investigation into how the initial perceptions of the mechanism of heat transfer were transformed with detailed experiments in recent years. A mechanistic approach has also been reviewed and presented here which has the potential to make CFD simulations much closer to real world conditions once it is implemented into the CFD set-up. A brief review of Navier-Stokes equations solved by ANSYS™ CFX™ is also given.

MATLAB™ Modelling

Chapter 3 presents the mathematical modelling, comparison of results to experimental/real-world data for PHEs and STHE vaporizers and discussion on observations.

CFD Validation

Chapter 4 presents the CFD modelling and validation of – a) single-phase heating, b) phase-change in single-tube geometry, c) phase-change in multi-tube geometry, and d) selection of a substitute fluid for pentane vaporization simulation studies in view of the lack of experimental data available for pentane.

Heat Transfer Performance vs. Liquid Level

Chapter 5 presents the observations and discussions on the study done on a slice of STHE kettle type vaporizer.

Droplet Carryover Analysis

Chapter 6 presents the concept of droplet trajectory prediction based on MATLAB™ code with vapor velocity data extracted from CFD-Post™. It also presents results from CFD study for worst case scenario of droplet ejection right underneath an outlet in vapor space.

Conclusions and Future Work

Chapters 7 & 8 present the conclusions from current project, summarize constraints while suggesting approaches to mitigate these constraints and present some preliminary analysis and lab design.

2.0 Literature Review

2.1 Heat Exchangers

Heat Exchangers (HEs) are a crucial component of all power generation systems. In geothermal power plants these are employed at two essential stages: a) transfer of heat from geothermal brine to working fluid, b) cooling and condensing the working fluid post turbine. Some plants might employ another HE as recuperator to recover heat from spent working fluid to preheat working fluid. The transfer of heat from brine to working fluid leads to vaporization of the working fluid. This can be divided into three stages – a) sensible heating of liquid phase (preheating), b) latent heating (vaporization), c) sensible heating of vapor phase (superheating). In smaller plants all three stages might occur within same HE whereas in larger plants every stage has one or more dedicated HEs (Figure 7).

Figure 7: A 20.5 MWe unit at Ngatamariki plant (3 preheaters, 1 vaporizer and 1 superheater) (Type – STHE)

A variety of HEs are available depending on operating conditions (OCs) and application requirements. Some of the mainstream HE types are [147]: Double

pipe (hair pin) heat exchanger, Shell and tube heat exchanger (STHE), Coiled tube heat exchanger (CTHE), Finned-tube heat exchanger, Air cooled heat exchanger, Plate-fin heat exchanger, Regenerator, Plate heat exchanger (PHE), Spiral plate heat exchanger (SPHE), Printed circuit heat exchangers (PCHEs), Lamella heat exchanger, Heat pipe heat exchanger, Plate coil heat exchanger (PCHE), Scraped surface heat exchanger, Helical baffled STHEs.

HEs can be classified on a number of bases, as is shown in Figure 8 [120].

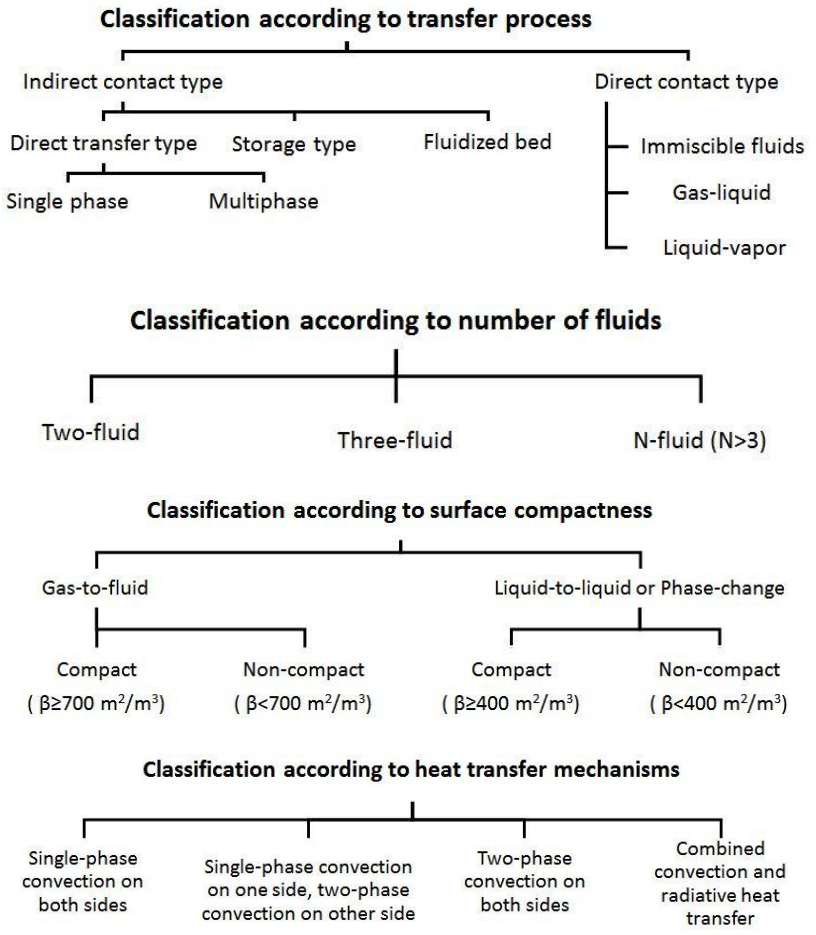

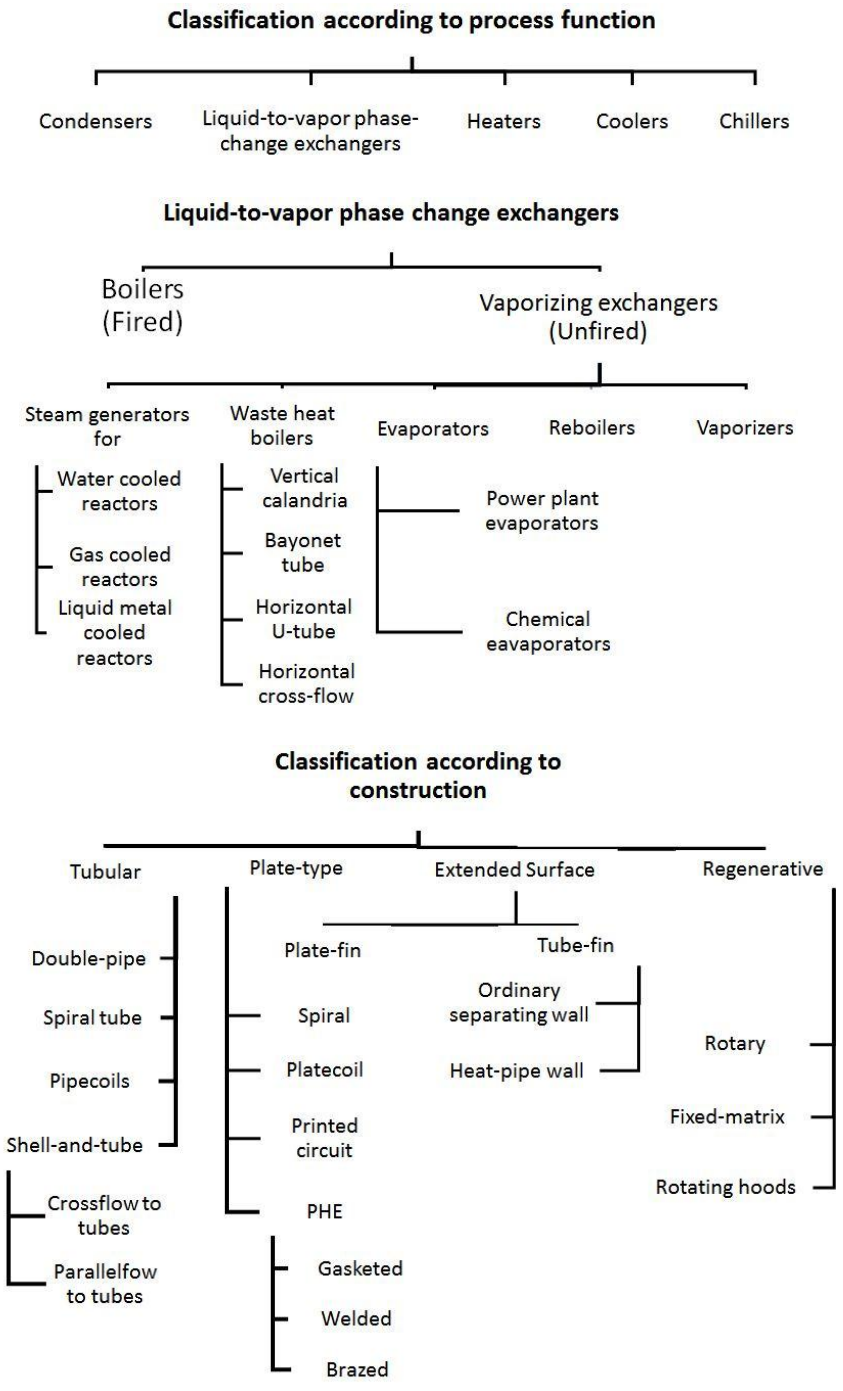

Figure 8 - Detailed classification of Heat Exchangers

STHEs are the “workhorses” of the industrial heat transfer processes. More than 90% of the heat exchangers used in the industry are of this type [147]. They are the first choice because of well established procedures for design and manufacture from a wide variety of materials, many years of satisfactory service and availability of codes & standards for design & fabrication. They are produced in the widest variety of sizes and styles. There is virtually no limit on the operating temperature and pressure [147]. Figure 9 provides an overview of classification standard for STHEs [147].

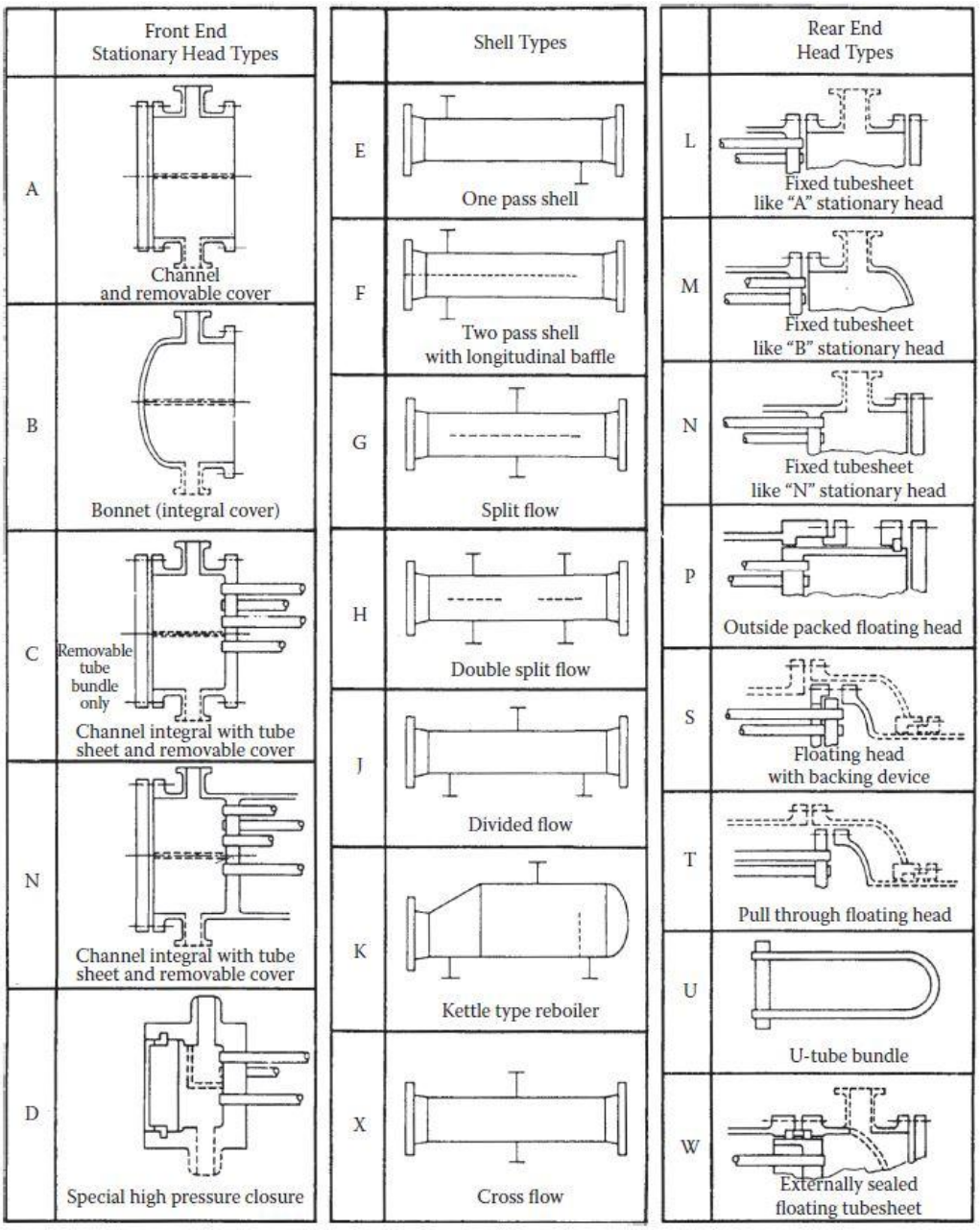

Figure 9: Nomenclature for heat exchanger components [Standards of Tubular Exchangers Manufacturers Association, 9th edition, 2007]

The major geometrical factors that affect the performance of heat exchangers are tube-pitch & arrangement, and how the tube-side or shell-side passes are

configured. The tube-pitch is the ratio of distance between the centres of two tubes to the outer diameter of tubes. The tube-arrangement and pitch are explained in Figure 10 [147].

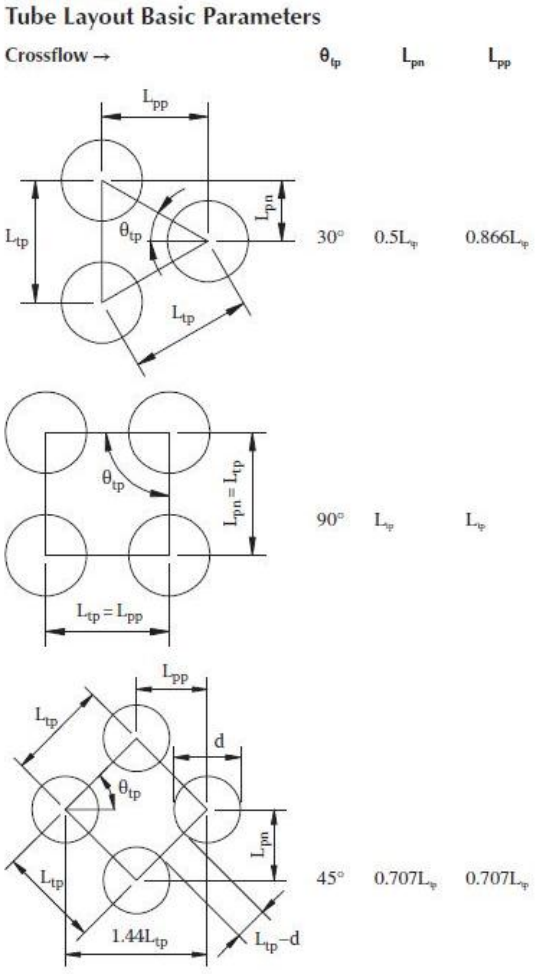

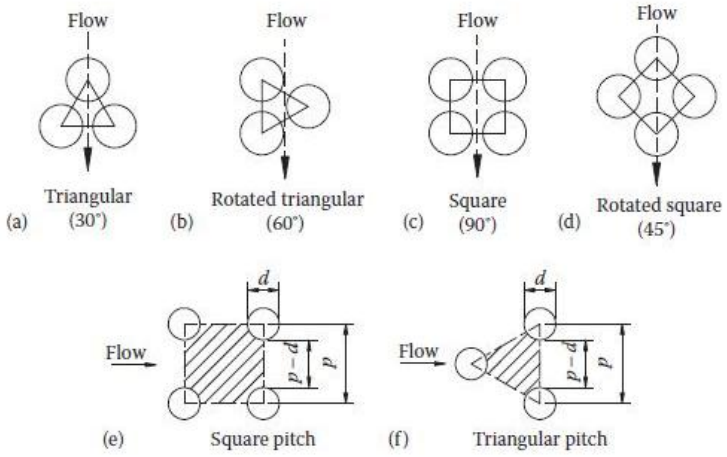

Figure 10 - Basic terms regarding tube arrangements and Tube-layout patterns: a) 30o; b) 60o; c) 90o; d) 45o; e) flow area for square pitch; and f) flow area for triangular pitch

The manufacturing of STHEs is regulated by various codes and standards which are briefly summarized Appendix 1: HE Standards & Codes.

In smaller ORC installations PHEs are also increasingly being used due to following benefits:

- high turbulence
- true counter-flow
- low weight
- smaller footprint
- expansion/reduction capabilities
- easy accessibility for maintenance
- quick process control, and
- low hold-up volume

Figure 11 [147] provides an overview of constructional features of a plate heat exchanger.

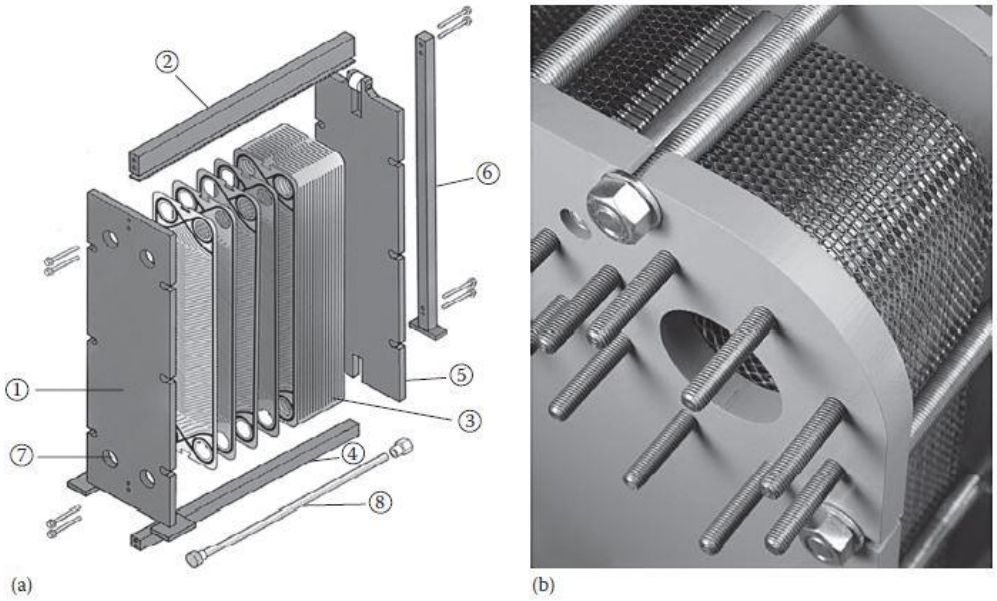

Figure 11: PHE; (a) Construction details—schematic (1, Fixed frame plate; 2, Top carrying bar; 3, Plate pack; 4, Bottom carrying bar; 5, Movable pressure plate; 6, Support column; 7, Fluids port; and 8, Tightening bolts.) and (b) closer view of assembled plates

2.2 Heat Transfer in Heat Exchangers

Processes that require vapor generation commonly use shell-and-tube heat exchangers (STHEs). Also, STHEs are used for condensing vapor. In both the applications, boiling and condensation, the phase change is usually occurring on the shell-side, which is a very complex and not yet fully understood process. Any predictive models existing at the moment are either based on very limited amount of experimental data or require too much input information which is normally not available. The thermal design of reboilers is complex as they are characterized by a 2-phase flow controlled by a general natural recirculation pattern, which makes it difficult to model the heat transfer on the outside tube wall linked to the hydrodynamic conditions of the evaporating fluid [90]. Also, the heat transfer coefficient is dependent on the position of the tube and layout of the bundle, and the magnitude of this influence is also dependent on the heat flux applied and pitch-to-diameter ratio [95]. However, modelling is necessary for efficient and cost-effective design process. The goal is usually to design a heat exchanger with high overall heat transfer coefficient, minimal pressure drop and even thermal stress distribution. Thus, the efficient designs of STHEs often require high fluid velocities on the shell side, while an optimal and cost-effective design would necessitate as much reduction in structural support as possible [51]. However, increase in the shell-side fluid velocities in conjunction with reduced structural support can potentially lead to excessive, and possibly damaging, flow-induced vibrations of tubes. Therefore, it is of utmost importance to have good knowledge about two-phase flow phenomena on the shell side, because it forms an integral part of models predicting the two-phase flow induced vibrations.

The design for the complete life-cycle of a heat exchanger has numerous considerations which can be broadly divided into following stages [121]:

- Problem formulation
- Concept development
- Detailed exchanger design
- Manufacturing
- Utilization considerations (operation, maintenance, phase-out and disposal)

The first three stages of the design of a STHE are interlinked through various feedback loops and start with the specification of heat duty required and operating conditions, working fluid(s), selection of a few of the TEMA types of heat exchangers which are suitable for our use, and the inlet temperature of the hot fluid. The critical component of the design is heat duty required from the heat exchanger and the size of the exchanger will depend on the heat transfer coefficient. The heat transfer coefficient is dependent on a number of parameters such as tube length, tube diameter, tube bundle diameter, tube pitch, surface roughness, configuration of passes, working pressures, working fluid, degree of superheat available etc. Some of these parameters cannot be changed and others are varied to achieve the best heat transfer performance. The heat transfer performance and the pressure drop need to be carefully balanced against each other as most of the factors that enhance heat transfer performance also lead to greater pressure drop which may not be allowable in all cases. Starting with these constraints and any others that may vary on a case-to-case basis, the design phase of a heat exchanger starts with the thermal design (including pressure drop analysis) preceding the mechanical design which is mostly limited to stress calculation and flow induced vibration analysis.

A general approach which may be adopted for heat exchanger design is shown in Figure 12 [147].

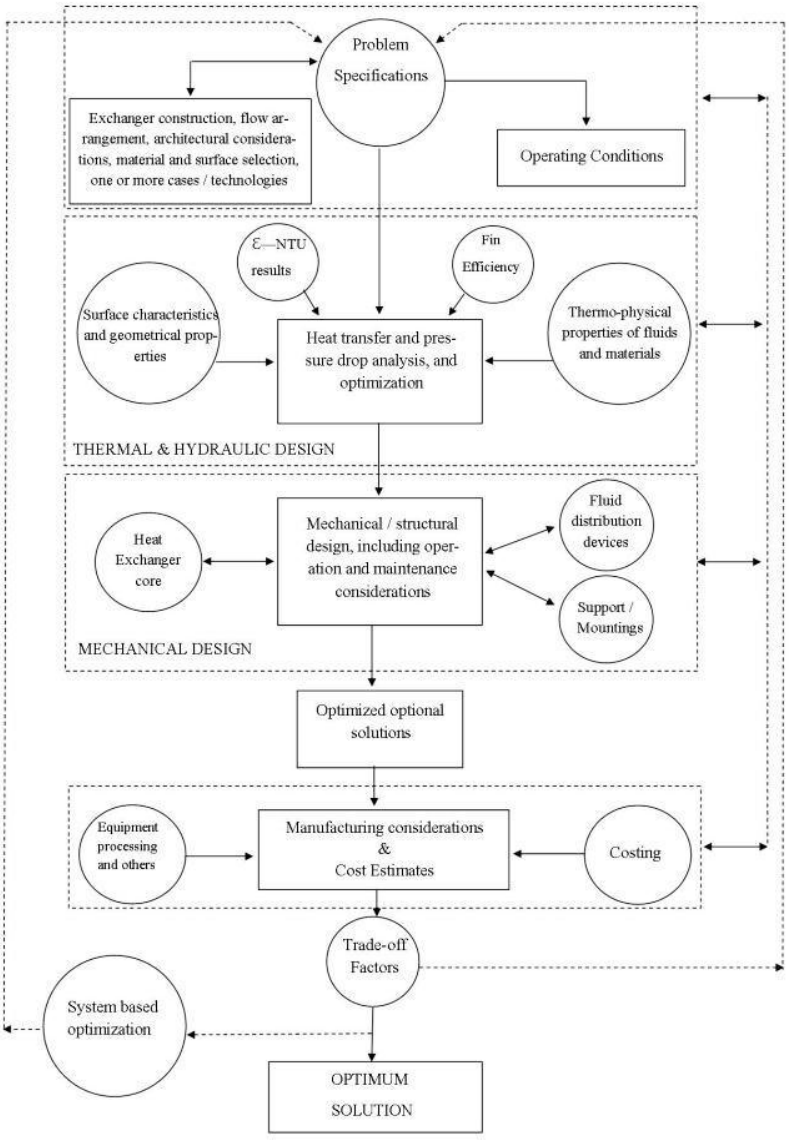

Figure 12 - General methodology for heat exchanger design

The most important parameter determining the final size of the heat exchanger is its overall heat transfer coefficient which is a combination of tube-side and shell-side heat transfer coefficient. Given the conservative approach of current

standard design methodology (owing to incomplete inclusion of all the parameters influencing the heat transfer performance), the heat exchangers are oversized, and any improvement in the accuracy of heat transfer performance will directly translate into right-sizing of the heat exchangers and cost savings as heat exchangers form a major part of initial capital investment.

The two-phase flow pattern (results of an experimental observation are presented in Figure 13 [12]) has a large influence on the heat transfer rate in a STHE dealing with phase change on the shell-side, especially by the recirculation occurring among the tube bundle. The recirculation pattern is again dependent on the heat flux [12] and on the configuration and number of tube-side passes. Another important design consideration is the vapor disengagement area, as the disengagement effects can not only alter the pressure drop profile in upper parts of the bundle at heat fluxes higher than 20,000 W/m^2 and thus reducing the mass flux at the top but can also reduce the heat transfer coefficient increase up the bundle [12].

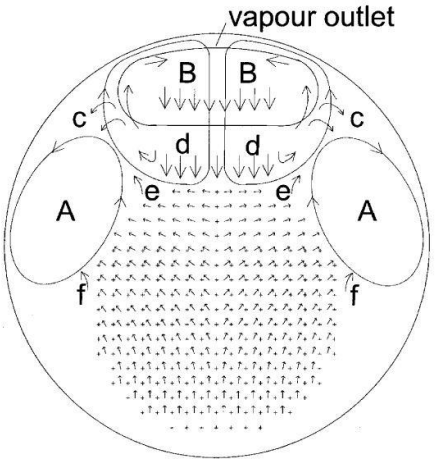

Figure 13 - Flow pattern in thin kettle reboiler slice, at 50,000 W/m2

As a consequence of many uncertainties in the predictive models for heat transfer in flooded-type evaporators, safety margins taken for the thermal

design of heat exchangers are quite large, and result in an overly conservative design of vaporizers [1, 90, 115].

The heat transfer coefficient varies across a wide range on the shell-side. It is mainly due to the 'bundle effect' and recirculation occurring on the shell-side. The local heat transfer coefficients in case of bundle boiling also increase with an increase in the local vapor quality, and are larger than the corresponding nucleate pool boiling heat transfer coefficient [145].The variation in the heat transfer coefficient as the boiling regime goes through changes (from natural convection, through to nucleate boiling and finally film boiling) as fluid rises through the tube bank is aptly represented by Figure 14 [56]. The transition in the

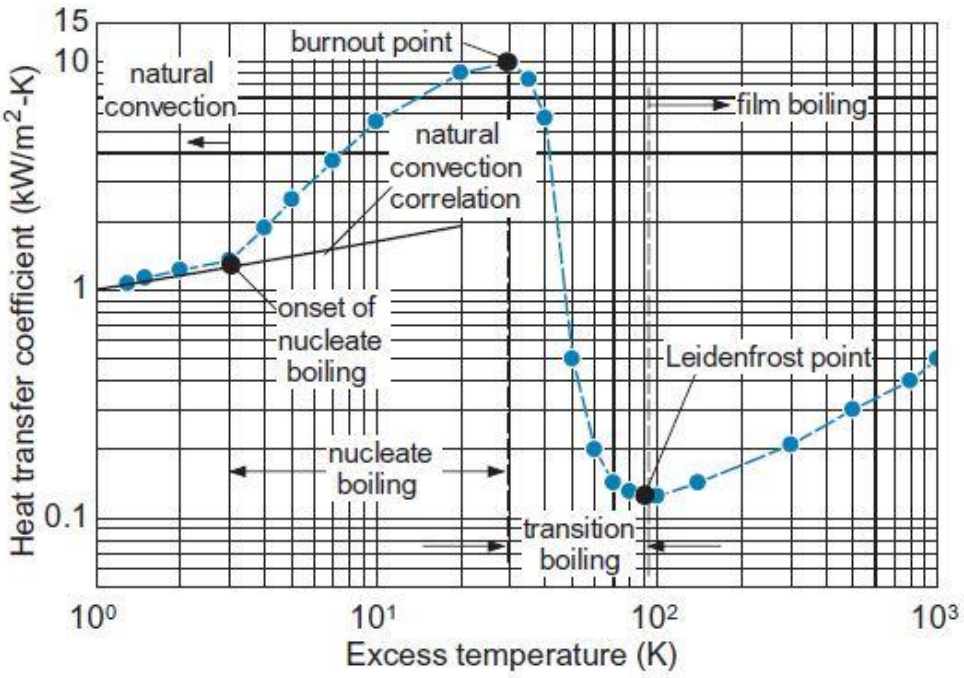

Figure 14 - Heat Transfer Coefficient as it changes along the boiling curve, Nukiyama (1934)

2.2.1 Two Phase Flow Patterns in Tube Bundles

Heat transfer on the shell-side and particularly vaporization is of utmost interest and importance for the power-generation industry, as it is not understood comprehensively at the moment and any variations or unexpected occurrences in this process can have cascading and damaging effects on the plant efficiency and/or even hardware. The main difficulty in the thermal design of horizontal vaporizers is the determination of shell-side heat transfer coefficient and in order to have a better design and prediction of shell-side heat transfer coefficient, more information on the two phase flow distribution in tube bundles is required [1, 89].

An illustration of the complexity of the problem can be given via Figure 15 [53] where a wide disparity is seen between visual results from two different studies and also between observed and calculated results. To overcome, the differences in results produced by visual observations, recently studies are being done to investigate gas-liquid flow across tube bundles via digital particle velocimetry (DPIV) techniques. These studies are still focusing on pre-mixed gas-liquid flows and examples from one such study can be seen in Figure 16 [96].

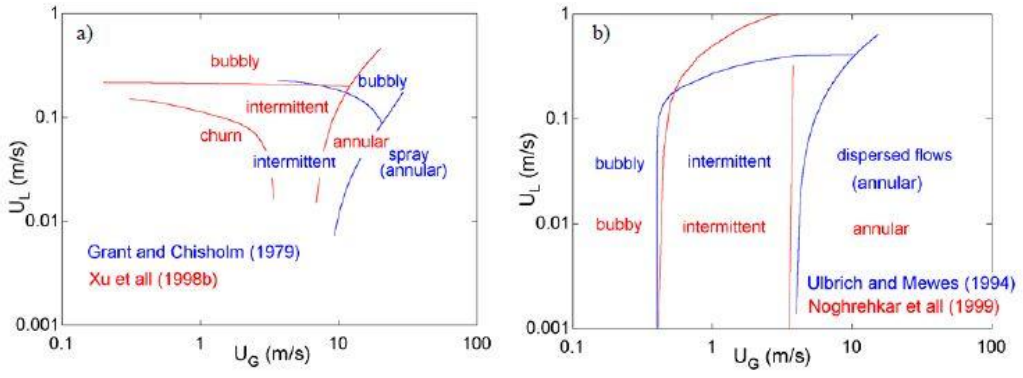

Figure 15 - Comparison of shell-side flow patterns maps. a) Maps based on visual observations; b) Maps based on objective methods

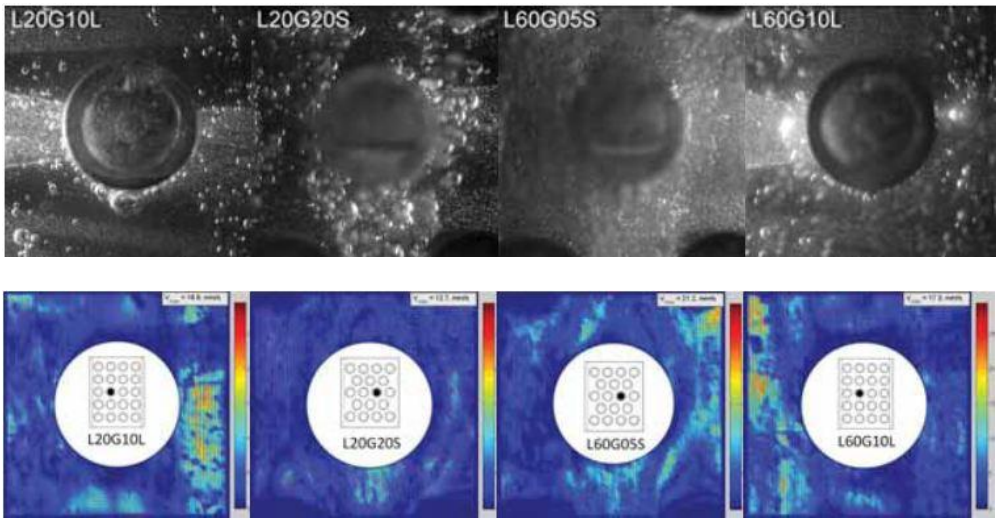

Figure 16 - Exemplary images from study done on flow patterns using DPIV techniques

The vapor and liquid phase velocity fields and the related void fractions are important for the operational characteristics of steam/vapor generators: void fraction determines the swell level position, both void fraction and phases' velocity fields determine the two-phase flow structure and heat transfer from the tubes to the boiling mixture, and a possible occurrence of the critical heat transfer due to tube dryout [153]. There is a close connection between the heat transfer regimes and flow regimes existing on the shell-side [55, 90].

Aprin et.al. [90] identified two distinct flow regimes along with an intermittent regime between the two: 'bubbly' flow and 'dispersed' flow (shown in Figure 17 [90]) separated by 'intermittent' flow. Bubbly flow is characterized by a vapor phase distributed as discrete bubbles in a continuous liquid phase, and is found in the lower part of the tube bundle. Dispersed flow is characterized by a continuous vapor phase in which liquid droplets are carried. In the bubbly flow regime, the bubbles produced on the tubes are smaller than the distance between the tubes, and slide along the tube wall; heat transfer is governed by nucleate boiling heat transfer mechanism, and is dependent only on heat flux.

In the dispersed flow regime, vapor bubbles coalesce, and vapor phase tends to occupy the space between the tubes, coupled with an increase in the vapor velocity. The thickness of the liquid layer on the tubes decreases, and the nucleation boiling on the tube surface is totally replaced by evaporation at the liquid/vapor interface; heat transfer being of convective type, and dependent on the vapor mass flow rate and vapor quality.

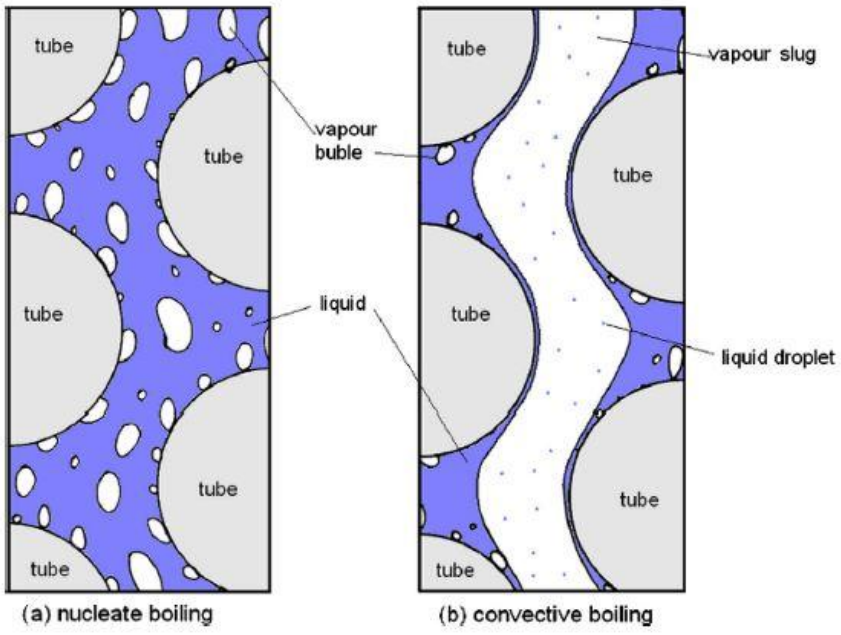

Figure 17 - Heat transfer mechanisms for boiling flow, a) Nucleate boiling mechanism in staggered smooth tube bundle, b) Convective boiling mechanism in staggered smooth tube bundle

There are various issues that need to be understood w.r.t. to the vaporization process occurring on the shell-side in a heat exchanger:

- Level of liquid in the vaporizer
- Accurate prediction of local heat transfer coefficient at different regions in the heat exchanger
- Void fraction data

The design of such equipment has primarily been based on correlations derived out of single-tube pool-boiling data with various correction factors being employed to account for the effect of neighboring tubes. It is now widely accepted that this approach has led to overly conservative designs [115]. It is primarily due to the lack of sufficient information about local hydrodynamic and boiling characteristics in a multi-tube bundle.

It has been estimated that nearly half of all process heat exchangers operate in two-phase flow [50]; however, our understanding of two-phase cross-flow in tube bundles is far from satisfactory, in comparison to that related to in-tube phenomena [51]. It has been observed that for any complete modelling of the two-phase flow regimes and recirculation patterns, surface tension effects will have to be included to deal with the disengagement process [12].

There have been numerous studies into the two-phase flow pattern on the shell-side and it is an area of continuously ongoing research. Notable examples of previous studies are the ones done by Schrage et.al. (1988), [115], [106], [153], [44], [73], [50] [51]. The two main areas of research are void-fraction prediction correlations and frictional pressure drop prediction correlations. The void fraction and pressure drop measurements obtained by these investigators produced bundle average or pitch average values that were used in the formulation of various correlations. These correlations were formulated without any reference to the flow phenomena that occurred in the passages between the tubes. For example, shell-side two-phase frictional multiplier correlations are extensively used. They are based on the assumed similarity with pipe frictional pressure drops. However, shell-side pressure drop is mechanistically different; as the pipe flow pressure drops are due to wall friction, whereas shell-side pressure drops are due to flow separation and re-attachment phenomena [32].

2.2.2 Void Fraction in Tube Bundles

To understand and model the two-phase flow on the shell-side, the most important piece of information is the void fraction data, as it is an important parameter for both the heat transfer and pressure drop. This is because changes in pressure throughout the bundle alter the saturation temperature and hence the heat transfer coefficients [99].

There are 3 main types of flow models that can be used for prediction of void fraction values, and their use depends on the particular application. These are:

a) Homogeneous flow model
b) In-tube flow model
c) Separated flow model

An accurate representation of the pressure drop in a tube bundle is, therefore, necessary for a satisfactory model to be developed. For the calculation of the pressure drop in the bundle, the flow can be assumed to be homogeneous or separated. A homogeneous model is used when it is assumed that the liquid and the vapor phases have equal velocity and are in thermodynamic equilibrium. In this case the void fraction can be determined from the vapor quality. In a separated flow model, the liquid and the vapor have different velocities and there is an interaction between both the phases, hence the void fraction must be calculated from an empirical correlation.

The measured void fraction data are also seen to be significantly lower than the values predicted by the homogeneous flow model [115] evaluated at an approximately averaged pressure used in the experiment, and given by:

$$\alpha_H = \frac{1}{1 + \left(\frac{1-x}{x}\right)\left(\frac{\rho_g}{\rho_l}\right)} \quad (1)$$

For a given quality in the equation 1, a higher phase density ratio leads to a lower value for the predicted void fraction, as was found by comparison of void fraction values of R-113 (obtained by [115]) to the values of void fraction for air-water mixture (obtained by [113]), with lower values for R113 as the density ratio for R-113 is four times that for air-water mixture. With an increase in the quality, the effect of the density ratio on void fraction is reduced, and similar void fraction values are obtained.

Overprediction by the homogeneous model has been noted by several authors ([30, 106, 113, 114]) as pointed out by [53]. This overprediction is again attributed to the assumption of no slip (i.e. mixing is occurring between the two phases) between the phases in the homogeneous flow model, the validity of which depends on the degree of mixing achieved by the two phases. At low mass velocities, the effect of buoyancy is significant, especially at low qualities, and there is considerable difference in phasic velocities. At high mass velocities and low values of quality, turbulence in the liquid phase helps in the mixing of the two phases and a more homogeneous mixture is obtained and the values obtained approach those predicted by the homogeneous model [53]. Similarly, the in-tube void-fraction models based on the Lockhart – Martinelli parameter, overpredict the void fraction values as compared to the data of Dowlati et.al. [106] although the overprediction has not been quantized by authors [115].

Void fractions tend to increase rapidly with height in a tube bundle, but may decrease somewhat in the upper regions. Relatively large vapor concentrations are observed in the central region of the tube bundle due to strong recirculation effects of vapor from the upper portions of the bundle that enter the central region, in addition to vertical vapor acceleration at the bundle exit. Horizontal void concentrations are observed to be fairly uniform [73].

Also, most of the studies done to develop two-phase void fraction prediction models used adiabatic two-phase flows [89], which is a situation totally different from actual operating conditions, where the vapor is generated on the tubes and thermohydraulic parameters keep changing in both vertical and horizontal directions inside a tube bundle.

2.2.3 Heat Transfer during Boiling

Boiling is a complex process in which mass, momentum and energy transfer (single- and two- phase) involving a solid wall, liquid and vapor are tightly coupled [87]. A single bubble on a hot surface is assumed to nucleate when the superheated liquid layer above the surface becomes thick enough to enable the vapor phase trapped in it to overcome the surface tension force holding the liquid layer flat and grow and consequently depart from the surface. The overall heat transfer in a tube bundle is a result of tube-side heat transfer coefficient, and nucleate boiling & convective boiling regimes on the shell side.

2.2.3.1 Nucleate Boiling

Commonly used nucleate boiling correlations can be divided in two broad categories on the basis of the parameters they use to calculate the nucleate boiling heat transfer coefficient [23]:

a) Reduced pressure based correlations – these predict the boiling heat transfer from the macroscopic heat transfer perspective, notable examples being the Cooper correlation [23, 24], Borishanski correlation [23], Mostinski correlation [23], and Gorenflo correlation [33]. (Reduced pressure is the ratio of operating pressure to critical pressure.)

b) Thermophysical properties based correlations – these are generated on the basis of microscopic heat transfer mechanisms associated with bubble growth dynamics, notable examples being Rohsenow correlation [126], Stephen & Abdelsalam correlation [82], Forster & Zuber correlation [59].

Another classification of the correlations is based on their origin and mechanism, viz.:

a) Empirical Correlations - based on curve-fit of the experimental data, e.g. Jung correlation [29], Stephen-Abdelsalam correlation [82]
b) Semi-empirical Correlations – based partially on experimental data and partially on actual physics (variations in thermophysical properties and their effects on bubble dynamics and heat transfer coefficient), e.g. Rohsenow correlation [126]

2.2.3.2 Pool Boiling

Pool boiling heat transfer has been extensively studied over decades, but it is only recently that the effect of boundary heating conditions (water-heated tubes vs. electrically heated tubes) on the heat transfer during the boiling process started being noted. Different heating methods lead to different boiling curves. The fluid-heated smooth tube boiling heat transfer by McManus (1986) [133] differs by as much as 50% from the electrically-heated boiling heat transfer data by Memory [128, 131] as is pointed out in [23].

In an experimental study of pool boiling of R123 on four commercial enhanced tubes, done by Kedzierski [84], it was found that the boiling curves generated in the fluid-heated boiling experiments were located to the left of those generated by electrically-heated boiling experiments, indicating that the fluid-heated boiling process has better performance as compared to

electrically-heated boiling process. Similar behavior was observed by Darabi et.al. [65].

The understanding of the underlying mechanisms responsible for this behavior is not yet complete, due to scarce water- or fluid- heated boiling data in relation to the electrically heated boiling data.

The two main points regarding the heat transfer coefficient from a tube that have been established by many recent experimental investigations are [34]:

a) There exist common relative dependencies of the heat transfer coefficient on the reduced pressure at constant heat flux, and on heat flux at constant reduced pressure, which hold within comparatively narrow limits of error for all hydrocarbons in nucleate pool boiling on horizontal copper tubes with mean surface roughness heights of about 0.4 μm, and
b) The heat transfer coefficient at constant values of heat flux, reduced pressure and surface roughness also follows a common dependence on the thermophysical properties of the fluid boiling on the tubes, which is expressed by the ratio of the slope of the vapor pressure curve and surface tension.

The dependence of heat transfer coefficient in pool boiling conditions (single-tube boiling) on ‘heat flux’, ‘reduced pressure’ and ‘thermophysical properties (of working fluid, specifically hydrocarbons)’ can be correlated by general semi-empirical functions with comparatively narrow limits of error that do not reach far beyond the experimental scatter occurring when different sources are compared for the same substance under similar conditions [34].

Recently, a new theoretical approach to understanding the pool boiling heat transfer mechanisms has been proposed [125], where a statistical

thermodynamic heat transfer theory has been proposed, which is applicable to heat transfer mechanisms of both conduction and internal convection. It is able to model the kinetics of phase transition mechanisms at the interface of two different phase materials. It can exactly account for the heat flux profiles for the four mechanisms of natural convection, nucleate boiling, transition boiling and film boiling. In other words, it produces heat fluxes in pool boiling as a function of temperature, time and space in the whole range of boiling regimes. This can be applied and extended to flow boiling situations, and enhancing the heat transfer of thermodynamic devices [125].

The heat transfer mechanisms and their relative contribution in the overall heat transfer process is a subject of intense investigation and a review of the literature reveals a significant difference in opinion among researchers. The overall heat transfer during single bubble generation in pool boiling conditions can be divided into distinct mechanisms –

- transient conduction,
- micro-convection (a.k.a. bubble agitation),
- micro-layer evaporation (a.k.a. micro-evaporation), and
- three-phase contact line heat transfer

The relative contributions of these mechanisms are different during bubble growth and bubble departure. The various mechanisms of heat transfer during bubble generation are clearly outlined in Figure 18 [87].

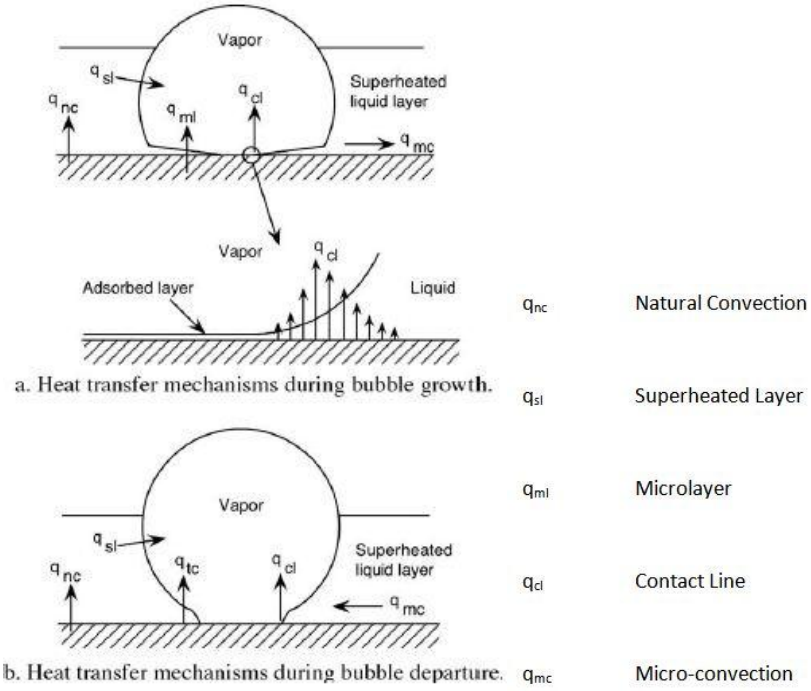

Figure 18 - Delineating various heat transfer mechanisms during bubble growth and departure

Different researchers have given varying amounts of contributions to these mechanisms and developed their models accordingly.

Mikic & Rohsenow (1969) [11] developed their transient conduction model building on the work of Han & Griffith (1965) [20, 21]. The physical model is shown in Figure 19 [11]. The heat transfer mechanism as per Mikic & Rohsenow is shown in Figure 20 [87].

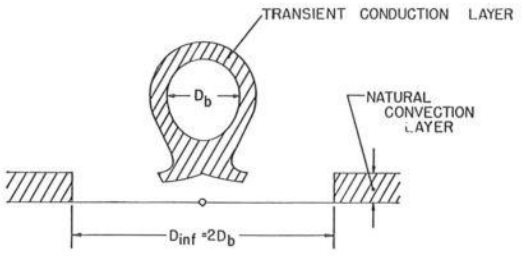

Figure 19 - Physical model of transient conduction mechanism

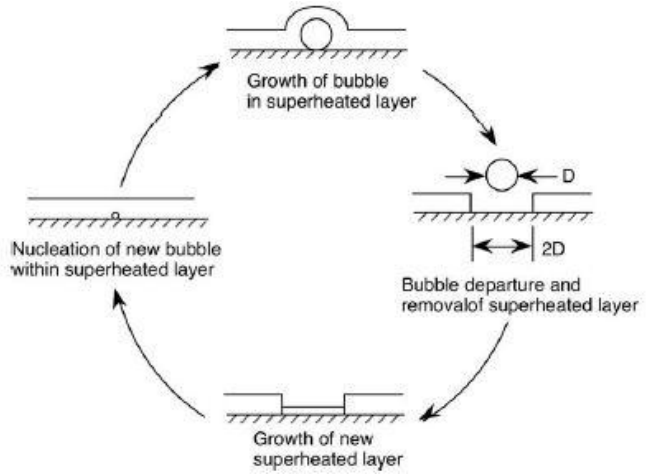

Figure 20 - Bubble heat transfer mechanism suggested by Mikic & Rohsenow (1969)

Microlayer heat transfer, a.k.a. microlayer evaporation has been put forward as the domination mechanism by a number of researchers, Snyder & Edwards (1956), Moore & Mesler (1961) [43], Hendricks & Sharp (1964) [119], Cooper & Lloyd (1969) [97], Wei et.al. [67], Cornwell & Houston [86]. The model for bubble growth with microlayer heat transfer presented as the dominant mechanism is shown in Figure 21 [97].

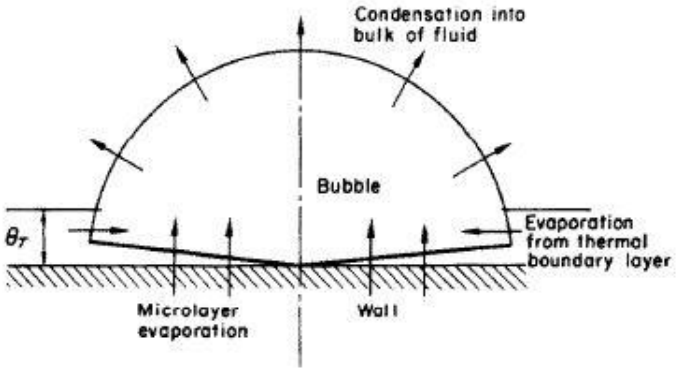

Figure 21 - Model for bubble growth

The contact line heat transfer model was put forward by Stephan & Hammer (1994) [105]. According to [105], because of the thin liquid film in the micro region (Figure 22 [105]), the heat fluxes can be very high, provided that the thermal conductivity of the working fluid is much lower than that of the wall material. Usually this is the case for the combinations of a metallic wall and organic/inorganic working fluids. The high evaporation rates in the micro region then create a significant transverse liquid flow which is driven by mechanisms implying variations of K and T_i.

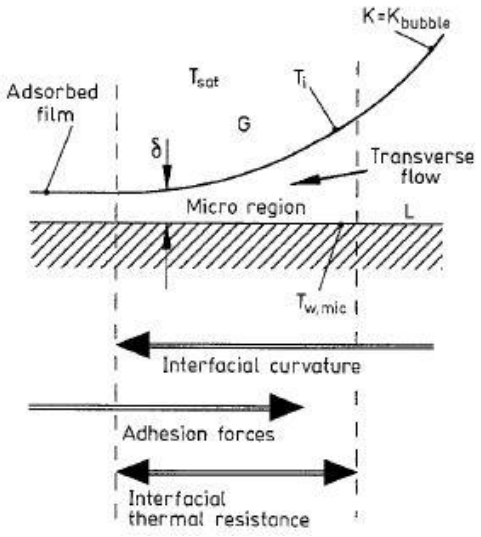

Figure 22 - Significant phenomena in the micro region (Contact line heat transfer model)

In recent experimental investigations the mechanisms of heat transfer during bubbling events under pool boiling conditions have been studied on micro-scales and all the different mechanisms have been properly delineated and their relative contributions measured and presented. The dominant mechanisms have been found to be transient conduction and micro-convection. e.g. Kim [87] states that the dominant heat transfer mechanisms are transient conduction and micro-convection (bubble agitation) while the microlayer evaporation and contact line heat transfer have a less than 25% contribution.

Myers et.al. [71] have put forward findings similar to Kim [87], clearly stating transient conduction and/or micro-convection (bubble agitation) as the dominant heat transfer mechanisms. Moghaddam and Kiger [135] also presented results limiting the contribution of microlayer evaporation to maximum of 28.8% (in agreement with Judd & Hwang [117]), and negligible contribution by contact line heat transfer mechanism; and the contribution of micro-convection was observed to increase as the wall temperature increased, while transient conduction is more dominant at lower surface temperatures. The main mechanisms are therefore transient conduction and micro-convection with their relative dominance a function of surface temperature; transient conduction dominating at low surface temperatures and micro-convection dominating at high surface temperatures. Another significant finding is that transient conduction starts well before the bubble departure, which is in complete contrast to the usual definition of transient conduction in boiling literature. This is significant because although the study by Kim [87] demonstrates and states the transient conduction as one of the two dominant mechanisms, their definition is different from the definition given to transient conduction by Mikic & Rohsenow [11]. Mikic & Rohsenow [11] developed a heat transfer model for bubble growth and departure that assumed that the departing bubble scavenges away the superheated layer surrounding the bubble over an area twice as large as the bubble departure diameter allowing colder bulk liquid to contact the surface, while no wall heat transfer was assumed during the bubble growth. The superheated layer is only renewed during the waiting time (the time after bubble departure and before nucleation of a new bubble) by transient conduction into semi-infinite liquid. This transient conduction into this bulk liquid was assumed to be dominant mode of heat transfer. On the other hand, the study by Kim [87], found contrary to what as expected as per the Mikic & Rohsenow theory as the large heat transfer by

transient conduction was observed during the wall rewetting process before the bubble actually departs and not during the regrowth of the superheated liquid layer after bubble departure.

However, an important point to note here is that the above mentioned studies pertain to growth of a single bubble and heat transfer mechanisms involved, whereas for a STHE, the situation is that the bubbles form on the underside of the tube as a result fluid flow becoming stagnant at this point, and then slide upwards parallel with the surface creating a thin film underneath in which the local heat transfer from the surface is largely due to liquid convection and evaporation under the sliding bubbles, and this mechanism of heat transfer becomes increasingly important as the vertical velocity of the fluid w.r.t. the horizontal tube increases [25, 85, 86], as is clear from the graph showing variation in heat transfer coefficient along the circumference of the tube in Figure 23[86].

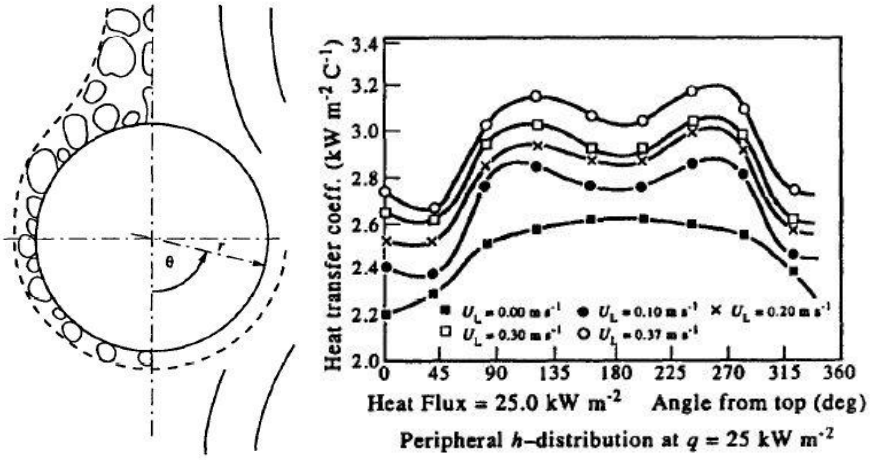

Figure 23 - a) Bubble Layer Model, b) Peripheral variation in heat transfer coefficient with various approach velocities for boiling of R-113 at 1 atm. at flux of 25,000 W/m2

Based on experiments [86], Cornwell gave the following correlation for nucleate pool boiling:

$$Nu = A * F(p) * {Re_b}^{0.67} * Pr^{0.4}; \quad (2)$$

$$where, \quad A = 9.7 * {P_{crit}}^{0.5}, P_{crit}\ is\ in\ bars;\ \ F(p) = 1.8{P_{red}}^{0.17} + 4{P_{red}}^{1.2} + 10{P_{red}}^{10}$$

Complementing the findings of Cornwell (maximum heat transfer coefficient at sides of tube, minimum at top and intermediate value at bottom of tube; but highest at bottom and lowest at top in case the vertical flow velocity is zero, ideal pool boiling condition), is the experimental investigation done by Kang [83], which also shows that the maximum heat transfer coefficient occurs at the bottom of the horizontal tube, and decreases all the way to the top of the tube in pool boiling conditions (no vertical flow velocity), with the difference being magnified with increasing heat flux, as can be seen in the figure below:

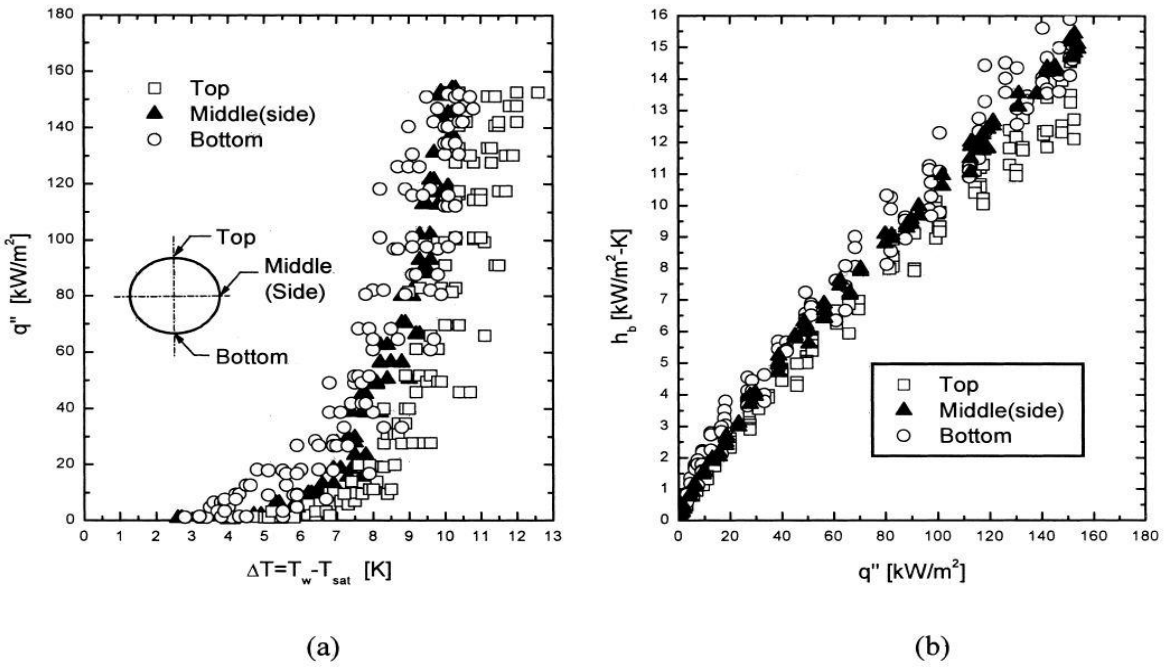

Figure 24 - Comparison of the results due to changes in thermocouple position for the horizontal tube of D = 19.05 mm, and roughness = 60.9 nm; a) heat flux versus tube wall superheat, b) local pool boiling heat transfer coefficient versus heat flux (39)

It is to be kept in consideration that both of the above experiments were conducted with electrically heated tubes, which have been shown to have completely different boiling behavior as compared to water heated tubes [23]. Also, the experiment done by Kang had only 3 tubes in same axial plane. So, it is reasonable to say that the experiment conducted by Kang is more representative of circumferential variation of heat transfer performance of a single tube rather than representing bundle boiling behavior. The experiment done by Cornwell & Houston had just one tube and hence it can also not be taken as being representative of boiling in bundle configuration, and has electrically heated tubes; which means that the variation of heat flux that occurs in a water-heated tube bundle has not been represented by the experiment owing to constant heat flux value for the electrically-heated tubes.

Sergio et.al. [136] presented findings that show a change in circumferential distribution of heat transfer coefficient (reverse of superheat), which shows highest superheat at the bottom of the tube in case of high flux values (> 10,000 W/m^2), and lowest superheat at the bottom for lower flux values. These findings indicate that at low heat flux values bottom of the tube has the best heat transfer performance, whereas at higher heat flux values the bottom of the tube shows weakest heat transfer performance as compared to the sides and the top (in contradiction to the findings of Cornwell & Houston and Kang, given above). The authors suggest that this phenomenon may be caused by partial dryout at the bottom of the tube at high heat flux values. Sergio et.al. [136] also had a single electrically heated tube, with no flow velocity. During the literature survey, no data was found pertaining to circumferential variation of heat transfer performance for a tube in water-heated bundle boiling configuration.

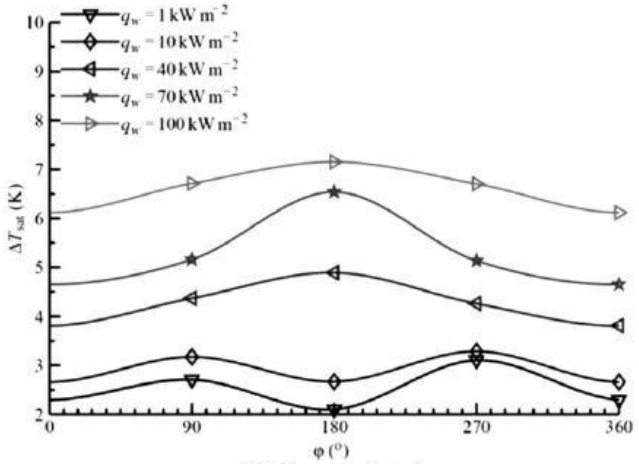

p = 8.6 bar, plain tube

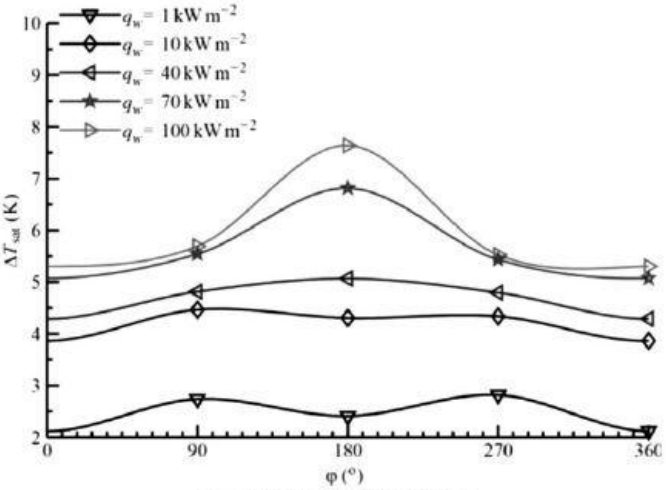

p = 10.1 bar, plain tube

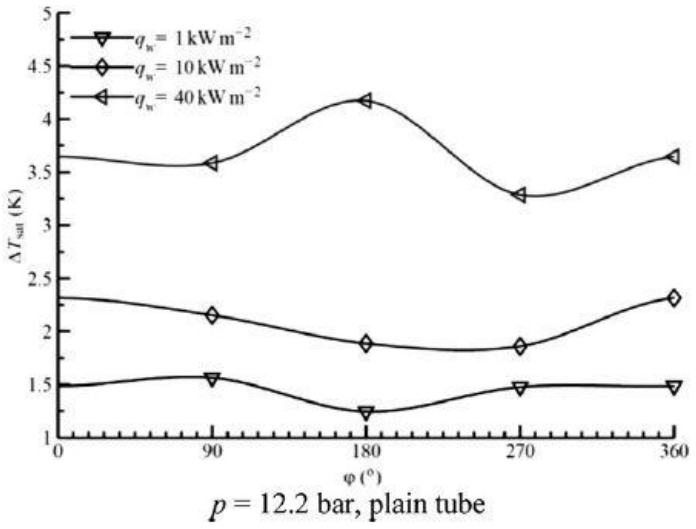

Figure 25 - Circumferential superheat versus the angle for plain tube, φ=0, at top of tube

The trend is completely reversed for micro-finned tubes, and the reason given is that the presence of micro-fins at the bottom of the tube not only shifts the initiation of periodical partial dryout but also increases the heat transfer, Sergio et.al. [136]. The study had electrical heating for both plain and micro-finned tubes.

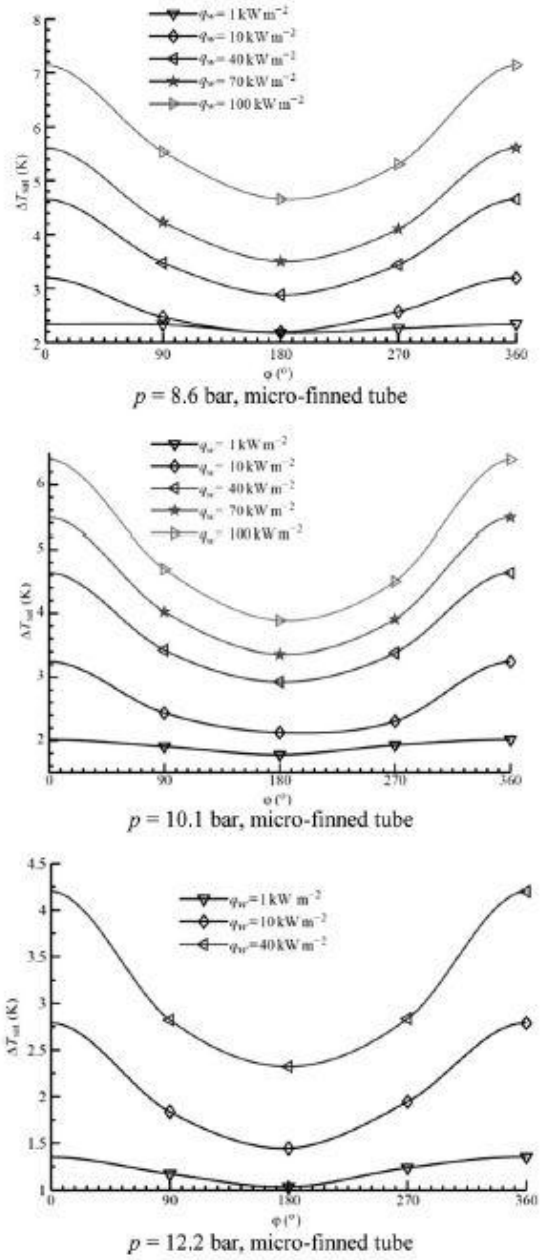

Figure 26 - Circumferential superheat versus the angle for micro-finned tube, φ=0, at top of tube

2.2.3.3 Bundle Boiling

An important heat transfer process employed in many industrial applications is the evaporation on outside of tube bundles, horizontal in orientation. The equipment which utilise this mode of heat transfer are flooded evaporators, waste heat boilers, fire-tube steam generators, kettle & thermosiphon reboilers etc. Nearly all the research looking at this mode of heat transfer has focused on either overall bundle boiling data, on mean measurements for selected tubes in the bundle, on bundles immersed in a pool of liquid without measurements of liquid flow rates or on idealized small bundles. Some of the exchangers executing this mode of heat transfer operate in simple vertical upward cross-flow, e.g. flooded evaporators; but others may be configured as single segmental baffled heat exchangers where the main component of cross-flow is horizontal and has all the associated problems of leakage streams as in similar single-phase flows [145].

The difference in the boiling curve generated for a tube bundle (assuming the entire bundle to be a single heat transfer surface) versus boiling curve for a single tube is represented clearly in Figure 27 [80].

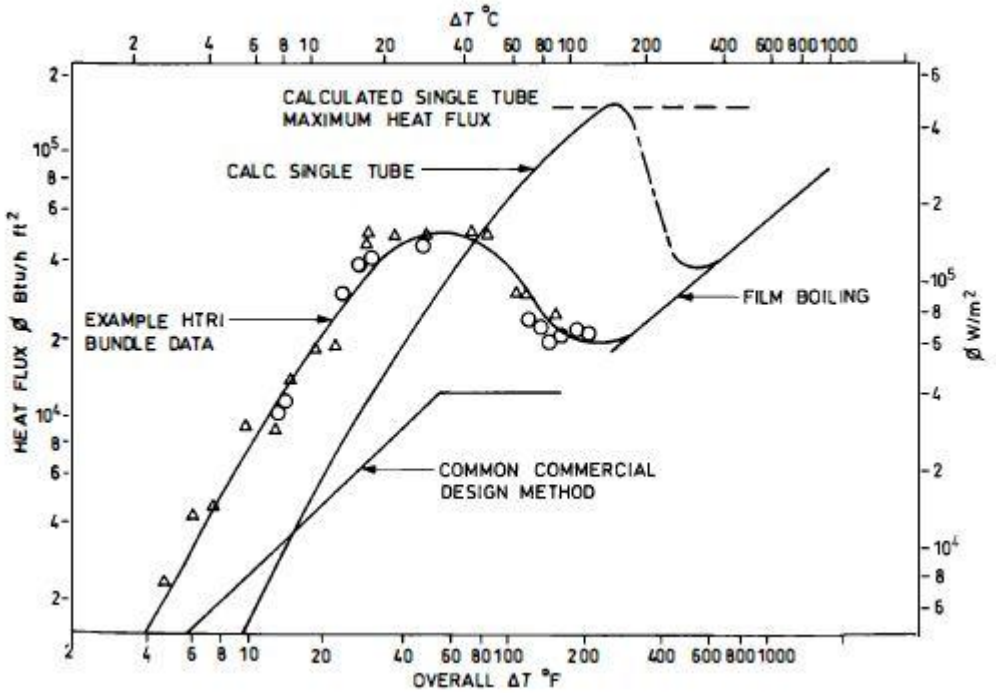

Figure 27 - Tube bundle boiling data compared to a single tube

Very few methods have been specifically developed for modeling flooded evaporators. These are commonly designed assuming constant capacity rates and constant heat transfer coefficients. For evaporators and condensers this is not the case where both the heat capacity and heat transfer coefficients may undergo substantial change. The flow pattern that exists in a tube bundle depends on the bundle orientation and how the bundle is circuited on the tube side (number and configuration of passes). For a horizontal tube bundle the flow pattern would depend on whether it is a natural circulation reboiler or a flooded refrigerant evaporator. Complete evaporation occurs in a flooded refrigerant evaporator [99]. The sensitivity of heat transfer coefficient to changes in quality and flow-rate as predicted by models is much lower than the measured changes, and in some cases opposite trends are exhibited [13]. Very little work has been done to clarify the effects of pitch-to-diameter ratio and

tube bundle layout on the heat transfer coefficient and two-phase pressure drop in tube bundles [95].

Prediction methods for local bundle boiling heat transfer coefficients are much less advanced than for boiling inside the tubes. Most of the bundle boiling methods available were developed from limited databases, typically obtained only in one laboratory for one or two fluids, and hence cannot be considered to be generally applicable methods, and will likely be unreliable when applied to other fluids, pressures and bundle geometries. Very few correlations specifically for the prediction of local bundle boiling heat transfer coefficients currently exist. Most of these methods use a modified form of the popular Chen (1963) in-tube boiling correlation, which thus ignores the physical differences between internal and external two-phase flows. Any discussion of the local distribution and interaction of the liquid and vapor phases within a tube bundle must begin with the local void fraction.

The Thome & Robinson (2006) model, which is the newest and thought to be the most accurate model for predicting bundle boiling heat transfer coefficients is based on only one tube diameter / tube-pitch combination (19mm, 22.23mm), and all the tests were at one saturation temperature of 5^{o}C, for an equilateral triangle layout. Although this method is quite general, and different fluids can be used by inputting their nucleate boiling curve, it is still based on a very limited range of experiments and cannot be thought of as a general correlation [145]. It does take into account the void fraction, which can be calculated from the Feenstra-Weaver-Judd model. Figure 10 is a composite diagram and it is not necessary that all of the flow regimes and heat transfer regimes depicted in the diagram will be found in every flooded evaporator. The types of flow and heat transfer regimes that will be encountered depend on the operating conditions. In the given figure, it is assumed that subcooled

liquid enters the bottom from the inlet nozzle and flows upwards to bottom tube row. Here, the initial heat transfer process is therefore single-phase convection to the subcooled liquid, which is then followed by subcooled boiling until the liquid reaches its saturation temperature. So, in the lower part of the bundle, bubbly flow will exist until it transitions into the bubble jet flow between the tubes. Various flow regimes that can develop in a flooded vaporizer are shown in Figure 28 [144].

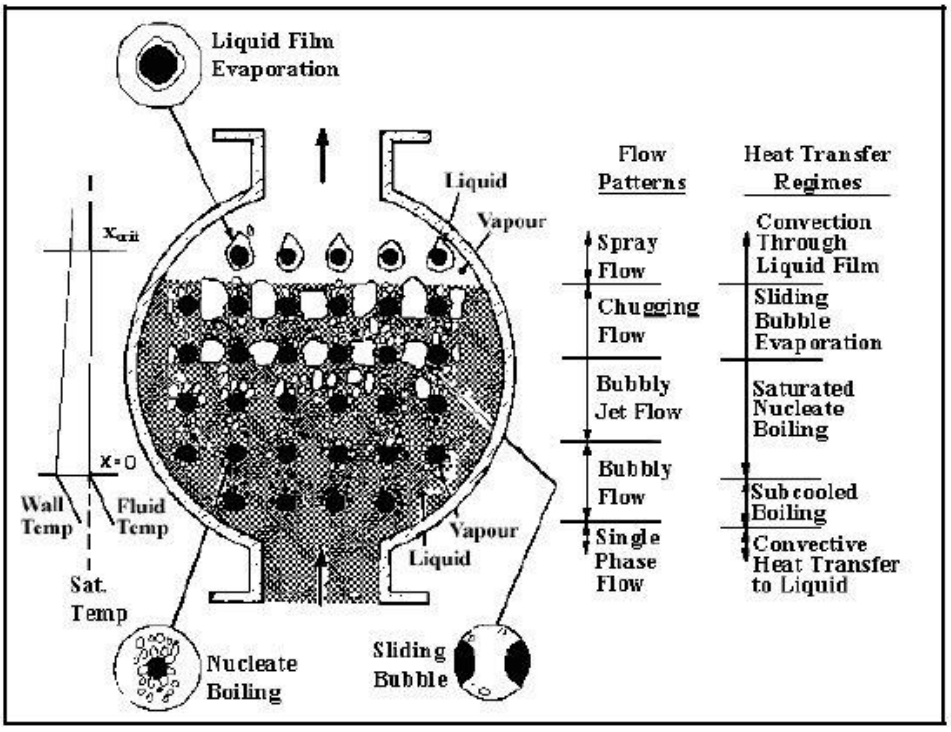

Figure 28 - Schematic representation of different types of flow regimes and heat transfer regimes that may be encountered in a flooded type evaporator

The flow then enters a chugging type of flow regime with large bubbles and liquid slugs populated with numerous small bubbles. Consequent to chugging flow, at some critical conditions, which will depend on a multitude of factors, it transitions into spray flow, in which large droplets impinge on the tubes,

forming a thin liquid film over the tubes, and heat transfer in this regime is mainly by thin film evaporation. There are always chances of carryover, i.e. liquid leaving the flooded evaporator along with the vapor; this is undesirable in most of applications. To prevent this from happening, either a demister pad is used, or the shell diameter is large compared to the tube bundle diameter to act as a vapor disengagement space. Also, in some applications, a superheater is used after the flooded evaporator.

The main bundle effects are [36]:

- Flow induced convection
- Tube-row effect
- Onset of dryout
- Effects related to flow pattern: bubbly, dispersed, annular , and mist flow
- Heat flux effect in the bundle
- Vapor quality
- Mass flux
- Tube type
- Tube layout
- Refrigerant
- Effects of oil

It has been shown experimentally that sliding bubbles enhance the heat transfer at the sides and it was concluded that the disruption of the liquid boundary layer was more important than the evaporation of the microlayer under the sliding bubble [99]. The two main factors affecting the boiling performance in tube bundles are:

a) Convective effects due to fluid velocity and rising bubbles

b) Effects of static head which cause increased saturation temperatures in the lower part of the bundle and hence reduce the local driving temperature difference

As a flooded evaporator is a once through device, with 100% leaving quality, boiling occurs over a wide range of conditions. Depending on the pool boiling performance level of the tube, it will one of the two characteristics in convective vaporization: [99]

a) If the tube has a high pool boiling coefficient the tube will not be very sensitive to convective effects. It will, however, be quite sensitive to heat flux which indicates that the performance is dominated by nucleate boiling.
b) If the tube has a low pool boiling coefficient, it will benefit substantially from convective effects. However, its performance in convective vaporization will not be very sensitive to heat flux.

Webb and Gupte, also showed that the forced convection enhancement was more beneficial to the integral-fin tube than to the enhanced nucleate boiling tubes.

The bundle enhancement effect is much more pronounced at low heat flux values (< 30,000 W/m^2) as compared to higher heat flux values (> 30,000 W/m^2), with the bundle heat transfer coefficient sometimes being up to 3 times the heat transfer coefficient of a single tube [145]. It is because of the fact that, at low heat flux values, the dominant heat transfer mechanism is convective boiling, and thus the overall heat transfer coefficient of a tube bundle at low heat flux values is much higher than nucleate boiling heat transfer coefficient of a single tube. Whereas, at high heat flux values, the dominant mechanism of heat transfer is nucleate boiling, and thus the bundle enhancement effect has a smaller magnitude as compared to low heat flux conditions.

The bundle enhancement effect also depends on the type of tubes being used – whether enhanced surface, or plain surface. At lower heat flux values, the enhanced surface tubes show a clear and present advantage over the smooth tubes by having much higher heat transfer coefficients, but this advantage starts to diminish as the heat flux approaches critical heat flux (CHF) value [36], whereas smooth tubes show a continuous increase in heat transfer coefficient with increasing heat flux (up to Critical Heat Flux). Some studies also show that the heat transfer coefficient for enhanced tubes eventually shows a decrease in value with increasing heat flux, and certainly levels out in almost all cases at a heat flux value of nearly 50,000 W/m^2 [22, 139], although it needs to be mentioned that the heat transfer coefficient for enhanced tubes is usually up to 2-4 times that for smooth tubes. This shows a fundamental difference between smooth and enhanced surface tubes performance. Another limiting factor for the use of enhanced tubes is especially in lower rows of tube bundle, where the fluid enters with few to several degrees of subcooling, as the enhanced tubes are not effective for either single-phase heating or subcooled boiling [145].

The behavior of enhanced tubes is quite different to those of smooth tubes during boiling at low heat flux values, showing better bubble generation and departure characteristics (Figure 29 [22]), both of which contribute to the better performance of the enhanced tubes as compared to smooth tubes; better bubble incipience leads to increase in vigorousness of boiling and better bubble departure (negligible coalescence) promotes the effectiveness of heat exchange at the liquid-bubble interface. Also, the process of nucleate boiling starts on enhanced tubes at heat flux values much lower than the values required for nucleate boiling to start on smooth tubes.

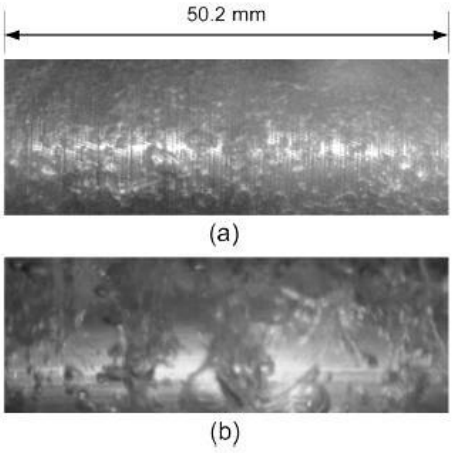

Figure 29 - Snapshots of boiling on, a) enhanced tube surface, and b) smooth surface of a plain tube, at flux of 31,500 W/m^2

But, with increasing heat flux values the boiling behavior of enhanced tubes seems to approach that of smooth tubes (Figure 30 [22]), which may explain the levelling out of heat transfer performance of the enhanced tubes with increase in heat flux.

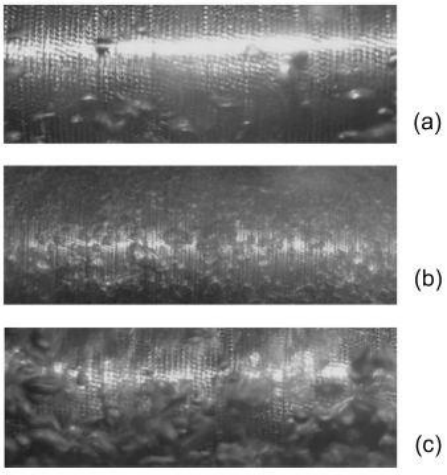

Figure 30 - Boiling on enhanced tubes at three different heat flux values at saturation temperature of 4.4 deg Celsius, a) 15,100 W/m^2, b) 31,500 W/m^2, c) 60,200 W/m^2

The value of heat transfer coefficient also shows an increase with increase in the vapor quality of the system, and this effect is much more pronounced at lower heat flux values [118, 145]. The flow becomes convection dominated at high vapor qualities [145]. Also, the boiling performance of enhanced tubes is affected significantly by the saturation temperature of the working fluid, especially at high heat flux values (which is dependent on the working pressure of the evaporator) [22].

The strongest influence on the heat transfer coefficient continues to be that of heat flux [36, 145], followed by properties such as reduced pressure, heater material, surface conditions and fluid properties. This might be because of the direct effect of heat flux on nucleation density which defined the area under bubble and area under liquid.

For flow boiling, the total heat flux is classically assumed to have two components: a) convective evaporation, b) nucleate boiling. Nucleate boiling is the process when the liquid layer near the heated surface becomes superheated enough to allow nucleation and bubble formation. Convective boiling, characterized by the conductive and convective heat transfer through the liquid layer on the tube wall, is the process when vaporization occurs at the liquid/vapor interface on the surface of the liquid layer present on the tube wall [90]. An asymptotic approach is widely used to arrive join the two together, whether as heat flux, or as heat transfer coefficient [118].

In almost all of the studies carried out to develop a model for thermal design of a vaporizer, the aim has been to develop a practical approach, using prototypes or real vaporizers, while using classical models of two-phase flows and validating the correlations for the geometry and fluid that were used in the experimental set-up. These models may therefore be inaccurate when used for different geometries and fluid, and this has been found to be so in various

studies [90]. This suggests that the parameters used in these models are not representative of the actual mechanisms occurring inside the tube bundle [90], as most of the present models have been developed by modifying a correlation that were originally developed for in-tube boiling and other experimental conditions not truly representative of the conditions existing around a tube bundle in a vaporizer. It will continue to be an issue as long as the correlations do not take into account all the mechanisms occurring that influence the heat transfer performance in a vaporizer.

These models can be broadly classified into two categories: a) superposition type models, b) asymptotic models [3, 13, 23, 60, 61, 90, 99].

The superposition models are of the type:

$$h_{bundle} = S(h_{nb}) + F(h_{cb}) \quad (3)$$

Where, S is the suppression factor (S < 1), and represents a diminishing effect on the nucleate boiling, as compared to when it is happening on a single tube. And, F is the enhancement factor (F > 1), representing the enhancement of heat transfer by convection due to two-phase flow. It depends on the flow regime.

The asymptotic models are of the type:

$$h_{bundle} = [{h_{nb}}^{n} + {h_{cb}}^{n}]^{1/n} \quad (4)$$

The exponent 'n' (> 1), has been specified different values by different researchers, in an attempt to fit it to the experimental data. In comparison to the superposition model, the asymptotic model has the advantage of varying the transition between nucleate and convective boiling, by varying the

coefficient '*n*'; and, the deviation from the experimental data, using asymptotic approach, has been lower than 20% in all the studies [13, 90].

Heat transfer mechanisms in a vaporizer can be divided into categories of tube-scale heat transfer mechanisms and shell-scale heat transfer mechanisms. The tube scale heat transfer mechanisms vary with the angular orientation of the tube surface w.r.t. the fluid around it, particularly at low heat flux values [60, 90, 145]. At the shell scale, heat transfer is controlled by the induced natural two-phase recirculation. Also, it has a self-changing attitude, as the tube-side heat transfer is affected by the two-phase conditions existing on the outside of tubes, and the heat transfer on the tube-side influences the overall two-phase flow pattern on the shell side. For a better prediction of heat transfer performance of a vaporizer, the heat transfer coefficient calculation correlation(s) must take into account the local flow regime in different parts of the vaporizer, and change itself accordingly as the two-phase flow regime changes in different sections of a vaporizer.

As the heat transfer during bundle boiling is a combination of nucleate boiling and convective boiling, a number of models have been proposed in an attempt to outline the contribution from each mechanism. The nucleate boiling regime dominates in the lower part of the tube bundle, where the two-phase cross-flow is not strong; the heat transfer coefficient remains almost constant in this stage being independent of the vapor quality and mass flow rate, and shows an increase with increasing heat flux. In the upper part of the tube bundle, the heat transfer coefficient depends on the vapor quality and not on the heat flux (as is seen by convergence of data series on to same line in Figure 4), which is representative of the convective boiling regime, and the heat transfer performance increases with increase in vapor quality. Also, with an increase in

mass flow rate, the heat transfer coefficient will achieve a given value at lower vapor quality for a higher mass flow rate, Figure 5.

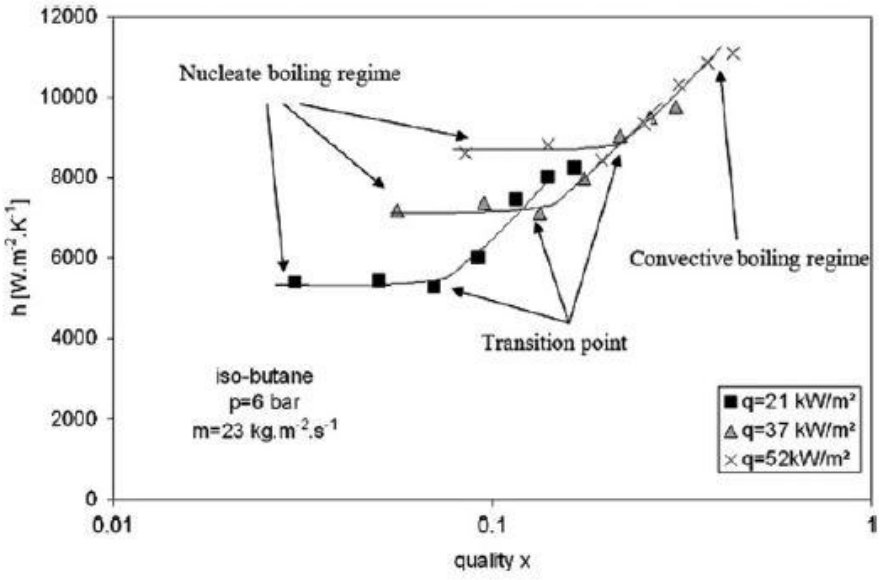

Figure 31 - Variation of heat transfer coefficient according to vapor quality for iso-butane boiling on staggered smooth tube bundle. Influence of heat flux. (45)

The main parameters governing the local heat transfer along the tube bundle are: a) heat flux (influences the nucleate boiling heat transfer regime, lower tubes), b) vapor mass flow rate (represents vapor quality and mass flow rate, influences the convective boiling heat transfer regime, upper tubes).

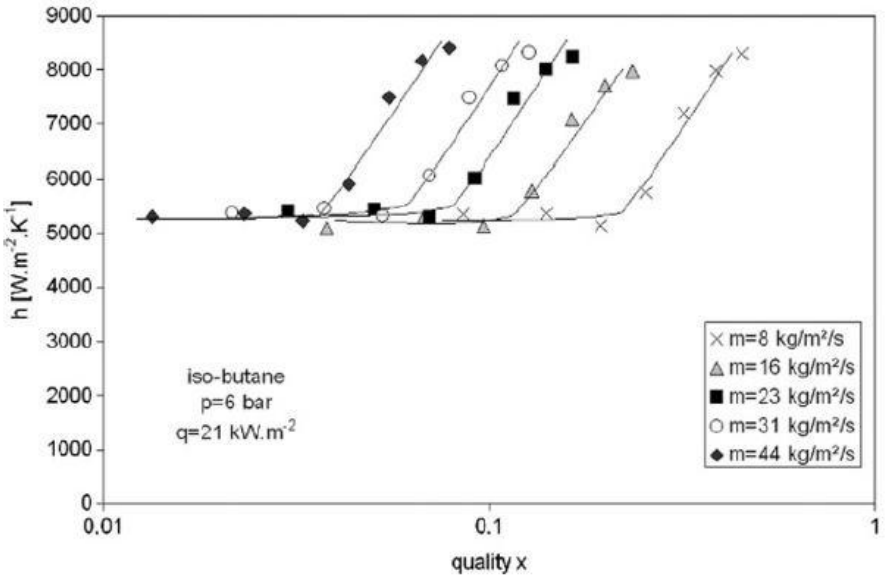

Figure 32 - Variation of heat transfer coefficient according to vapor quality for iso-butane boiling on staggered smooth tube bundle. Influence of hydrocarbon mass flow rate. (45)

In a study done by Aprin et.al. [90], a comparison was carried out between various models used by industry for design of vaporizers, and Figure 6 shows the heat transfer coefficient prediction with an increase in vapor quality. According to the models used, a decrease in heat transfer coefficient with increase in vapor quality is predicted, which is contrary to experimental evidence that shows the 'bundle effect' to have the opposite effect, i.e. an increase in heat transfer coefficient throughout the bundle [25, 90].

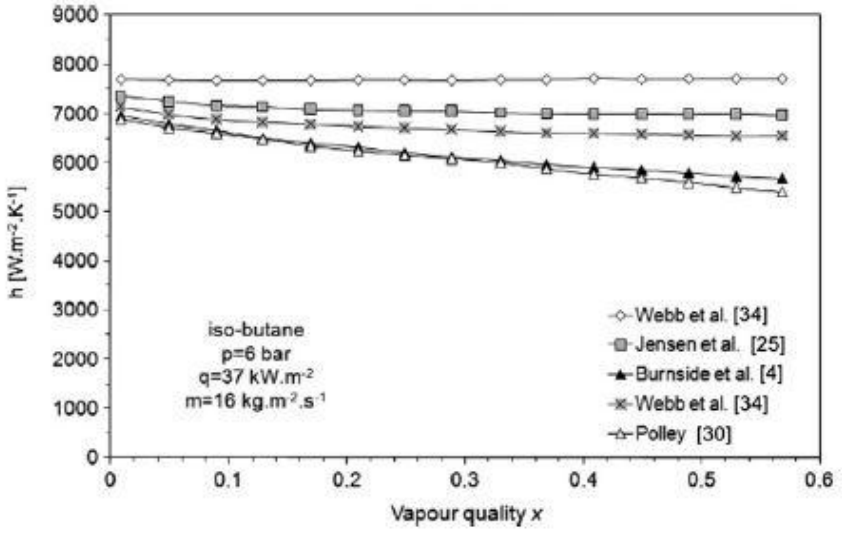

Figure 33 - Comparison of heat transfer correlations (45)

In a study done by Burnside and Shire [13], they found the overall heat transfer coefficient to be almost similar to the nucleate boiling coefficient, in contrast to studies done by Cornwell & Scoones (1988), and Hwang & Yao [140, 141]. Also, Burnside et al. stated that the entire heat transfer was dominated by nucleate boiling conditions, in complete contrast to Cornwell, who stated that there is virtual absence of nucleation except at the lowest tubes in the bundle, indicating that once enough bubbles have been produced, the other mechanisms (convection and sliding bubbles) are sufficient to transfer that heat from the tubes [25]. Hwang & Yao also attributed the higher heat transfer performance of a tube in a bundle than in infinite pool, because of changes in flow geometry due to adjacent tubes, and to the resulting thermal environment. All of these experiments used electrically heated tubes, indicating that any comparison between the two studies is reasonable within limits because although the boundary heating conditions are same, but there might be other differences such variations in surface roughness (impacting rate of nucleation) and operating conditions during the experiments need to be

matched. Dowlati et.al. [115] also stated that even under fully developed boiling conditions, the heat transfer performance of a tube in a bundle is higher than heat transfer performance of a single tube.

The value of heat transfer coefficient is also dependent on the type of refrigerant being used, and this can sometimes necessitate the tube surface to be linked to the type of refrigerant being used [139]. E.g. low vapor density refrigerants (like R-123) have larger bubble sizes as compared to those for high vapor density refrigerants (like R-134a), and this translates into tailoring the tube surface for the type of refrigerant being used so as to maximize the number of nucleation sites and hence the heat transfer performance. The organic fluid of interest to the current project is n-Pentane and it is a low vapor density refrigerant. The refrigerant chosen to find parameters to model bubble dynamics for n-Pentane simulations is R113 as the density ratio is similar to n-Pentane at pressures of interest (Table 1) (Source: RefProp).

FLUID	LIQUID DENSITY	VAPOR DENSITY	DENSITY RATIO
Values at Pressure = 10 bar			
n-Pentane	502.67	27.955	17.98
R113	1243	69.298	17.94
R123	1207.8	60.445	19.98
R134a	1149.3	49.222	23.35
Values at Pressure = 20 bar			
n-Pentane	431.64	63.5	6.797
R113	1069.3	155.38	6.882
R123	1051.7	133.64	7.87
R134a	1011.4	107.63	9.39

Table 1 - Density values for different organic fluids

2.2.3.4 Effect of surface roughness on heat transfer

The minute changes in surface roughness characteristics have a huge bearing on the heat transfer coefficient especially at low to intermediate heat fluxes and intermediate reduced pressure values, as the surface tension reduces with increase in working pressure and consequently the cavity radius required for bubble nucleation decreases causing an increase in the nucleation site density and eventually a higher heat transfer coefficient [22, 34, 90]. This can be seen in Figure 34 [34].

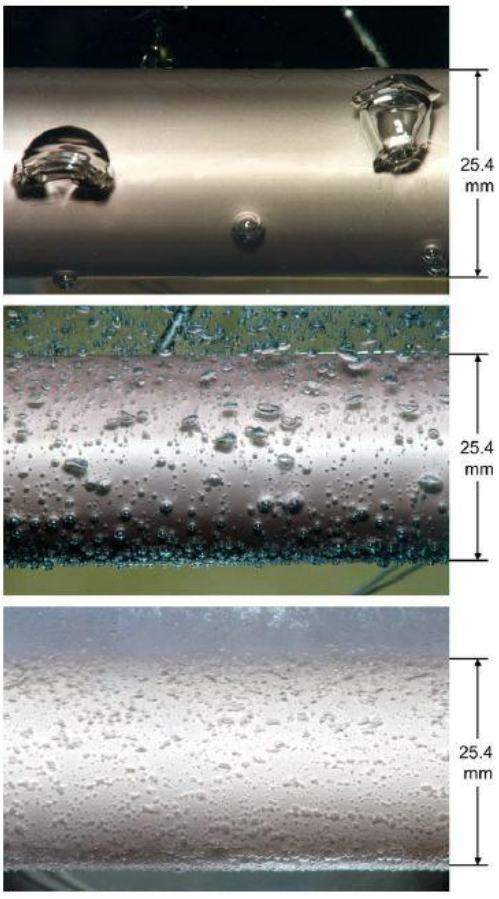

Figure 34 - Variation in size and number of bubbles with reduced pressure for three different values of reduced pressure, a) TOP - 0.010; b) MIDDLE - 0.15; c) BOTTOM - 0.80

The effects of surface roughness on heat transfer coefficient start decreasing with increasing pressure (higher reduced pressure) and heat flux [83, 94, 108] as is clear from Figure 35 [94] the heat transfer coefficient values for different surface roughness tubes start to merge for reduced pressure values = 0.4. In the current project the reduced pressure for pentane is 0.4242 (Rotokawa) and 0.667 (Ngatamariki) for the two different vaporizers considered, and so the effect of surface roughness does not need to be modelled in detail due to its reduced influence.

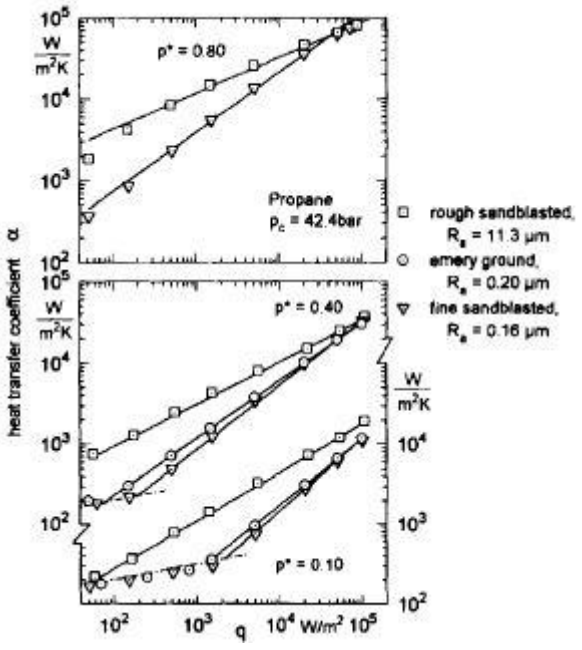

Figure 35 - Heat transfer coefficient versus the heat flux for propane boiling on the mild steel tube with different surface roughness values at three normalized pressures

Even for those correlations taking into account the surface roughness values, the differences in bubble formation that are responsible for differences in heat transfer performance cannot be considered sufficiently by the average value of a single, integral roughness parameter, R_a. The effect of surface roughness on the heat transfer performance is most pronounced at low to intermediate heat

fluxes and intermediate reduced pressures, which is because of the fact that at low to intermediate values of heat flux and reduced pressure the contribution of the ‘sliding bubble’ phenomenon on the overall heat transfer coefficient is maximal [34]. In other words, the effect of surface roughness characteristics is most pronounced when, either the number of active nucleation sites is too high (at high heat fluxes and/or high pressures) or the number of sliding bubbles is too low (low reduced pressures and intermediate heat flux) [34]. The influence of the surface roughness structure of the heating element is one of the factors that interferes with the influences of most other parameters in the nucleate pool boiling, because the ‘size distribution’ of the tiny cavities within the roughness structure and the ‘local distribution’ of the cavities on the surface of a evaporator tube are influencing the heat transfer during the growing period of the bubble and also while they are sliding along the tube surface [34]. The influence of these distributions is not considered in any of the correlations explicitly, instead only an integral roughness parameter, the mean roughness height, R_a, is used to characterize the influence of roughness on the heat transfer coefficient for the entire tube length [34].

Also, the review done by Gorenflo [34], indicates with ample evidence that the experimental differences found in the dependence of heat transfer coefficient on the heat flux and reduced pressure for different hydrocarbons is not caused so much by the different thermophysical properties, as by the effect of differences in the design and roughness structures of the heating tubes and in the experimental procedure and measuring equipment at different research laboratories. An experimental investigation by Jabardo et.al. [81] revealed that although commonly used nucleate boiling heat transfer coefficient prediction correlations assume a constant increase with increasing surface roughness, but with high surface roughness values (R_a> 6 μm) the correlations tend to

overestimate the heat transfer coefficient and experimental observations show that the heat transfer performance of very rough surfaces is actually worse than the smooth surface tubes, which means that the correlations must be used with only low average surface roughness values as the actual trend is of decline in heat transfer performance with increase surface roughness.

Most of the experiments carried out to develop heat transfer coefficient prediction correlations/methods have been at low saturation temperatures (pertaining to working fluid) and low pool temperatures. It is known that the overall characteristics of boiling are directly or indirectly influenced by the behavior of a single bubble on the heating surface, and the heat transfer mechanism for single bubble growth can be related to thermal boundary layer characteristics on the hot tube surface. These are controlled by wall & pool temperatures during the waiting period and by the interface temperature gradient (which is dependent on wall, saturation and pool temperatures) during the growth period [75]. Consequently, the temperatures closely related to nucleate pool boiling performance are the pool temperature (can be subcooled, saturated or superheated), saturation temperature (working fluid) and hot tube wall temperature.

There are three main types of tube surfaces available for use in vaporizer designs: smooth, corrugated and porous coated tubes. Out of these the porous coated tubes have the onset of nucleate boiling at the lowest values of wall superheat [74].

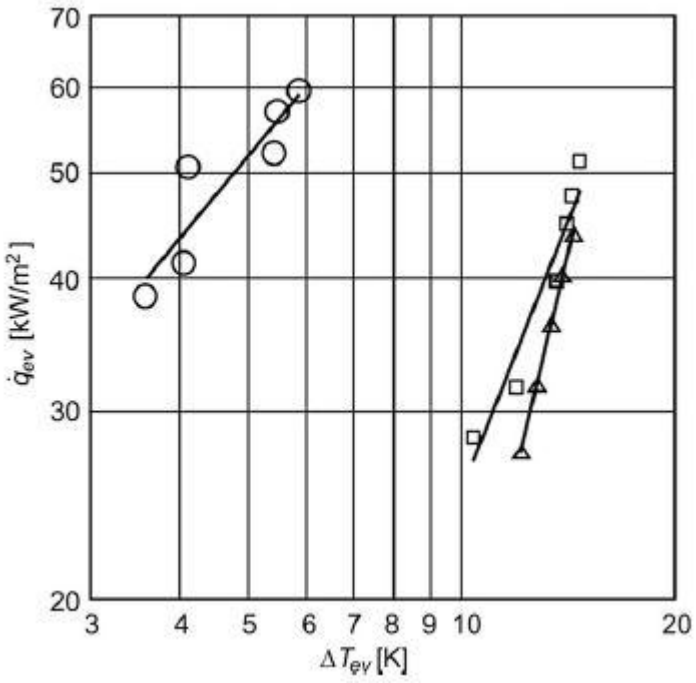

Figure 36 - Boiling curves of R-141b on tube bundles, O = porous coated tubes, □ = corrugated tubes, Δ = smooth tubes (34)

The porous coating creates a large number of stable, active nucleation sites and thus increasing the number of active boiling sites and hence the resultant improvement in the heat transfer performance. The diameter of the mouth of the pore cavity defines the nucleation radius and therefore governs the wall superheat at which the cavity will become activated [74]. This statement posits an interesting fact and gives rise to the question that, whether designed porous coatings can be used to increase the heat transfer performance in applications with known values of wall superheat?

An important operational parameter for evaporators is the liquid head (level of working fluid above the upper most tube row) which is necessary to obtain a predictable performance and avoid two-phase flow oscillations; another problem arises with deeply immersed bundles of liquid subcooling at bottom

of the bundle and also the liquid head strongly affects the recirculation pattern of the liquid inside the shell and has a resulting effect on the heat transfer performance of the heat exchanger [74].

Bundle boiling heat transfer is enhanced by nucleate boiling where the rising and expanding bubbles together with convective effects produce greater turbulence and thus increase the fluid circulation. But, the increased nucleation ability of porous coating on evaporator tubes may produce too many excessively large bubbles and may thus expose the upper rows to vapor phase and reducing their thermal performance [74].

The values of heat transfer coefficients seem to differ little between staggered and in-line tube bundles, particularly at high working pressures and high heat flux values; although staggered bundles have a higher pressure drop as compared to in-line tube bundles. Generally, the heat transfer coefficients increase with increasing pressure, pertaining to both tube bundle arrangements. But, the differences in heat transfer coefficients due to pitch-to-diameter ratios increased only when convection due to increasing quality was the dominant mechanism (at low heat flux and low mass velocity conditions). The tendency for little difference in heat transfer coefficient values at high pressures is due to the fact that although convective effects are reduced at high pressures (because of increase in two-phase mixture density and hence decrease in mixture velocity, thereby suppressing the enhancement of convection heat transfer), but the higher pressure lead to higher nucleation rates that counterbalance the reduced convection effects [95].

2.2.4 Various Nucleate Boiling Models

- **Rohsenow Correlation**

Rohsenow (1952) suggested that the heat transfer is enhanced during nucleate boiling due to local liquid circulation caused at the surface by formation and detachment of bubbles, and thus implied that the micro-topology and physics of boiling and bubble departure have strong influence on the value of the heat transfer coefficient [36, 61]. It includes a constant whose value can be taken from a database, and if not present in the database it is taken 0.013 [61].The correlation is [61, 126]:

$$Q_{flux} = \mu_{WF} * H_{latent} * \left[\frac{g(\rho_{liq} - \rho_{vap})}{\sigma}\right]^{0.5} \left[\frac{Cp_{WF}\Delta T_{excess}}{Constt_{Rohsenow} H_{latent} Pr_{WF}^{n}}\right]^{3} \quad (5)$$

(n = 1.7 for organic fluids, 1.0 for water)

$$h_{nb,Rohsenow} = \frac{Q_{flux}}{\Delta T_{excess}} \quad (6)$$

Equation gives the simple method to calculate nucleate boiling coefficient for experimental studies. A more detailed method for designing and analysis is given below:

$$Re_{WF} = \left(\frac{Q_{flux}}{H_{latent}\rho_{liq}}\right) L_{char,nb} \left(\frac{\rho_{liq}}{\mu_{WF}}\right) \quad (7)$$

$$Nusselt_{WF} = \frac{1}{Constt_{Rohsenow}} (Re_{WF})^{[1-0.33]} (Pr_{WF})^{-0.7} \quad (8)$$

$$Nusselt_{WF} = \frac{1}{Constt_{Rohsenow}} (Re_{WF})^{[1-0.33]} (Pr_{WF})^{-0.7} \quad 9$$

$$L_{char,nb} = \left[\frac{\sigma}{g(\rho_{liq} - \rho_{vap})}\right]^{[1/2]} \quad 10$$

$$h_{nb,\,Rohsenow} = \frac{Nusselt_{WF} k_{WF}}{L_{char,nb}} \quad 11$$

- **Stephan – Abdelsalam Correlation** [82]

Stephan and Abdelsalam proposed four different correlations applying a statistical multiple regression technique [82] for different fluid classes : water, hydrocarbons, cryogenic fluids and refrigerants. The correlation being presented here is the correlation given for hydrocarbons, with upper limit of reduced pressure being 0.9 and it has a mean absolute error of 12.2 %:

$$h_{nb,\,Stephan-Abdelsalam} = 0.0546 \left(\frac{k_{WF}}{D_{bubble}}\right)\left[\left(\frac{\rho_{gas}}{\rho_{liq}}\right)^{1/2}\left(\frac{Q * D_{bubble}}{k_{WF} T_{sat}}\right)\right]^{0.67}\left(\frac{H_{latent} D_{bubble}^2}{\alpha_{WF}^2}\right) \quad 12$$

$$D_{bubble} = 0.0146 * \beta \left[\frac{\sigma}{g(\rho_{liq} - \rho_{gas})}\right]^{1/2} \quad 13$$

The contact angle β is assigned a fixed value of 35 degrees irrespective of the fluid, and temperature is in Kelvin scale. All the thermodynamic properties are for saturated liquid state unless otherwise mentioned.

For refrigerants, the following form of correlation is provided with upper limit of reduced pressure being 0.78, and mean absolute error of 10.57 %.

$$h_{nb,Stephan-Abdelsalam} = 207\left(\frac{k_{WF}}{D_{bubble}}\right)\left(\frac{Q_{flux}D_{bubble}}{k_{WF}T_{sat}}\right)^{0.745}\left(\frac{\rho_{gas}}{\rho_{liq}}\right)^{0.581}\left(\frac{\nu_{WF}}{\alpha_{WF}}\right)^{0.533} \quad 14$$

- **Mostinski Correlation [23]**

Mostinski (1963) ignored surface effects and applied the principle of corresponding states to nucleate pool boiling heat transfer, correlating data as a function of the reduced pressure of the fluid and critical pressure. It is a 'dimensional' correlation where the heat transfer coefficient is in W/m^2K, and heat flux is in W/m^2.

The critical pressure must be in kN/m^2, or kPa [146].

$$h_{nb,Mostinskii} = A^* * Q^{0.67} * F_P \quad 15$$

$$A^* = 3.596 * 10^{-5}\left(P_{crit,WF}\right)^{0.69} \quad 16$$

$$F_P = 1.8(P_r)^{0.17} + 4(P_r)^{1.2} + 10(P_r)^{10} \quad 17$$

- **Cooper Correlation [23, 24]**

Cooper (1984), proposed a new pool boiling correlation using reduced pressure as a variable, and included the surface roughness of the surface along with molecular weight of the working fluid:

$$h_{nb,\,Cooper} = Constt * 55 * P_r^{\,0.12-0.2log_{10}R_p}(-log_{10}P_r)^{-0.55}M^{-0.5}Q_{flux}^{\,0.67} \quad (18)$$

Constt. = 1.7, for cylindrical surfaces and upward facing flat surfaces; 1.0, for other geometries.

It covers reduced pressure from 0.001 to 0.9, and molecular weights from 2 to 200 [146]. It is a 'dimensional' correlation where the heat transfer coefficient is in W/m^2K, and heat flux is in W/m^2.

It is widely regarded as the most accurate correlation in existence to calculate nucleate boiling heat transfer coefficient for single tube [23, 34, 146]. It is also able to highlight the influence of reduced pressure on the heat transfer coefficient [90]; i.e. the increase in the value of the heat transfer coefficient with an increase in reduced pressure.

- **Forster-Zuber Correlation [59]**

$$Q_{flux} = 0.00122\left[\frac{k_{WF,liq}^{\,0.79}Cp_{WF,liq}^{\,0.45}\rho_{WF,liq}^{\,0.49}}{\sigma^{0.5}\mu_{WF,liq}^{\,0.29}\Delta i_{vap}^{\,0.29}\rho_{WF,vap}^{\,0.24}}\right](T_{wall} - T_{sat,WF})^{1.24}\Delta P_{sat,WF}^{\,0.75} \quad (19)$$

It is a 'dimensional' relation with heat flux being in kW/m^2; thermal conductivity in kW/m-K; specific heat capacity in kJ/kg-K; liquid and vapor densities in kg/m^3; temperatures in degree Celsius; surface tension in N/m; latent heat of vaporization in kJ/kg; liquid viscosity in $N\text{-}s/m^2$; and pressure in Pa. The pressure term, ΔP, is the difference in saturation pressures corresponding to the difference between the wall temperature and saturation temperature of the working fluid. The problem with this correlation is that it does not take into account the heater surface/boiling fluid combination.

Note: The values of heat transfer coefficient calculated by this correlation are extremely close to the ones calculated by ASPEN.

- **Fazel – Roumana Correlation** [127]

$$h_{nb,\,Fazel-Roumana} = \frac{3.253\sigma^{0.125}H_{latent}^{0.125}\left(Q_{flux}\right)^{0.876}}{T_{sat}\alpha^{0.145}} \qquad 20$$

- **Gorenflo Correlation [28]**

The generalization in the Cooper correlation in terms of the square root of the molecular weight is an over-simplification and can result in considerable errors [60]. An alternative form of reduced pressure correlation was developed by Gorenflo. It has a database form in which the reference value of heat transfer coefficient is used for different fluids at a standard heat flux of 20,000 W/m^2. This is the main limitation of this method; calculation of reference values for any working fluid is required before the correlation can be applied. This method is applicable over the reduced pressure range from about 0.0005 to 0.95. For the fluids present in the database, this method is considered most reliable [146].

$$h_{nb,Gorenflo} = h_{ref}F_{PF}\left(\frac{Q_{flux}}{Q_{ref}}\right)^{nf}\left(\frac{R_p}{R_{p,ref}}\right)^{0.133} \qquad 21$$

$$Q_{ref} = 20{,}000\frac{W}{m^2};\ R_{p,ref} = 0.4\mu m \qquad 22$$

$$F_{PF} = 1.2P_{red}^{0.27} + 2.5P_{red} + \frac{P_{red}}{1 - P_{red}} \qquad 23$$

$$nf = 0.9 - 0.3P_{red}^{0.3} \quad (24)$$

Above equations for F_{PF} & nf are valid for all fluids except water and liquid helium. For water, the above relations are:

$$F_{PF} = 1.73P_{red}^{0.27} + \left(6.1 + \frac{0.68}{1 - P_{red}}\right) P_{red}^2 \quad (25)$$

$$nf = 0.9 - 0.3P_{red}^{0.15} \quad (26)$$

- **Leiner – Gorenflo Correlation [93]**

To avoid the role of reference values in the Gorenflo correlation, [93] developed new non-dimensional forms of the correlation that apply for any arbitrary fluid. Following are the non-dimensional forms of heat transfer coefficient, heat flux, and surface roughness.

$$h = h^* \left(P_{crit}\left(R_{gas\ constt}/MT_{crit}\right)^{1/2}\right) \quad (27)$$

$$h^* = AF_{pres}\left(Q_{flux}^*\right)^n (R^*)^{0.133} \quad (28)$$

$$Q_{flux}^* = \frac{Q_{flux}}{P_{crit}\left(R_{gas\ constt}T_{crit}/M\right)^{1/2}} \quad (29)$$

$$R^* = \frac{R}{\left(R_{gas\ constt}T_{crit}/P_{crit}N_{mol}\right)^{1/3}} \quad (30)$$

$$F_{pres} = 43000^{(n-0.75)}\left[1.2P_r^{0.27} + \left(2.5 + \frac{1}{1 - P_r}\right) P_r\right] \quad (31)$$

$$A = 0.6161C^{0.1512}K^{0.4894} \quad (32)$$

$$C = \frac{(Cp_L)_{P_r=0.1}}{R_{gas\ constt}} \quad (33)$$

$$K = \frac{T_{crit}ln(P_r)}{(1 - T_{crit})} \quad (34)$$

$$n = 0.9 - 0.3P_r^{0.15} \quad (35)$$

- **Ribatski – Saiz Correlation** [54]

$$h = {Q_{flux}}^{m}{F_{material}}{P_{red}}^{0.45}[-log(P_{red})]^{-0.8}Ra^{0.2}M^{-0.5} \quad (36)$$

$$m = 0.9 - 0.3{P_{red}}^{0.2} \quad (37)$$

$F_{material} = 100\ for\ Copper, 110\ for\ Brass, 85\ for\ Stainless\ Steel$

- **Gorenflo & Kenning Correlation** [33]

It is an evolution of Gorenflo's correlation and is currently implemented in the VDI Heat Atlas. It also relies on the estimation of heat transfer coefficient for different fluids at a reference state first of all, at reduced pressure of 0.1 and heat flux of 20,000 W/m^{2}and roughness of 0.4 μm for Copper. The upper limit of reduced pressure is 0.9, and the lower limit is 0.1 bar absolute pressure.

$$h = h_{ref}F_{q,flux}F_{press}F_{Ra}F_{wall} \quad (38)$$

$$h_{ref} = 3.58 * {P_f}^{0.6} \quad (39)$$

$$P_f = \frac{\left.\frac{dP}{dT}\right|_{sat}}{\sigma} \quad (40)$$

It can be simplified using Clausius – Clapeyron relation [136].

$$P_f = \frac{H_{latent}\rho_{liq}\rho_{vap}}{\sigma T_{sat}(\rho_{liq} - \rho_{vap})} \quad (41)$$

$$F_{q,flux} = \left(\frac{Q_{flux}}{Q_{ref\ flux}}\right)^n ; n = 0.95 - 0.3 * {P_{red}}^{0.3} ;\ Q_{ref\ flux} = 20{,}000\ W/m^2 \quad (42)$$

$$F_{press} = 0.7{P_{red}}^{0.2} + 4P_{red} + \frac{1.4P_{red}}{(1 - P_{red})} \quad (43)$$

$$F_{Ra} = \left(\frac{Ra_{actual}}{Ra_{ref}}\right)^{2/15} ;\ Ra_{ref} = 0.4\ \mu m \quad (44)$$

$$F_{wall} = \left(\frac{b}{b_{Cu}}\right)^{0.5} ; 'b'\ is\ effusivity, = (k * \rho * Cp)^{0.5}, \begin{cases} 'k'\ is\ thermal\ conductivity \\ '\rho'\ is\ density \\ 'Cp'\ is\ specific\ heat\ capacity \end{cases} \quad (45)$$

For water, following set of relationships are to be used:

$$n = 0.9 - 0.3 * {P_{red}}^{0.15} \quad (46)$$

$$F_{press} = 1.73{P_{red}}^{0.27} + 6.1{P_{red}}^{2} + \frac{0.68{P_{red}}^{2}}{\left(1 - {P_{red}}^{2}\right)} \quad (47)$$

- **Aprin et.al.** [90]

It suggests two different sections in a vaporizer and different correlations for each section. The division is based on the values of superficial gas velocity, with limits provided as 0.15 m/s and 0.35 m/s. It is suggested to use Cooper correlation for regions at < 0.15 m/s and a correlation is provided for sections having superficial gas velocity > 0.35 m/s. For the intermediate section, the maximum of the two predictions is to be used. The transition for the heat transfer mechanism is located in the intermediate region, with the transition point being at 0.12 m/s for low heat flux values and for larger values (> 52,000 W/m^2) being at 0.3 m/s.

$$h = \frac{Nu * D_{tube,ext}}{k_{WF,vap}} \quad (48)$$

$$Nu = 387{P_{red}}^{0.17}{Re_{vap}}^{0.34}{Pr_{vap}}^{0.33} \quad (49)$$

$$Re_{vap} = \frac{V_{vap}\rho_{WF,vap}D_{tube,ext}}{\mu_{Wf,vap}} \quad (50)$$

$$V_{vap} = \frac{Mass_{flux}x}{\rho_{WF,vap}\varepsilon} \quad (51)$$

$$Pr_{vap} = \frac{\mu_{WF,vap}Cp_{Wf,vap}}{k_{Wf,vap}} \quad (52)$$

$$\varepsilon = \frac{\frac{x}{\rho_{WF,vap}}}{1.047\left(\frac{x}{\rho_{WF,vap}} + \frac{1-x}{\rho_{WF,liq}}\right) + \frac{0.23}{Mass_{flux}}} \quad (53)$$

- **Kutateladze Correlation [88]**

$$h = \left[(3.37 * 10^{-9})\frac{k_{WF}}{L_{char,nb}}\left(\frac{H_{latent}}{Cp_{WF}Q_{flux}}\right)^{-2} {M_{star}}^{-4}\right]^{\frac{1}{3}} \quad (54)$$

$${M_{star}}^{-4} = \frac{\left(\frac{P}{\rho_{vap}}\right)^2}{(\sigma g)/(\rho_{liq} - \rho_{vap})} \quad (55)$$

$$L_{char,nb} = \left[\frac{\sigma}{g(\rho_{liq} - \rho_{vap})}\right]^{[1/2]} \quad (56)$$

2.2.5 Various Bundle Boiling Prediction Models

- **Palen et.al. Model [107]** (Superposition approach):

$$h_{bundle} = h_{ST,nb} F_b F_c + h_{nc} \quad (57)$$

h_{nc} becomes significant only at very low temperature differences.

- F_b *is a factor that accounts for the effect of circulation in the bundle.*
- F_c *is a factor that accounts for the effect of multicomponents.*

For design purposes, Palen suggests a simple expression to calculate F_c:

$$F_c = \frac{1}{1 + 0.023 Q_{flux}^{0.15} (BR)^{0.75}} \quad (58)$$

F_b can be calculated by a approximate formula given by Taborek [61]:

$$F_b = 1.0 + 0.1 \left(\frac{0.785 D_b}{C_1 (p_t / D_o)^2 D_o} - 1.0 \right) \quad (59)$$

- D_b *&* D_o *are bundle and tube diameters.*
- p_t *is the tube pitch.*
- *C_1 has a value of 1.0 for square & rotated square layouts, and 0.866 for triangular & rotated triangular layouts.*

At high heat fluxes, bundle boiling performance is similar to pool boiling performance, mainly because nucleate boiling is the dominant regime at high heat flux conditions. At lower heat flux values, the bundle boiling performance is much higher than nucleate boiling because convection plays a significant role at low heat flux conditions. Plain, smooth tubes derive large gains from bundle boiling effects, whereas enhanced/high-flux tubes don't gain much from bundle boiling effects.

- **Thome & Robinson Model** (Asymptotic approach):

The method is proposed by Thome and Robinson [72], and although the experiments were on a single-geometry tube bundle, the format is general enough to be adapted to other conditions.

An asymptotic method is used to calculate the bundle boiling heat transfer coefficient from the nucleate boiling heat transfer coefficient and convection boiling heat transfer coefficient.

$$h_{bundle} = (h_{nb}^2 + h_{cb}^2)^{1/2} \quad 60$$

- The nucleate boiling heat transfer coefficient is calculated using the Cooper correlation.
- The convective boiling heat transfer coefficient is then calculated as the unknown variable in above equation, and it was assumed to be for a thin liquid film flowing over the tubes in the bundle (as per [25]). These convective heat transfer values were then empirically fitted to give the following liquid film convection expression:

$$h_{cb} = 4.032 Re_{\delta}^{0.236} Pr_L^{0.4} \left(\frac{k_L}{\delta}\right) \quad 61$$

Where,

Pr_L is the liquid Prandtl number,

k_L is the liquid thermal conductivity,

δ is the liquid film thickness, and

Re_{δ} is the liquid film Reynolds number,

Various formulae / correlations used:

$$Re_{\delta} = \frac{4\rho_L u_L \delta}{\mu_L} \tag{62}$$

The mean liquid velocity in the film:

$$u_L = \frac{m_{total}(1-x)}{\rho_L(1-\varepsilon)} \tag{63}$$

To find liquid film thickness:

$$\delta = \frac{D_{\delta} - D}{2} \tag{64}$$

$$D_{\delta} = \sqrt{\frac{4A_L}{\pi} + D^2} \tag{65}$$

$A_L = A_{cross-flow}(1-\varepsilon)$, where ε is the void fraction.

$$A_{cross-flow} = A_{hex} - \frac{\pi D^2}{4} \tag{66}$$

$$A_{hex} = 6\left(\frac{L_{pp}}{3}\right)\left(\frac{L_{pn}}{2}\right) \tag{67}$$

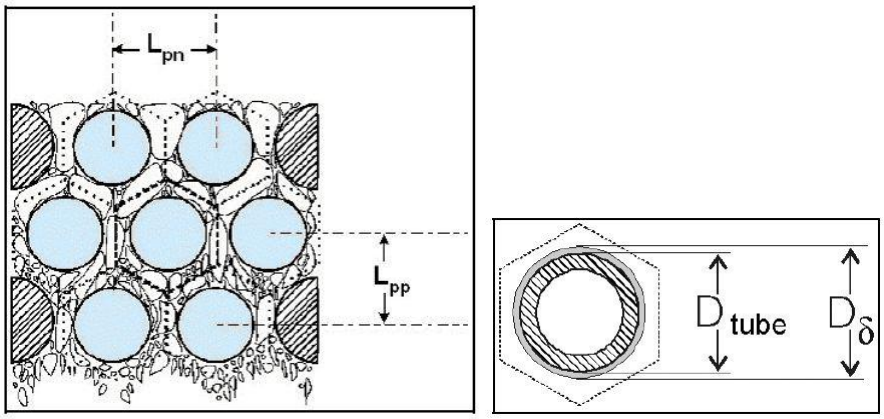

Various void fraction prediction methods available in literature based on fitting to experimental data:

$$\frac{1}{1-\varepsilon} = 1 + \frac{8}{X_{tt}} + \frac{1}{X_{tt}^2} \quad --- \; Ishihara\ et\ al.\ (1980)$$

$$\frac{1}{1-\varepsilon} = 1 + \left(\frac{6}{X_{tt}}\right)^{0.71} \quad --- \; Cornwell\ et.\ al.\ (1980)$$

$$\frac{1}{(1-\varepsilon)^2} = 1 + \frac{20}{X_{tt}} + \frac{1}{X_{tt}^2} \quad --- \; Fair\ \&\ Klip\ (1982)$$

$$X_{tt} = \left(\frac{1-x}{x}\right)^{0.9} \left(\frac{\rho_{vap}}{\rho_{liq}}\right)^{0.57} \left(\frac{\mu_{liq}}{\mu_{vap}}\right)^{0.11} \quad --- \; Martinelli\ parameter\ [123]$$

FEENSTRA – WEAVER – JUDD (2000) METHOD TO PREDICT VOID-FRACTION:

This method [106] does not depend on Martinelli parameter. It incorporates an expression for S (velocity ratio), which obeys correct limits at vapor qualities of 0 and 1.

The factors influencing 'S' were identified as following:

- Two-phase density
- Liquid-vapor density difference
- Pitch flow velocity of the fluid
- Dynamic viscosity of the liquid
- Surface tension
- Gravitational acceleration
- Gap between neighboring tubes
- Tube diameter
- Tube pitch
- Frictional pressure gradient

$$\varepsilon = \frac{1}{1 + S\left(\frac{(1-x)}{x}\frac{\rho_{vap}}{\rho_{liq}}\right)} \tag{68}$$

$$S = 1 + 25.7(Ri * Cap)^{0.5}\left(\frac{L_{tp}}{D}\right)^{-1} \tag{69}$$

$$Ri = \frac{\left(\rho_{liq} - \rho_{vap}\right)^2 g\left(L_{tp} - D\right)}{G^2},\ Richardson\ Number \tag{70}$$

$$Cap = \frac{\mu_{liq} u_{vap}}{\sigma},\ Capillary\ Number \tag{71}$$

$$u_{vap} = \frac{x * G}{\varepsilon * \rho_{vapor}},\ Mean\ vapor\ phase\ velocity \qquad 72$$

This method requires an iterative procedure for computation. It is also widely considered as the most accurate and reliable method available to predict void fractions in two-phase flows over tube bundles.

2.3 Computational Fluid Dynamics (CFD) Approach

Originally, the process of heat exchanger design has been based on empirical correlations and formulas developed by a number of researchers based on experimental data and observations and using coefficients and exponents for data fitting. It is an effective technique for designing equipment with similarities in geometry and operating conditions during the experiments, but it fails in being a universal method and also does not represent the extent and manner of influence of different factors that affect the final thermal performance of heat exchangers.

Various approaches to designing and rating heat exchangers can be summarized as:

- Empirical
    - limited range of validity & applicability to geometry and operating conditions
    - high accuracy
    - require large amounts of experimental data
    - lack any physical basis
- Semi-empirical
    - limited physical basis
    - range of validity & applicability is larger than empirical methods
    - high accuracy
- Mechanistic
    - solve the basic heat, momentum and mass transfer equations to account for all phenomena
    - universally applicable
    - very high accuracy (presumed)

    - very high computational requirements
    - not-yet-feasible
- CFD
    - mechanistic basic transfer models
    - closure models used are empirical/semi-empirical in nature

The most commonly used approach for macroscopic formulation of the thermo-fluid dynamics of the two-phase systems is the two-fluid model in Euler-Euler framework where both the phases are treated as inter-penetrating continua. In this approach, balance equations for mass, momentum and energy are written for each phase, that is vapor and liquid, separately and weighted by the so-called volume fraction which represents the ensemble averaged probability of occurrence for each phase at a certain point in time and space. Exchange terms between the phases appear as source/sink terms in the balance equations. These exchange terms consist of analytical or empirical correlations, expressing the interfacial forces, as well as heat & mass fluxes, as functions of average flow parameters. Since most of these correlations are highly problem-specific, their range of validity has to be carefully considered and entire model has to be validated against experiments [38].

This approach is laid out clearly in Figure 37 [100].

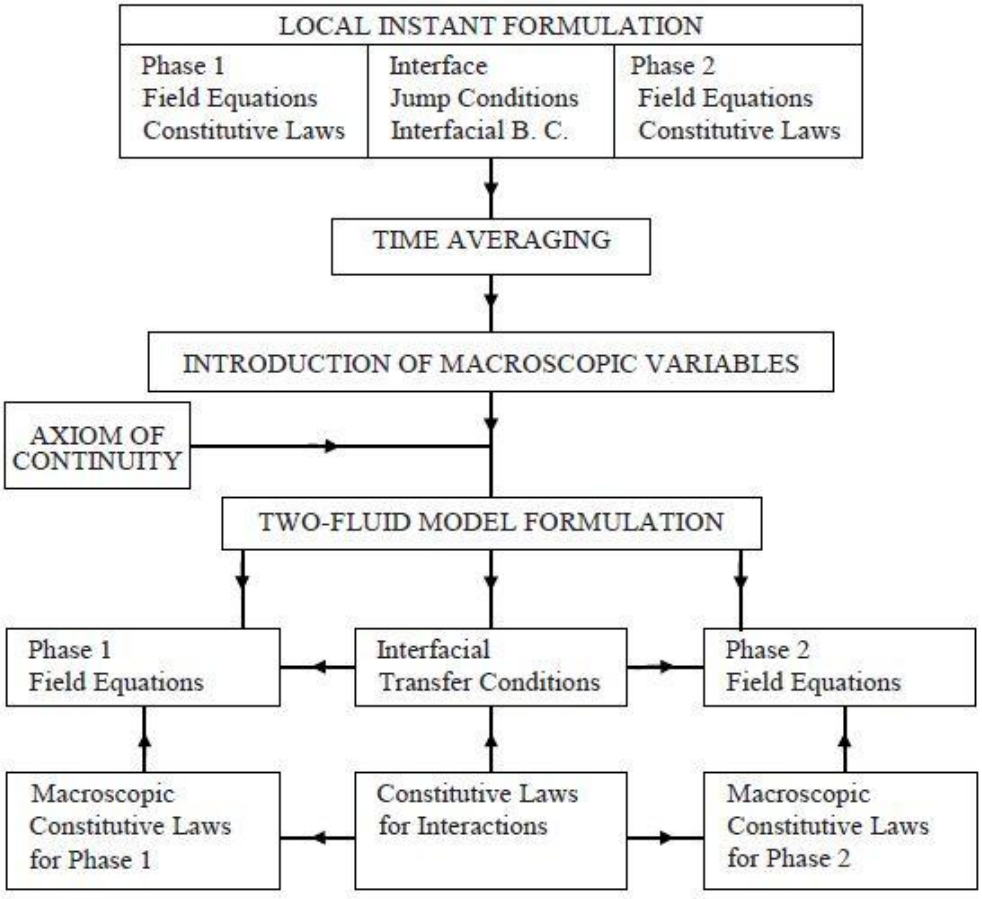

Figure 37 - Two-fluid Model

2.3.1 Navier-Stokes Equations

[ANSYS™ CFX™ Theory Guide, [5]]

The set of equations solved by ANSYS™ CFX™ are the unsteady Navier-Stokes equations in their conservation form. The instantaneous equations of mass, momentum and energy conservation can be written as follows in a stationary frame:

2.3.1.1 The Continuity Equation

$$\frac{\partial \rho}{\partial t} + \nabla.(\rho U) = 0 \tag{73}$$

2.3.1.2 The Momentum Equations

$$\frac{\partial (\rho U)}{\partial t} + \nabla.(\rho U \otimes U) = -\nabla p + \nabla.\tau + S_M \tag{74}$$

Where the stress tensor, τ, is related to the strain rate by

$$\tau = \mu\left(\nabla U + (\nabla U)^T - \frac{2}{3}\delta \nabla.U\right) \tag{75}$$

$T \rightarrow Stress\ vector$

2.3.1.3 The Total Energy Equation

$$\frac{\partial (\rho h_{tot})}{\partial t} - \frac{\partial p}{\partial t} + \nabla.(\rho U h_{tot}) = \nabla.(\lambda \nabla T) + \nabla.(U.\tau) + U.S_M + S_E \tag{76}$$

Where h_{tot} is the total enthalpy, related to the static enthalpy $h(T, p)$ by:

$$h_{tot} = h + \frac{1}{2}U^2 \tag{77}$$

The term $\nabla.(U.\tau)$ represents the work due to viscous stresses and is called viscous work term. This models the internal heating by viscosity in the fluid and is negligible in most flows. The term $U.S_M$ represents the work done due to external momentum sources and is currently neglected.

2.3.1.4 The Thermal Energy Equation

An alternative form of the energy equation, suitable for low-speed flows. To derive it, an equation is required for the mechanical energy K.

$$K = \frac{1}{2}U^2 \tag{78}$$

The mechanical energy equation is derived by taking the dot product of U with the momentum equation.

$$\frac{\partial(\rho K)}{\partial t} + \nabla.(\rho\, U\, K) = -U.\nabla_p + U.(\nabla.\tau) + U.S_M \tag{79}$$

Subtracting this equation from the total energy equation yields the thermal energy equation:

$$\frac{\partial(\rho h)}{\partial t} - \frac{\partial p}{\partial t} + \nabla.(\rho\, U\, h) = \nabla.(\lambda\, \nabla T) + U.\nabla_p + \tau{:}\nabla U + S_E \tag{80}$$

The term $\tau{:}\nabla U$ is always positive and is called the viscous dissipation. This models the internal heating of the fluid by its viscosity and is negligible in most flows.

The full thermal energy equation can be simplified to following form with two different sets of assumptions:

$$\frac{\partial(\rho h)}{\partial t} + \nabla.(\rho\, U\, h) = \nabla.(\lambda\, \nabla T) + \tau{:}\nabla U + S_E \tag{81}$$

a) If h is actually interpreted as Internal Energy,

$$e = h - \frac{P}{\rho} \tag{82}$$

Then the full thermal energy equation can be written as:

$$\frac{\partial(\rho e)}{\partial} + \nabla.(\rho\, U\, e) = \nabla.(\lambda\, \nabla T) - p\, \nabla.U + \tau : \nabla U + S_E \qquad 83$$

This is equivalent to the simplified thermal energy equation if $-p\, \nabla.U$ is neglected and h is interpreted as e. This interpretation is appropriate for liquids where, variable-density effects are negligible. *For liquids that have variable specific heats (implemented through CELs or other methods), the solver includes the P/ρ contribution in the enthalpy tables. This is inconsistent, because the variable is actually Internal Energy. For this reason, the thermal energy equation should not be used in this situation, particularly for subcooled liquids*.

b) On the other hand, if $\frac{\partial p}{\partial t}$ and $U.\nabla p$ are neglected in the full thermal energy equation, then the simplified thermal energy equation follows directly. This interpretation is appropriate for low Mach number flows of compressible gases.

The thermal energy equation, despite being a simplification, can be useful for both liquids and gases in avoiding potential stability issues with the total energy formulation. For example, the thermal energy equation is often preferred for transient liquid simulations. On the other hand, if proper acoustic behavior is required (for example, predicting sound speed) or for high speed flows, then the total energy equation is required.

2.3.2 Hydrodynamic Equations used in multi-phase applications of ANSYS™ CFX™

The following is a summary of the equations of momentum and mass transfer for inhomogeneous multiphase flow in CFX:

2.3.2.1 Momentum Equations

$$\frac{\partial}{\partial t}(r_\alpha \rho_\alpha U_\alpha) + \nabla.\left(r_\alpha(\rho_\alpha U_\alpha \otimes U_\alpha)\right) = -r_\alpha \nabla p_\alpha + \nabla.\left(r_\alpha \mu_\alpha(\nabla U_\alpha + (\nabla U_\alpha)^T)\right) + \sum_{\beta=1}^{N_p}\left(\Gamma_{\alpha\beta}^{+} U_\beta - \Gamma_{\beta\alpha}^{+} U_\alpha\right) + S_{M\alpha} + M_\alpha \quad (84)$$

- $S_{M\alpha}$ describes momentum sources due to the external body forces and user-defined momentum sources.
- M_α describes the interfacial forces acting on phase α due to presence of other phases. Additional information on the models for interfacial forces is in 2.3.2.5 Interphase Momentum Transfer.
- $\left(\Gamma_{\alpha\beta}^{+} U_\beta - \Gamma_{\beta\alpha}^{+} U_\alpha\right)$ represents momentum transfer induced by interphase mass transfer.

2.3.2.2 Continuity Equations

$$\frac{\partial}{\partial t}(r_\alpha \rho_\alpha) + \nabla.\left(r_\alpha(\rho_\alpha U_\alpha)\right) = S_{M\,S\,\alpha} + \sum_{\beta=1}^{N_p} \Gamma_{\alpha\beta} \quad (85)$$

- $S_{M\,S\,\alpha}$ describes the user specified mass sources
- $\Gamma_{\alpha\beta}$ is the mass flow rate per unit volume from phase β to phase α. This term occurs only if interphase mass transfer takes place

2.3.2.3 Volume Conservation Equation

This is the constraint that the sum of volume fractions of different phases is unity.

$$\sum_{\alpha=1}^{N_p} r_\alpha = 1 \tag{86}$$

This equation may also be combined with the phasic continuity equations to obtain a transported volume conservation equation. Taking the continuity equation, dividing it by phasic density and sum over all the phases:

$$\sum_{\alpha} \frac{1}{\rho_\alpha}\left(\frac{\partial}{\partial t}(r_\alpha \rho_\alpha) + \nabla.(r_\alpha \rho_\alpha U_\alpha)\right) = \sum_{\alpha} \frac{1}{\rho_\alpha}\left(S_{M\,S\,\alpha} + \sum_{\beta=1}^{N_p} \Gamma_{\alpha\beta}\right) \tag{87}$$

If the phases are treated as incompressible with no sources, the equation simplifies to:

$$\sum_{\alpha} \nabla.(r_\alpha U_\alpha) = 0 \tag{88}$$

The simplified form requires volume flows to have zero divergence.

2.3.2.4 Pressure Constraint

The complete set of hydrodynamic equations represent $4N_p + 1$ equations in the $5N_p$ unknowns - $U_\alpha, V_\alpha, W_\alpha, r_\alpha \; and \; p_\alpha$. This means that $N_p - 1$ more equations are required to close the system. These are provided by constraints on the pressure, namely that all the phases share the same pressure field:

$$p_\alpha = p \; for \; all \; \alpha = 1, \dots \dots \dots, N_p \qquad 89$$

2.3.2.5 Interphase Momentum Transfer

These equations pertain to inhomogeneous multiphase flow. Interphase momentum transfer, $M_{\alpha\beta}$, occurs due to interfacial forces acting on phase α due to interaction with another phase β. The total force on phase α due to interaction with other phases is denoted M_α:

$$M_\alpha = \sum_{\beta \neq \alpha} M_{\alpha\beta} \qquad 90$$

As the interfacial forces between two phases are equal and opposite, the net interfacial forces sum to zero:

$$\left(M_{\alpha\beta} = -M_{\beta\alpha}\right) \Rightarrow \sum_{\alpha} M_\alpha = 0 \qquad 91$$

The total interfacial force acting between two phases may arise from several independent physical effects:

$$M_{\alpha\beta} = M_{\alpha\beta}^D + M_{\alpha\beta}^L + M_{\alpha\beta}^{LUB} + M_{\alpha\beta}^{VM} + M_{\alpha\beta}^{TD} + M_S + \dots \qquad 92$$

The forces represented above represent respectively:

- Interphase Drag
- Lift Force
- Wall Lubrication Force
- Virtual Mass Force

- Interphase Turbulent Dispersion Force
- Solids Pressure Force (for dense solid particle phases only)

2.3.2 Heat Transfer modeling in ANSYS™ CFX™

2.3.2.1 Modeling of subcooled boiling at a heated wall

Subcooled boiling is observed at heated surfaces, when the heat flux applied to the wall is too high to be transferred to the core flow of liquid by the single-phase convective-conductive mechanisms, with the term "subcooled" meaning that the saturation temperature of the fluid is exceeded only in a local vicinity of the wall whereas the average temperature in the bulk is still below saturation temperature [37]. The modeling phase change simulations in ANSYS™ CFX™ are handled by the Wall Boiling Model.

2.3.2.2 Wall Boiling Model

[ANSYS™ CFX™ Theory Guide, [5]]

Wall boiling starts when the wall temperature achieves a value that is sufficiently large to initiate the activation of wall nucleation sites and this value is typically a few degrees above the saturation temperature of the fluid. Evaporation starts in the microscopic cavities and crevices which are always present on the solid surface. Liquid becomes supersaturated locally in these nucleation sites, leading to growth of vapor bubbles at the sites. The bubbles detach from the sites when they are sufficiently large so that the external forces (viz. inertial, gravitational or turbulent) exceed in magnitude the surface tension forces that keep the bubbles attached to the wall. As the bubbles depart from the wall, they are displaced by superheated liquid in the vicinity of the nucleation sites, after which the nucleation site is free to create another bubble. In the regions of the wall, where there is no bubble growth, the wall heat transfer to the liquid is described by single-phase convective heat transfer.

The detailed physics of the bubble growth is very complex and occurs on very small length scales in the vicinity of the wall. It is unrealistic to model the detailed physics in a phase-averaged Eulerian multiphase model. It is equally unrealistic to resolve the small length scales with ultra-fine meshes. The model used in ANSYS™ is so-called mechanistic model, which aims to model the important physical sub-processes using engineering correlations. The model is a sub-grid scale model, in the sense that the complex physics is assumed to take place very close to the wall at a distance which is smaller than the mesh resolution at the wall. These processes are handled by the wall heat flux partitioning algorithm implemented in ANSYS™ CFX™ based on the works of Kurul & Podowski (1991) and later refined by Egorov. This model is also known as RPI Model (RPI – Rensselaer Polytechnic Institute). In it, a number of the sub-models of the overall mechanistic model were taken from correlations originally developed for exploitation in the one-dimensional thermo-hydraulic simulation models.

PARTITIONING OF THE WALL HEAT FLUX

A fundamental feature of the mechanistic model of wall nucleation is the algorithm for deciding how the wall heat flux is to be partitioned amongst the separate physical processes of evaporation and sensible heating of the liquid phase. In regions of the wall not influenced by nucleation sites, it is sufficient to consider the wall heat flux as contributing solely to single-phased liquid convective heat transfer. However, in the vicinity of the nucleation sites, some of the heat contributes to vapor production and the remainder to super heating of the liquid phase as it displaces the rising bubbles and this process has been termed as Quenching.

The mechanistic heat partitioning model has the following general structure:

$$Q_w = Q_l + Q_e \quad (93)$$

Where, Q_l is consumed for heating the subcooled liquid, and Q_e is the evaporation heat flux. Q_l is further divided into two components:

$$Q_l = Q_c + Q_q \quad (94)$$

Where, Q_c is the heat flux corresponding to convective heat transfer, and Q_q is the heat flux corresponding to quenching. So, the partition is now expressed in its complete form:

$$Q_w = Q_c + Q_q + Q_e \quad (95)$$

One of the limitations of the model is that the vapor is assumed to be saturated everywhere, and no part of the wall heat flux is arranged for superheating in case of dryout conditions.

The heat partitioning model considers the whole wall surface being separated into two fractions;

a) Fraction A_2 is influenced by vapor bubbles forming on the wall
b) Fraction A_1 is the rest of the wall surface; $A_1 = 1 - A_2$

For the wall region A_1, the wall heat flux is modelled in a similar way as for the single-phase flow of pure liquid, by using the turbulent wall function procedure in the case of turbulent flow. This part of Q_l called the convective heat flux can be correlated for turbulent flow as:

$$Q_c = A_1 h_c (T_w - T_l) \quad 96$$

Where T_w is the temperature of the solid wall, T_l is the temperature of the liquid at the wall and h_c is the turbulent heat transfer coefficient, which depends on the velocity field and on the near-wall grid cell size (This is a serious limitation and was removed later by Egorov).

The wall area fraction A_2 represents the remaining part of the wall surface, which exchanges heat with both phases. The already mentioned evaporative heat flux Q_e comes from this part of the surface and is consumed for evaporation of the initially subcooled liquid:

$$Q_e = \dot{m}\left(h_{g,sat} - h_l\right) \quad 97$$

Where $\dot{m}$ is the evaporation mass transfer rate per unit wall area, and $h_{g,sat}$ and h_l are the specific enthalpies of the saturated vapor and the subcooled liquid respectively.

A part of the heat flux to the liquid, coming from the wall area fraction A_2 is transported between the bubble departure and the next bubble formation at the same nucleation site. This additional mechanism of heating the liquid phase called quenching, is modelled as:

$$Q_q = A_2 h_q (T_w - T_l) \quad 98$$

The area fraction values A_1 & A_2 play an important role in the heat flux partitioning model. They are related to the nucleation site density per unit wall

area n and to the influence area of a single bubble forming at the wall nucleation site. The latter value is modelled by introducing the bubble departure diameter value d_w which can generally serve as a length scale of the wall boiling mechanism. The default value (user modifiable) chosen by RPI for the bubble influence zone is twice as large as d_w, and this gives the non-dimensional area fraction of bubble influence as:

$$A_2 = min(\pi d_w^2 n, 1) \qquad 99$$

The two most important parameters governing the heat partitioning model are the nucleation site density (n) and bubble departure diameter (d_w). In the RPI wall-boiling model, they are correlated to the wall superheat $\Delta T_{sup} = T_w - T_{sat}$ and to the near-wall liquid subcooling $\Delta T_{sub} = T_{sat} - T_{liq}$ respectively.

There a number of sub-models implemented in the wall boiling model that act as closure correlations for the basic mechanistic approach, although these sub-models are themselves of empirical/semi-empirical nature.

- Wall Nucleation Site Density
- Bubble Departure Diameter
- Bubble Detachment Frequency
- Bubble Waiting Time
- Area Influence Factors
- Convective Heat Transfer
- Quenching Heat Transfer
- Evaporation Rate

2.3.3 FVM/FEM

[Source: ANSYS™ CFX™ manuals and Autodesk™ Help]

The CFD approach implements and uses the Finite Volume Method (FVM). In this technique the region of interest is divided into sub-regions called 'control volumes'. The governing equations are integrated over the control volume assuming a piece-wise linear variation of the dependent variables (u, v, w, p, T). This piece-wise linear variation both the accuracy and complexity. Using these integrations, the solver essentially balances the fluxes across the boundaries of individual control volumes. The fluxes are calculated at the mid-point between the discrete nodes in the domain. In a topologically regular mesh (same number of divisions in any one direction), this flux calculation is simpler as compared to an irregular mesh (e.g. automatically generated tetrahedral mesh) where the computational effort is significantly increased. As a result, an approximation of the value of each variable at specific points throughout the domain can be obtained and finally a full picture of the behavior of the flow is derived.

In Finite Element Method (FEM), a method weighted residuals is generally used. In this method, the governing partial differential equations are integrated over an element after having been multiplied by a weight function. The dependent variables are represented on the element by a shape function which is the same form as the weight function. The shape function may be one of many types – linear for 2D triangular elements, bi-linear for 2D quadrilateral elements, linear for 3D tetrahedral elements, tri-linear for 3D hexahedral elements and mix for 3D 5 & ^ sided elements. The main advantage as well as the disadvantage of the finite elements is that it is a mathematical approach in which it is difficult to put any physical significance on the terms in the algebraic equations. Finite elements, unlike finite volumes, do not deal with fluxes. However, the application of finite elements on any geometric shape is the same.

METHOD	ADVANTAGES	DISADVANTAGES
Finite Element Method	1. More mathematics involved 2. Natural boundary conditions (for fluxes) 3. Master element formulation 4. Same effort for geometry of any shape	1. More mathematics involved – less physical significance
Finite Volume Method	1. Fluxes have more physical significance	2. Irregular geometries require far more effort

2.3.4 Justification for selected software

For the current project, ANSYS™ CFX™ and Fluent™ were chosen because of following reasons – a) existing licences and High Performance Computing facilities at the University of Canterbury, b) experienced faculty, c) widespread use among engineering students which can serve as base for discussions and learning.

2.3.5 Literature review of CFD studies of HEs

2.3.5.1 Need and Significance of CFD Analysis

There is an ever-growing need for the use of heat exchangers in widening ranges of temperature & pressure conditions along with increasing options for the motive fluids that can be used. The experimental approach is unable to keep up with this pace and has financial constraints as well. This has prompted the use of CFD to gain knowledge about thermal and flow characteristics of existing exchangers thus validating the CFD models by comparison against experimentally accumulated data. These models can be further used to optimize & modify the existing range of heat exchangers and also speed up the

pace of development of new types of heat exchangers. CFD simulations enable us to improve upon existing designs and test new designs for any industrial equipment due to the fact that it is economically non-viable to manufacture full scale prototypes of all the conceivable designs. CFD simulations form a filter mechanism at a fraction of a cost of actual manufacture and testing to narrow down to a few final designs that can be then manufactured and tested.

The comparison of experimental approach vis-à-vis the CFD analysis approach can be briefly outlined as:

EXPERIMENTAL APPROACH:

Advantages:

- Provides highly reliable empirical/semi-empirical correlations
- Provides knowledge about safety and life-time in a more reliable manner
- Does not suffer from simplifications and assumptions that are required in numerical simulations
- The predictions are highly accurate within the range of validity.

Limitations:

- Extremely expensive
- Time consuming
- Requires intricate and costly set-up of sensors to gain full knowledge of the thermal and flow dynamics. These models provide excellent predictions, but these are not based in the actual physics of the process.
- Correlations derived have narrow validity range

CFD APPROACH:

Advantages:

- Ability to visualize the flow (velocity & pressure) and temperature fields on the shell-side aids in simplifying the assessment of weaknesses
- Ability to test large number of new designs and different parameters at a small fraction of the financial & time requirements as compared to the experimental approach

Limitations:

- Need for validation when major parameters are changed (fluid, pressure, surface characteristics)
- Current models are based on empirical closure models
- Requirement of extensive and costly computational resources for industrial scale simulations
- Very specific experimental data is required for development and validation of models. This is because of the fact that ANSYS™ CFX™ does not physically resolve all the phenomena such as nucleation, bubble departure etc. Instead, it used empirical correlations to account for these phenomena and these calculated effects are then used as source and sink terms in the mass, momentum and energy transfer equations.

There are a number of papers and literature present for single phase heat transfer [10, 40, 52, 68, 76-79, 101, 111, 112, 129, 130, 137, 149, 151, 152, 154] but only a few on phase change, and those mostly in simple geometries such as annuli. During the literature review, no articles were found that would deal with phase change in large geometries such as vaporizers while providing

details of parameters (e.g. bubble departure diameter, mean bulk bubble diameter, nucleation site density) required to validate and tune CFD set-ups. The data available for multi-tube geometries enables only qualitative sort of CFD validation, viz. vapor flow patterns and the variation of heat transfer coefficient around the circumference of a tube. There is a significant leap in both complexity and computational resources' requirement between single phase and multi-phase simulations. Figure 38 shows plots from single phase heat transfer simulations for non-baffled and baffled STHEs, with details of work outlined in 4.1.1 CFD Analysis of TEMA-E type STHE.

.

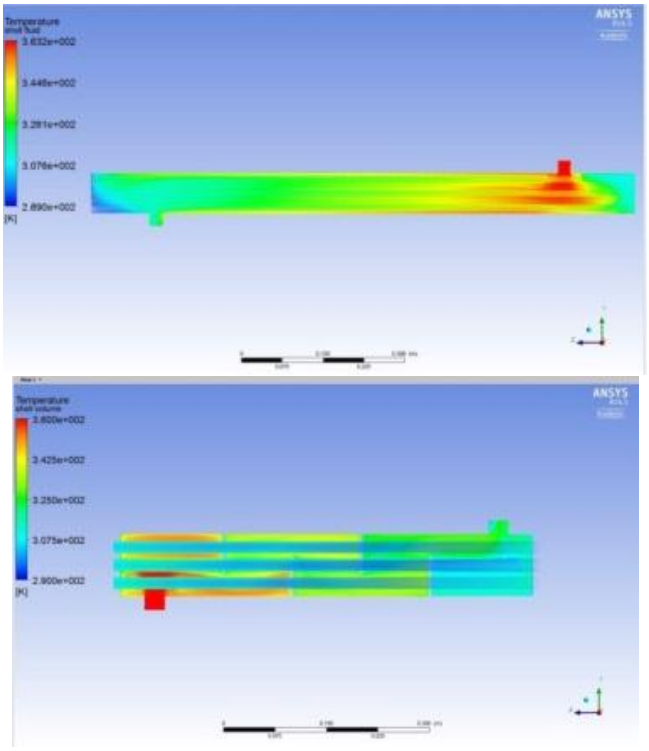

Figure 38 - a) Non-baffled STHE, b) Baffled STHE – Temperature Volume Rendering

The CFD analysis of vaporizers is complicated. The modeling of phase change processes is an inherently complex process, and the sheer complexity of

geometry and large sizes of vaporizers make the simulation process intensely computational resource hungry. It is necessitated because of the fact that the use of empirical/semi-empirical models, which are essentially reduced-dimensional models, can predict deficiencies in design but are unable to pin point the location and factors of weaknesses [40].

The CFD simulations can also be used to check flow maldistribution issues and effects of baffle cut and baffle spacing [40]. The single phase simulations were also carried out on Shell and Plate HEs and Helical Baffled STHEs.

The CFD simulations for phase change are done using the most commonly used approach for macroscopic formulation of the thermo-fluid dynamics of the two-phase systems: the two-fluid model in Euler-Euler framework where both the phases are treated as inter-penetrating continua. In this approach, balance equations for mass, momentum and energy are written for each phase, i.e. gas and liquid, separately and weighted by the so-called volume-fraction which represents the ensemble averaged probability of occurrence for each phase at a certain point in time and space. Exchange terms between the phases appear as source/sink terms in the balance equations. These exchange terms consist of analytical or empirical correlations, expressing the interfacial forces as well as heat and mass fluxes, as functions of the average flow parameters. Since most of these correlations are highly problem specific, their range of validity has to be carefully considered and entire model needs to be validated against experimental data. To compare results between different experiments using different working fluids and at different pressures, values of relevant dimensionless groups need to be paid special attention. For bubbles freely rising in a column of water under the action of gravity, following variables were determined to be governing their shape by [26, 148] :

- Terminal velocity

- Characteristic length, defined as the diameter of the volume-equivalent sphere
- Density of the carrier fluid
- Viscosity of the carrier fluid
- Surface tension
- Gravitational acceleration

For boiling phenomenon, the important dimensionless numbers are [38, 39]:

- Tube Reynolds number (for in-tube flows) ($\rho V_l L/\mu_l$) – It is the ratio of inertial to viscous forces.
- Liquid-gas density ratio,
- Weber number ($\rho_G {V_{rel}}^2 L/\sigma$) – It is used in analysing fluid flows where there is an interface between two fluids, especially for multiphase flows with strongly curved surfaces.
- Jakob number ($\frac{c_{p,liq}\rho_l}{H_{latent}\rho_g}(T_{wall}-T_{sat})$) – It plays an important descriptive role in virtually all direct contact processes that involve a change of phase [3].
- Boiling number ($q"/H_{latent}\rho_g V_g$) – It can be seen as the ratio of a) mass of vapor generated per unit area of heat transfer surface, to b) mass flow rate per unit flow cross-sectional area [62].

For bubble dynamics, the relevant dimensionless numbers are [38, 39]:

- Bubble Reynolds number ($\rho_g V_b D_b/\mu_f$) – It is the ratio of inertial forces to viscous forces.
- Eötvös/Bond number ($\Delta\rho g L^2/\sigma$) – It is the ratio of body forces to surface tension forces.

- Morton number ($g\mu_f^4\Delta\rho/\rho_f^2\sigma^3$) – It is used in conjunction with Eötvös/Bond number for characterizing shapes of bubbles/drops moving in a surrounding continuous medium.

The physics of the bubble growth is very complex and occurs on very small length scales in the vicinity of the heated wall. It is unrealistic to model the detailed physics in a phase-averaged Eulerian multiphase model. It is equally unrealistic to resolve the small length scales with ultra-fine meshes. The wall-boiling model implemented in CFX is a so-called mechanistic model, which aims to model the important physical sub-processes (such as bubble dynamics) using engineering correlations as closure models for the constitutive equations. This means that the accuracy of the simulation's results is directly dependent on the case set-up being within the validity range of the correlations used. On the other hand, it translates into reduced computational expense by getting rid if the need for ultra-fine meshes which are problematic in other ways as well in addition to increased computational requirements, such as convergence issues. It is a sub-grid model, in the sense that the complex physics is assumed to take place at length scales smaller than the mesh resolution. Use of sub-grid models is common in CFD analysis throughout the flow domain and not just at the walls, e.g. turbulence models. The first and most well-known model of this kind was formulated by Kurul and Podowski (1991) from the Rensselaer Polytechnic Institute. It is known as the RPI Model. In this model, a number of sub-models of the overall mechanistic model were taken from correlations originally developed for exploitation in one-dimensional thermo-hydraulic simulation methods. Tu and Yeoh [48] point out that the Kurul and Podowski model suffers from two major drawbacks:

- Firstly, the model is only applicable to subcooled boiling flows where bubbles are immediately released into the bulk subcooled liquid. This

assumption is possibly valid if horizontally orientated pool boiling flow is considered. But, the bubbles have a tendency to slide before lifting off into the bulk liquid especially in vertical convective subcooled boiling flows. In such cases, transient conduction due to sliding bubbles becomes the dominant mode of heat transfer. For vertical subcooled boiling flows, it is important that the wall heat flux partitioning model incorporates the area of influence and transient conduction component due to these sliding bubbles.

- Secondly, the bubble release frequency, which proportionally affects the quenching heat flux value, is determined by Cole's empirical correlation which has been employed rather successfully to solve subcooled boiling flows at high pressures, the range of applicability of the relationship for low-pressure subcooled boiling flows remains open to debate. The uncertainty of evaluating the bubble release frequency through empirical correlations should be minimized and replaced by mechanistic approach.

The authors present a modification of the wall heat flux partitioning algorithm along with a mechanistic approach to calculating bubble detachment frequency. The model for the bubble detachment frequency relies on the bubble contact angle, which is again taken to fit with the data. It thus is also based on fitting the parameters to the experimental data.

The solver chosen for the present study is ANSYS™ CFX™ (v15.0 and v17.0) due to reasons cited in 2.3.4 Justification for selected software, and also the presence of the bubble dynamics and wall boiling models in the mentioned modules.

2.3.5.2 CEL Routines:

CFD set-ups for phase change simulations are combination of mechanistic and empirical/semi-empirical correlation based approach. The correlations used are derived for a particular range of validity in terms of geometry and operating conditions. Therefore, these correlations need to be tuned for CFD analysis of any experiment based on detailed data from the experiment. A literature review of the articles [15-19, 37-39, 41, 42, 46, 48, 49, 57, 69, 70, 132, 150] dealing with phase change reveals the following main points about the CFD model set-up w.r.t. parameters that need to be tuned based on experimental data:

- **Crucial Model Components**
  - Wall Heat Flux Partitioning
  - Bubble size distribution
  - Interfacial area calculation
  - Bubble departure diameter and bubble detachment frequency
- **Recommended Customizations**
  - Bulk bubble diameter
  - Bubble Departure Diameter
  - Variable Thermophysical Properties
  - Wall Roughness Modeling
  - Modification in wall heat flux partitioning method

2.3.5.3 Bulk Bubble Diameter Modeling

Sensitivity of the Void Fraction prediction on the Bubble Diameter

(Degree of subcooling has a significant impact)

It is clearly seen from [17, 42] that the prediction of the void fraction is based on the specification/calculation of the bubble diameter. This requires the

presence of experimental data for fine tuning of the models of used in CFX to enable a successful simulation of the experimental conditions and results. Also, the more sophisticated approach of predicting the bubble diameter distribution by coupling the population balance model with the two-fluid model was attempted by [17, 39, 42, 69]. While this approach makes the model less dependent on the user inputs, it adds more empirical terms for the bubble break-up and coalescence, which in turn need to be accurately modelled. This approach was able to capture the bubble coalescence away from the heated wall, however the overall void fraction predictions were found to be less sensitive to the bubble size away from the wall in these cases, since the experiments had low subcooling and hence less condensation in the bulk. A similar study by Morel & Lavieville showed that the population balance model is still some way away from providing accurate predictions in the boiling flows and the bulk bubble diameter variations do not significantly affect the void fraction predictions in regimes where the liquid subcooling is low. However, for high subcooling cases, as observed by Vyskocil & Macek, the overall void fraction predictions would also depend on the bulk condensation and bubble size prediction models.

It varies along the flow direction and also in the direction normal to the flow. It is a very important modeling parameter. Local bubble diameter size defines the interfacial area density in the bulk flow, which influences the interfacial momentum transfer terms (drag force and wall lubrication force) and interfacial heat and mass transfer terms (bulk condensation and evaporation). As is pointed out by Koncar-Krepper [17], a smaller bulk bubble diameter increases the condensation rate (large interfacial area) and the two-phase region is narrower and more gas phase is accumulated near the heated wall.

A summary of different approaches to modeling the bulk bubble diameter in addition to manual specification of a single value is given here, based on the literature review:

Model used by Tu-Yeoh, 2002 - [70]

$$d = \frac{d_1(\theta - \theta_0) + d_0(\theta_1 - \theta)}{\theta_1 - \theta_0} \qquad 100$$

Here d_0 and d_1 are the bubble diameters at reference liquid subcoolings θ_0 and θ_1. Outside this subcooling range the diameters are assumed to be constant. The values being: $d_1 = 1.5mm$, $\theta_1 = 0K$; $d_2 = 0.15mm$, $\theta_2 = 13.5K$. Reference subcooling conditions need to be taken from experiments. The effect of modeling the bulk bubble diameter is more pronounced on the velocity and turbulent kinetic energy profiles and very little on predicted void fraction profiles.

Model used in Anglart-Nylund – [57]

To close the phase transition model in the bulk bubbly flow with a mean bubble diameter, d_B, Kurul & Podowski and also Anglart et.al. [57, 58] proposed to calculate the bulk bubble diameter locally as a linear function of liquid subcooling, T_{sub}.

$$d_b = \begin{cases} 0.00015 & for\ \Delta T_{sub} > 13.5\ K \\ -10^4 \Delta T_{sub} + 0.0015 & for\ 0 < \Delta T_{sub} \leq 13.5\ K \\ 0.0015 & for\ \Delta T_{sub} \leq 0\ K \end{cases} \qquad 101$$

Model used in Zeitoun-Shoukri [103, 104]

The authors implemented a low-pressure correlation (proposed by Zeitoun-Shoukri [103, 104]) for mean bubble diameter:

$$\frac{D_s}{\sqrt{\frac{\sigma}{g\Delta\rho}}} = \frac{0.0683\left(\frac{\rho_l}{\rho_g}\right)^{1.326}}{Re^{0.324}\left(Ja + \frac{149.2\left(\frac{\rho_l}{\rho_g}\right)^{1.326}}{Bo^{0.487}Re^{1.6}}\right)} \quad 102$$

Here D_s is the mean Sauter bubble diameter, g is the gravitational acceleration, *Re* is the flow Reynolds number, *Bo* is the boiling number, and *Ja* is the Jakob number based on the liquid subcooling. The mean bubble diameter, *d*, is estimated from mean Sauter bubble diameter, D_s.

Model used in Koncar-Kljenak-Mavko - [18]

In the CFX code, the local bulk bubble diameter is treated as an adjustable parameter independent of the bubble departure diameter. The authors propose a simple model of radial distribution (moving from heated surface to outer pipe surface in an annular heating geometry) of the bubble diameter. The shift of the maximum local bubble diameter away from the heated wall is modeled by a linear evolution in the radial direction as:

$$d_b^* = min\left(d_{bw} + y_w, d_{b,max}\right) \quad 103$$

$$d_b = d_b^*.exp\left(-\frac{\Delta T_{sub} - \Delta T_{sub,w}}{2.\Delta T_{sub,w}}\right) \quad 104$$

Here the bubble departure diameter d_{bw} is imposed in the near wall cell. The radial distance from the near-wall cell centre is denoted by y_w. The maximum allowed bubble diameter $d_{b,max}$ in the subcooled flow is prescribed as 2 d_{bw}. The second equation describes the decrease of the bubble diameter due to the

condensation in the subcooled flow field, where $\Delta T_{sub,w}$ is the local subcooling in the near-wall cell. Thus, in the proposed model the local bulk bubble diameter (d_b) in the flow field is coupled with the bubble departure diameter (d_{bw}) generated in the near-wall cell.

Models used in Krepper-Koncar-Egorov 2007 [37], Cheng-Li-Wang [42] & Lee et.al. 2002 [142]

All these articles use the same form of equation (with slightly different values) for bulk bubble diameter calculation based on degrees of subcooling values of vaporizing fluid:

Krepper-Koncar-Egorov 2007 [37]

($d_{B,1}$ = 0.1mm, $T_{sub,1}$ = 13.5K; $d_{B,2}$ = 2mm, $T_{sub,2}$ = -5K)

$$d_B = \frac{d_{B,1}\left(T_{sub} - T_{sub,2}\right)}{T_{sub,1} - T_{sub,2}} + \frac{d_{B,2}\left(T_{sub,1} - T_{sub}\right)}{T_{sub,1} - T_{sub,2}} \qquad 105$$

Re-arranging,

$$d_B = \frac{\left(d_{B,1} - d_{B,2}\right)T_{sub}}{T_{sub,1} - T_{sub,2}} + \frac{\left(d_{B,2}T_{sub,1} - d_{B,1}T_{sub,2}\right)}{T_{sub,1} - T_{sub,2}} \qquad 106$$

Cheng-Li-Wang [42]

(Values being: *For Case 1:* d_0 = 0.15mm, T_0 = 13.5K; d_1 = 5mm, T_1 = -5K; *and for Case 2:* d_0 = -0.15mm, T_0 = 13.5K; d_1 = 7mm, T_1 = -5K)

$$d = \frac{(d_1 - d_0)T_{sub}}{T_1 - T_0} + \frac{(d_0T_1 - d_1T_0)}{T_1 - T_0} \qquad 107$$

Lee et.al. 2002 [142]

(*$d_{B,1}$ = 0.1mm, $T_{sub,1}$ = 13.5K; $d_{B,2}$ = 2-8mm (5mm gives best results), $T_{sub,2}$ = -5K*)

$$d = \frac{d_1 - d_0}{T_1 - T_0} T_{sub} + \frac{d_0 T_1 - d_1 T_0}{T_1 - T_0} \qquad 108$$

2.3.5.4 Bubble Departure Diameter

The model(s) for bubble departure diameter are included in the wall-boiling model itself and bubble departure diameter directly affects the gas phase generated on the heated wall. The bulk bubble diameter is used to calculate the interfacial area density as is clear from the following equation:

$$A_l = 6\alpha_G / d_B \qquad 109$$

It is also used to calculate:

- non-dimensional parameters required by the simulations (e.g. Reynolds and Prandtl numbers)
- interphase drag coefficient (area and volume of dispersed phase particles)
- interfacial area density (interphase connect area)
- lift force
- wall lubrication force

Bubble departure diameter at a heated wall has a strong impact on the share of the heat transfer components (wall heat flux partitioning) and also on the calculated amount of vapor production.

There are a number of different correlations available for bubble dynamics developed across a range of conditions, with the majority being for the adiabatic flows. The behavior of bubbles when they are generated within the flow as opposed to injection in adiabatic flows is quite different. In the project the models being used are those that have been shown in literature to work well within CFX and give reasonable agreement with experimental results.

The conventional linear formula proposed by Tolubinski and Kostanchuk for calculation of bubble departure diameter as a function of local subcooling has been verified to be lacking in physical and experimental basis [42].

The authors in [42] have proposed a modified bubble departure diameter correlation based on the Unal's semi-mechanistic model and empirical correlation of Tolubinski-Kostanchuk. They assumed that the bubble departure diameter at low pressure still obeys the empirical correlation of Tolubinski-Kostanchuk and the bubble departure coefficient (c_{bw}) can be solved by uniting the two models and using the inlet parameters as follows:

$$(d_{bw})_{inlet} = c_{bw} exp\left(\frac{-\Delta T_{sub,inlet}}{45}\right) = \left(\frac{2.42 \times 10^{-5}.p^{0.709}a}{\sqrt{b\varphi}}\right)_{inlet} \quad 110$$

The undetermined parameter bubble departure coefficient (c_{bw}) (also the minimum/reference diameter in ANSYS™ CFX™) is obtained (by Unal's model (applicable only at inlet section)) and used to predict the bubble departure diameter along the whole heated section (by Tolubinski-Kostanchuk model).

The bubble departure computed in this manner is based on – pressure, wall material, wall subheating, local liquid subcooling etc. and will have a broad range of application from low to high operating pressures.

2.3.5.5 Saturation Temperature Variation

In the Wall Boiling model implemented in CFX, the saturation temperature is specified as a constant value. This will work well for small geometries where the pressure does not change much between the inlet and the outlet, but it will give inaccurate predictions when the pressure drop is significant either due to viscous losses or hydrostatic head. In such cases, the saturation temperature is

specified as a CEL routine. The saturation temperature can be varied in two ways:

- By assuming a linear variation between the inlet and outlet pressure values
- By an equation derived from curve-fitting in MATLAB™ with pressure as the independent parameter

2.3.5.6 Wall Roughness Model

The authors of [17] introduce two two-phase wall functions – a) for adiabatic flows, and b) for boiling flows (a.k.a. two-phase wall model).

As per Ramstorfer et.al. [46], most of the models proposed for the liquid velocity field in the bubble-laden boundary layer flows were developed for non-boiling flow, where the gas bubbles are injected through the porous channel walls. These approaches essentially rely on the void fraction as a key input parameter which cannot be extended to the subcooled boiling flow conditions. It is because of the fact that the void fraction can be fairly easily and accurately determined in the non-boiling case from the volume of gas injected through the porous walls. But, in case of boiling flows, the void fraction results from the whole process of bubble nucleation, growth, detachment and collapse. As such, being determined by the complex interaction of various sub-processes, its estimation based on the given thermophysical conditions in the near-wall region, such as wall superheat, subcooling, pressure etc., is inevitably affected by much uncertainty. Also, the bubbles collapse once they leave the superheated wall layer, the vapor phase exists only in a thin near-walled region.

The two-phase wall function for the boiling flows is the same as the rough wall treatment implemented in ANSYS™ CFX™.

The wall function is explained in detail in Ramstorfer et. al. 2008 [46].

A little about the two-phase wall model:

The bubble layer created on the hot surface is assumed to act like a rough surface.

The standard formulation for logarithmic law of the wall for the rough surfaces (as given in Ramstorfer et.al. [46]):

$$u^+ = \frac{1}{k} ln y^+ + C - \Delta u^+;\ \Delta u^+ = \frac{1}{k} ln(1 + C_{kr} k_r^+);\ C_{kr} = 0.5$$

$$k_r^+ = \frac{\rho_l k_r u_\tau}{\mu_l}; C = 5.3, k = 0.41, u^+ = \frac{\overline{u}}{u_\tau}, y^+ = \frac{u_\tau y}{\nu}, or, y^+ = \frac{\rho y u_\tau}{\mu}$$

It is commonly used for sand-grain roughness.

It is implemented in the CFX Solver as: (Source: ANSYS™ CFX™ Theory Guide, [5])

$$u^+ = \frac{1}{k} ln(y^+) + B - \Delta B; \Delta B = \frac{1}{k} ln\left(1 + 0.3 {h_s}^+\right); B = 5.2, k = 0.41 (von\ Karman\ constant)$$

$$y^+ = \frac{\rho \Delta y u_\tau}{\mu}; u_\tau = \left(\frac{\tau_\omega}{\rho}\right)^{1/2}; u^+ = \frac{u}{u_\tau}; Wall\ friction\ velocity, u_\tau\ or\ u_\omega = \sqrt{\frac{\tau_w}{\rho}}$$

The dimensionless roughness height is calculated as:

$$k_r^+ = \frac{u_\tau k_r}{\nu}; and\ in\ ANSYS™\ CFX™\ as\ h^+ = \frac{h u_\tau}{\nu}$$

The flow regime can be classified as hydrodynamically smooth, transitional or fully-rough based on the dimensionless roughness height (a.k.a. roughness

based Reynolds number). The implementation is a bit different in [46] and the CFX Solver Theory Guide:

a) $k_r^+ < 2.25$, $2.25 \leq k_r^+ < 90$, $k_r^+ > 90$

b) $h^+ < 5$, $5 \leq h^+ < 70$, $h^+ > 70$

Details of the implementation as given in [46]:

$$\Delta u^+ = \begin{cases} 0, & k_r^+ < 2.25 \\ \frac{1}{k} ln\left(\frac{k_r^+ - 2.25}{87.75} + C_{kr} k_r^+\right) sin[0.426(ln k_r^+ - 0.811)] & 2.25 \leq k_r^+ < 90 \\ \frac{1}{k} ln(1 + C_{kr} k_r^+) & k_r^+ \geq 90 \end{cases} \quad 111$$

Where $C_{kr} = 0.5$, commonly used for sand-grain roughness.

NOTE: The equation being used by CFX in the transition region is not given in documentation (*reason given is that it is proprietary*). The roughness height (*used as input to the model*) fitted from the experimental data basically represents an equivalent roughness height incorporating the dynamic effect of the vapor bubble layer on the liquid flow. The bubble-equivalent roughness height (*can be specified or provided by an appropriate model/correlation*) is then used to calculate the actual near-wall velocity profile. [46] have used the bubble diameter at the instant of departure as the bubble equivalent roughness height and the model used for bubble diameter at the instant of departure is the Zeng et.al. model [92] (*where the bubble departure diameter is obtained from a balance of drag, shear-lift, buoyancy and bubble growth forces*). As such the departure diameter is determined as mainly dependent on the wall superheat and wall friction velocity.

The model assumes that for boiling on the heated surface the roughness height can be represented by a functional dependence on the bubble departure diameter and contribution of nucleate boiling heat flux to the total heat flux. The ratio of nucleate boiling heat flux to the total heat flux represents the boiling activity. So, evidently as the boiling activity increases such that the ratio (q_{nb}/q_w) approaches unity the dynamic influence of the bubble layer on the liquid flow in terms of k_r becomes maximal. On the other hand at very low nucleate boiling heat fluxes, associated with the hot surface being sparsely populated with bubbles, the bubble influence on the liquid flow vanishes and k_r goes to zero.

Koncar Krepper [17] specify the roughness height (k_r) as:

$k_r = \eta d_{bw} \left(\frac{q_{nb}}{q_w}\right)^{\zeta} = \eta d_{bw} \left(1 - \frac{q_{1\Phi}}{q_w}\right)^{\zeta}, \eta = 0.5, \zeta = 0.174, q_{1\Phi} = \frac{\rho_l c_p u_W}{T^+_{y^+(nw)}}(1 - A_{bub})\left(T_w - T_{l,(nw)}\right)$, which is same as the convection heat flux (one of the three partition terms) in CFX where it is implemented as $Q_c = (1 - A_w)h_c(T_w - T_l)$. The bubble departure diameter is the one calculated from the Tolubinski-Kostanchuk model, or any other desired model or CEL routine.

Different authors use different models/correlations for the roughness height (*for rough wall functions*):

- Koncar-Matkovic 2012 - [19]: $k_r = d_{bw}$ equal to bubble departure diameter (Model used: *Tolubinski-Kostanchuk*)
- Koncar-Krepper 2008 - [17]:$k_r = \eta d_{bw} \left(\frac{q_{nb}}{q_w}\right)^{\zeta} = \eta d_{bw} \left(1 - \frac{q_{1\Phi}}{q_w}\right)^{\zeta}$
- Rzehak-Krepper 2011 - [38]: $k_r \propto N d^3_{Wbw}$, dependent on 'bubble departure diameter' & 'nucleation site density'. The constant of

proportionality has no theoretical basis and its value has been determined by matching to the experimental data.

Effect of implementing the boiling wall function:

- Improvement in void-fraction prediction
- Best prediction (compared to measured values) of gas and liquid phase velocities
- Over-prediction of turbulent kinetic energy in the near-wall region and good agreement after that (while the single phase models give slight over-prediction throughout the domain)
- No difference in liquid temperature prediction

As per [19], with the inclusion of the wall roughness model, we observe a over-prediction of velocity in the boiling region and significant under-prediction of turbulence. These deficiencies of the numerical models are alleviated to a large extent by modeling the bulk bubble diameter rather than specifying it.

2.3.5.7 Mechanistic Approach: Bubble Dynamics & Modified Wall Heat Flux Partitioning Model

2.3.5.7.1 Bubble Departure & Lift-Off Diameter

Zeng et.al. [92] describe the instant at which a vapor bubble detaches from its nucleation site as the point of departure and the instant at which it detaches from the heated surface is referred to as the lift-off point. Zeng et.al. [66] demonstrate that while a vapor bubble is attached to its nucleation site it grows asymmetrically. The asymmetrical growth has been modeled by considering a vapor bubble growing at an inclined angle θ_i as depicted in Figure 16. θ_i is referred to as the "inclination angle". To calculate the forces due to bubble growth in the direction of the flow (x-direction) or normal to the heating

surface (y-direction), knowledge of the inclination angle is required. This was a major limitation in [66], which was removed in [92], where the inclination angle is determined as a part of the solution as opposed to the empirical constant in [66]. The analysis presented by Zeng et.al. [66, 91, 92] is for Horizontal Flow Boiling.

The forces as per Tu & Yeoh [48] are (Figure 39):

$$\sum F_x = F_{s,x} + F_{du,x} + F_{sL} + F_h + F_{cp}\,;\ \sum F_y = F_{s,y} + F_{du,y} + F_{qs} + F_b$$

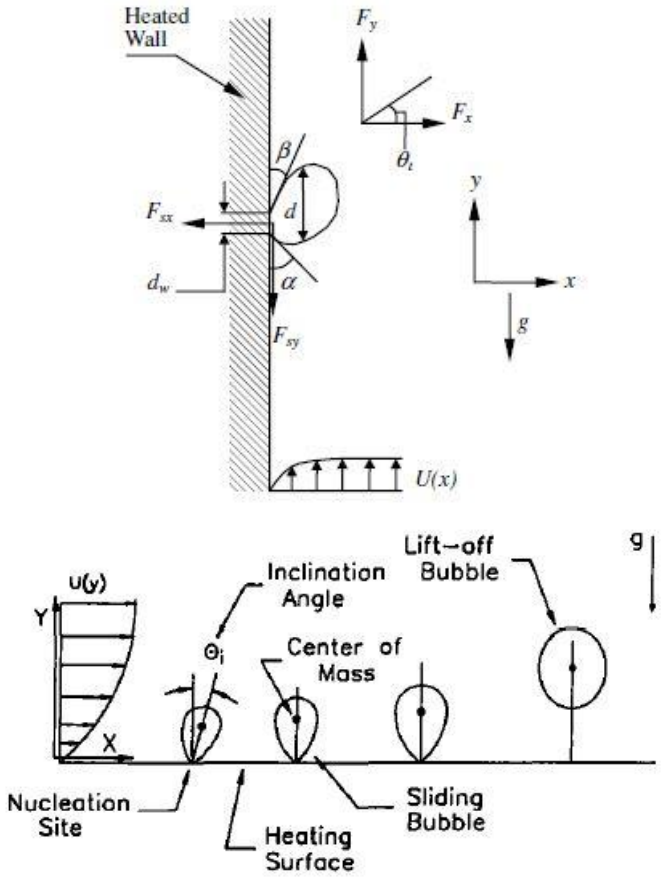

Figure 39 - Schematic drawing illustrating the forces acting on a growing vapor bubble, Tu & Yeoh [48] (LEFT) and Zeng et.al. [91, 92] (RIGHT); α, β and θ_i are advancing, receding and inclination angles

respectively; d_w is the surface/bubble contact diameter and d is the vapor bubble diameter while it is attached to the wall

Rewriting the forces as per Tu & Yeoh [48] for flow direction in Figure 15b:

$$\sum F_y = F_{s,y} + F_{du,y} + F_{sL} + F_h + F_{cp} + F_b; \sum F_x = F_{s,x} + F_{du,x} + F_{qs}$$

The forces as per Zeng et.al. [92] are (Figure 15b):

$$\sum F_y = F_{s,y} + F_{du,y} + F_{sL} + F_h + F_{cp} + F_b ; \sum F_x = F_{s,x} + F_{du,x} + F_{qs}$$

There is one noticeable difference in the two models: While Tu & Yeoh consider the buoyancy force in the direction of the flow, Zeng et.al. consider buoyancy force to be acting in the direction normal to the flow direction. It is because the flow is vertical-upward in case of Tu & Yeoh and horizontal in case of Zeng et.al.

According to Zeng et.al. [66, 91, 92] the contact diameter approaches zero towards lift-off, the surface tension force is assumed to be negligible in comparison to growth and buoyancy forces [91]. The use of this assumption greatly simplifies the prediction of departure and lift-off diameters since knowledge of the contact diameter and advancing & receding contact angles is not required. As a consequence of this assumption, the authors recommend that the usefulness of the model should be judged based on its agreement with limited available experimental data. It is observed that the bubble lift-off size increases as the wall superheat increases which is expected, since the growth force, which retards the vapor bubble lift-off, increases with increasing wall superheat. The authors observe that while a vapor bubble is attached to its nucleation site, it is inclined in the flow direction by angle θ_i due to quasi-steady drag. It is postulated that immediately following the departure, the bubble attempts to right itself such that the inclination angle becomes zero.

Therefore, once the bubble departs from its nucleation site, it slides along the heating surface in the flow direction with zero inclination angle until it lifts off the heating surface some finite distance downstream.

In our discussion, we will consider the vertical upward flow as in Tu & Yeoh.

Description of the forces:

- Surface Tension Force

$$F_s \rightarrow Surface\ Tension\ Force;\ \ F_{s,x} = -d_w\sigma\frac{\pi}{\alpha-\beta}[cos\ \beta - cos\ \alpha]$$

$$F_{s,y} = -d_w\sigma\frac{\pi(\alpha-\beta)}{\pi^2-(\alpha-\beta)^2}[sin\ \alpha + sin\ \beta] \quad (112)$$

- Quasi-steady Drag

$$F_{qs} = 6C_D\mu_l\Delta U\pi r; r \rightarrow bubble\ radius = \frac{d}{2}; \quad (113)$$

$$C_D = \frac{2}{3} + \left[\left(\frac{12}{Re}\right)^n + 0.796\right]^{-1/n}; n = 0.65, Re \rightarrow \quad (114)$$

$$bubble\ Reynolds\ number \rightarrow \frac{\rho_l u_\tau x}{\mu_l}, also = \frac{2Ur}{\nu}$$

$$u_\tau \rightarrow friction\ velocity, U \rightarrow uniform\ flow\ velocity, \nu \rightarrow kinematic\ viscosity(= \mu/\rho)$$

$$\Delta U \rightarrow relative\ velocity\ between\ bubble\ center\ of\ mass\ and\ bulk\ liquid$$

- Growth Force (*unsteady drag due to asymmetrical growth of the bubble and the dynamic effect of the unsteady liquid such as the history force and the added mass force*) ($\dot{d}$& $\ddot{d}$ are the first and second order derivative of diameter w.r.t. time)

$$F_{du,x} = -\frac{1}{4}\rho_l \pi d^2 \left(\frac{3}{2} C_s \dot{d}^2 + d\ddot{d}\right) \cos\theta_i \; ; C_s = \frac{20}{3}$$
$$F_{du,y} = -\frac{1}{4}\rho_l \pi d^2 \left(\frac{3}{2} C_s \dot{d}^2 + d\ddot{d}\right) \sin\theta_i \qquad (115)$$

- Shear Lift Force

$$F_{sL} = \frac{1}{8} C_L \rho_l \Delta U^2 \pi d^2 \qquad (116)$$

$$C_L = 3.877 G_s^{-1/2} \left[\frac{1}{Re^2} + 0.014 G_s^2\right]^{\frac{1}{4}} \qquad (117)$$

$$G_s \rightarrow dimensionless\ shear\ rate \rightarrow \left(\frac{dU}{dx}\right)\left(\frac{r}{\Delta U}\right) \qquad (118)$$

Gradient $\frac{dU}{dx}$ *can be determined through universal velocity profile for turbulent flow*

$$\frac{U}{u_\tau} = 2.5 \ln(9.8x^+) \; ; x^+ = \frac{\rho_l \Delta U d}{\mu_l} ; u_\tau \; is \; friction \; velocity \qquad (119)$$

- Buoyancy Force

$$F_b = \frac{1}{6}\pi d^3 (\rho_l - \rho_g) g \qquad (120)$$

- Hydrodynamic Force

$$F_h = \frac{9}{8}\rho_l \Delta U^2 \frac{\pi d_w^2}{4} \quad (121)$$

- Contact Pressure Force

$$F_{cp} = \frac{\pi d_w^2}{4}\frac{2\sigma}{d_r} \quad (122)$$

Symbols: g is acceleration due to gravity; d_w is surface-bubble contact diameter; d is vapor bubble diameter at the wall, $r = d/2$; ΔU is the relative velocity between the bubble center of mass and liquid; C_D & C_L are drag and shear lift coefficients; r_r is the curvature radius of the bubble at reference point on the surface $x=0$, which is almost equivalent to five times of the bubble diameter, $r_r \sim 5r$ [66].

The surface-bubble contact diameter (d_w) changes from the point of inception until the point of sliding or lift-off. Tu & Yeoh [49] present it as a function of bubble contact angle θ as:

$$d_w = 1 - \exp(-2\theta^{0.6}) D_{d\ or\ l} \quad (123)$$

For the experiments of Lee et.al. [142], the bubble contact angles have been taken at 35^o and 45^o [49]. The advancing and receding angles are estimated based on bubble contact angles as:

$\alpha = \theta + \theta', and\ \beta = \theta - \theta'$, where θ' of 5^o is adopted and a value of 10^o is applied for the inclination angle θ_i.

The bubble growth is defined based on a diffusion controlled solution [132]:

$$d(t) = \frac{4b}{\sqrt{\pi}} Ja \sqrt{\eta t}; \quad 124$$

$$Ja = \frac{\rho_l C_{pl} \Delta T_{sat}}{\rho_g h_{fg}}; \quad 125$$

$$\eta = \frac{k_l}{\rho_l C_{pl}} \quad 126$$

Here, η is thermal diffusivity and 'b' is an empirical constant that is intended to account for the asphericity of the bubble and is taken = 0.21.

In this case, while a vapor bubble remains attached to the heated wall, the sum of the parallel and normal forces must satisfy the following conditions: (i) $\sum F_x = 0$, and (ii) $\sum F_y = 0$.

- If first condition is violated prior to second condition, i.e. $\sum F_x > 0$ while $\sum F_y = 0$, the bubble will lift-off without sliding. The point at which $\sum F_x$ is just greater than zero is the criterion for departure and lift-off.
- If $\sum F_y > 0$ while $\sum F_x = 0$, the bubble will start to slide along the heated surface before lifting off. The point when $\sum F_y$ is just greater than zero, is the criterion for departure.

Therefore, a pre-requisite to predicting the departure diameter is to determine which condition is violated first.

When the sum of the parallel forces (y-direction) equals zero, a bubble could begin sliding while still being attached to the wall. Therefore,

- Bubble departure (sliding, when it departs the nucleation site) diameter (D_{sl}) is obtained by solving $\sum F_y = 0$.

$$\sum F_y = F_{s,y} + F_{du,y} + F_{qs} + F_b \quad (127)$$

Similarly, for a bubble ready to lift-off and detach from the wall, the sum of the normal forces (x-direction) is equal to zero. Hence,

- By solving $\sum F_x = 0$, the bubble lift-off diameter (D_l) is calculated.

$$\sum F_x = F_{s,x} + F_{du,x} + F_{sL} + F_h + F_{cp} \quad (128)$$

The advancing and receding contact angles as well as the bubble inclination angle and the surface-bubble contact diameter evolve from the point of inception to the point of departure along the heated wall. The evolution processes of these angles are as yet unknown [47]. These have to be taken as constant and fitted to experimental data.

2.3.5.7.2 Bubble Growth & Waiting Time, Bubble Detachment Frequency

Yeoh et.al. [49, 132] present a mechanistic approach to determine the bubble frequency based on the description of the ebullition cycle in nucleate boiling where the waiting time (t_w) and the growth time (t_g) of the bubble play role in determining the frequency of the bubble departure.

The period between the times when one bubble leaves the nucleation site (begins to slide of lifts off) and when the next bubble is generated is called waiting time:

$$t_w = \frac{1}{\pi\eta}\left[\frac{(T_{sup}+T_{sub})C_1 r_c}{T_{sup}+\left(\frac{2\sigma T_{sat}}{C_2\rho_g h_{fg} r_c}\right)}\right]^2; \quad 129$$

$$where, T_{sub} = T_{sat} - T_{liq}; C_1 = \frac{1+\cos\theta}{\sin\theta}; C_2 = \frac{1}{\sin\theta},$$

$$and, r_c = F\left[\frac{2\sigma T_{sat} k_l}{\rho_g h_{fg} Q_w}\right]^{\frac{1}{2}}; F = \left(\frac{1}{C_1 C_2}\right)^{\frac{1}{2}}; T_{sup} = T_{wall} - T_{sat}$$

Here, Q_w is the wall heat flux and F is the degree of flooding of the available cavity size.

The growth time t_g can be determined by using bubble sliding diameter in the bubble growth equations:

$$t_g = \frac{1}{16}\frac{\pi}{\eta}\frac{D_{sl}^2}{b^2 Ja^2}; \quad 130$$

$D_{sl}\ is\ determined\ from \sum F_y = 0$

The frequency of the bubble departure is evaluated as:

$$f = \frac{1}{t_w + t_g}$$

The lift-off period t_l can be determined by using bubble lift-off diameter in the bubble growth equations:

$$t_l = \frac{1}{16}\frac{\pi}{\eta}\frac{D_l^2}{b^2 J a^2}; \quad 131$$

$D_l\ is\ determined\ from \sum F_x = 0$

The sliding time t_{sl} is the difference between the bubble lift-off period and the bubble growth period:

$$t_{sl} = t_l - t_g$$

The sliding distance can subsequently be estimated to be:

$$l_s = \frac{2}{3} C_v t_{sl}^{3/2}; \quad 132$$

$$C_v = 3.2u_l + 1$$

Here, C_v is an acceleration coefficient which reflects the rise of the bubble velocity in time after it starts to slide away from a nucleation site. u_l is the tangential liquid velocity adjacent to the heated surface.

2.3.5.7.3 Modified Wall Heat Flux Partitioning Model

Enhancement in heat transfer during forced convective boiling can be attributed to the presence of both sliding and stationary bubbles. There are essentially two mechanisms:

- Latent heat transfer due to microlayer evaporation
- Transient conduction as the disrupted thermal boundary layer reforms during the waiting period (i.e. incipience of the next bubble at the same nucleation site)

TRANSIENT CONDUCTION

This occurs in regions at the point of inception and in regions being swept by sliding bubbles.

For a stationary bubble it is evaluated as:

$$Q_{tc} = 2\sqrt{\frac{k_l \rho_l C_{pl}}{\pi t_w}}(T_{wall} - T_l) R_f N_a \left(K \frac{\pi D_d^2}{4}\right) t_w f + 2\sqrt{\frac{k_l \rho_l C_{pl}}{\pi t_w}}(T_{wall} - T_l) R_f N_a \left(\frac{\pi D_d^2}{4}\right)(1 - t_w f) \quad (133)$$

Here, D_d is the bubble departure diameter. The first term of the RHS of the equation accounts for the transient conduction occurring in the projected area of detached bubble during waiting time. The second term considers the transient conduction happening within the area of growing bubble after the waiting time before bubble departure – growth period. For a sliding bubble, the heat flux due to transient conduction that takes place during the sliding

phase and the area occupied by the sliding bubble at any instant of time is given by:

$$Q_{tcsl} = 2\sqrt{\frac{k_l \rho_l C_{pl}}{\pi t_w}}(T_{wall} - T_l) R_f N_a l_s D t_w f + 2\sqrt{\frac{k_l \rho_l C_{pl}}{\pi t_w}}(T_{wall} - T_l) R_f N_a f t_{sl} \left(\frac{\pi D^2}{4}\right)(1 - t_w f) \quad (134)$$

Here, D is given by:

$$D = \frac{D_{sl} + D_l}{2}$$

And ***K*** is a ratio of the "area of influence – decides the area from where the liquid is drawn in when the bubble leaves the heater surface" to the projected area of the bubble. It is usually taken as = 1.8

The reduction factor R_f depicts the ratio of the actual number of bubbles lifting off per unit area of the heater surface to the number to the number of active nucleation sites per unit area, i.e.

$$R_f = \frac{1}{l_s/s}, when \quad l_s \geq s;\ l_s = 1, when\ l_s < s$$

Here, l_s is the sliding distance and s is the spacing between nucleation sites, which can be estimated from

$s = \frac{1}{\sqrt{N_{a,tot}}}$.

The nucleation site density can be calculated as per the usual Lemmert-Chawla correlation,

$$N_a = 185\left(\Delta T_{sup}\right)^{1.805}$$

An approach to calculating nucleation site density based on fractal distribution of nucleation sites on heated surfaces is given by Yeoh et.al. [49].

The area of the heater surface under the influence of stationary and sliding bubbles is:

$$A_q = R_f \left[N_a \left(K \frac{\pi D_{sl}^2}{4} \right) t_w f + N_a \left(\frac{\pi D_{sl}^2}{4} \right) (1 - t_w f) + N_a l_s K D t_w f + N_a f t_{sl} \left(\frac{\pi D^2}{4} \right) (1 - t_w f) \right] \quad 135$$

FORCED CONVECTION

The heat flux due to forced convection can be obtained according to the definition of local Stanton number for turbulent convection. It acts on the areas of heater surface that are not under the influence of the bubbles.

$$Q_c = St\ \rho_l C_{pl} u_l \left(1 - A_q\right)\left(T_{wall} - T_{liq}\right) \quad 136$$

Here, u_l is the adjacent liquid velocity.

EVAPORATION

The heat flux attributed to vapor generation is given by the energy carried away by the bubbles lifting off from the heated surface. It also represents the energy of vaporization whereby the bubbles of lift-off size (diameter, D_l) are produced:

$$Q_e = R_f N_a f \left(\frac{\pi D_l^3}{6}\right) \rho_g h_{fg} \quad 137$$

The total heat flux is the combination of the following heat flux components:

$$Q_{wall} = Q_c + Q_{tc} + Q_{tcsl} + Q_e \quad 138$$

When there are no sliding bubbles, the model is similar to the Kurul-Podowski model.

Flowchart for the modified Wall Heat Flux Partitioning Model – [49]

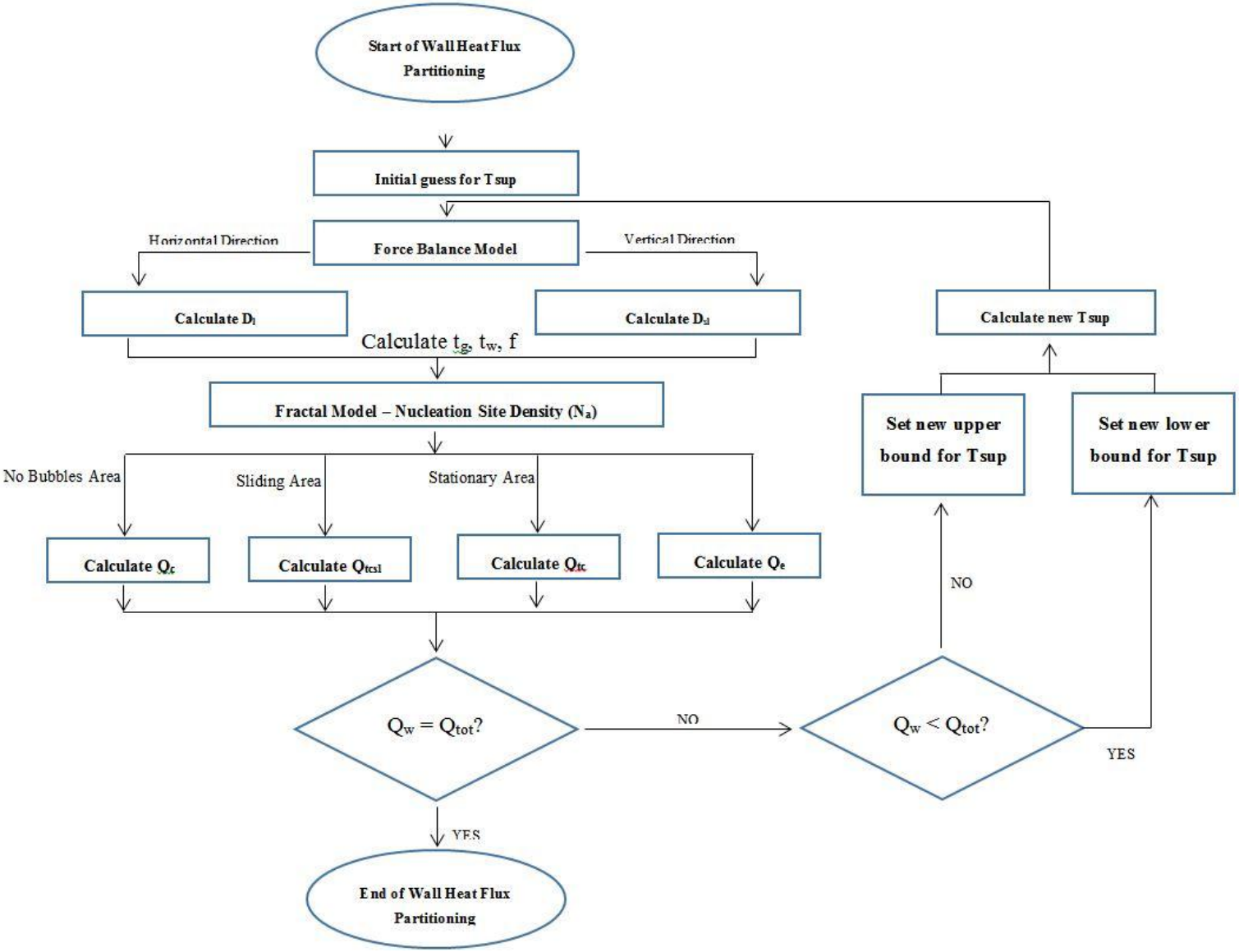

2.3.6 Justification for lesser fidelity and scope of CFD analysis results – based on lack of experimental data

The current project will be able to achieve a high degree of fidelity in its results regarding single-phase CFD analysis and single-tube boiling CFD analysis due to availability of well-established theoretical models and detailed experimental data respectively. For the multi-tube geometries, the project will form a foundation based on qualitative and quantitative validation against limited experimental data and coupled with theoretical models available for such cases. A substitute fluid will be selected for obtaining values required for CFD set-up of boiling simulations in absence of experimental data for pentane. This can be achieved with high degree of confidence due to well-established dimensionless numbers that characterize bubble dynamics and boiling process along with the known dependence of heat transfer performance on thermophysical properties of a fluid. The MATLAB™ code for Plate Heat Exchanger and Shell-and-Tube Heat Exchanger vaporizer are based on established correlations and will be compared against real world data as well.

3.0 MATLAB™ Modeling

The initial part of the project focuses on modeling of entire ORC power plant with focus on developing detailed models, based on published and proven correlations & methods, for heat exchangers. The theoretical modeling was firstly done using EES and subsequently MATLAB™.

3.1 Model for Plate Heat Exchanger

PHEs are being used in more and more applications due to their high rate of heat transfer and high heat duty per unit volume of the exchanger. This prompted an investigation into comparison to experimental data for a PHE against predictions from theoretical methods for PHE design and analysis.

Using a model presented in Dovic et.al. [27, 31] a comparison was carried out between theoretically predicted values and experimental data collected from the ORC-B unit operating in University of Canterbury.

3.1.1 Brief summary of the model:

A PHE can be divided into a number of repeating units and the analytical analysis of the flow in these repeating units is conducted. The basic repeating units are also termed as "basic cells". The figures below show the basic cells and the flow pattern in them.

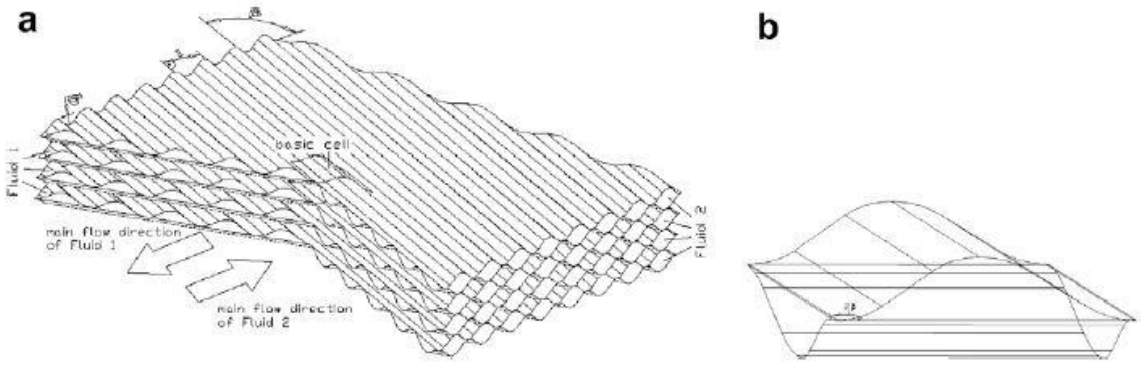

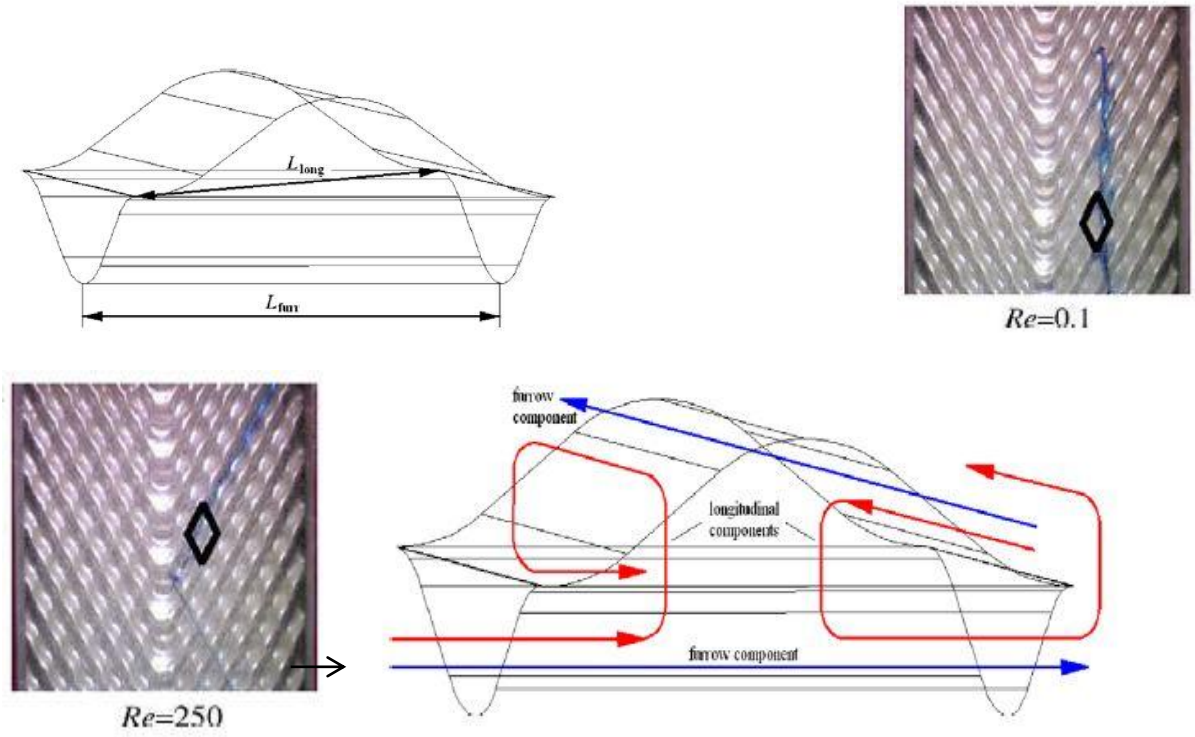

Figure 40 - Basic cell and the nomenclature; Visualization of the flow - [27]; Flow pattern in the basic cell

The flow of calculations is:

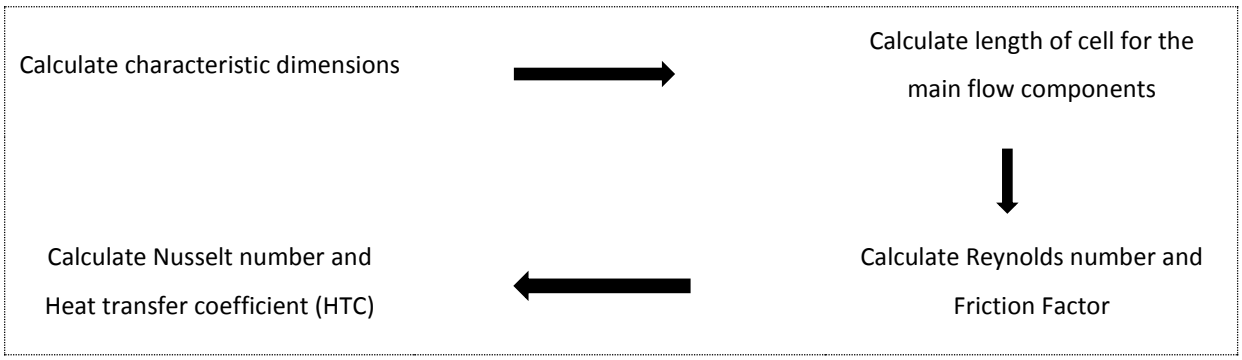

$$Nu_{sine} = 0.38 * 0.40377 \left(4 f_{app} Re_{sine}{}^{2} \left(Dia_{hyd,sine} / L_{cell} \right) \right)^{0.375} Pr^{1/3} \left(\frac{\mu_{bulk}}{\mu_{wall}} \right)^{0.14} \quad 139$$

$$\frac{Nu}{Nu_{sine}} = \frac{Dia_{hyd}}{Dia_{hyd,sine}} ; HTC = \frac{Nu * k}{Dia_{hyd}}$$

Theoretical determination of the Heat Transfer Coefficient (HTC) requires knowledge of the chevron angle, stamping depth and pitch which were unavailable for the PHE under consideration. The most usual values for chevron angles used in the PHEs are 25^o to 35^o. Table 2 shows the theoretical HTC values for a number of different chevron angles. Further analysis requires accurate knowledge of the stamping depth and pitch. The current analysis uses the most commonly used values in the industry (as per literature reviewed).

The experimentally determined value for the HTC was obtained from the analysis done by Michael Southon [Masters Student, University of Canterbury]: **52.71 W/m^2-K**

CHEVRON ANGLE	HTC (W/m^2-K)
25	52.76
30	54.89
35	56.66
40	58.15
45	59.41
50	60.48
55	61.38
60	62.14
65	65.07
70	68.55

Table 2 - Theoretically calculated values of HTC for different Chevron angles

3.2 Modeling for STHE Vaporizer

The motivation for developing a code for STHE vaporizer analysis came from the absence of any literature that can give us a detailed picture of thermophysical condition of working fluid outside the tube rows. The methods found in literature dealt with overall rating of the vaporizer whilst providing us geometrical parameters. These methods are good for initial design and rating of these units but they are not helpful when we want to troubleshoot a unit, if for example it is not achieving its predicted heat duty or degree of superheating. For such cases, we need to have a picture of what happens to working fluid throughout the geometry of HE unit. To achieve this objective a code has been developed that is able to predict the quality and temperature of working fluid in a row-wise manner from bottom to top tube row. This is termed as 'vertical discretization'. The next step of the project would be to make it both vertically and horizontally discretized which will potentially be able to simulate the real world process much more realistically. These aspects are explained in next section.

3.2.1 Overview of the method

The model developed for STHE vaporizer considers bottom-to-top flow [Figure 41] with hot fluid inside the tubes. The cold fluid essentially has a pure cross flow across the tube bank with the inlet at the bottom and outlet at the top. The tube layout pattern has a significant bearing on both the heat transfer performance and pressure drop characteristics of the heat exchanger. The first step towards effective use of a theoretical model is to be able to do a row-wise simulation of the vaporizer, as the correlations required change with change in quality (void fraction) of the working fluid. This is a coarse form of discretization which can be made finer once it is finalized for use as a design tool. The tubesheet design code is actually capable of providing information regarding the free-flow area through any tube-row at any vertical distance from the bottom of the tubesheet circle and so it can be vertically discretized to any desired level.

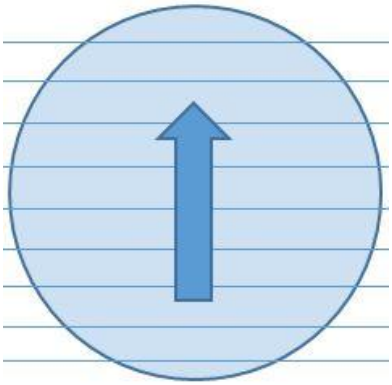

Figure 41 - Schematic of discretization adopted for the MATLAB™ code

This is an issue when the tube-side fluid undergoes phase change as the current code is not able to change heat transfer coefficient calculation method for the tube-side due to the fact that the entire length of the tube is considered at once. To overcome this, following method is proposed to be implemented into the MATLAB™ code – horizontal segmentation in addition to vertical segmentation [Figure 42].

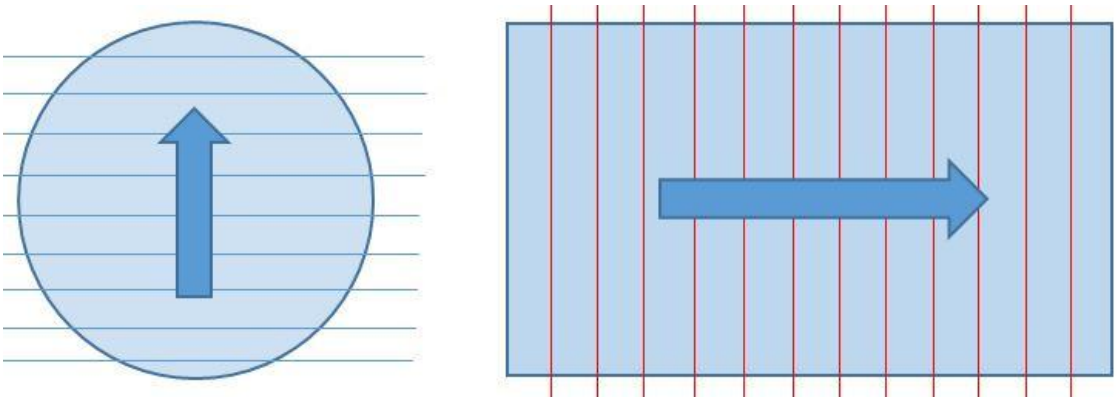

Figure 42 - Future work on increasing the discretization capability of the MATLAB™ code

The reason to use cross-flow from bottom-to-top for simulating a vaporizer is based on [115], where it is mentioned that Cornwell et.al. (1980) demonstrated that in the centre region of a kettle-type vaporizer, the bulk of the fluid flow was in vertical upward direction. This indicated that a study of the two-phase flow characteristics in the centre region of a vaporizer can be performed by using a simpler tube bundle simulating only the vertical channels of the centre regions of the vaporizer. Circulation rates in the kettle-type vaporizers can then be obtained by a force-balance between the single-phase and two-phase friction, acceleration and static losses in the bundle, and the static head of the single-phase liquid surrounding the bundle.

Major steps of the method:

- Tubesheet is designed as per tube diameters (Internal Diameter (ID) & Outer Diameter (OD)), tube layout angle, pitch ratio, shell inner diameter and specified fill percentage (for tube-bank, as percentage of ID) [see Figure 43]
- Each tube row is analyzed separately with varying mass flux as the free flow area for the shell-side fluid changes with each tube row.
- The final outputs are : overall heat duty, quality and thermal conditions of the working fluid (WF) & hot fluid (HF) row-wise, heat transfer coefficients (HTCs) for HF and WF (overall and row-wise)

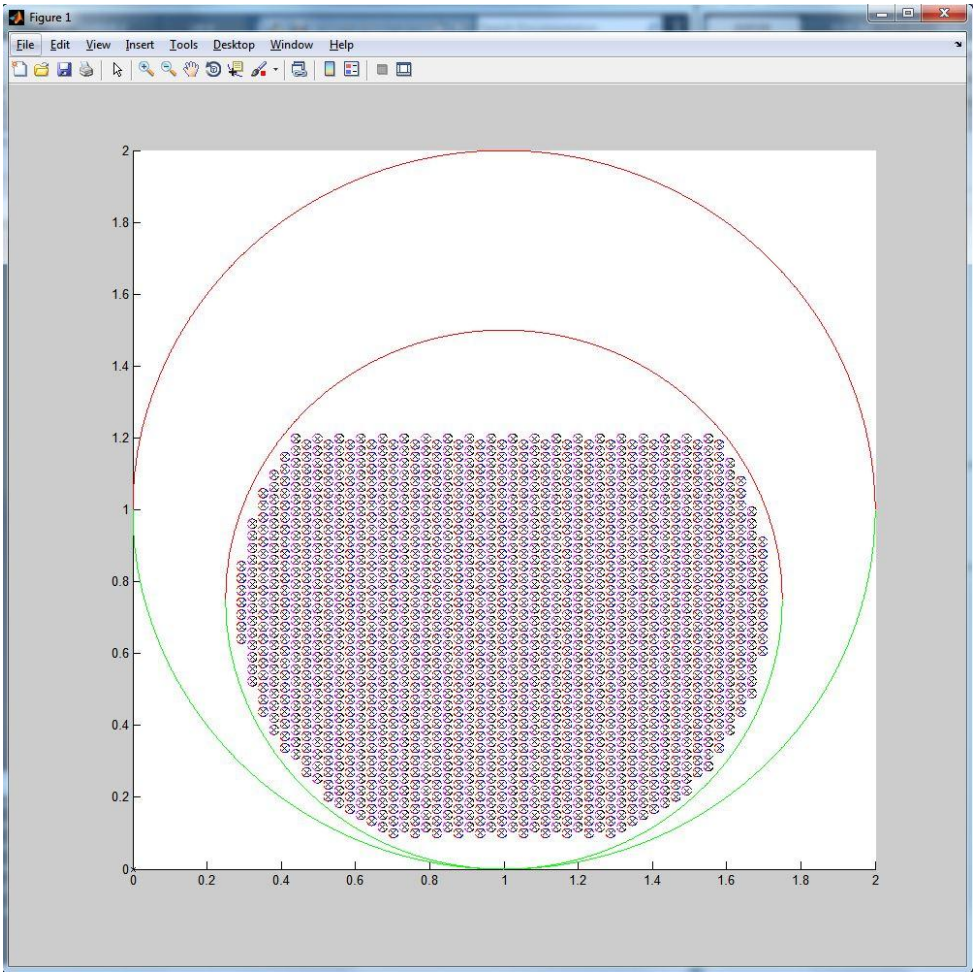

Figure 43 - Tubesheet design from MATLAB™ code

3.2.1.1 Correlations used in the MATLAB™ code

SHELL-SIDE FLUID

- For subcooled conditions near the bottom tube rows, the heat transfer coefficient is calculated by using the method outlined in VDI Heat Atlas [9].

- For vaporization occurring in the next set of tube rows, Aprin Model [89, 90] has been implemented to calculate heat transfer coefficients. The VDI model was deemed insufficient for this situation when compared to Aprin model as the Aprin model calculates different Reynolds and Prandtl numbers for determining the heat transfer coefficients depending on the void fraction/quality. The void fraction has been calculated from obtained quality value using the Feenstra-Weaver-Judd method [106].
- For flow of vapor phase of working fluid through the top tube rows (in case of dry-out being achieved), correlations for forced convective flow of gas have been coded. The correlation used is the one developed by Churchill & Bernstein (1977) [134].

TUBE-SIDE FLUID

- Tube-side heat transfer coefficient is calculated keeping in mind condensation of the hot fluid. This is calculated using the Dobson-Chato correlation [98].

The MATLAB™ code was compared against real world data from Rotokawa and Ngatamariki power plants in New Zealand. It matches real world data for the Ngatamariki plant very closely predicting a superheating of ~ 2 degrees. There was no precise figure available for degree of superheating for the Ngatamariki plant but it is known that the power plant is having trouble in getting 2 degrees of superheat.

Figure 44 shows a general representation of the vaporizer geometry. The narrow portion is the preheating zone where the working fluid enters, and the larger diameter portion is the boiling zone. The MATLAB™ code was tested in two different modes:

- It was assumed that the temperature of the working fluid is within 1 degree of the saturation temperature [as per the specified operating pressure] when it enters the boiling zone and the code was applied accordingly. This mode was not able to predict same values as real world data.
- In second mode, the working fluid is assumed to be at inlet temperature (as per real world data) at the bottom of the tube row and then the code is allowed to run. In this case, the values predicted by MATLAB™ code match closely (Table 4 - Comparison of MATLAB™ results to real world data for Rotokawa and Ngatamariki vaporizers) the real world values with the effectiveness value also being reasonable and realistic.

Figure 44 - Representative geometry for the vaporizers analyzed

The hot fluid enters in vapor state and leaves as subcooled liquid. Although the heat transfer coefficient calculated for the tube-side in the MATLAB™ code takes care of condensation, but it is not yet able to calculate precise values of overall conductance in a length-wise manner for the vaporizer due to the fact that only vertical discretization of the vaporization is being performed by the current MATLAB™ code. Once, length-wise discretization is coded and coupled with the current code, then the MATLAB™ simulation will be much more similar to real-world conditions.

There is one major tuning factor in the MATLAB™ code which can be tested and tuned only with an extensive analysis of the real-world data. This analysis was not possible as a part of this project as the major focus was on developing a CFD approach. This tuning factor is the effectiveness (ϵ) value in ϵ-NTU calculation. There was not found a ϵ-NTU correlation for the kind of geometry being simulated. The current geometry has features of three different flow arrangements – cross-flow, counter-flow and boiling on tube-rows. Also, the empty regions on the sides of tube-bank give rise to swirl flows of liquid-vapor mixture whose impact is hard to code into MATLAB™ due to absence of empirical/semi-empirical methods to do so.

The value of effectiveness (ϵ) found by fitting the MATLAB™ code results to the real-world data is 0.93 & 0.99 for Rotokawa and Ngatamariki plants respectively. This value does closely match the effectiveness (ϵ) values suggested by looking at existing data (Figure 45, Figure 46) for calculation of effectiveness if NTUs are known.

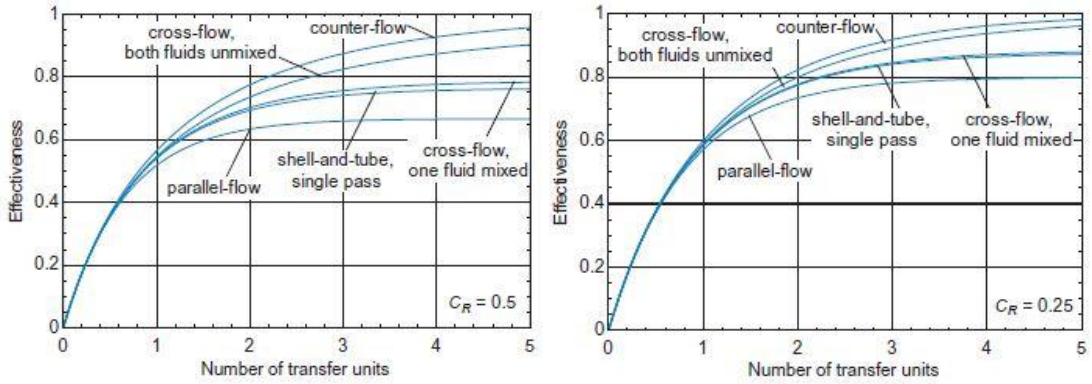

Figure 45 - Effectiveness vs. NTU for Capacity Ratio 0.5 (left) and 0.25 (right)

The values obtained from the Equation 141 [56] for calculation of effectiveness if NTUs are known if capacity ratio = 0 are plotted in Figure 46. The NTU values in the case of the vaporizer being simulated in MATLAB™ are above 7 for all tube rows.

$$\epsilon = 1 - \exp(-NTU) \qquad 140$$

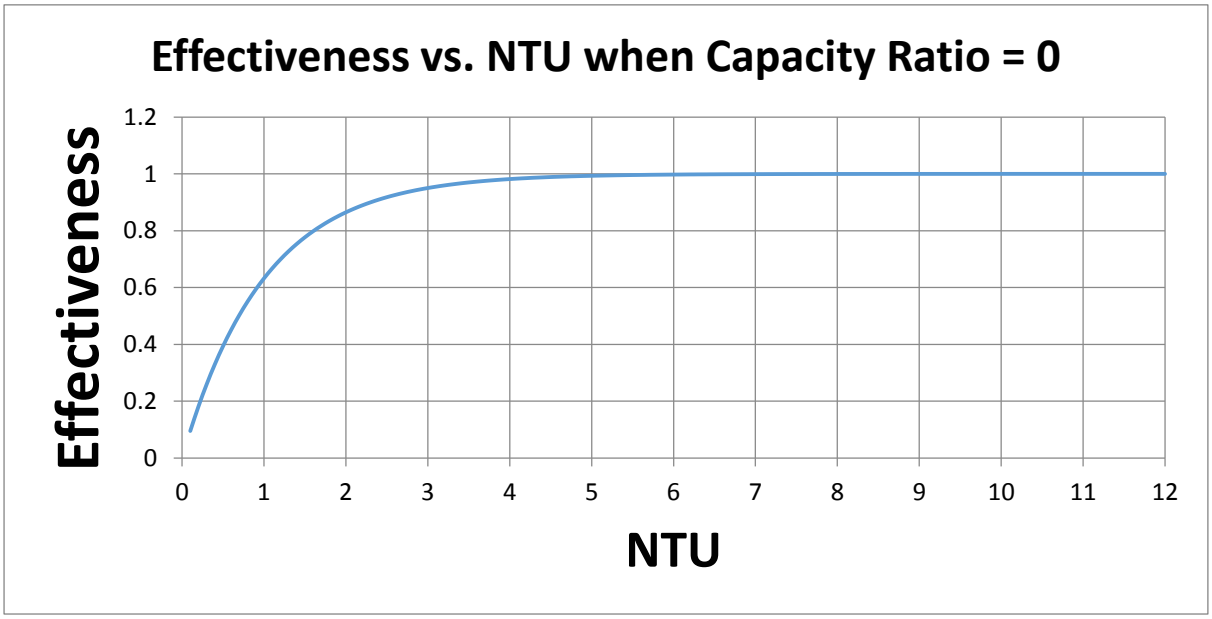

Figure 46 - Effectiveness vs. NTU for Capacity Ratio = 0 based on correlation given above

	ROTOKAWA	NGATAMARIKI
Number of tubes	680	1297
Tube ID [mm]	17.25	23.62
Tube OD [mm]	19.05	25.4
Tube Length [m]	11.582	18.28
Shell ID/OD Preheating Zone [mm]	762/794	1626/NA
Shell ID/OD Boiling Zone [mm]	1118/1162	1928/NA
Tube Pattern	Triangular	Triangular

Tube Pitch [mm]	25.4	NA
Tube Bundle Diameter [mm]	800	1375 (approx.)
Tube Bundle Diameter / Shell Diameter	0.71	0.71

Table 3 - Geometrical data regarding the Rotokawa and Ngatamariki vaporizers

3.2.1.2 ROTOKAWA & NGATAMARIKI PLANTS' STUDY

	ROTOKAWA				NGATAMARIKI			
	Real – world Data		MATLAB™ Results		Real – world Data		MATLAB™ Results	
Steam In Temperature	224.5 497.65	C K	T_{sat}	C K	Not available	C K	T_{sat}	C K
Steam Condensate Out Temperature	205.6 478.75	C K	205.29 478.44	C K	178 451.15	C K	178.15 451.3	C K
Water Tsat	225.92 499	C K	225.92 499	C K	194.64 467.79	C K	194.64 467.79	C K
Steam Pressure	25.6	Bara	25.6	Bara	13.7	Bara	13.7	Bara
Water Tsat	498.36 215.21	K C	498.36 215.21	K C	467.18 194.03	K C	467.18 194.03	K C
Hot Fluid MFR	43 11.94	T/hr Kg/sec	43 11.94	T/hr Kg/sec	109 30.27	T/hr Kg/sec	109 30.27	T/hr Kg/sec
Pentane In Temperature	130.9 404.05	C K	130.9 404.05	C K	154 427.15	C K	154 427.15	C K
Pentane Out Temperature	171.1 444.25	C K	173.95 447.1	C K	Not available	C K	450.48 177.33	C K
Pentane Pressure	22.9	Bara	22.9	Bara	24.6	Bara	24.6	Bara
Pentane Tsat	445.7 172.55	K C	446.47 173.32	K C	449.40 176.25	K C	449.40 176.25	K C
Working Fluid MFR	259 71.94	T/hr Kg/sec	259 71.94	T/hr Kg/sec	910 252.77	T/hr Kg/sec	910 252.77	T/hr Kg/sec
Pentane Superheating	Not available	K C	0.7407 0.7407	K C	Can't calculate	K C	0.25 0.25	K C
Effectiveness (Tuning factor)	0.91				0.99			

Table 4 - Comparison of MATLAB™ results to real world data for Rotokawa and Ngatamariki vaporizers

The saturation temperature for pentane (working fluid) in above table for both real world data and the MATLAB™ calculations is obtained from CoolProp™ tool for MATLAB™.

3.2.1.3 Predictions of standard vaporizer design methods

A review of the geometrical specifications of the heat exchangers in view of the real world operating conditions' data is also carried out with standard vaporizer design method given by Palen [107].

A quick look at the hot fluid inlet and outlet conditions given in Table 4 for Rotokawa and Ngatamariki power plants provides us with the heat duties:

	HEAT DUTY
Rotokawa:	22.5 MW
Ngatamariki:	61.5 MW

Using the heat duty values and the geometrical configuration for the vaporizer units in the Palen method:

	Area Specified	**Area Required**
Rotokawa:	467.77 m^2	240.15 m^2
Ngatamariki:	1890 m^2	2250 m^2

Substituting the values for hot fluid and natural convection heat transfer coefficients from the vertically discretized MATLAB™ code into Palen method:

	Area Specified	**Area Required**
Rotokawa:	467.77 m^2	226.5 m^2
Ngatamariki:	1890 m^2	2103 m^2

A discussion with the plant manager revealed that the Rotokawa unit has no superheaters after the vaporizer unit and hence the vaporizer needs to ensure a large degree of superheating (>5) so as to prevent any potential danger to turbine in case of droplet carryover. While in case of Ngatamariki plant, there is a superheater unit after the vaporizer and it is this plant that is facing issues with regards to generation of sufficient degree of superheating. The

predictions from the standard method do confirm these real world observations but they are not capable of revealing the changes in the thermodynamic quality of working fluid as it rises through the tube bundle. The MATLAB™ code developed can provide significant benefits here by giving a detailed picture of how much of the tube bank is submerged in liquid and the number of tube rows exposed to vapor phase or foam as the case maybe for different vaporizers.

3.2.1.4 Major constraints for the MATLAB™ code

There are 2 major constraints that need to be kept in mind while interpreting the predictions of the MATLAB™ code:

a) The MATLAB™ code always over-predicts the temperature of vaporized working fluid on the outside of tubes. This is evident when same effectiveness value is used for Rotokawa plant as for Ngatamariki plant and the MATLAB™ code predicts 15 degrees of superheating which is not real. This is because of the fact that the code uses a forced convection heat transfer coefficient calculation sub-routine once the thermodynamic quality becomes 1 for the working fluid. This is very different to real world scenario where foam covers the tube-bank all the way to the top-tube row and a few inches above it. This foam is visible in CFD-Post™ analysis of simulations done on the STHE slice. But the MATLAB™ code is unable to account for it. This needs to be looked into during the next stage of code improvement.
b) The MATLAB™ code is also unable to account for the vapor flow patterns around the tube-bank. Although this constraint is mitigated to a certain indeterminate extent by the use of empirical/semi-empirical methods which have been derived for vaporizers over the years as these correlations would have these influences built into them. Although a CFD analysis does show that the ratio of tube bundle diameter to shell diameter changes the extent and reach of the vapor swirls. No correlation was found that had a factor dependent on ratio of tube bundle diameter to shell diameter

Conclusion

In conclusion it can be said that the MATLAB™ code does make predictions quite close to the real world data with just one tuning factor which can be fine-tuned with analysis of a larger amount of data from different geometry vaporizer units. The code has the benefits of modularity and as better correlation come out in literature, either for convective or nucleate

boiling, they can be easily added into the code to make it more accurate. If used for single-phase heating, then there are no shortcomings in the code as there is no foaming involved.

Future work

As a future work on this code there are few possible improvements to look into:

a) Addition of pressure drop calculation in a row-wise manner and this can be then validated against real-world data. This pressure data calculation, once validated, can then be used to analyse the relationship between liquid level and heat transfer performance using the same principle as in Chapter 5.
b) The second improvement is with regards to incorporating the influence of foam on heat transfer in the top tube rows so as to remove the issue of overprediction of vapor phase temperature.
c) An important addition would be to make it discretized in horizontal dimension as well.

4.0 CFD Analysis and Data Selection

The use of CFD to analyse real world situations has been on an upward trend with more functionality being added to the solver packages coupled with development in capabilities of hardware resources to simulate larger meshes with increases parallelization capabilities. In an ideal situation the use of experimental, analytical and CFD results will coincide resulting in a full understanding of the process.

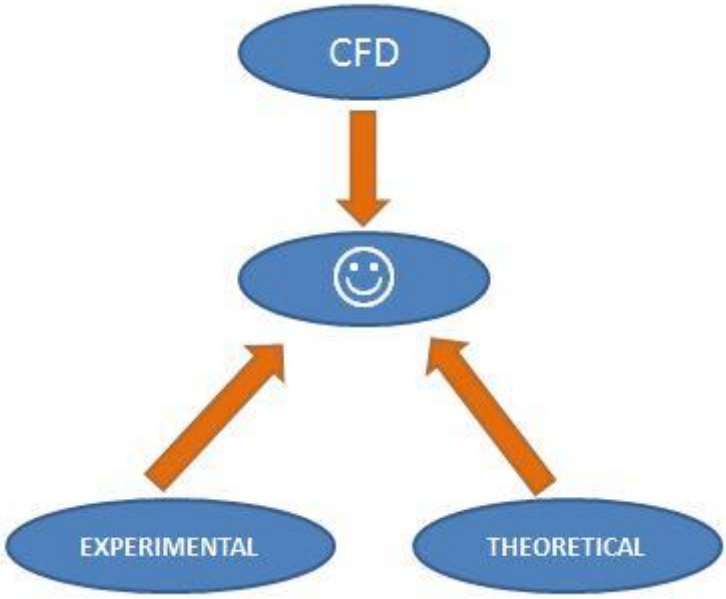

Figure 47 - Best possible result while using all the possible approaches to understand a process

The aim of this project is to demonstrate the feasibility and usefulness of one of the currently available CFD solver packages (ANSYS™ CFX™) in analysing large-scale vaporizers with an aim of gaining insight into their operational problems so that effective methods can be suggested to improve their operational efficiency. This analysis also provides us knowledge about the impact of user modifiable parameters in ANSYS™ CFX™ and parameters that must be measured in future experiments to fine tune the case set-ups in ANSYS™ CFX™. The default set-up in ANSYS™ CFX™ was found to be inadequate to handle the complex physics of boiling of a fluid in multi-tube configuration. User generated CFX™ Expression Language (CEL) codes are required to run such complex cases and these require some inputs from experiments, as will be elaborated upon later in the chapter. To achieve the project goals, following steps were decided upon:

a) Understanding set-up and analysing results with single-phase heat exchangers (

4.1 Single-Phase CFD Validation & Analysis),

b) Setting up phase change simulation for single tube geometries and learn to fine-tune & validate the same against experimental data (4.2.1 Single-Tube Geometries),

c) Validating the multi-tube CFD simulations against limited experimental observations (4.2.2 Multi-Tube Geometry),

d) Selection of a substitute fluid in the absence of pentane boiling data,

e) Making CAD model of full scale vaporizer that is to be analyzed.

The knowledge gained from the above steps will be applied to develop a method to analyse two issues regarding Vaporizers:

a) Impact of liquid level in the vaporizer on its heat transfer performance
b) Probability of liquid droplet carryover out of a vaporizer

4.1 Single-Phase CFD Validation & Analysis

The first step in starting the work on CFD simulations of heat exchangers was to set-up and validate CFD analysis of a heat exchanger that does not involve any phase change. The reasons were to gain an understanding of the software package (viz. ANSYS™) and process of setting up a simulation.

The literature review done for single-phase CFD analysis shows that most of the studies are done with a constant temperature boundary condition for the tube walls. This is a simplification adopted to shorten the solver time. But this fails to capture the real-world scenario of conjugate heat transfer. To capture the real-world situation in CFD analysis we need to factor in both the shell-side and tube-side fluids. TEMA-E type of shell-and-tube heat exchanger (STHE) was chosen for the purpose because of the extensively validated empirical model available for this particular type of HE, viz. Bell-Delaware Method [107].

General data for single-phase CFD analysis:

- Meshing for the single-phase simulations is unstructured tetrahedral type with advanced sizing function activated on curvature. This was found to be the norm

during the literature review because of complex geometries of the units and also the physics being less complex than phase-change CFD (where near-wall phenomena are critically important to be modelled correctly).

- The software package chosen to carry out the analysis is – ANSYS™ Fluent™. The package was chosen subsequent to the literature review on single-phase CFD analysis which showed it to be a solver of choice by multiple researchers.
- The turbulence model chosen is $k-\epsilon$ Realizable. It falls in the category of two-equation models which are widely used for turbulence models in industrial CFD. These models solve two transport equations and model the Reynolds stresses using an eddy viscosity approach. It has been popular in industrial flow and heat transfer simulations on account of inherent robustness, economy (computational resources' requirement) and reasonable accuracy for a wide range of flows [7]. It was found to give best matching results for single-phase HE simulation by [40] in a comparison study and along with being choice of almost all the authors in the literature reviewed. ANSYS™ Fluent™ recommends usage of the Realizable $k-\epsilon$ over standard $k-\epsilon$. The main differences are: a) Realizable $k-\epsilon$ contains an alternative formulation of turbulent viscosity which ensures realizability (positivity of normal stresses and Schwarz inequality for shear stresses) by making C_μ variable by sensitizing it to the mean flow (mean deformation) and the turbulence (k, ϵ), b) A modified transport equation for the dissipation rate, $\mathcal{E}$, based on the dynamic equation of the mean-square vorticity fluctuation [6, 7].
- For the solver run, a coupled pressure-velocity scheme is selected with second-order discretization selected for momentum, turbulent kinetic energy, turbulence dissipation rate and energy with standard scheme selected for pressure.
- The problem is initialized using the Hybrid Initialization option in ANSYS™ Fluent™ which is a collection of boundary interpolation methods. It is the default initialization method for single-phase steady state flows [7]. It solves the Laplace equation to produce a velocity that conforms to complex domain geometries, and a pressure field which smoothly connects high and low pressure values in the computational domain [6]. All other variables (temperature, turbulence) are patched based on domain averaged values or a predetermined recipe, details of which can be found in [6].

- The convergence criteria were specified to be 1e-6 for energy residual and 1e-4 for other residuals.

The scope of single-phase CFD simulations has been limited to demonstration as a proof-of-concept that CFD can be used to analyse and design single-phase HEs with conjugate heat transfer and as a result getting close to the real world conditions (unlike the literature reviewed where constant temperature/heat flux boundary condition is used).

In case of single-phase CFD analysis no tuning of the set-up (in the sense of parameters etc., although grid-independence studies are required) is required unlike for phase-change CFD analysis.

4.1.1 CFD Analysis of TEMA-E type STHE

The geometry of the exchanger examined can be seen in Figure 48.

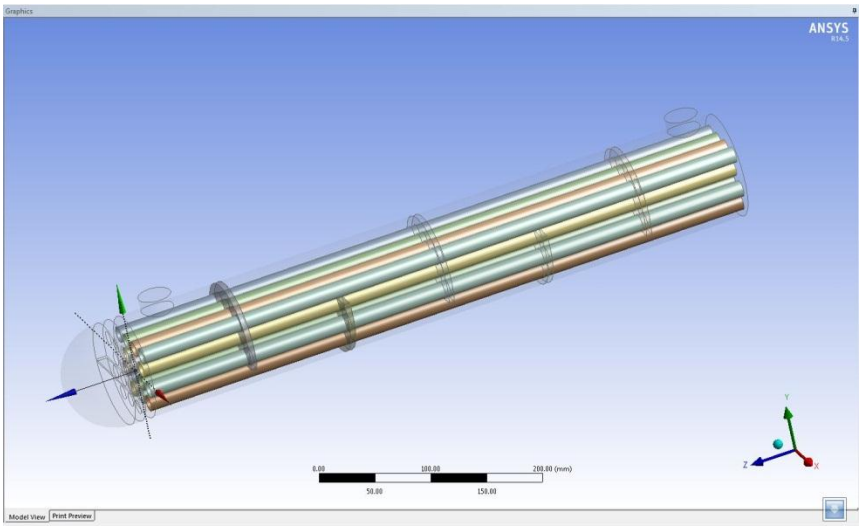

Figure 48- 3-D model of the exchanger used for single-phase CFD analysis

The shell-side (length = 576 mm) is single-pass has 5 baffles with 21% baffle cut and spacing equal to shell diameter [96 mm]. The tube-side has 2-pass configuration with 7 tubes in each pass. The meshes used are (Figure 49) are unstructured.

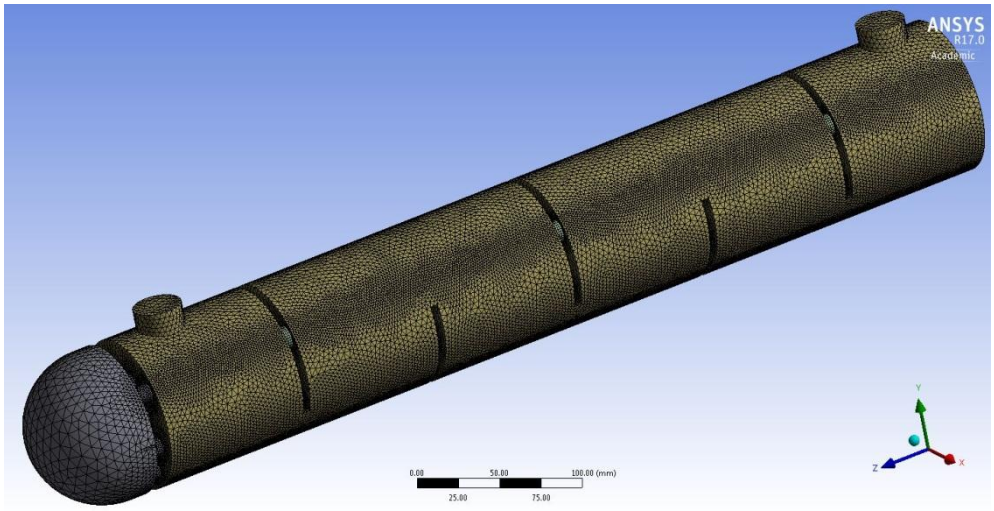

Figure 49 – Meshing of the geometry used for single-phase CFD analysis

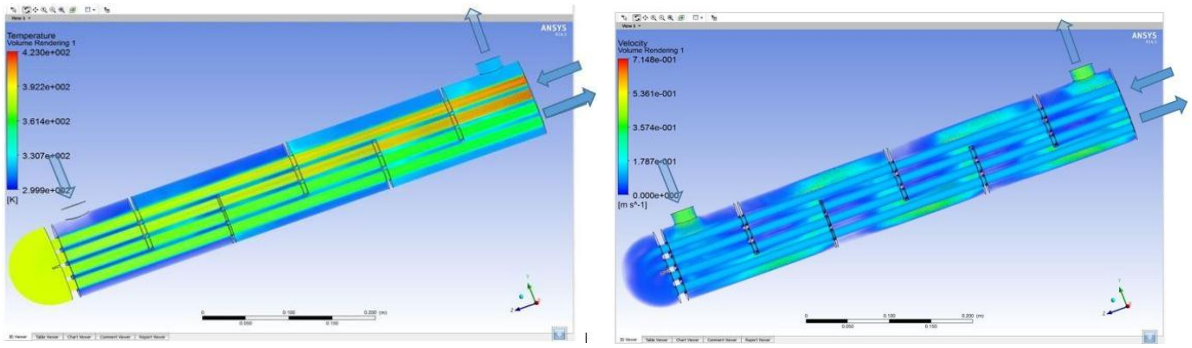

Figure 50 - a) Temperature, and b) Velocity field renderings for the TEMA-E STHE

The results of the comparison w.r.t. heat duty and temperatures (both fluids) between CFD simulation and Bell-Delaware Method [107] are shown in Table 6. Five different meshes were tested with increasing refinement from Mesh 1 to Mesh 5. The details of the meshing can be seen in Table 7. For all meshes under all operating conditions solved in ANSYS™ CFX™ the maximum and minimum deviations are:

Shell-side outlet temperature Deviation [%]		Tube-side outlet temperature Deviation [%]		Shell-side Heat Duty Deviation [%]	
MAX	MIN	MAX	MIN	MAX	MIN
2.17	0.006	1.97	0.29	21.16	0.5

Table 5 - Maximum and Minimum deviations seen in the mesh dependence runs

	Method used for prediction	**Shell-side Outlet Temperature (K)**	**Tube-side Outlet Temperature (K)**	**Shell-side Heat Duty (kW)**
Case-1: SS MFR = 0.1 kg/sec TS MFR = 0.1 kg/sec SS Inlet Temp = 300 K TS Inlet Temp = 400 K	**MATLAB™ (Bell-Delaware)**	338.41	361.25	16.489
	Mesh - ANSYS™ Fluent™	339.50	359.88	16.660
	Deviation (%)	0.32	-0.3792	1.04
	Mesh – 1 ANSYS™ CFX™	331.059	368.37	13
	Deviation (%)	-2.17	1.97	-21.16
	Mesh – 2 ANSYS™ CFX™	332.6	366.9	13.64
	Deviation (%)	-1.72	1.56	-17.28
	Mesh – 3 ANSYS™ CFX™	333.38	366.75	13.96
	Deviation (%)	-1.49	1.52	-15.4

	Mesh – 4 ANSYS™ CFX™	335.53	367	14.86
	Deviation (%)	-0.85	1.59	9.94
	Mesh – 5 ANSYS™ CFX	336.9	365.9	15.45
	Deviation (%)	-0.45	1.28	6.36
Case-2: SS MFR = 0.2 kg/sec TS MFR = 0.1 kg/sec SS Inlet Temp = 300 K TS Inlet Temp = 400 K	**MATLAB™ (Bell-Delaware)**	323.86	351.93	20.28
	Mesh – ANSYS™ Fluent™	323.19	352.96	19.52
	Deviation (%)	-0.2069	0.2927	-3.7475
	Mesh – 1 ANSYS™ CFX™	321.21	358.2	17.75
	Deviation (%)	-0.82	1.78	-12.47
	Mesh – 2 ANSYS™ CFX™	321.8	356.25	18.25
	Deviation (%)	-0.64	1.23	-10.01
	Mesh – 3 ANSYS™ CFX™	322.85	354.37	19.13
	Deviation (%)	-0.31	0.69	-5.67
	Mesh – 4 ANSYS™ CFX™	322.68	353.58	18.98
	Deviation (%)	-0.36	0.47	-6.41
	Mesh – 5 ANSYS™ CFX™	323.39	353.24	19.57
	Deviation (%)	-0.14	0.37	-3.5
Case-3: SS MFR = 0.3 kg/sec TS MFR = 0.1 kg/sec SS Inlet Temp = 300 K TS Inlet Temp = 423 K	**MATLAB™ (Bell-Delaware)**	322.33	357.26	27.88
	Mesh - ANSYS™ Fluent™	320.71	360.09	25.97
	Deviation (%)	-0.5027	0.7921	-6.85
	Mesh – 1 ANSYS™ CFX™	319.85	363.52	24.89
	Deviation (%)	-0.77	1.75	-10.7
	Mesh – 2 ANSYS™ CFX™	320.45	361.7	25.64
	Deviation (%)	-0.58	1.24	-8.03
	Mesh – 3 ANSYS™	321.6	360.6	27.08

	CFX™			
	Deviation (%)	-0.23	0.93	-2.87
	Mesh – 4 ANSYS™ CFX™	322.35	360.5	28.02
	Deviation (%)	0.006	0.91	0.5
	Mesh – 5 ANSYS™ CFX™	321.5	358.31	27.2
	Deviation (%)	-0.26	0.29	-2.44
SS MFR: Shell-side Mass Flow Rate; **TS MFR**: Tube-side Mass Flow Rate (per tube)				

Table 6 - Comparison of CFD Simulation results vis-a-vis Bell-Delaware Method for TEMA-E type STHE

Given below are plots for mesh dependence runs:

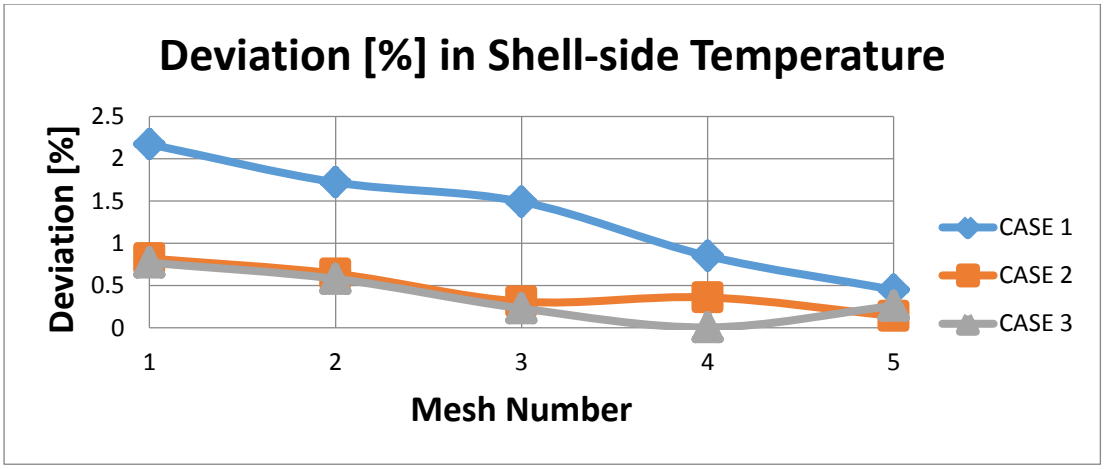

Figure 51 - Deviation [%] in Shell-side Temperature

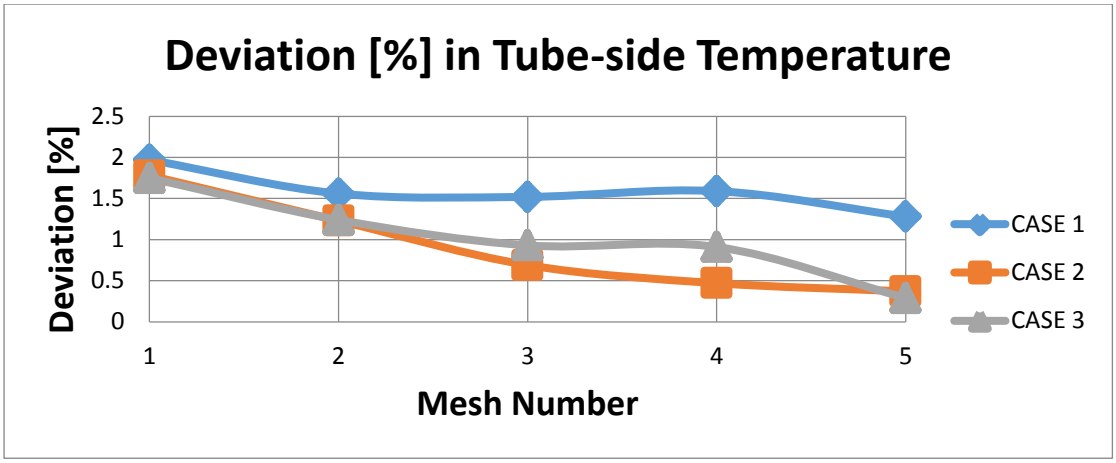

Figure 52 - Deviation [%] in Tube-side Temperature

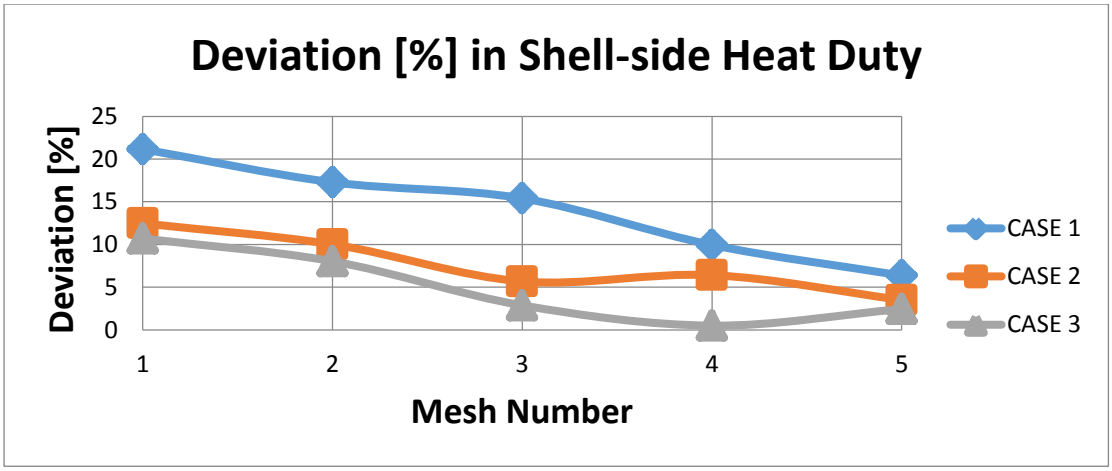

Figure 53 - Deviation [%] in Shell-side Heat Duty

MESH DETAILS	Mesh - 1	Mesh - 2	Mesh - 3	Mesh – 4	Mesh – 5
RELEVANCE	-100	-50	0	25	50
Nodes – Meshing	951705	2023784	5041842	7062854	10246473
Elements - Meshing	630173	1348471	3434431	4848605	7094726
Nodes – CFX	181012	368203	871191	1197541	1696955
Elements – CFX	630173	1348471	3434431	4848605	7094726
Element Mid-side Nodes	KEPT	KEPT	KEPT	KEPT	KEPT
Mesh Metrics – Average values					
Orthogonality	0.797	0.827	0.842	0.845	0.85
Aspect Ratio	2.1003	1.93	1.85	1.83	1.83
Skewness	0.29	0.25	0.24	0.23	0.23
Element Quality	0.778	0.814	0.831	0.834	0.84

Table 7 - Details of different meshes used for the study in Table 3

4.1.1.1 Discussion

The close match in the results lends confidence in the CFD approach to single-phase heating/cooling heat exchanger application. There are a few assumptions made in the CFD geometry set-up, a) no leakage between baffle and exchanger shell, and b) no leakage

between the tube and baffle plate. The assumptions mentioned above require a little description of flow in a baffled shell-and-tube heat exchanger. The flow inside a shell-and-tube heat exchanger can be divided into five streams [107], as shown in Figure 54 [147].

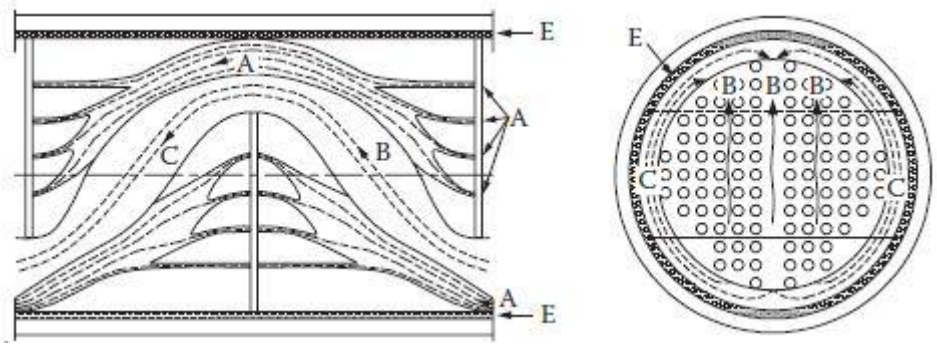

Figure 54- The division of flow in a STHE into five streams

The five streams shown in Figure 54 are [107]:

- **Stream A**: Leakage stream in the orifice formed by the clearance between the baffle tube hole and tube wall.
- **Stream B**: Main effective cross-flow stream, which can be related to flow across ideal tube banks.
- **Stream C**: Tube bundle bypass stream in the gap between the bundle and the shell wall.
- **Stream E**: Leakage stream between the baffle edge and the shell wall.
- **Stream F**: Bypass stream in flow channels due to omission of tubes in tube pass partitions.

The assumptions in the CFD simulation do not model Streams – A & E. As per [107], Stream E is considered by Tinker to be fully heat transfer ineffective, consistent with later developments. Stream A, as per [147], is fully heat transfer effective because of high heat transfer coefficients in the narrow space between tube wall and baffle hole. Although its contribution to overall heat transfer in the exchanger can be assumed to be small as the baffles cover a very small portion of the overall length of the tubes. This statement gets some credibility based on the close match of CFD results (where Stream A is not considered) and the results of Bell-Delaware method (where Stream A is considered).

The advantages of CFD analysis of a heat exchanger are multi-fold. In fact, for performance parameters such as temperatures of hot & cold fluids and heat duty of HE, the theoretical methods are much faster with high accuracy for geometries & operating conditions within the

validity range and require no specialized software packages. The advantage of CFD analysis lies in visualization of the thermal and velocity fields which can pinpoint the weaknesses in design such as re-circulation zones and the effects of inlet & outlet sections' design unlike the theoretical methods. Figure 50 shows the visualization of thermal and velocity fields for the HE being simulated.

The CFD results can probably be more closely matched to the theoretical data by fine tuning the geometry and mesh resolution. This is worth looking into when ample experimental data is available. For the current goal of understanding CFD set-up process and demonstrating its usefulness as a tool for studying and designing heat exchangers, the match in the results was deemed satisfactory.

4.1.2 CFD Analysis of a Combined Multiple Shell Pass Helical Baffled STHE & Shell-and-Plate Heat Exchanger (SPHE)

The use of CFD analysis with HEs such as TEMA-E type STHE lies in detection of exact geometrical features that impede the performance of the exchanger, e.g. recirculation zones or improper distribution/collection of fluids at inlet/outlet sections. The setup of CFD simulation can be validated in such cases against experimental data or proven theoretical design methods. Once the setup of physics for CFD simulation is known, it can be used to investigate the performance of HEs that differ in geometrical features/configuration but where the underlying physics of heat transfer is essentially similar. Therefore, the CFD setup validated for TEMA-E type STHE is now used to investigate the performance of some novel designs of HEs which don't have theoretical methods available for their design & development. The analysis was carried out on two such designs:

1. Combined multiple shell pass helical-baffled STHE (CMSP-STHE)
2. Shell-and-plate HE (SPHE)

4.1.2.1 Combined Multiple Shell Pass Helical Baffled STHE (CMSP-STHE)

This relatively novel design of HE is being researched upon due to the following shortcomings in typical STHE [112]:

- High pressure drop on shell-side due to sudden contraction and expansion of the flow in the shell-side and the fluid impingement on the shell walls caused by segmental baffles
- Impaired heat transfer efficiency due to the flow stagnation in so-called "dead-zones", which are located at the corners between baffles and shell wall
- Low shell-side mass velocity across the tubes due to the leakage between baffles and shell wall caused by inaccuracy in manufacturing tolerance and installation
- Short operation life due to the vibration caused by the shell-side flow normal to the tubes

Geometry, Meshing, Set-up and Results: CMSP-STHE

The geometry of the helical-baffled HE is shown in Figure 55 for the case with constant temperature boundary condition (BC) on the tube walls. The first study was done at operating conditions used in [112] to check the model set-up by validating against the results. The

second study was done with conjugate heat transfer where both, shell-side & tube-side fluids are simulated, Figure 56.

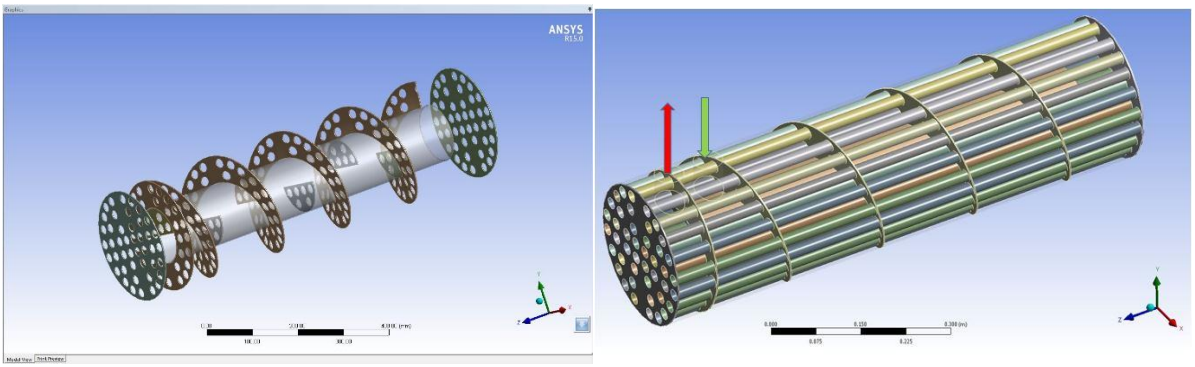

Figure 55 – a) Helical baffles in outer shell pass and segmental baffles in inner shell pass, b) Fully assembled geometry for case with shell-fluid simulation with walls at constant temperature BC

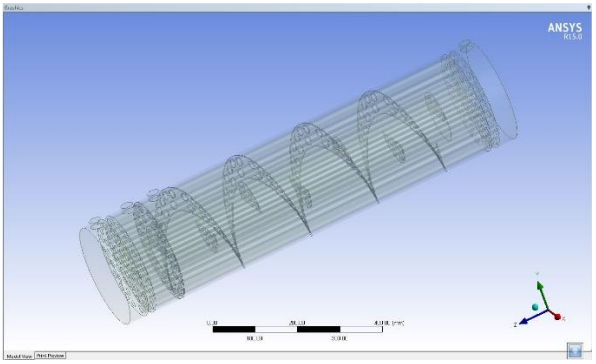

Figure 56 - Showing shell-side and tube-side fluids with solid parts hidden

The mesh sizes are:

- For shell-side fluid only (Figure 57) – 1.5m Nodes & 8m Elements
- For case with both fluids (Figure 57) simulated – 1.95m Nodes & 11.5m Elements

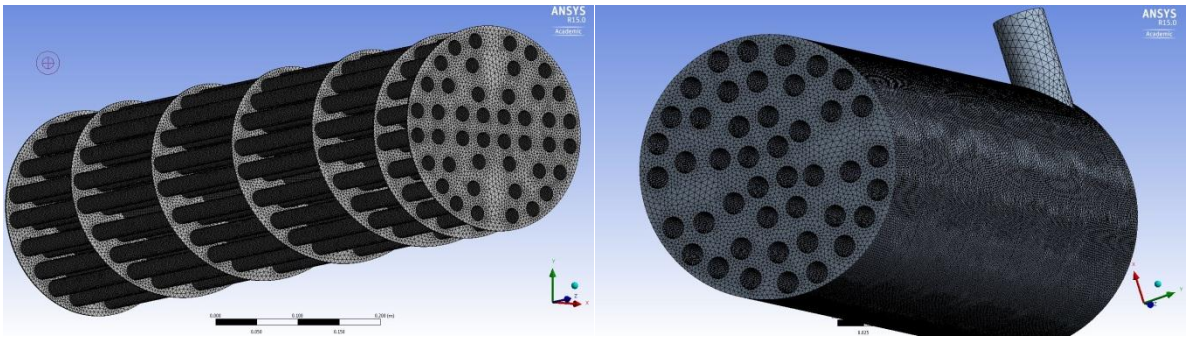

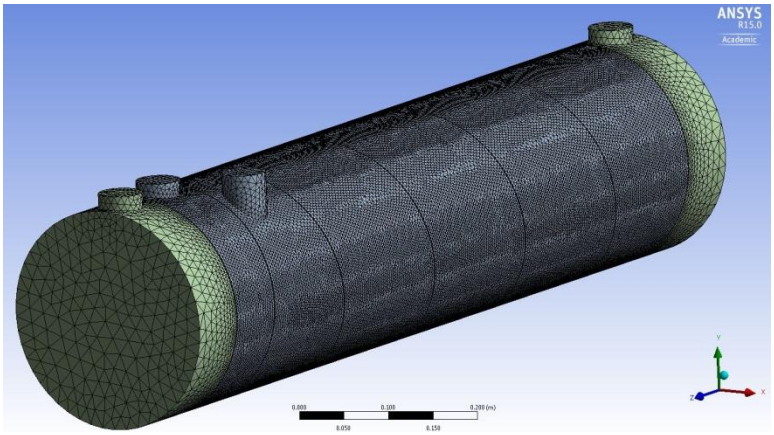

Figure 57 - a) Meshing of the baffles, b) Meshing of the shell-side fluid only case, c) Meshing for the conjugate heat transfer case set-up

The CFD analysis is useful in getting thermal and flow field distributions as shown in Figure 58.

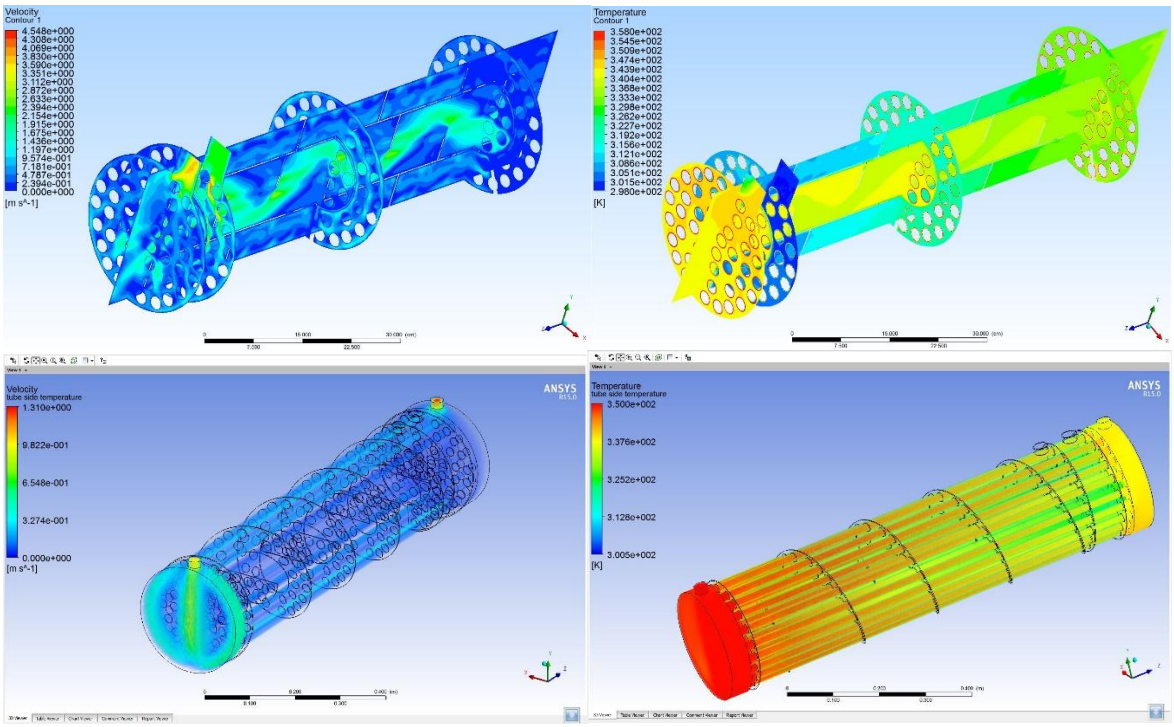

Figure 58 - a) & b) Velocity and temperature distributions [shell-side fluid] for constant tube wall temperature boundary condition, c) & d) velocity and temperature distributions [tube-side fluid] for conjugate heat transfer

4.1.2.2 Shell-and-Plate Heat Exchanger (SPHE)

Shell-and-plate HEs are another novel design with some crucial advantages in terms of cost effectiveness and minimal maintenance [147]. SPHEs are capable of handling liquids, gases, steam and two-phase mixtures while being designed for pressures up to 100 barg and temperature limit of 538^{o}C. The manufacturers use in-house gathered experimental data to design the heat exchangers. In such cases, CFD enables us to learn about the flow fields (velocity, temperature & pressure). The model set-up is very simple and similar to the TEMA-E STHE geometry.

Figure 60 [147] shows the units for SPHE by one of the manufacturers along with internal construction details. A 3-D model (Figure 61) was developed similar to this for CFD analysis, Figure 61. The mesh (Figure 59) size is 0.35m Nodes with 2m Elements. In Figure 61, we can see the simulation results in terms of temperature fields.

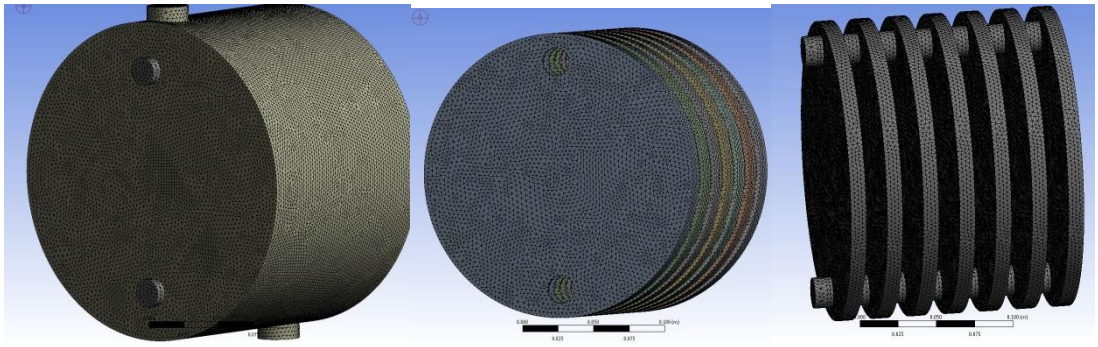

Figure 59 - Meshing of the SPHE a) Full assembly, b) Solid plates, c) Plate-fluid only

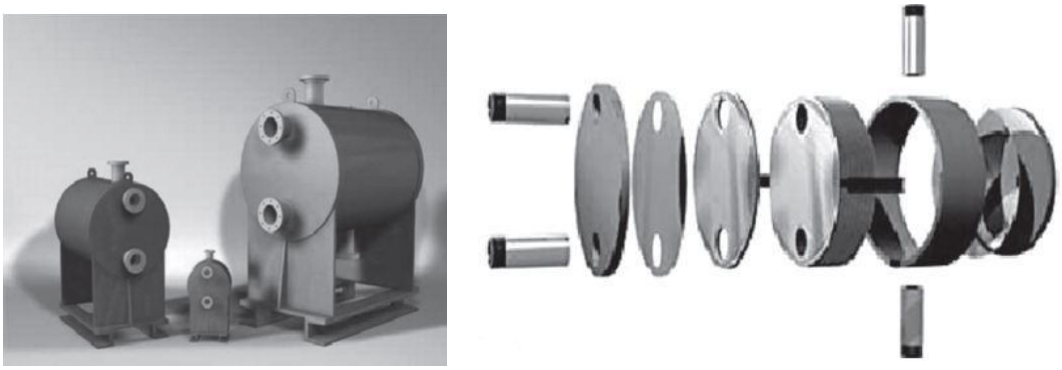

Figure 60 - a) Supermax SPHE Units, b) Internal details

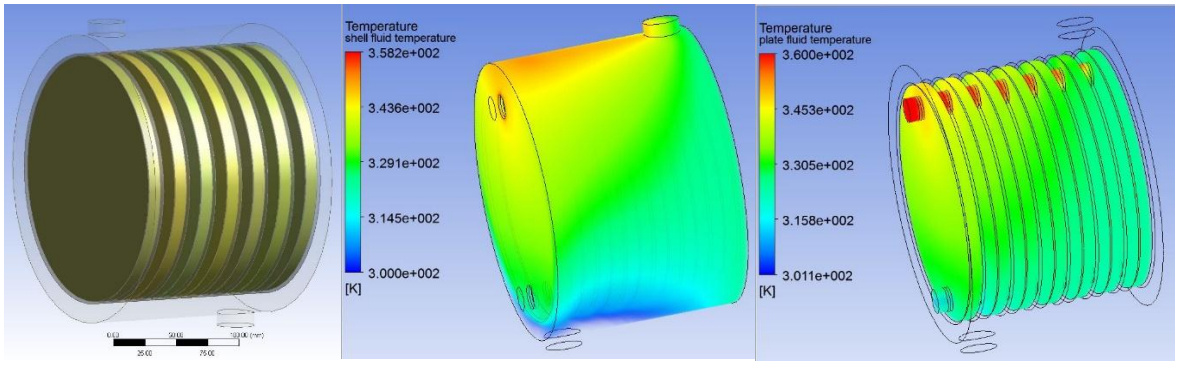

Figure 61 – a) Model for the shell-and-plate HE, b) Shell-side fluid temperature field, c) Plate-side fluid temperature field

4.1.2.3 Discussion

The CFD simulation of SPHE geometry was carried out simply as a proof of concept to demonstrate the usefulness of CFD in visualizing and understanding internal flow dynamics of novel designs and this can be used to further optimize the design by making changes in geometrical configuration to either minimize or completely remove some or all of the dead/re-circulation zones. No experimental data was found during literature review done for SPHEs which could be used for validating the CFD setup and no empirical method to calculate heat transfer coefficients for SPHEs. Still, the results of CFD analysis can be assumed to be very close to reality based on the fact that CFD simulation of single-phase heat exchangers requires no special parameters that might make the set-up case dependent, as observed during CFD analysis of TEMA E-type STHE. The major factor in such simulations is proper meshing of the geometry.

4.2 Phase-change CFD Analysis & Validation

4.2.1 Single-Tube Geometries

CFD analysis of phase-change heat exchangers (e.g. vaporizers) requires more sophisticated approaches. The modelling of the phase change process is inherently complex, and the sheer complexity of geometry and large sizes of industrial vaporizers make the simulation process demanding in computational resources. It is necessitated because the use the alternative simpler methods may predict deficiencies in design but are unable to pin point the location and possible factors of weaknesses.

The CFD analysis of a vaporizer is more complex than CFD analysis of a single-phase heat exchanger (preheater/superheater) due to the interaction at the interface between two phases which gives rise to various types of flow fields or local interfacial structures. A model with two-fluid (liquid & gas), four-field (continuous & dispersed for both liquid & gas) approach can allow for the definition of eight types of local interfacial structures as shown in Figure 62,[15].

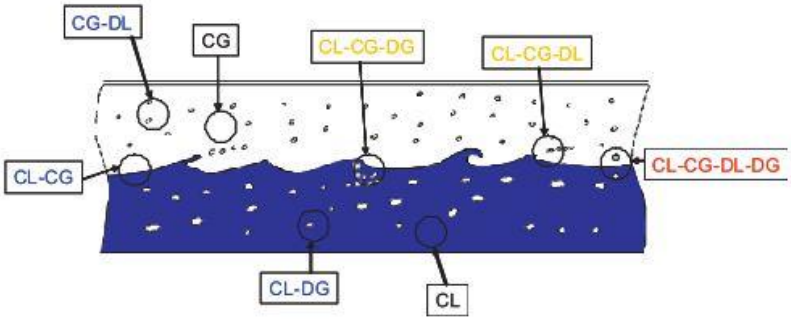

Figure 62 - Illustration of different types of local interfacial structures

The models used for phase change CFD need to be validated against experimental data. Table 8 shows the availability of data for validation of CFD models. The current project focuses on high pressure boiling of the refrigerants. The available experimental data is mostly for single tube geometries with electric heaters being used as heat source. The main requirements from the available experimental data for it to be used as a basis for tuning of the CFD model set-up are: a) bubble departure diameter data, b) bulk bubble diameters (min, max, mean and if possible their variation with distance from the heated surface), c) void fraction data. Measurement of such details in the boiling process requires complicated sensor network and this is a big limitation in conducting multi-tube experiments due to increasing complexity and cost of such set-ups. Another point to note is that these experiments are mostly aimed at

improving the solver package and validating some theoretical model that can afterwards be integrated into the solver. The current project undertakes the approach of using single-tube boiling experimental data to narrow down on the crucial parameters that require tuning for CFD simulations. These parameters (viz. bubble departure diameter, bulk bubble diameter) can then be used for tuning multi-tube boiling simulations, using pentane as a fluid, by choosing a substitute fluid that would have similar values for required parameters and for which experimental data is available.

CFD Model **Validation Data Availability**	**HIGH PRESSURE**	**LOW PRESSURE**
WATER	HIGH	LOW
REFRIGERANTS	VERY LOW	MEDIUM

Table 8 - Availability of data for validation of CFD models

4.2.1.1 First Case – Low pressure R113 Boiling

One of the works being looked at is the R113 upward subcooled boiling experiments done at Arizona State University (Case-6) ([122]). The experiments were performed in a 3.66m long annular channel at 2.69 bar operating pressure. The inner tube of the channel is of 304 stainless steel (ID = 14.60mm, OD = 15.78mm). A section was chosen for detailed observations (see Figure 63). The entrance to the measurement section is 1.56m downstream of the beginning of the 2.75m heated section. The outer tube of the 0.521m long measurement section is made of optical quality quartz (ID = 38.02mm, OD = 42.02mm). The measurement plane was located 0.424m (≈ 19 hydraulic diameters) downstream of the measurement section entrance.

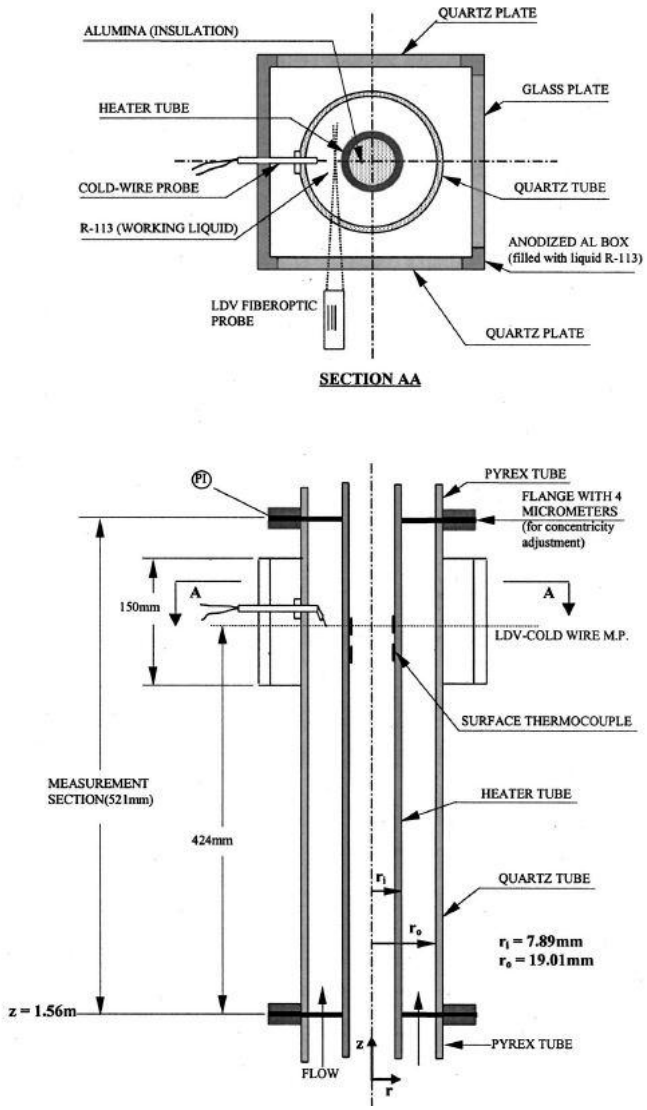

Figure 63 - The measurement section of the experimental apparatus

The experimental data was analyzed using CFD simulations by Koncar-Krepper [17]. One of the cases set-up and analyzed is shown here (Experimental case – 6), Figure 64. The analyzed case, viz. Case 6, has an inflow rate of 784 kg/m^{2}s and applied heat flux is 116000 W/m^2. At the mentioned conditions R113 has a saturation temperature of 80.5^oC and the inlet temperature is kept at 50.2^oC.

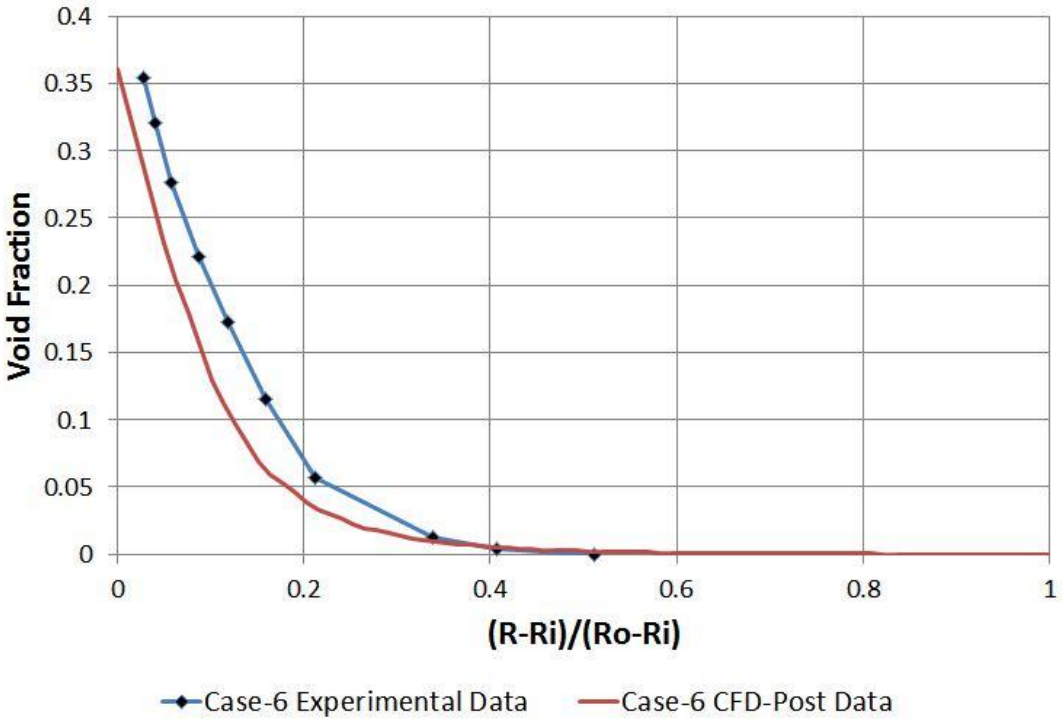

Figure 64 - Showing the experimental void fraction data vs CFD-Post™ data

The Figure 65 shows the CFD simulations done with increasing bulk bubble diameter, viz. 0.6mm, 0.9mm, 1.2mm, 1.8mm and 3mm for operating conditions as per Case-1 in the experimental set-up with the 1.4mm simulation closely matching the CFD results of [17].

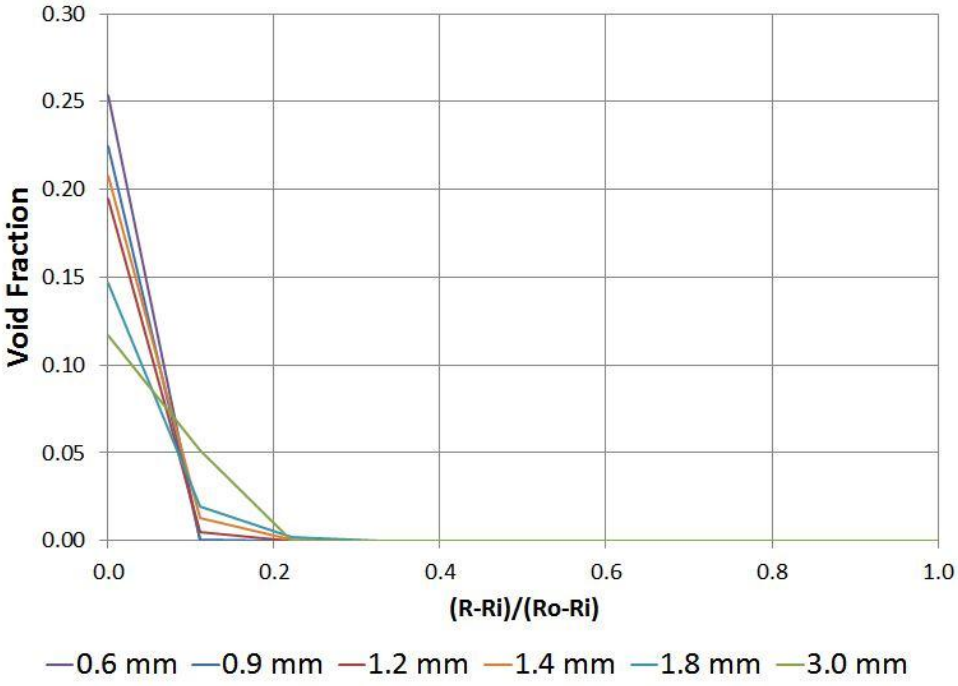

Figure 65 - Vapor volume fraction vs. Radial Distance for different bulk bubble diameters – 0.6mm, 0.9mm, 1.2mm, 1.8mm and 3mm

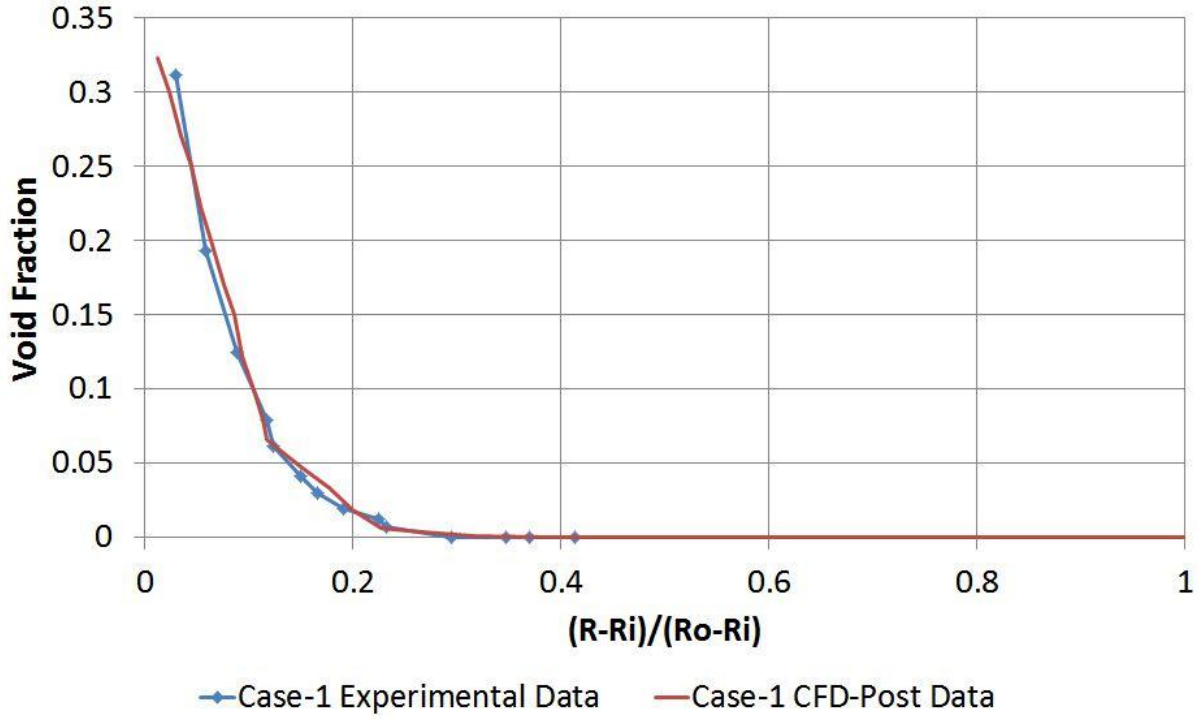

Figure 66 - CFD Simulation results vs. the Experimental Results for Case-1 with the Wall Roughness activated

The results (Figure 65) clearly show that the vapor volume fraction peak value and its distribution are dependent on the bulk bubble diameter specified/calculated. The simulations also show that smaller bulk bubble diameters lead to higher vapor volume fraction peak values (close to the heated surface) and in a narrower region, owing to higher condensation rate. The CFD simulations were done without any CEL modifications. The CFD simulations can be made more robust and less dependent on user them with following CEL modifications:

- **Saturation temperature variation**: As per the pressure values at inlet and outlet, the difference in Tsat values is 5K. Specifying a single value will no doubt reduce the accuracy of the simulation's predictions and this can be improved by inserting a simple MATLAB™ curve-fitted relationship between saturation temperature and pressure obtained from solver. This becomes more important with larger geometries due to greater changes in pressure in larger geometries. In the current case, the agreement between CFD and experimental results is very close without varying saturation temperature.
- **Bulk bubble diameter**: Instead of specifying a single value, a simple model based on liquid subcooling can be implemented if there is a big mismatch between CFD

predictions and experimental data. [see Appendix 3: Bulk Bubble Diameter Modeling CEL]

- **Boiling wall function approach**: It is essentially the rough wall model (see 2.3.5.6 Wall Roughness Model) available in ANSYS™ CFX ™. The approach has been applied to experimental case 1 and the results in Figure 66 demonstrate the improvement in the CFD simulation's prediction accuracy.

MESHING DETAILS:

The geometry is modelled as a 60^{o} sector of the annular channel and the mesh has 19 X (radial) 19 X (circumferential) 110 (axial) cells.

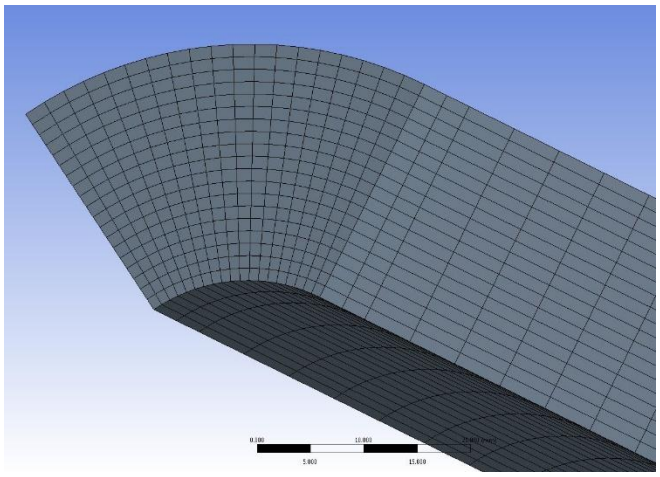

Figure 67 - Meshing of the 60 deg sector of tube geometry

4.2.1.2 Second Case – Low pressure Water Boiling

The second set of experiments were conducted by Lee et.al. [142] on low pressure upward subcooled boiling flow of water, and were analysed by Chen et.al. [41, 42].

The test loop (Figure 68 [142]) to observe the boiling of water consists mainly of the test channel, water storage tank, circulating pump, preheater and water purification unit. Distilled and degassed water is from the storage tank is pumped and flows through a turbine flowmeter and a preheater to the bottom of the test channel, which consists of a heated section where the subcooled boiling occurs. The two-phase mixture at the channel outlet flows back to the storage tank where vapor bubbles are condensed by cooling coils [142]. The test channel was a vertical concentric annulus, 2376mm long and with a heated inner tube. The inner test tube of 19mm in outer diameter is composed of a heated section and two unheated sections. The heated section is a 1670mm long Inconel 625 tube with 1.5mm wall thickness, and is filled with magnesium oxide powder insulation. The heated section is preceded and followed by 280mm long and 610mm long, thick walled copper tubes respectively. The inner tube is connected to a 54kW DC power supply and uniformly generates the heat in the heated middle section. The outer tube is comprised of two stainless steel tubes with 37.5mm inner diameter which are connected by a transparent glass tube to enable photographing and visual observation. The transparent glass tube is 50mm long and is located below the measuring plane, which is located 1610mm downstream of the beginning of the heated section [142].

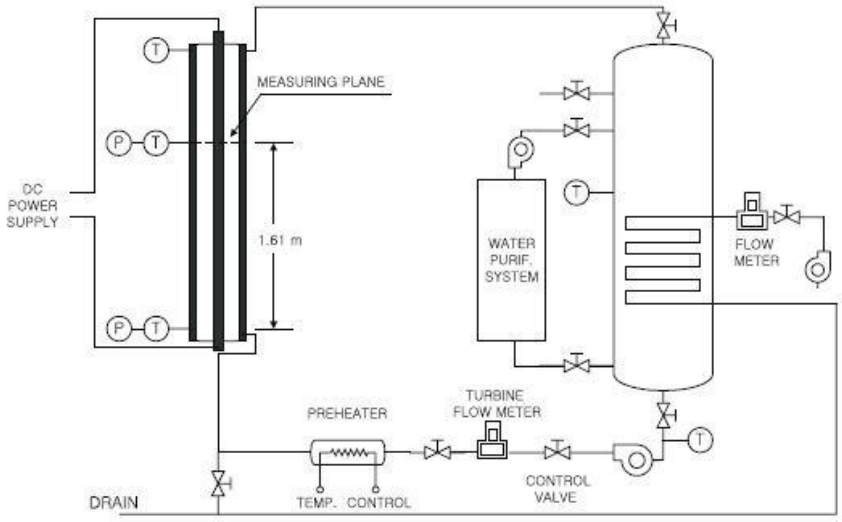

Figure 68 - Schematic of the test loop

The case being studied has applied heat flux = 152.9 kW/m^2 and mass flux = 474 kg/m^2-s, viz. Case 2. The experimental values are compared with CFD simulation results.

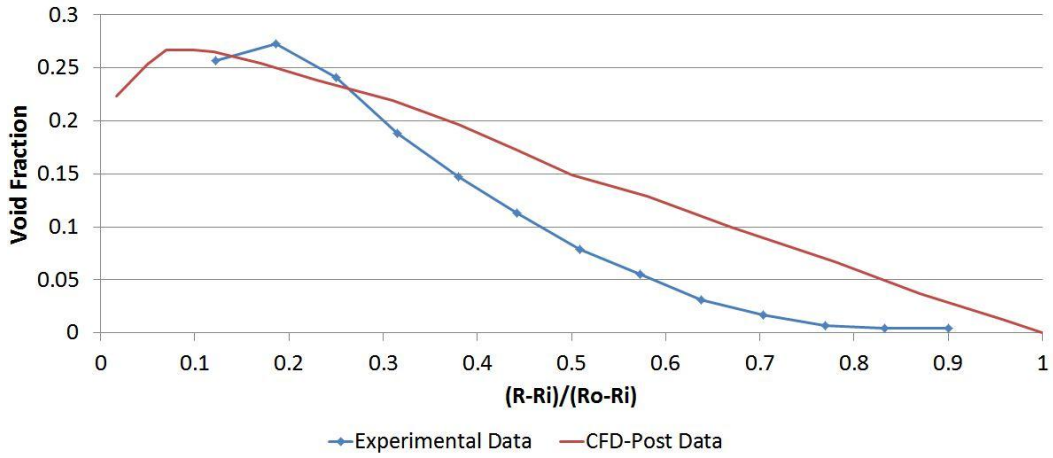

Figure 69 - Experimental values determined by Lee et.al. [142]; Vapor Volume Fraction vs. Radial Distance, CELs: Tsat, DiaBulk, DiaDep

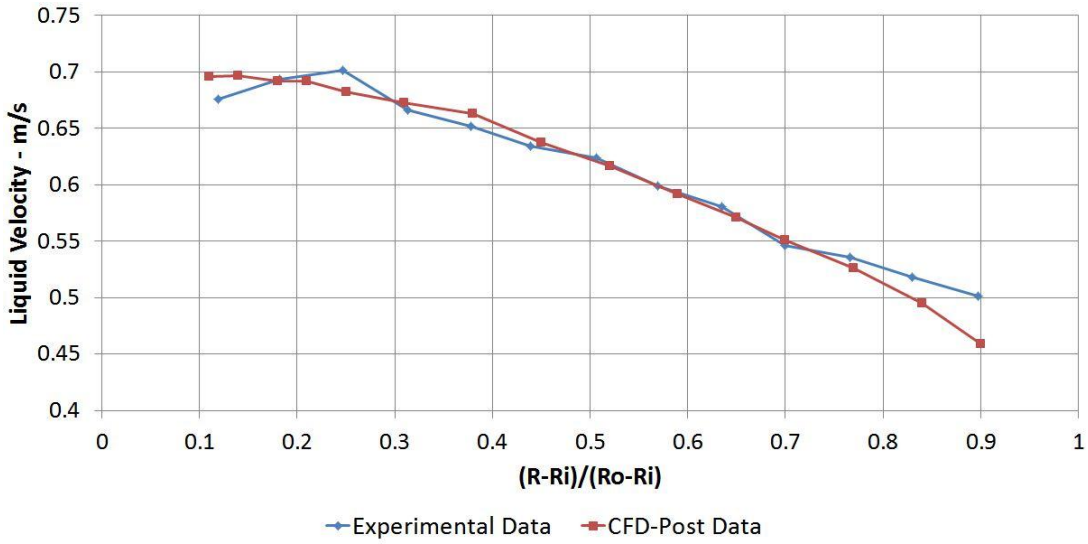

Figure 70 - Experimental values determined by Lee et.al. (92); Liquid Velocity vs. Radial Distance, CELs: Tsat, DiaBulk, DiaDep

Figure 69 shows the results of a CFD simulation with CEL routines included for saturation temperature variation and bulk bubble diameter modeling. The CELs enable varying saturation temperature for vaporizing fluid as the pressure changes along the domain, while the bulk bubble diameter CEL enables a varying value for bulk bubble diameter as per local superheating. The pattern of void fraction distribution is representative of the experimental observations, except that the void fraction does not decrease as rapidly as in experimental observations. The CEL routine for bubble departure diameter is yet to be included in the simulation and its impact on the accuracy of CFD predictions needs to be ascertained.

MESHING DETAILS:

The mesh has 20 (radial) X 2 (circumferential) X 100 (axial) cells. It is shown in the Figure 71.

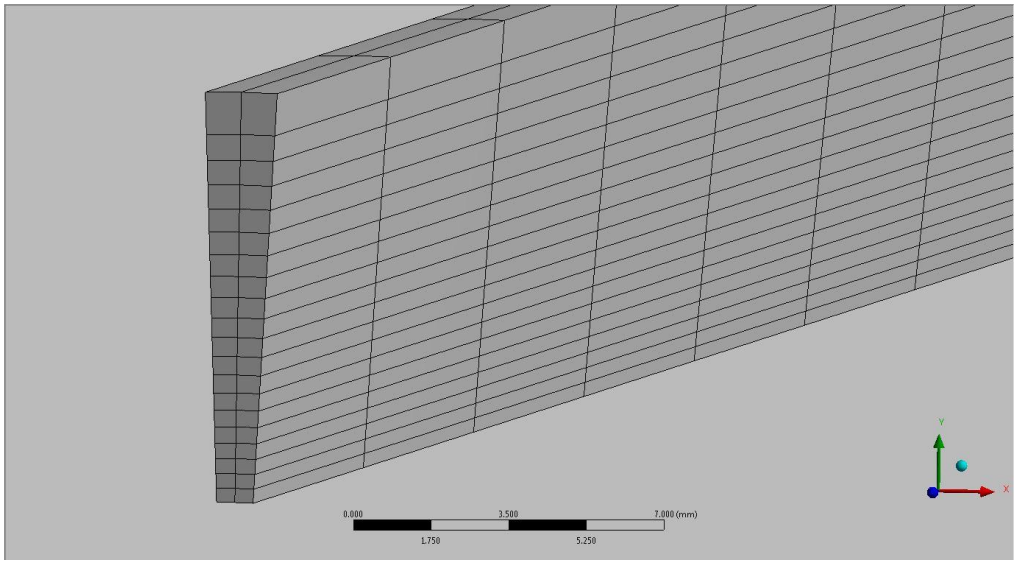

Figure 71 - Meshing for Phase Change CFD – 2

4.2.1.3 Third Case – High-pressure Water Boiling

Koncar et.al. [37] analyzed experimental data of Bartolomej & Chanturiya for boiling in pipe flow configuration with heat applied at outer boundary of the tube. The original article could not be located. The case study has heat flux = $5.7 \times 10^5\ W/m^2$, with mass flow = 900 kg/(s m^2) at a pressure of 4.5 MPa. The geometry analyzed quasi-3D in the sense that it is only a 1 degree extrusion and CFX does not do absolutely 2D simulations. So, a width of one element is defined throughout the length with symmetry boundary conditions prescribed for the sides. Inlet is defined by mass flow rate and outlet by average static pressure.

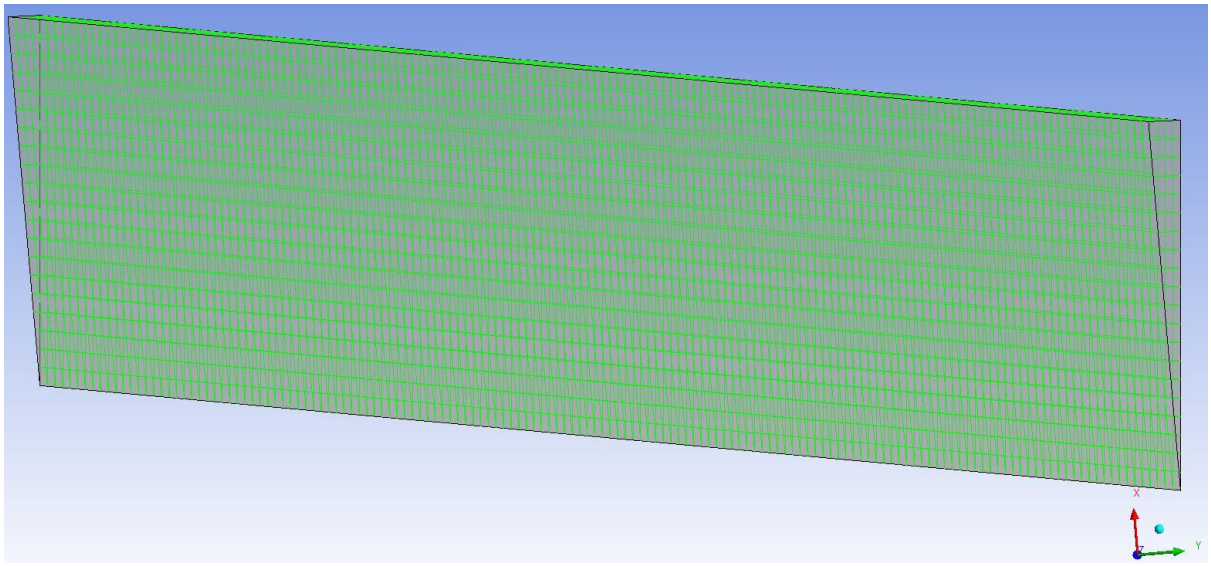

Figure 72 - Geometry and meshing for the CFD analysis

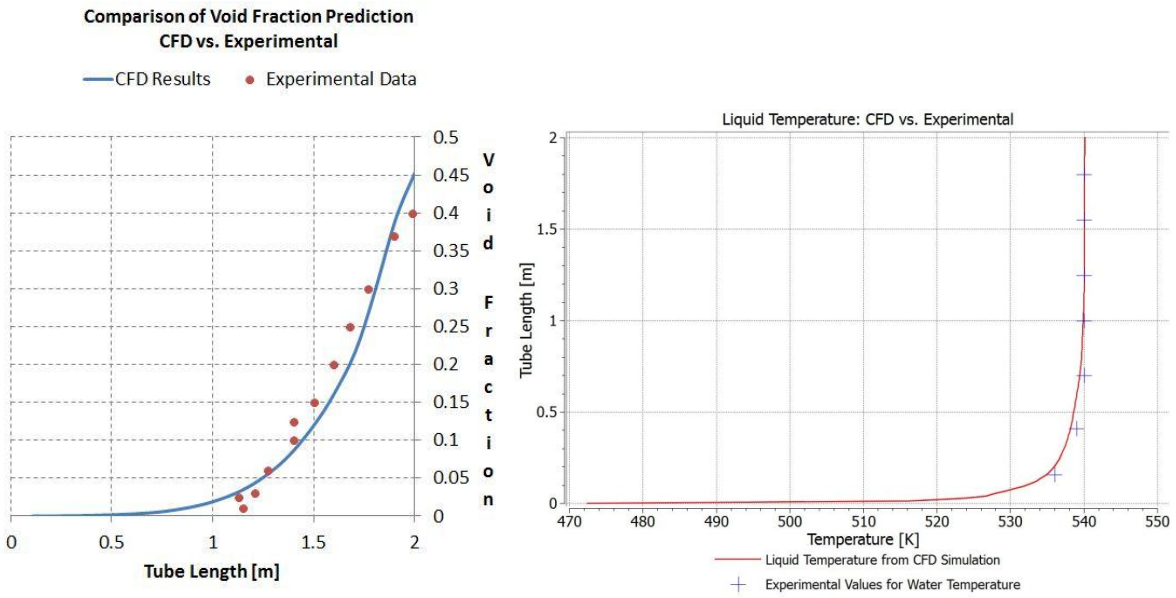

Figure 73 - Comparison of CFD Results vs. Experimental Data; a) Liquid Phase Temperature , b) Void Fraction along length of tube

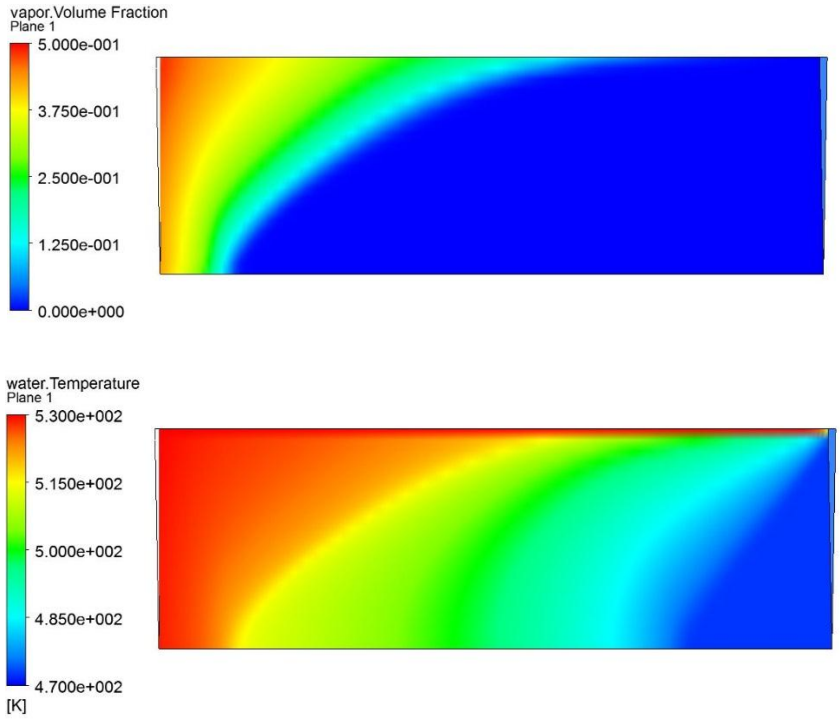

Figure 74 - CFD Results; a) Void Fraction, b) Liquid Phase Temperature

4.2.1.4 Discussion

The CFD simulations for single-tube geometry boiling were carried out to understand the process of CFD set-up for phase-change cases. Another objective was to find out the most crucial set-up parameters with regards to influence on simulation results. Both these objectives were achieved as a result of vast literature available for single-tube boiling. The literature found for single-tube boiling experiments contains detailed information about the conditions within the domain – temperatures for both phases, velocities for both phases, void fraction data across the domain, experimentally derived bulk bubble diameter correlations etc. This level of detail availability allows the CFD user to fine tune the set-up and closely match the results to experimental data. Except for the void fraction data for 2nd case, the CFD predicted values match the experimental data measurements very closely for all other comparisons. The level of match for this case can be increased by further fine tuning of CFD set-up. This was not conducted as a part of this study due to time constraints and also because of the fact that the desired outcomes from the project, viz. understanding CFD set-up for boiling cases and knowledge of critical set-up parameters, were attained. This knowledge will form the base for multi-tube CFD simulation analyses which is covered in next section.

4.2.2 Multi-Tube Geometry

The next step after CFD analysis and validation on single-tube geometry is to conduct CFD analysis of multi-tube geometries. No literature was found regarding experiments of boiling of pentane over multi-tube configurations providing measured parameters such as void fraction and mean bubble diameters. Validation in such cases was therefore limited to qualitative nature with quantitative validation limited to heat transfer coefficient values available for R113 in [86].

The CFD analysis for multi-tube configuration were carried out on a slice geometry of a shell and tube vaporizer with 2mm thickness. The width of the slice is given two mesh elements to force CFX solver to use 3-D routines, if required. The simulation results presented used Symmetry BC on both sides. The tubes in the geometry (Figure 75) have 20mm diameter and arranged in 30 degree staggered arrangement, with outer shell diameter being 500mm with total height from inlet (bottom) to outlet (top) being 750mm. Two different geometries were defined with differences in the outlet sizes to see what is the impact on vapor flow patterns.

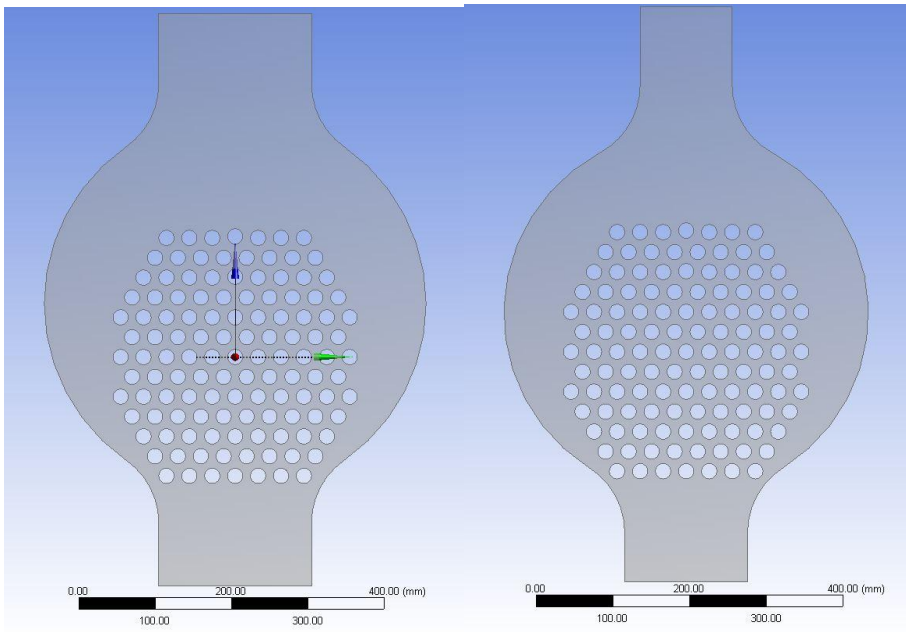

Figure 75 - STHE slice geometries analyzed

The total number of mesh elements is 0.27m with 0.18m nodes. The heated surfaces are provided with inflation layers (5 layers at growth rate of 1.2) (Figure 76) to allow for better simulation of the near surface heat transfer processes.

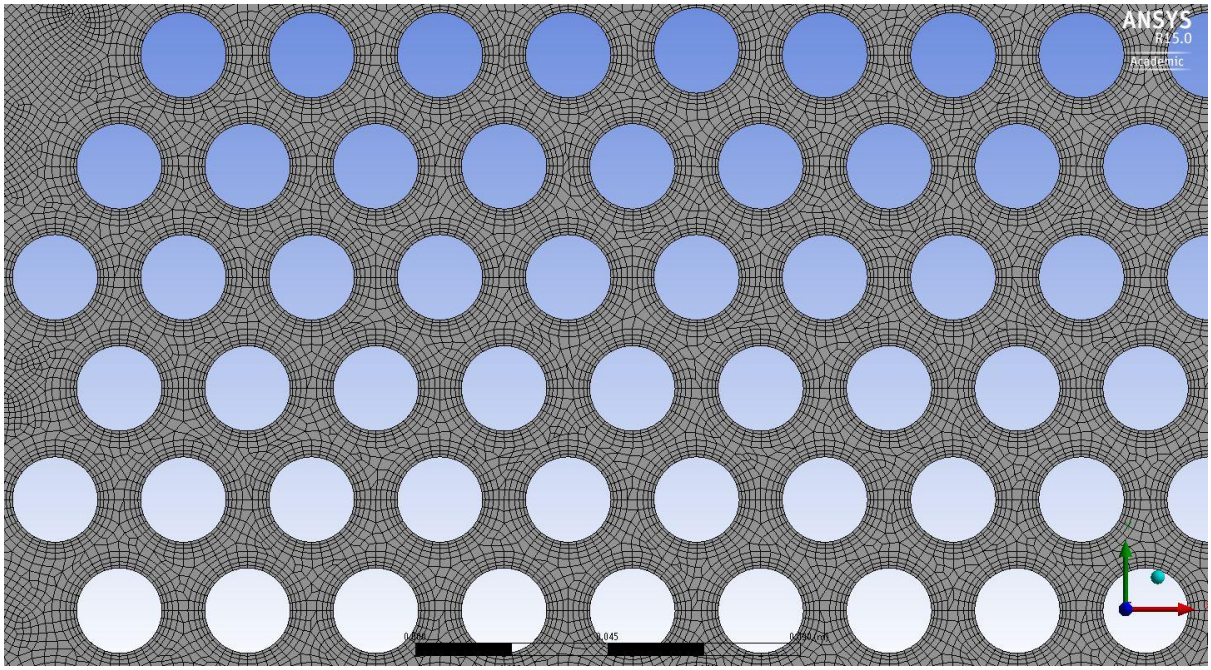

Figure 76 - Meshing of the STHE slice geometry

There are two major experimental observations for multi-tube geometries that can be used for a qualitative validation of the simulation results – a) vapor flow patterns, b) variation of heat transfer coefficient along the circumference of the tube w.r.t. direction of liquid flow.

4.2.2.1 Vapor flow patterns in multi-tube geometries

The vapor flow patterns were for boiling pentane at 1 atm were studied by [12] in a 241 tube bundle kettle reboiler thin-slice rig. The data measured was only pressure values. The rig is a gravity driven boiler/vented condenser loop. The feed enters the glass fronted shell (732mm internal diameter) having a depth of 56mm from the three 25mm ports in the curved shell wall at the bottom. The 19mm diameter tubes are electrically heated. The vapor outlet arrangement is shown in Figure 77 [12].

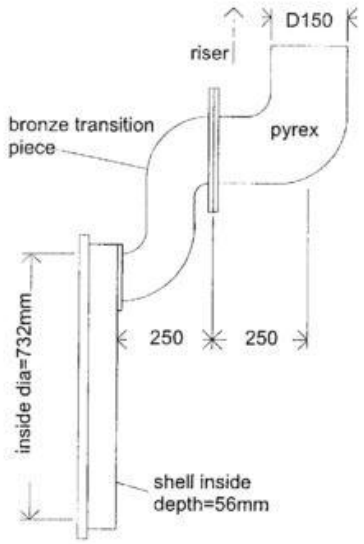

Figure 77 - Arrangement of outlet port

The comparison of flow pattern as determined by experimental observation to the one predicted by CFD simulation is shown in Figure 78, [12].

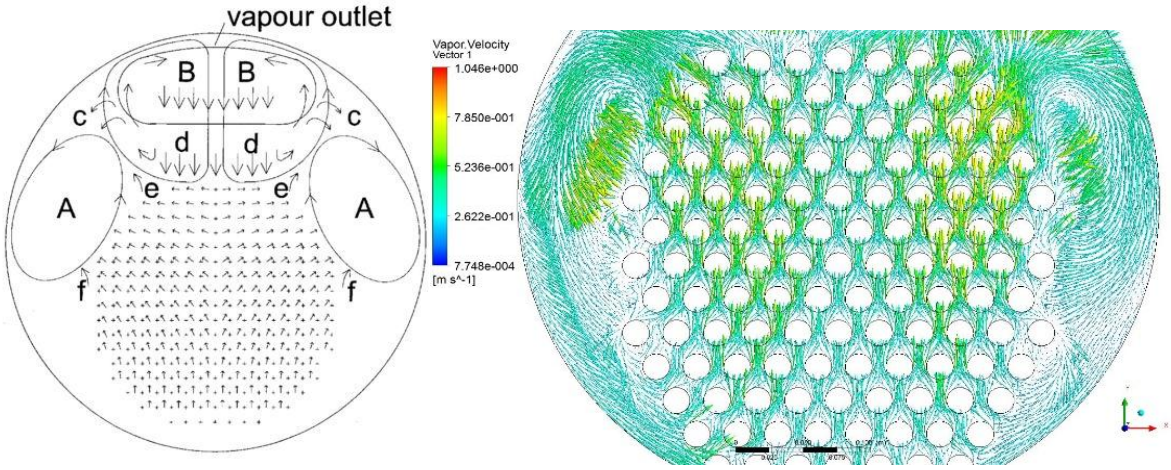

Figure 78 - Comparison of flow patterns in a STHE vaporizer slice: Experimental vs. CFD

The vapor flow patterns developed around the tube bundle are influenced by the gap between the tube bundle and the outer shell. In case of smaller gap between the tube bundle and the shell it was noticed that the vapor swirls extend to much lower tube rows and impacted the fluid as soon as it entered the domain, in the sense that the entering fluid encountered a hotter fluid being pushed down by vapor swirls even before the fluid came in contact with hot tubes (Figure 79). In case of larger gap between tube bundle and the shell, it was noticed that the vapor swirls were impacting only the top half of the tube row.

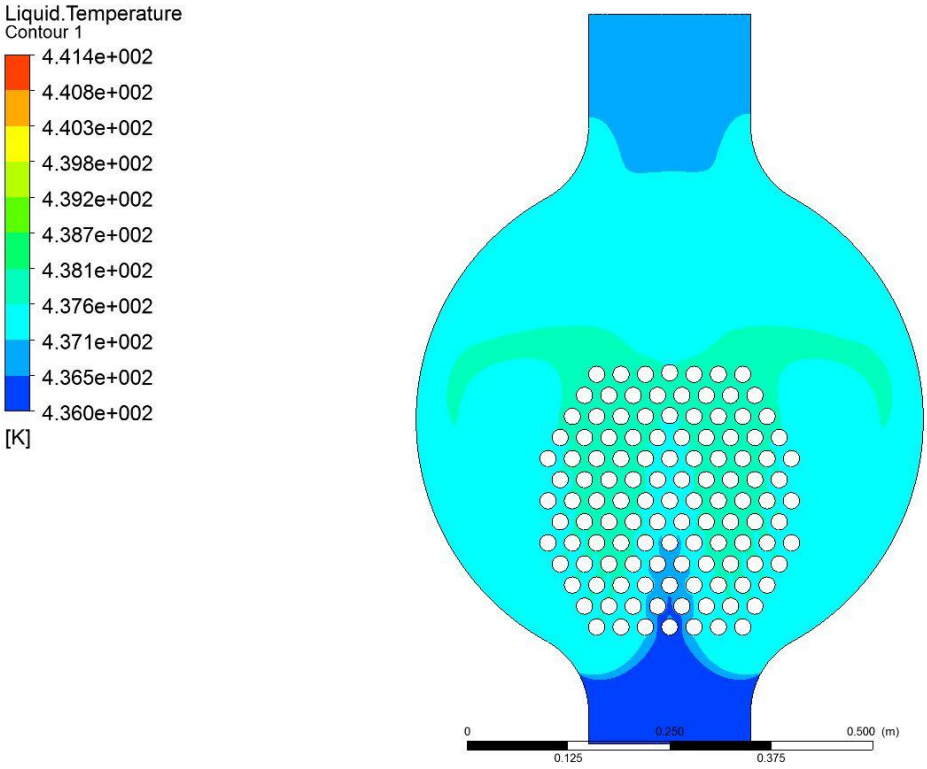

Figure 79 - Liquid temperature plot showing the influence of vapor swirls forcing hot liquid to meet the entering liquid

4.2.2.2 Circumferential variation of Heat Transfer Coefficient along periphery of tubes

The variation in values of heat transfer coefficient along the circumferential periphery of tubes in a multi-tube geometry was measured by [86] and are shown in Figure 80 [86]. R113 was used as the vaporizing fluid in the experiment. The article [86] does not mention the inlet temperature of the vaporizing fluid (R113).

The HTC plotted from ANSYS™ CFD-Post™ is Liquid HTC at heated surface. Very low values for HTC actually correspond to areas on surface that have vapor phase in contact with it. The Wall Boiling model (used on heated surface) calculates separate HTCs for liquid and vapor phases.

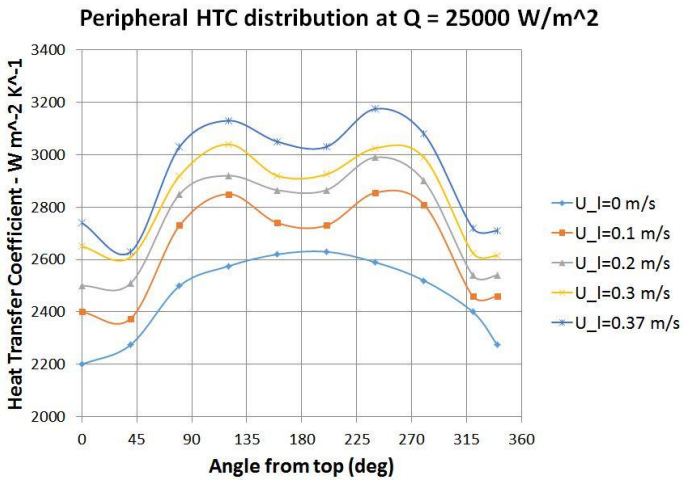

Figure 80 - Peripheral variation of heat transfer coefficient with various approach velocities for boiling of R113 at 1 atm at 25000 W/m^2 – Data read from paper and plotted in Excel – using fitted trendlines

Results from two different CFD simulations are presented here:

- **Mixture-model based, using constant temperature BC with R113 as the fluid, single tube geometry**: Three different inlet flow velocities are simulated. The flow is in the vertically upwards direction. In the CFD analysis done, the inlet temperature has 1 degree of subcooling ($T_{in} = T_{sat} - 1$). Three different inlet velocities have been simulated – 0.1 m/s, 0.2 m/s and 0.3 m/s. The fluid properties are defined as constant. The CFD simulation data is taken on the periphery of one tube from the tube-bank.

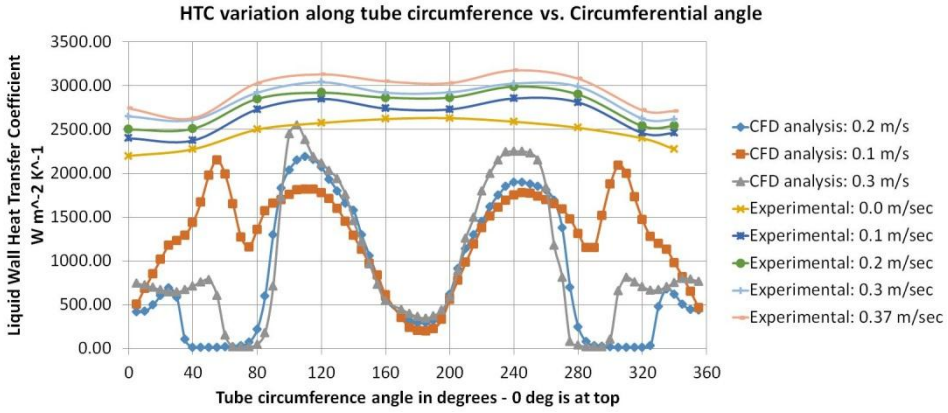

Figure 81 - Peripheral variation of heat transfer coefficient for R113 at 1.3 atm with constant temperature BC as predicted by CFD simulation – SINGLE TUBE GEOMETRY

- **Particle-model based, using heat flux boundary condition with water as the vaporizing fluid in a staggered multi-tube geometry**: The vaporizing fluid has 3.6 degrees of subcooling at the inlet with operating pressure of 10 bar with inlet velocity = 0.1 m/s. The CFD simulation data is taken on the periphery of one tube from the tube-bank.

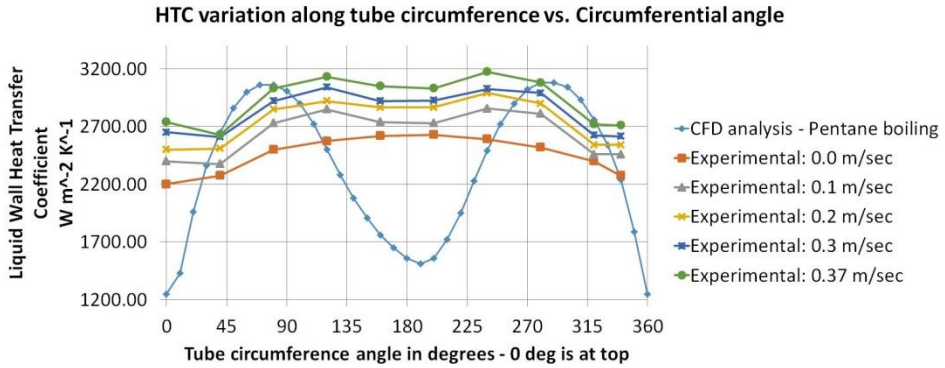

Figure 82 - Peripheral variation of liquid wall heat transfer coefficient for water at 10atm at 30000 W/m^2 as predicted by CFD simulation – MULTI-TUBE GEOMETRY

4.2.2.3 Discussion

Although the HTC variation trend in the CFD-Post™ data for both particle model (with constant heat flux boundary condition) and mixture model (with constant temperature boundary condition) is similar to the trend seen in the experiments with highest values noted on the sides of the tubes, but one significant difference is observed - the significant drop in liquid HTC values (obtained from CFD-Post™) on the top and bottom sides of the tube. The reason is: the values plotted in the graph correspond to liquid-phase HTC values. The Wall Boiling model implemented in ANSYS™ CFX™ calculates separate HTC values for liquid and vapor phases on the heated surface. The regions (top and bottom of the tube) with lowest liquid HTC values correspond to regions with highest evaporation of liquid phase which means that higher fraction of wall heat flux is being used up in vaporization of the liquid phase. Figure 83 shows the areas with maximum liquid-to-vapor phase change. This higher wall heat flux transfer to vaporization process may be causing the significant dip in HTC value for liquid phase.

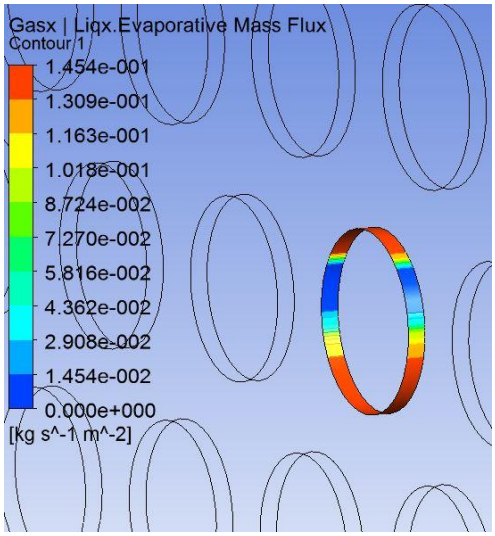

Figure 83 - Evaporative mass flux variation along the periphery of a tube

Another factor that maybe responsible for large variation in HTC values is the bubble sliding. The experimental data is gathered when the bubble sliding mechanism is active, but ANSYS™ CFX™ simulation does not factor in the influence of bubble sliding. The sliding of a bubble around the periphery of the tube will significantly impact the HTC values and also the physics of the process. This is a serious limitation of current implementation of the Wall Boiling model in ANSYS™ CFX™.

A major observation is made in case of staggered multi-tube geometry that although the tubes at the tube-bundle centre follow the experimental observation with regards to HTC variation on tube periphery, but the tubes at the periphery of the tube bundle and also top tube rows have different heat transfer coefficient distributions over the tube periphery. This is most probably due to vapor swirls that cause the fluid motion to be in different directions than the normal bottom-to-top flow at the top of tube bank and on its sides. This can be seen in Figure 84 and Figure 85.

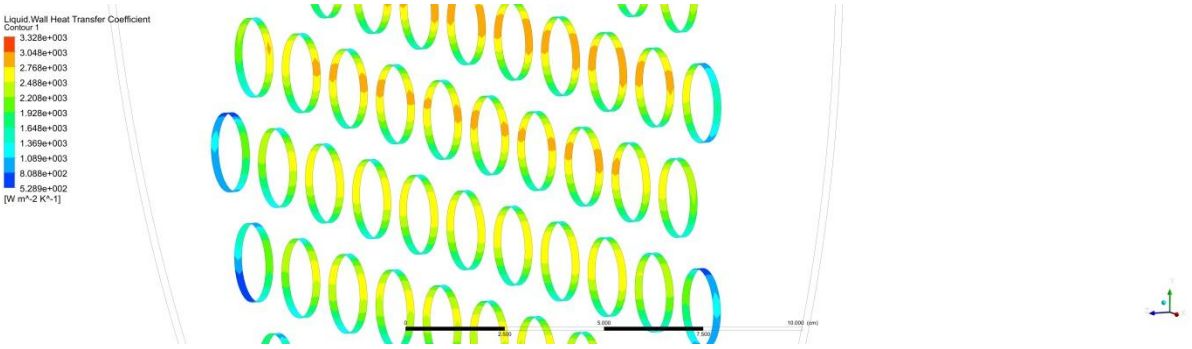

Figure 84 - - Peripheral variation of liquid wall heat transfer coefficient for water at 10atm at 30000 W/m^2 as predicted by CFD simulation

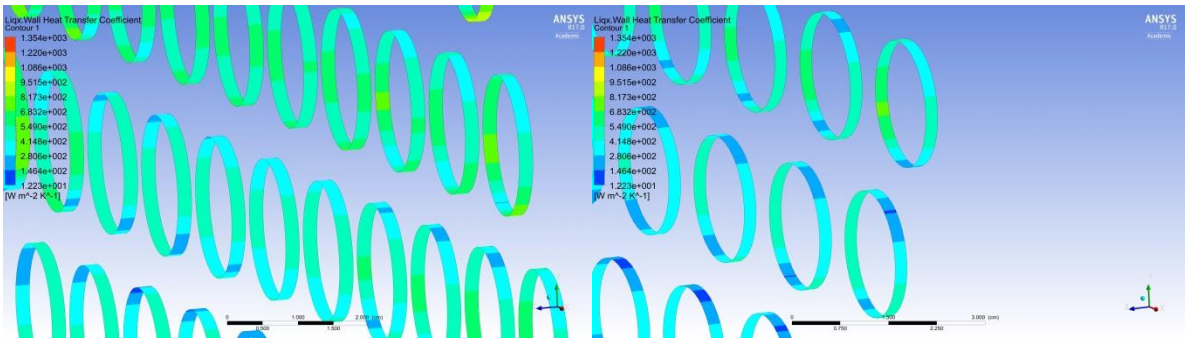

Figure 85 - Peripheral variation of liquid wall heat transfer coefficient for R113 at 1.3 atm as predicted by CFD simulation: a) at the centre of the tube bundle, b) at the periphery of the tube bundle

The impact of different and lower HTC values, predicted by CFD analysis, on the overall heat duty prediction and also vapor volume generation needs to be compared against experimental data which was not available at the time of this project. This comparison is essential before we can use the CFD approach to designing multi-tube HEs. At the current stage, the project has shown that the vapor flow patterns predicted by CFD analysis match the experimentally observed patterns closely. The quantitative validation, comparison of HTC values, has shown that the predicted trend is similar to experimental trend but this area needs to be investigated further. This investigation requires availability of more detailed

experimental data (overall temperature of exiting liquid and/or vapor, surface temperature values) and will form the core of future work on this project.

Building upon the work outlined in current chapter, the next step is to conduct parametric tests on STHE slice geometry to find the relationship between liquid level and heat transfer performance for the pentane boiling. Although, at the current stage the CFD simulation predicted values cannot be taken on their absolute magnitude as we have seen with HTC values, but the replication of real world trends by CFD simulation data does lend confidence into the trends that might be observed by a parametric study. This will be covered in the next chapter.

4.2.2.3.1 CELs implemented & Model choices

4.2.2.3.1.1 Blended Drag CEL

[Source: Dr. David Fletcher]

During starting simulation runs, it was noticed that the simulations crashed when high vapor volume fractions were present. This issue was reported to Dr. David Fletcher who reviewed the crashed results and pointed out that the major issue was the almost complete reversal in phase morphologies from the bottom of the domain to the top. The liquid is bulk phase at the bottom but it gets reduced to blobs of liquid in upper parts of domain due to vaporization on tubes. The default set-up of drag formulation in CFX is not able to detect this and this was narrowed down as one of the potential sources of crashes. Dr. David Fletcher provided us with a CEL that calculates the drag as a blend of treating liquid as bulk phase plus separated regions by obtaining the local volume fraction values from CFX solver. This was able to make the solutions reach much higher vapor volume fractions but still crashes were occurring at higher vapor volume fractions. This was resolved by using constant temperature boundary condition on "heated" surface rather than constant heat flux boundary condition. With the change in boundary condition type, the solutions could go up to full vaporization of liquid phase. Another change made was the use of mixture model rather than particle model for pairing of fluids (liquid and vapor phases of vaporizing fluid). This was necessitated because of the same reason that requires use of blended drag formulation. The particle model needs one continuous fluid while the other fluid(s) is(are) defined as dispersed fluid(s). This is allowable in situations where the dispersed fluid does not reach such high volume fraction values that it essentially becomes the continuous fluid. In our case, the vapor phase is non-existent at the bottom of the domain but reached volume fraction values of ~1 towards the top of the domain. This requires us to use the mixture model for fluid pairing which allows both fluids to be defined as continuous phases and when this is coupled with the blended drag formulation, the simulation is able to replicate the real world situation very closely, where the vapor phase exists as small bubbles in the lower parts of the tube bundle but the liquid phase exists as small dispersed droplets in the vapor space of the vaporizer (Figure 17).

4.2.2.3.1.2 HTC CEL

The implementation of Mixture Model for phase change simulations gives more realistic results as compared to Particle Model. Figure 86 shows the difference in CFD-Post™ results for Particle Model and Mixture Model. It is seen that the Mixture Model is better able to

reach the slug flow stage of boiling flow in a pipe while it is not visible for the Particle Model. It can be seen in Figure 86 where the vapor volume fraction is distributed uniformly with the use of Particle Model but we can see formations similar to slugs when Mixture model is used. For this reason, alongwith the fact that the Blended Drag CEL received from Dr. David Fletcher is based on Mixture Model, it makes sense to progress further in the project using the Mixture Model.

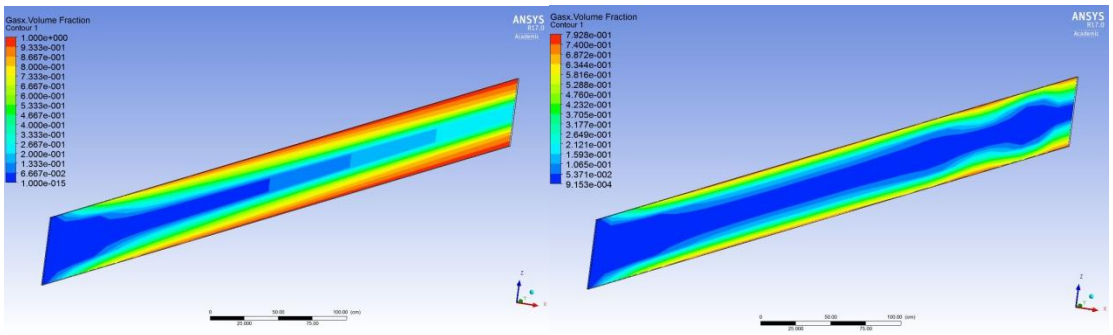

Figure 86 - Particle Model vs. Mixture Model

The implementation of Mixture Model, while advantageous in giving realistic results, brings with it a limitation that heat transfer coefficients for the two phases need to be specified/calculated by CEL. This brings user-dependency into the simulation which means that the set-up is case dependent and needs to be tuned for different operating conditions. ANSYS™ CFX™ provides the Two Resistance Model for this purpose.

TWO-RESISTANCE MODEL for Fluid Specific Heat Transfer Coefficients [4, 5]

It is designed for applications where it is necessary to consider interphase heat transfer on each side of the interface. This condition is met in our case where condensation of vapor or evaporation of liquid at the interface is highly likely to happen. As per ANSYS™ manuals also, the primary application that requires this is the Thermal Phase Change Model [see [4, 5]] for interphase mass transfer. In this class of models, we need to specify two heat transfer coefficients – one for each fluid of a specified phase pair. It is possible to specify a zero resistance condition on one side of the phase interface. This is equivalent to an infinite fluid specific Heat Transfer Coefficient. Its effect is to force the interfacial temperature to be same as the phase temperature.

4.2.2.3.1.3 CFD Model boundary conditions for heated surface

In the parametric study on STHE slice geometry, a constant temperature boundary condition will be used as it has been found to be more stable for simulations that have higher vapor volume generation. With constant heat flux boundary condition, the simulations crash with

'cal_TSUP' error and during the course of this project no suitable solution was found for this problem. The cause for the error – CFX-Solver™ is able to lower the heat flux in regions on heated surface where it encounters high vapor volume fraction while in case of constant heat flux boundary condition the solver crashes as boiling crisis is reached.

4.3 Selection of a substitute fluid for Pentane-boiling simulation set-ups

While using CFD analysis for a case with little or no experimental data available to validate and tune the model set-up, it becomes both essential and complicated to ascertain factors that can lend confidence into the model set-up. The process of bubble generation needs to be correctly modeled in the CFD model set-up to match simulation results to the experimental data. Bubble generation depends on the thermophysical properties of the liquid undergoing vaporization. The effect of these properties on boiling and bubble generation can be studied by analysing following dimensionless numbers.

For boiling phenomenon, the important dimensionless numbers are [38, 39]:

- Tube Reynolds number (for in-tube flows) ($\rho V_l L/\mu_l$) – It is the ratio of inertial to viscous forces.
- Liquid-gas density ratio,
- Weber number ($\rho_G {V_{rel}}^2 L/\sigma$) – It is used in analysing fluid flows where there is an interface between two fluids, especially for multiphase flows with strongly curved surfaces.
- Jakob number ($\frac{c_{p,liq}\rho_l}{H_{fg}\rho_g}(T_w - T_{sat})$) – It plays an important descriptive role in virtually all direct contact processes that involve a change of phase [3].
- Boiling number ($q"/H_{fg}\rho_g V_g$) – It can be seen as the ratio of a) mass of vapor generated per unit area of heat transfer surface, to b) mass flow rate per unit flow cross-sectional area [62].

For bubble dynamics, the relevant dimensionless numbers are [38, 39]:

- Bubble Reynolds number ($\rho_g V_b D_b/\mu_f$) – It is the ratio of inertial forces to viscous forces.
- Eötvös/Bond number ($\Delta\rho g L^2/\sigma$) – It is the ratio of body forces to surface tension forces.

- Morton number ($g\mu_f^4\Delta\rho/\rho_f^2\sigma^3$) – It is used in conjunction with Eötvös/Bond number for characterizing shapes of bubbles/drops moving in a surrounding continuous medium.

A comparison (Table 9) of the dimensionless numbers used to characterize boiling and bubble generation between pentane and R113 is done with assumed values of bubble mean diameter & relative velocities between phases. This comparison reveals that the pressure values at which dimensionless numbers have same values for the two fluids match closely for all cases except Eötvös number, pressure values for which are still within an order of magnitude of each other.

		Value	Pressure (atm)	
Dimensionless numbers affecting Bubble Dynamics				
Bubble Reynolds Number	n-Pentane	2000	1.97e+01	[For mean bubble diameter = 2 mm]
	R113	2000	1.58e+01	
Morton Number	n-Pentane	4e-11	1.97e+01	
	R113	4e-11	1.38e+01	
Eötvös Number	n-Pentane	7	1.79e+01	
	R113	7	6.91e+00	
Dimensionless numbers affecting Boiling				
Weber Number	n-Pentane	240	1.97e+01	[For gas phase velocity = 2 m/s, Relative phasic velocity = 2 m/s]
	R113	240	1.48e+01	
Boiling Number	n-Pentane	1e-02	1.97e+01	
	R113	1e-02	1.96e+01	
Jakob Number	n-Pentane	2.5	1.97e+01	
	R113	2.5	1.58e+01	

Table 9 - A comparison of dimensionless number (characterising boiling and bubble dynamics) between R113 and Pentane

If the pattern of variation thermophysical properties w.r.t. pressure is similar between two fluids then it stands to reason that they exhibit similar changes in bubble dynamics with pressure changes. A comparison (Figure 87, Figure 88) of the variation of thermophysical properties (enthalpy, density, entropy, specific heat, thermal conductivity, saturation temperature, surface tension & viscosity) vs. pressure between pentane, R113 and water reveals similar patterns of change among pentane and R113.

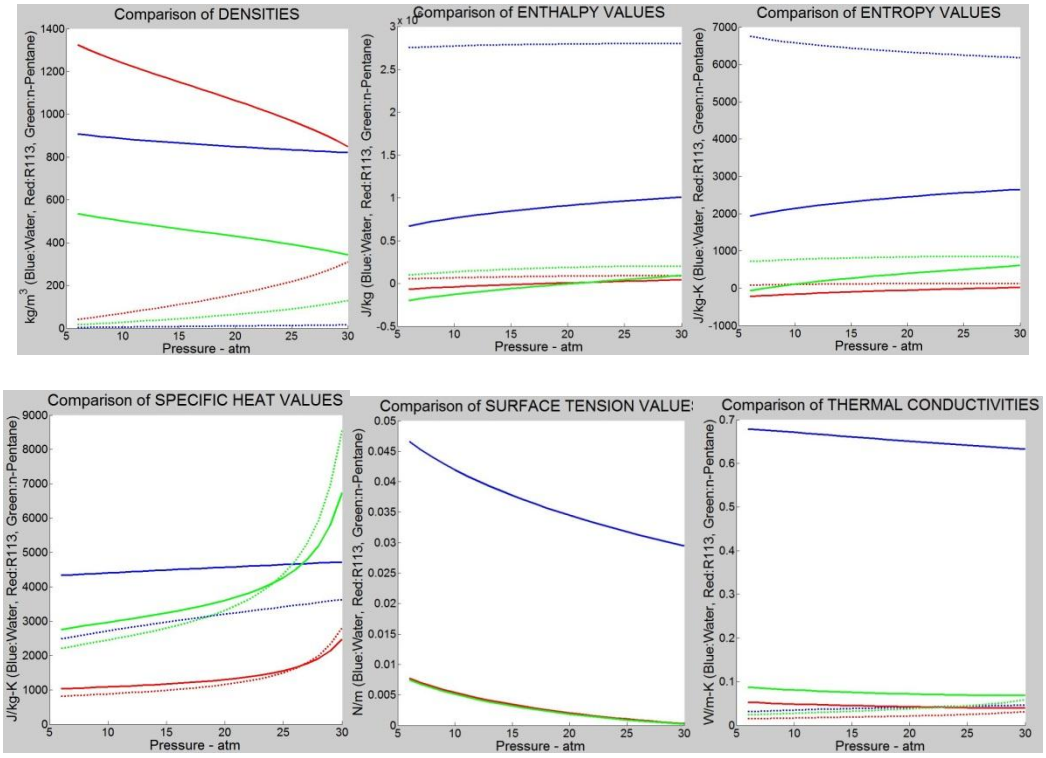

Figure 87 - Comparison of thermophysical properties among - R113, water, pentane (Solid lines - LIQUID; Dotted lines - VAPOR)[BLUE – Water, RED – R113, GREEN - Pentane]....contd.

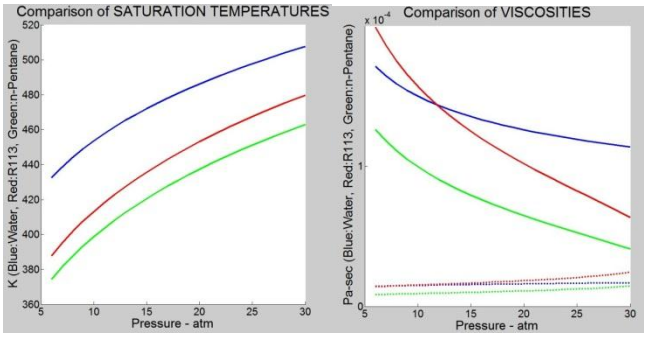

Figure 88 - Comparison of thermophysical properties among - R113, water, pentane (Solid lines - LIQUID; Dotted lines - VAPOR) [BLUE – Water, RED – R113, GREEN - Pentane]

This comparison led to selection of R113 as a fluid, CFD model set-ups for which can be used as a basis for setting up models for pentane. Another advantage of choosing R113 is the literature available on R113-boiling experiments. In the next chapter, the simulations have been carried out using R113 as the vaporizing fluid.

4.4 Preliminary CFD analysis on representative geometry

A preliminary CFD analysis has also been carried out on representative geometry (Figure 91). The term representative geometry here means a small geometry with same flow structure and inlet-outlet(s) arrangement as in full scale vaporizer's repeating unit (Figure 92).

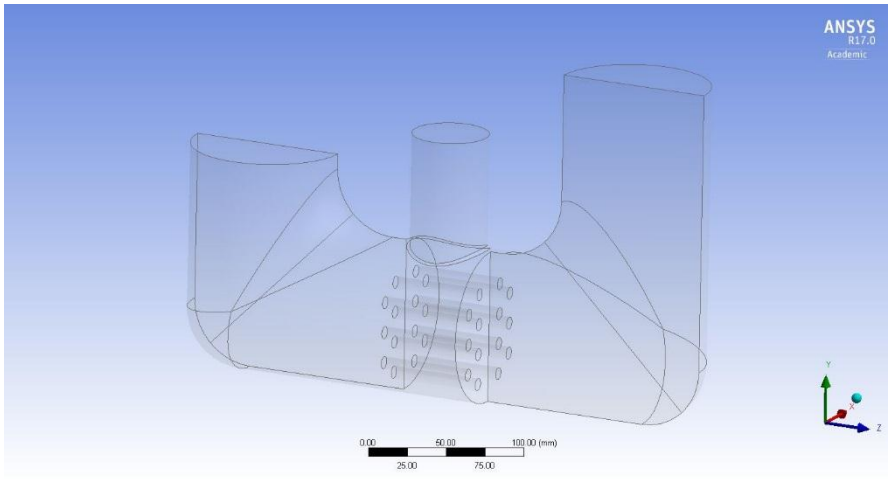

Figure 89 - Representative geometry

The representative geometry uses a relatively coarse unstructured tetrahedral mesh (Figure 90) with 0.96 million elements. The analysis is carried out under Transient conditions using water as vaporizing fluid at 1.6 bar and 1 m/s inflow rate.

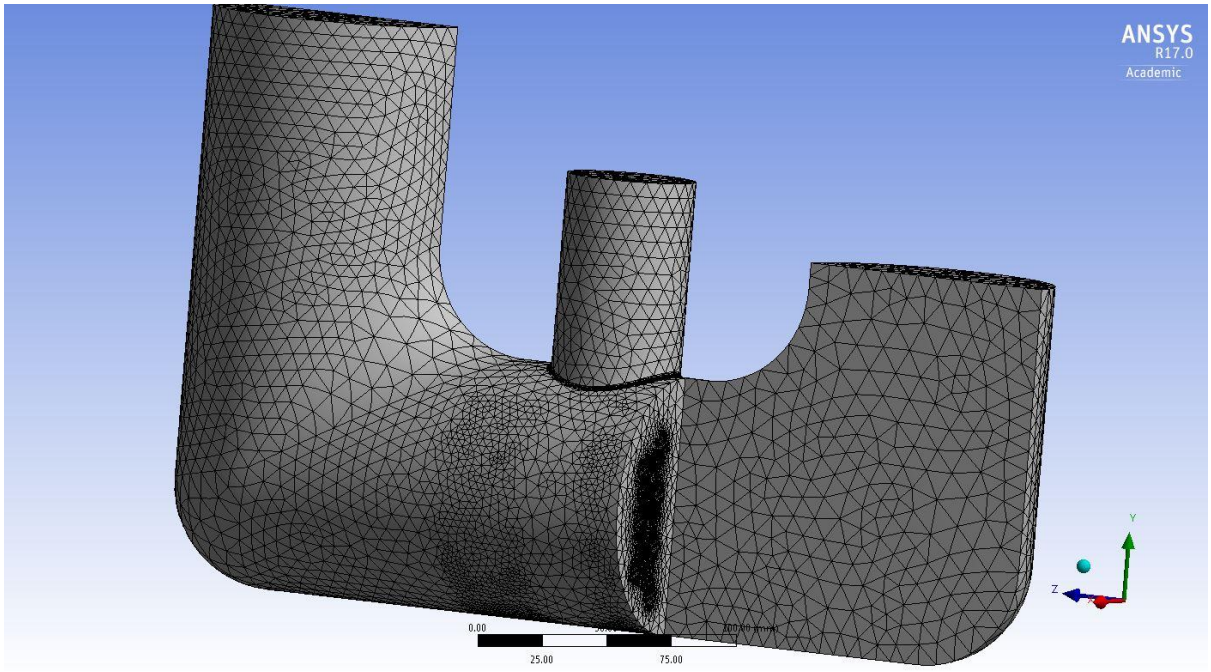

Figure 90 - Representative geometry's meshing

The CFX-Pre™ CFD set-up uses similar set-up as the multi-tube CFD simulations described in this chapter using $k - \varepsilon$ scalable model. The results from the CFD analysis are presented here:

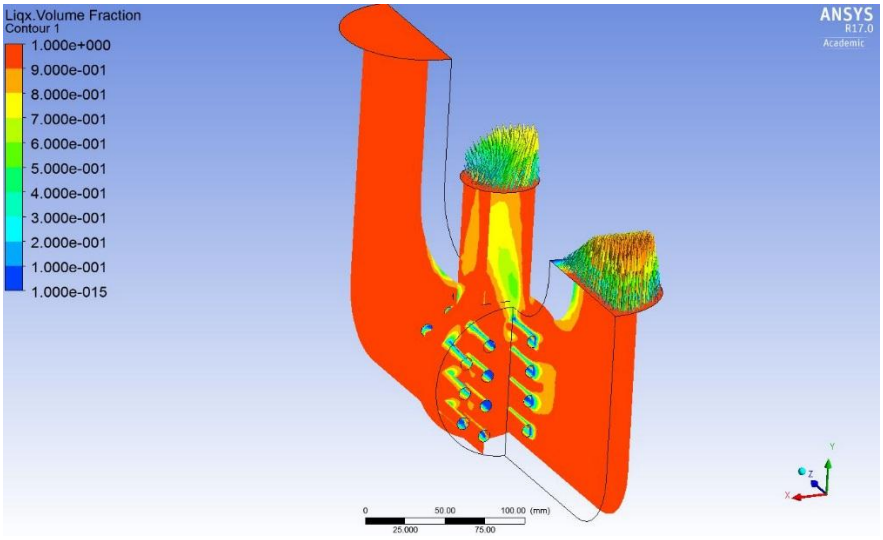

Figure 91 - CFD simulation results for scaled down representative geometry

The full scale representative geometry is seen in (Figure 92) along with the entire vaporizer's CAD drawing (Figure 93). The representative geometry has been chosen because of the repeating nature of internal geometry of full scale vaporizer with regards to flow path created by baffle arrangement.

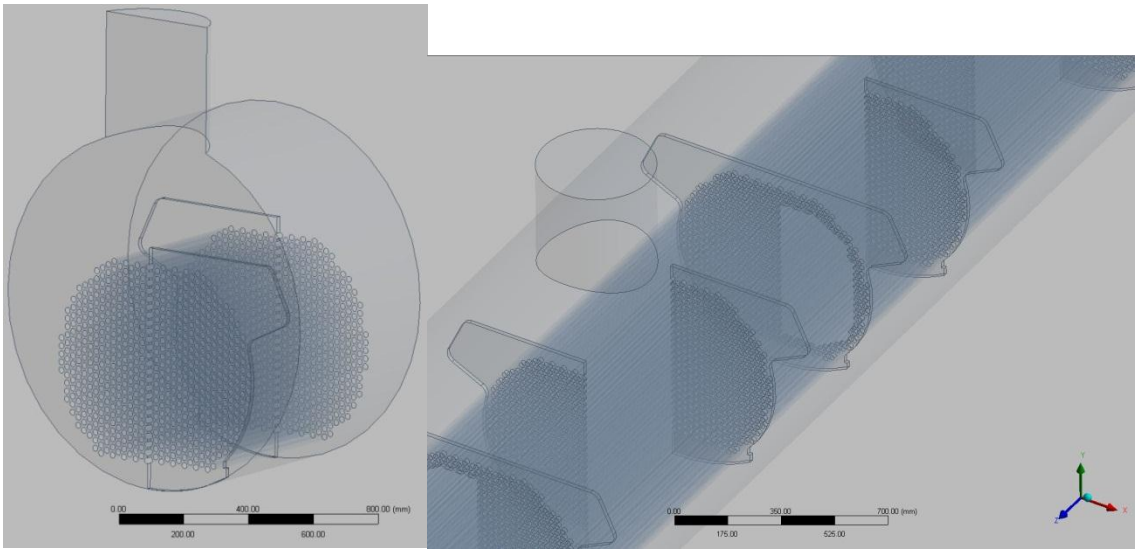

Figure 92 - Full scale representative geometry alongside a close-up view of the internal geometry of the vaporizer unit (Shell-fluid only shown here)

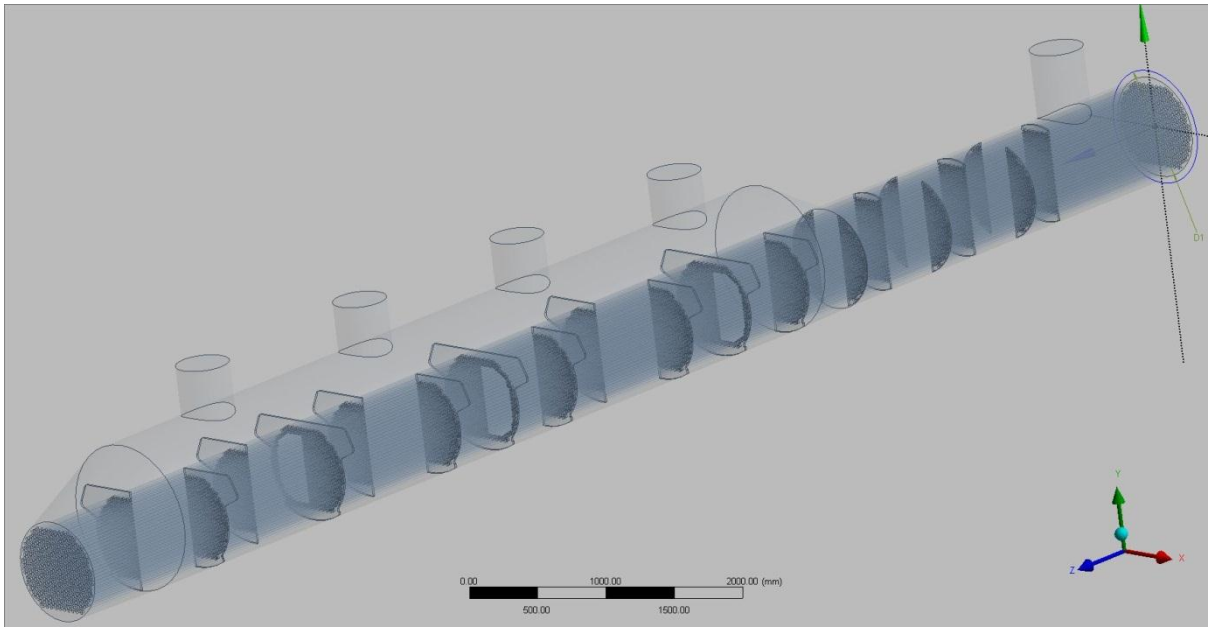

Figure 93 - Shell-side fluid only rendered for the full vaporizer unit

The CFD simulation's results present an expected picture with most of generated vapor escaping from the vapor outlet while some of it entrained in the flow of the liquid and gets carried around the baffle.

5.0 Heat transfer performance vs. Liquid Level

In this chapter, a parametric study is done on STHE slice geometry to see the effect on liquid level in the vaporizer when the inlet flow rate is changed keeping everything else constant. During interaction with geothermal power-plant engineering managers it was learned that the vaporizer unit plays a very crucial role in deciding the overall performance of the power plant in term of power generation and hence economic profitability of the plant. The term 'liquid level' needs to be clarified a little here as in case of vaporizing units there is no well-defined so-called liquid level. Instead, almost all of the tube bank, barring the first few tube rows, is covered with foam - a mixture of liquid and vapor phases of the working fluid – with increasing vapor quality (higher volume fraction for vapor phase) towards the top tube row. The measurement of liquid-level by plant operators is essentially a measurement of pressure difference with a side bridle to collect a level and feed a sight glass. The level of liquid in the sight glass essentially represents mass of liquid above the low point as an average rather than any actual liquid surface.

5.1 Method description

[The software used is ANSYS™ CFX™ v17.0]

The current study was started with the knowledge that CFD analysis of a large 3-D region would take computationally too long a time to allow for a parametric study. But it was also considered that the study should be simulating some important aspects of the actual boiling process that is occurring within a vaporizer. This conundrum was helped a little by the fact that researchers have noticed over the years that in the centre region (centre region means the centre of the tube bank when it is viewed as a circle of tubes) of a kettle reboiler, the bulk of fluid flow is in vertically upward direction [115]. Based on this knowledge, a simple slice geometry was designed with inlet at bottom and outlet at the top.

5.1.1 Geometry and Meshing details

The STHE slice geometry has 121 tubes, diameter 20 mm, arranged in 13 tube rows. The tube bundle diameter is 390 mm while the shell diameter is 550 mm. The entire domain height from inlet to outlet is 1075mm.

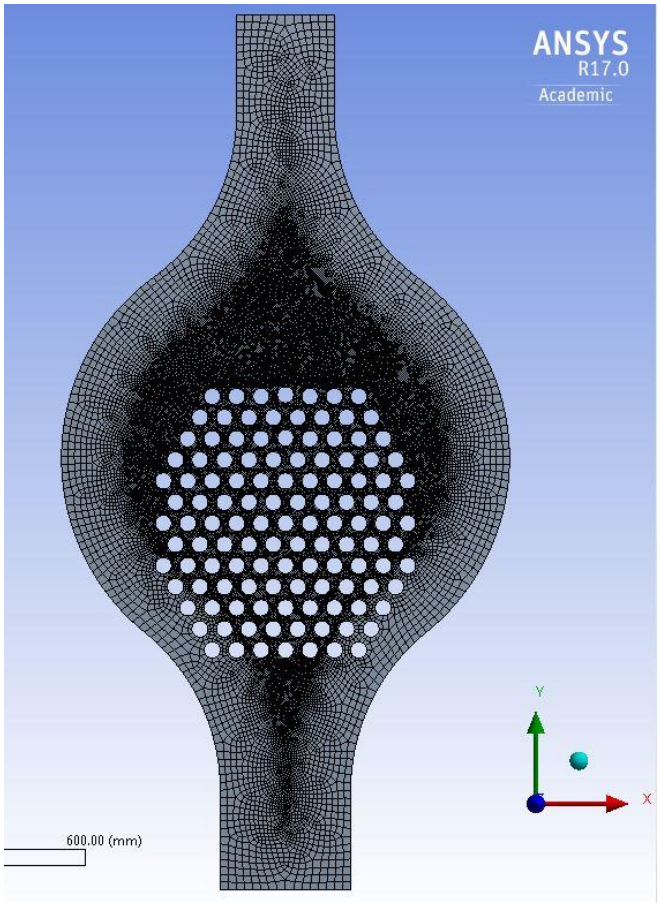

Figure 94 - Meshing of STHE slice used for CFD study

Meshing details:

MESH METRICS	VALUE
Number of nodes	297029
Number of elements	40907
Aspect ratio	1.5112
Element quality	0.914
Orthogonal quality	0.985
Skewness	0.125

Table 10 - Meshing details of STHE slice geometry used for CFD study

5.1.2 CFD set-up

The CFD set-up for STHE slice geometry uses Mixture Model with Blended Drag CEL. The geometry uses staggered (30^o) tube arrangement. It uses R113 as the vaporizing fluid with 10 degrees of superheating defined on the heated surface (tubes) using the constant temperature BC. The current parametric study is done for a generic vaporizer geometry as the aim for the current study was to observe the impact of inflow rate on the vapor generation within the vaporizer as predicted by CFD simulations. There is no real world data available to validate this study against at the time of this project.

The computation time for the mesh being used is 18.5 hrs for 2500 timesteps on a 10 core i7 4930K desktop computer. The number of timesteps solved is different for different inlet flow rates. The solution for each inlet flow-rate is carried out to ensure that considering the inlet velocity, the fluid is able to cover a distance equivalent to 2 passes through the tube bundle during the period simulated. This distance is kept at 700 mm. The CFD analysis is done as a Transient simulation.

CASE	INLET FLOW RATE – cm/sec	Timesteps solved / Timesteps to be solved
1	5	4000/3000
2	2.5	6500/6000
3	1	15500/15000
4	0.5	22000/30000
5	0.25	23500/60000**

*Table 11 - Timesteps solved for different inlet flow rates; [** top tube rows become exposed after this]*

5.1.3 Mesh dependence study on a smaller geometry

In view of the large computational time requirements for the STHE slice geometry, a smaller geometry was used for mesh-dependence study. This was designed with 2 outlets as that will be the form of geometry for representative geometry of full scale (Figure 92) pentane vaporizer (Figure 95).

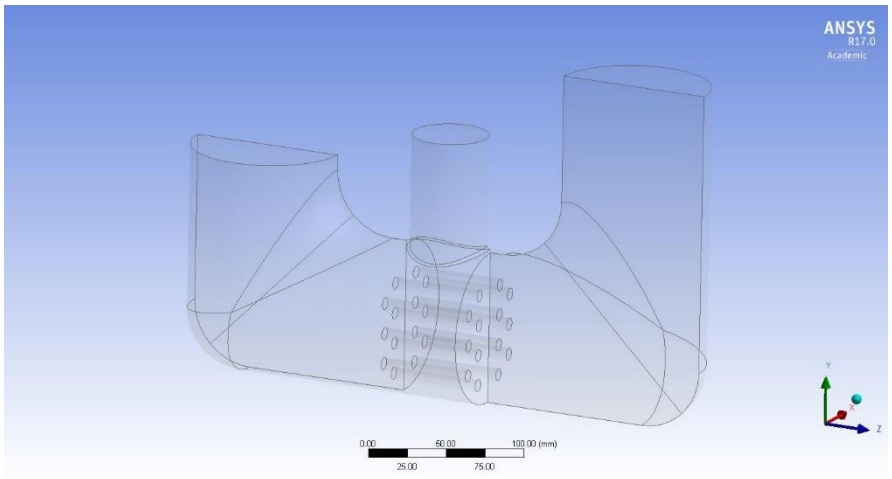

Figure 95 - Scaled down representative geometry of pentane vaporizer

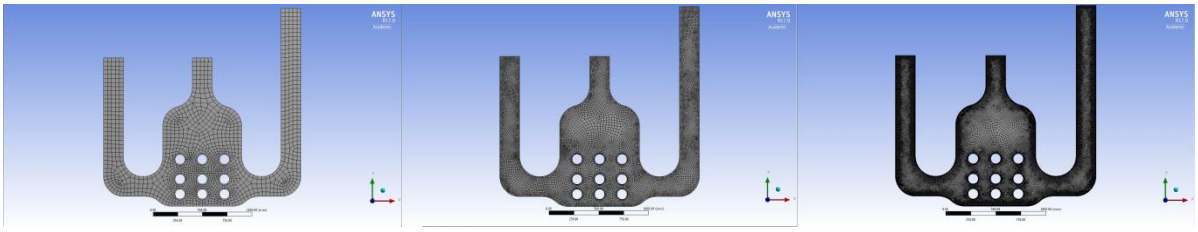

Figure 96 - Meshes increasing in refinement from left to right

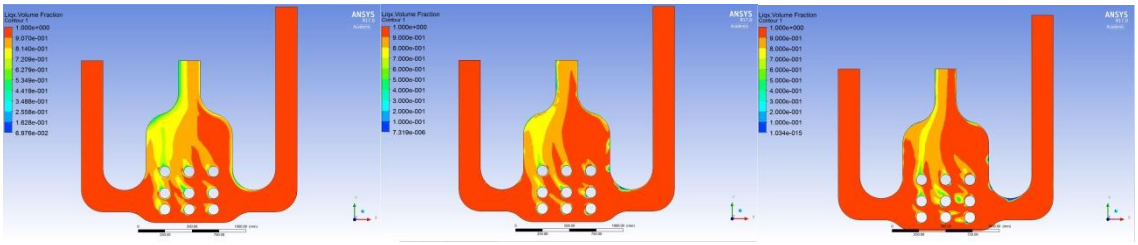

Figure 97 - Liquid volume fraction contours for meshes 1 to 3, left to right

The meshes are increasing towards fineness from Mesh 1 -> Mesh 2 -> Mesh 3.

PARAMETER	MESH-1	MESH-2	MESH-3
Vapor volume fraction at vapor outlet	0.2135	0.166	0.158
Averaged heat flux to liquid phase on heated surface – W/m^2	2.86e+6	2.31e+6	1.99e+6
Averaged heat flux to vapor phase on heated surface – W/m^2	127562	109015	93748
Total average heat flux – W/m^2	2.99e+6	2.42e+6	2.08e+6
Summed heat flux to liquid phase on heated surface – W/m^2	1.03e+9	1.29e+9	2.82e+9
Summed heat flux to vapor phase on heated surface – W/m^2	4.59e+7	6.08e+7	1.33e+8
Total summed heat flux – W/m^2	1.08e+9	1.35e+9	2.95e+9
Average HTC liquid phase on heated surface – W/m^2-K	2653.13	2946.92	3876.19
Average HTC vapor phase on heated surface – W/m^2-K	230.99	252.755	321.86

Table 12 – CFD-Post™ data on heat transfer performance for 3 different meshes analyzed

MESH METRICS	MESH-1	MESH-2	MESH-3
Number of nodes	12989	84337	462269
Number of elements	1694	11563	64844
Aspect ratio	16.977	6.756	2.85
Element quality	0.131	0.299	0.637
Orthogonal quality	0.967	0.978	0.989
Skewness	0.171	0.131	0.00727

Table 13 - Meshing details for 3 different meshes used for mesh-dependence study on 9-tube double outlet geometry

The mesh dependence reveals a significant influence of mesh size on the results of simulation. The current mesh dependence study has not done till the stage of mesh convergence due to time constraints. Future work with simulations on the STHE slice geometry needs to have a mesh-dependence study carried out.

5.2 Results from the parametric study on STHE slice geometry

5.2.1 CFD-Post™ monitoring locations

For analysing of data from different CFD analysis runs on the STHE slice geometry, two kinds of locations have been defined (Figure 98) – a) surface groups: 13 in number, one surface group refers to all the heated surfaces (tubes) in each tube row, b) planes: 35 in number, defined from below the first tube row to outlet channel at the top.

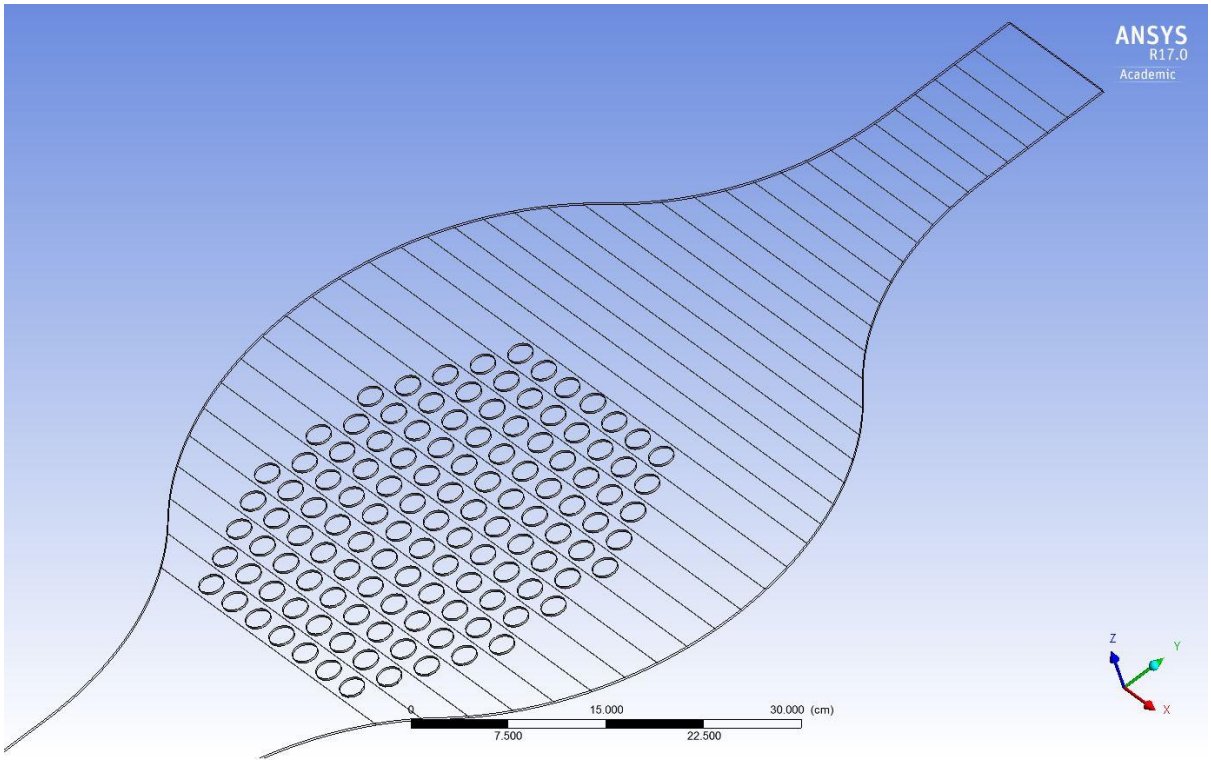

Figure 98 - Locations used for obtaining CFD-Post™ data in the parametric study on STHE slice geometry

5.2.2 Results presented:

a) Liquid + Vapor wall heat flux summed on each tube row

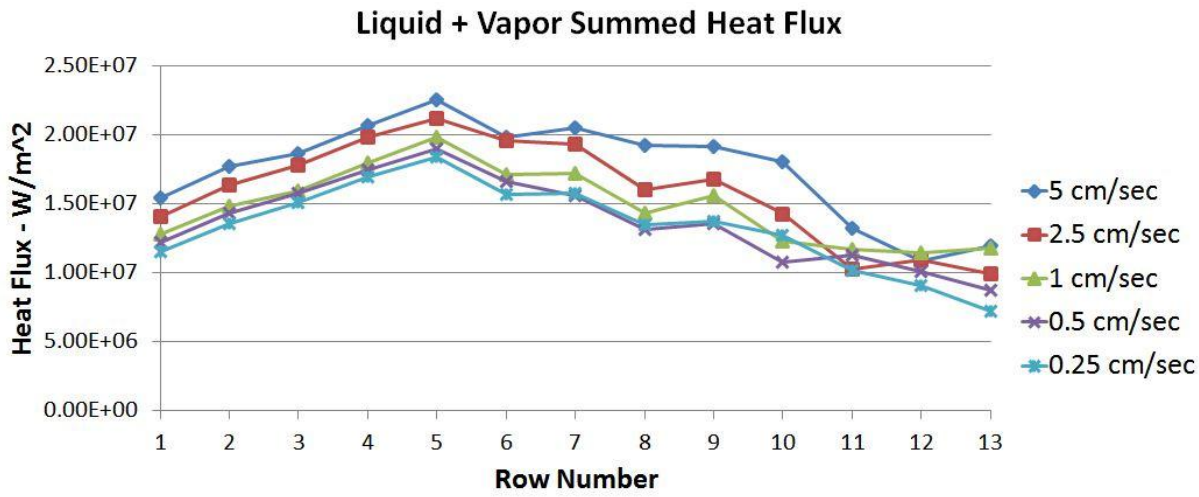

Figure 99 - CFD predicted summed values of heat flux transferred to liquid and vapor phases at each tube row

b) Liquid wall heat flux summed on each tube row

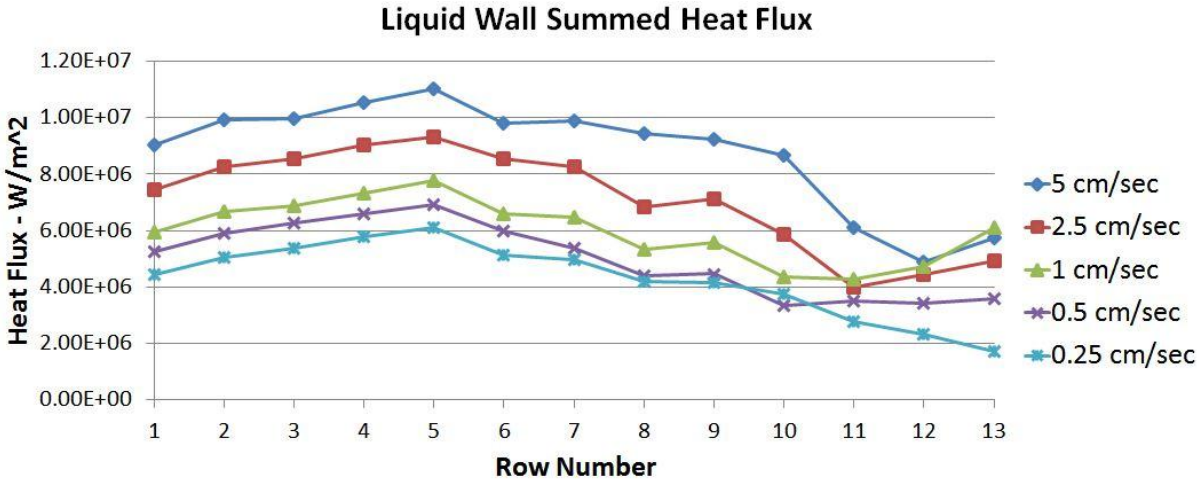

Figure 100 - CFD predicted summed values of heat flux transferred to liquid phase at each tube row

c) Vapor wall heat flux summed on each tube row

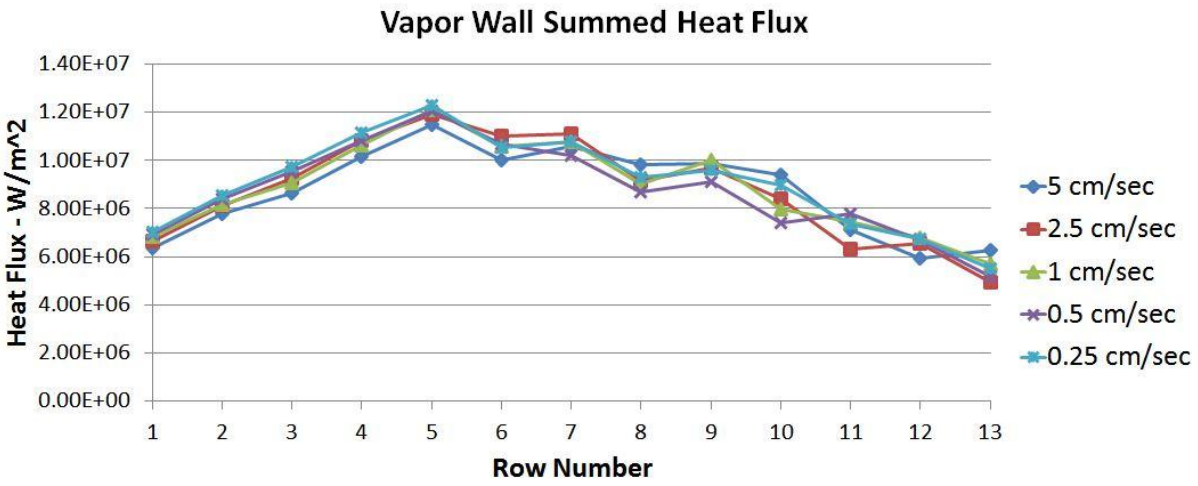

Figure 101 - CFD predicted summed values of heat flux transferred to vapor phase at each tube row

d) Liquid + Vapor wall heat flux averaged on each tube row

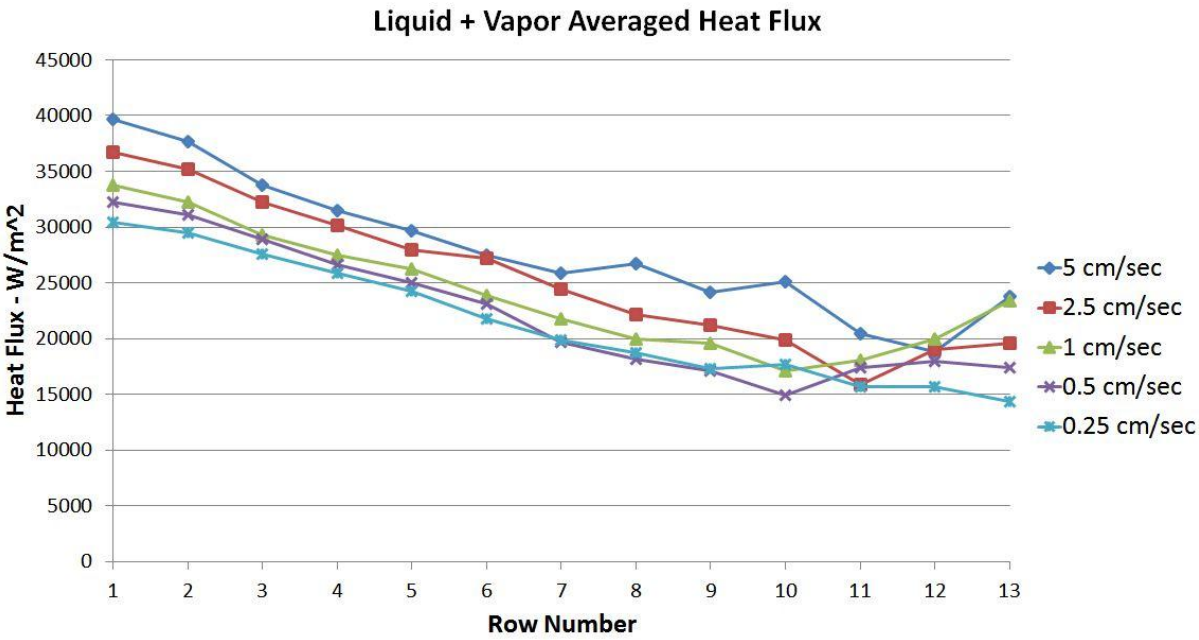

Figure 102 - CFD predicted averaged values of heat flux transferred to liquid and vapor phases at each tube row

e) Pressure at the monitoring planes

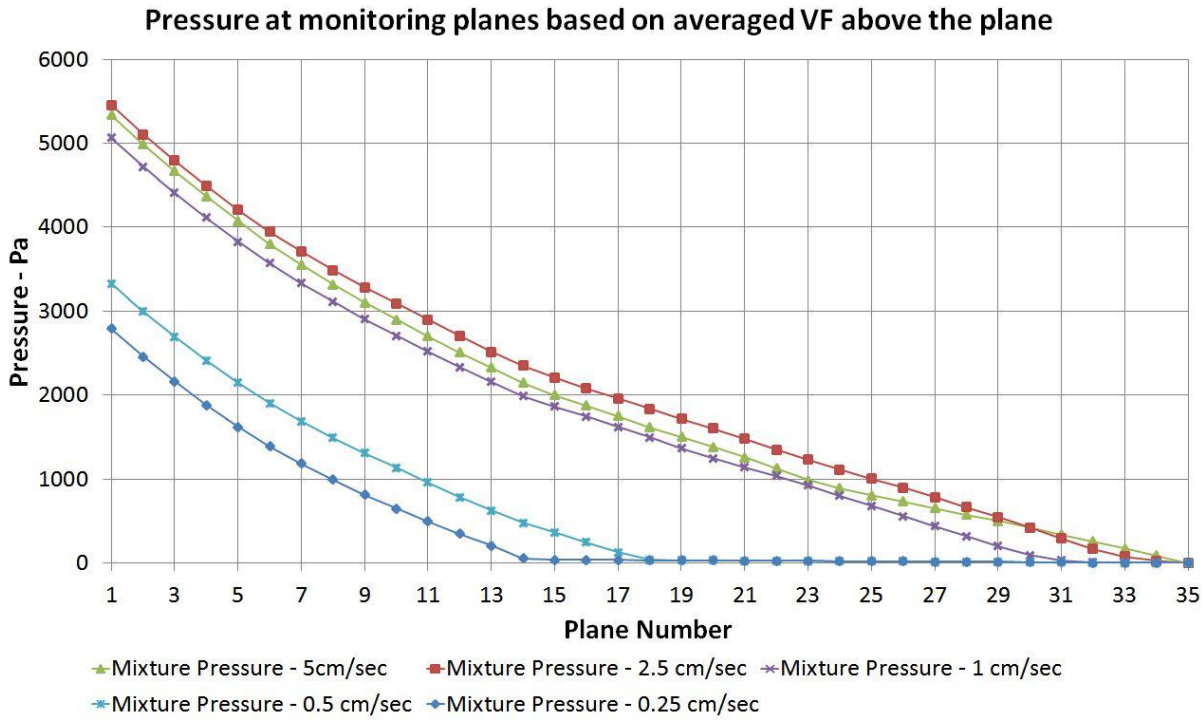

Figure 103 - CFD predicted values of mixture pressure (calculated from vapor volume fraction values obtained) at each monitoring plane

f) Vapor volume fraction at the monitoring planes

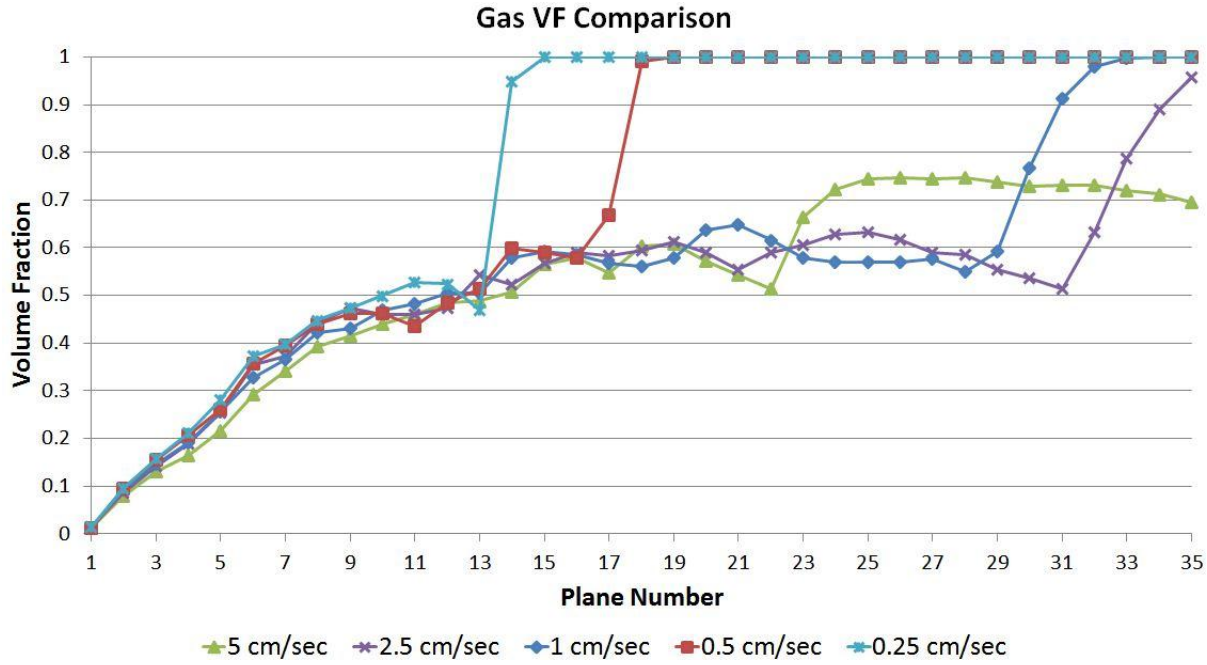

Figure 104- CFD predicted values of vapor volume fraction at each monitoring plane

g) Vapor wall heat transfer coefficient averaged on each tube row

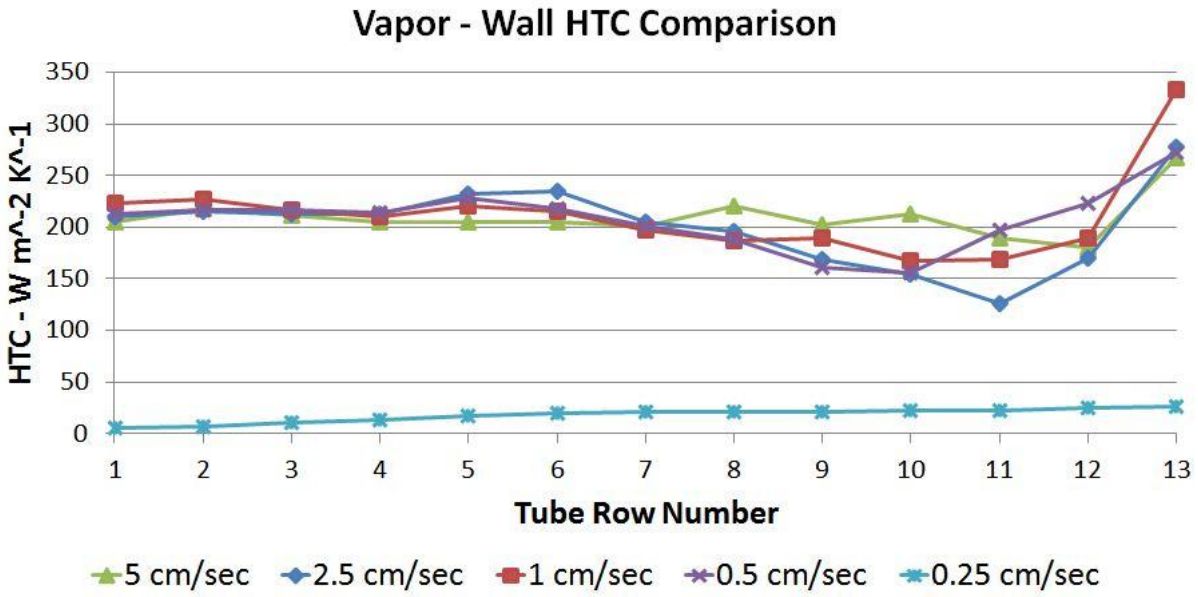

Figure 105 - CFD predicted values of liquid phase wall heat transfer coefficient at each tube row

h) Liquid wall heat transfer coefficient averaged on each tube row

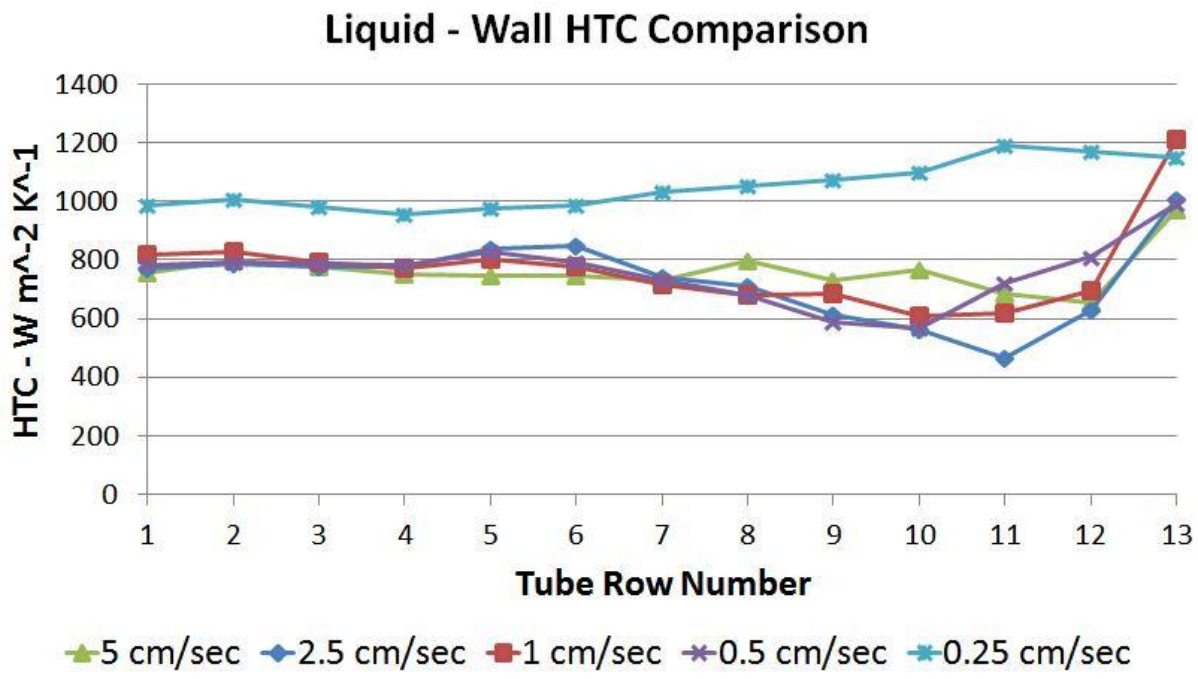

Figure 106 - CFD predicted values of vapor phase wall heat transfer coefficient at each tube row

i) Vapor phase volume fraction contours

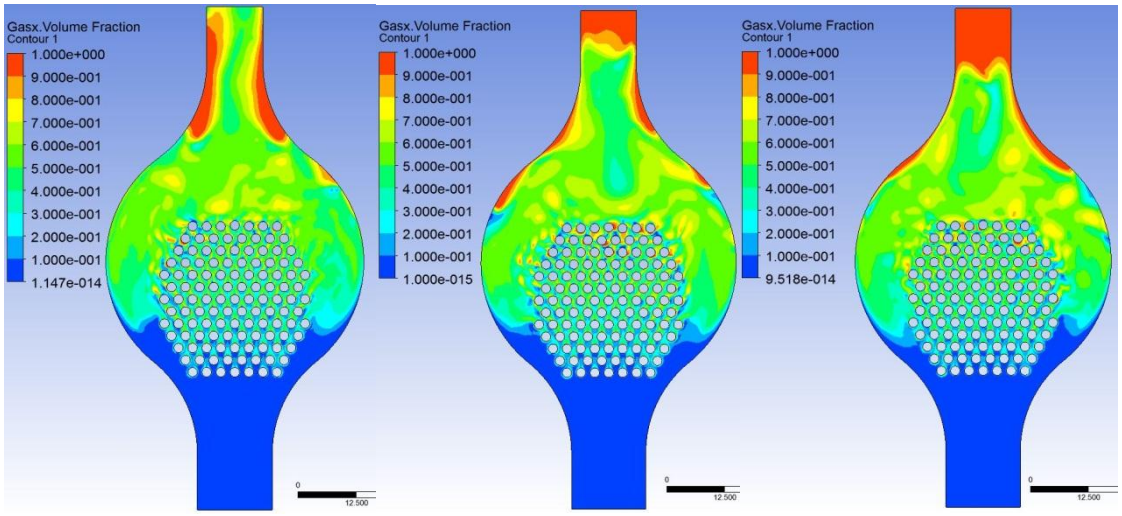

Figure 107 - Vapor volume fraction - a) 5 cm/sec inflow, b) 2.5 cm/sec inflow, c) 1 cm/sec

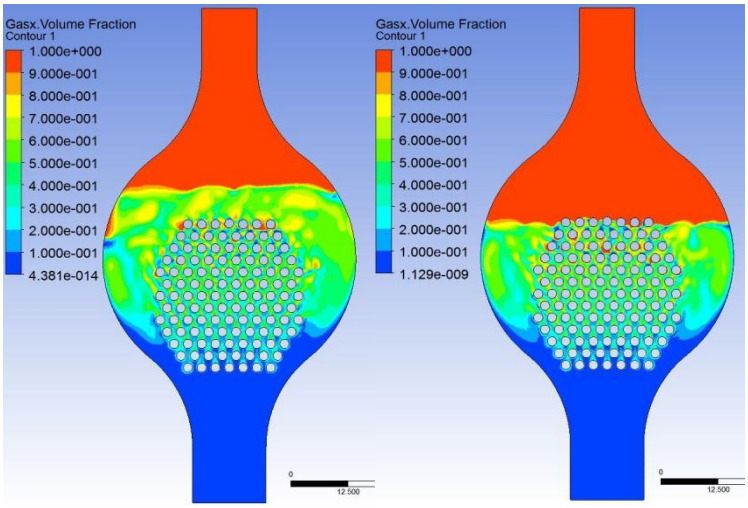

Figure 108 - Vapor volume fraction - a) 0.5 cm/sec inflow, b) 0.25 cm/sec inflow

Discussion

A parametric study of the STHE slice geometry has been carried out to observe the impact of vaporizing fluid's inflow rate on the heat transfer performance and vapor generation in the heat exchanger. An understanding of this relationship is crucial for economical and safe operation of a power plant. There are two types of power plants w.r.t. operation on working fluid after the vaporizer units. Some power plants have a superheating unit after the vaporizer unit whereas others use the vaporizer units themselves to generate sufficient superheat. In case of power plants using superheaters, the management of working fluid's inflow rate a matter of achieving maximum efficiency for the power plant. On the other hand, in case of

power plants with turbine units attached directly to the vaporizer units, the management of working fluid's inflow rate is matter of safety primarily as no liquid droplets can be allowed to reach the turbine units for safety of the turbine unit. The working fluid flow rate directly translates into the heat duty of the vaporizer unit and hence the power generation out of the power plant. So, the proper management of working fluid flow rate through the vaporizer unit is a matter of economic importance in all cases and a matter of safe operation as well in some of them.

Observations from parametric study:

- The volume fraction generation within the tube bundle is almost similar for all the inflow rates and the actual separation of phases actually happens after the tube row, except for the lowest flow rate tested, viz. 0.25 cm/sec, where the top tube rows become exposed fully to vapor phase.
- The volume fraction data at flow rates of 5cm/sec and 2.5 cm/sec presents a different trend from all other data points. It was expected to see a constant increase in vapor volume fraction as the flow rate is reduced. This holds true for all 5 flowrates if we consider the vapor volume fraction only at the outlet. However, if we look at the vapor volume fraction data throughout the height of the tube bundle, then we observe that the vapor volume fraction is actually higher for 5 cm/sec flowrate when compared to 2.5 cm/sec flowrate for a significant part of the vaporizer height. The pressure, based on volume fraction data, shows a similar trend in being less for 5 cm/sec as compared to 2.5 cm/sec except right at the outlet. This may be explained by the flow velocities, as a higher inflow rate of 5 cm/sec will probably be able to carry the generated vapor alongwith it to some extent until the vapor volume fraction becomes too high. This makes sense if we look at the pattern of vapor volume fraction for 5 cm/sec and 2.5 cm/sec inflow rates as the 2.5 cm/sec flow rate may not be high enough to carry the vapor through as 5 cm/sec inflow rate is able to do. There might be a transition sort of region between these flow rates. It is an interesting observation for another reason that these flow rates were arbitrarily selected.With regards to heat flux and HTC data, we see that the values of HTC are almost similar for all the flow rates, except 0.25 cm/sec, which corresponds to similar values of vapor volume fraction within the tube bank and it is known that ANSYS™ CFX-Solver™ calculates HTC values based on the distribution of heat flux from heated surface and this heat flux partitioning depends on the area fractions on heated surface under the influence

of liquid and vapor phases. The values of heat flux being transferred to both phases shows that heat flux transferred to vapor phase is similar in all cases while the liquid heat flux shows a constant decrease with decreasing inflow rate. The overall heat flux transferred decreased with decreasing mass flow rate which confirms the real world observation of heat duty decrease with decreasing mass flow rate for working fluid. The unexpected HTC values for lowest inflow rate, 0.25 cm/sec, are perplexing as the liquid HTC is seen to be marginally higher than all other cases while the vapor HTC is significantly lower than all other cases. This needs to be investigated further.

This has been seen in the results of CFD simulation that the chances of liquid entrainment in the vapor outflow from the vaporizer unit decrease with reducing mass flow rate along with a decrease in the heat flux being taken out of the heated surface in case of CFD simulations and geothermal brine in real world operation. The decrease in chances of liquid entrainment are also expected considering the physics of drag law and vapor velocity. Higher inflow rates mean that they can keep the vapor entrained even at high vapor volume fractions whereas for low inflow rates, the buoyancy of vapor phase is strong enough that it is able to separate from the liquid phase much earlier and at lower vapor volume fractions

There is a need for experiments to be performed on boiling process on multi-tube geometries with same level and detail of measured data as is available for single-tube boiling so that the simulations performed in this chapter can be validated against experimental data as well, in addition to having a sound theoretical foundation. The process of experimentation and CFD analysis feeds into each other in a symbiotic manner and this has been the reason behind surges in product and concept developments in the recent years as computational resources decrease in cost and increase their capabilities and ease of access. The current work achieves the CFD analysis of boiling on multi-tube geometries with full dry-out on top tube row with the aim of getting researchers interested in doing experimental work with such large geometries. A preliminary design for such a lab is also presented in Chapter 8.

The generation of high vapor volume fraction in multi-tube configurations in CFD simulations presented a lot of challenges that need to be overcome for successful simulations:

- Mass imbalance – All the simulations results for which have been presented in this chapter have mass imbalances (as reported by CFX-Solver™) under 4%. These values can spike up to 100% and more if CFX-Pre™ is not set-up properly. To reduce

imbalances following steps were taken – a) activate Velocity-Pressure coupling (used with High Resolution Rhie-Chow option), b) phases are solved as Coupled

- Wall Boiling Model – To allow for high vapor generation on the heated surface, the 'Maximum Area Fraction of Bubble Influence' parameter needs to be increased to 1 from its default value of 0.5. To enable heating of vapor phase as well, beta feature of 'Vapor Convective Heat Transfer' needs to be activated
- A custom CEL for blending the drag law needs to be used in case of conditions similar to current case – liquid phase reduces from inlet volume fraction of 1 to 0 at outlet and the reverse happens for vapor phase

Constraints on the CFD set-up used:

- Thermophysical properties were defined with constant values. In the future work, these will be made temperature- or pressure- dependent.
- The blended drag CEL uses values of vapor bubble and liquid droplet sizes to calculate drag forces. These values need to be made variable in future simulations. Also, there is experimental data available for R113 vapor bubble sizes that can be used to make the vapor bubble size definition based on real world data. The liquid droplet size needs to be based on some data (experimental) or some correlation(s) suitable as per the simulation's operating conditions.
- Resolution of the issue of ANSYS™ CFX™ Solver™ crash when the top tube row is exposed to vapor

Special note of CFD analysis of Case 5 with exposed top tube rows

In this case, a special approach is required with ANSYS™ CFX™ otherwise the solver ends with 'FINMES' crash once the top tube row starts getting exposed to vapor phase in very high vapor fractions. It is because of the fact that the Wall Boiling Model built into the Solver divides the heat flux coming from the heated surface into 3 components – liquid convection heat flux, heat flux being used as latent heat for bubble departure area and quenching heat flux under default formulations. It was learned in discussions with Dr. David Fletcher that this can be modified into a 4-way partition with the fourth component being transfer of heat flux to vapor phase. It was not included into the current scope of the project due to time constraints. But it will be included into the future work on the project to enhance the capabilities of CFD set-up. As a workaround, the wall boiling model on top tube rows was

de-activated at this stage and the simulation was continued. The steps to do so are outlined below:

1. Once the simulation crashes, start CFX™ Pre™
2. Turn Phase Change OFF on Fluid Pairs tab
3. Start the Solver and let it run for 5-10 iterations
4. Stop the Solver and start CFX™ Pre™
5. Remove the top tube rows from the Heated BC, where vapor volume fraction > 0.75, (with Wall Boiling model activated) and add as simple Heated surface with no Wall Boiling model.
6. Start the Solver™ and let it run.

In case of continuing the simulation to the stage where multiple top tube rows maybe exposed to vapor, this procedure needs to be done for each tube row individually. This issue will be looked into during future work on the project.

The current stage of the project gives us an insight into the effect of inflow rate on the vapor generation and outlet conditions from the vaporizer. The chosen inflow conditions show both the extremes of process – high liquid volume fraction at outlet at maximum inflow rate, and top tube row dryout at minimum inflow rate. This demonstrates that CFD simulations can be used to analyse and predict vaporizer performance. However, the project has opened up an equal number of questions as it has answered. The unexpected behavior of volume fraction data at 5 cm/sec may have been reasonably explained above as the liquid velocity does influence the amount of vapor it can keep entrained. The strange behavior of HTC at 0.25 cm/sec inflow rate begs further investigation. At the current stage, the work should give confidence to plant managers that CFD approach can prove to be an effective approach towards vaporizer analysis if experiments are conducted to validate and fine tune the presented approach.

6.0 Droplet Carryover Analysis

This chapter focuses on analysing the fate of a droplet that gets ejected out of the boiling froth in a kettle vaporizer. Droplet carryover from the vaporizer is undesirable whether a superheater is installed post vaporizer or not. To prevent droplet carryover, demisters are used in plant installations. Demisters prevent droplet carryover at the cost of pressure drop and hence capital costs for higher capacity pumping units and more drain on the power generation from the plant. In case of no superheater post the vaporizer unit, droplet carryover poses a serious threat to the overall life and efficiency of the turbine unit. In case of plants with superheaters droplet carryover may not present a physical danger to the plant components but the plant operators need to maintain a low inflow rate into the vaporizer unit to ensure high vapor quality which reduces the power generation from the plant.

This makes it desirable to understand the probability of droplets being carried out of a vaporizer unit. The fate of any droplet being ejected out of the froth can be one of the following – a) it is so large that gravity forces it to fall back, b) it is light enough that the buoyancy carries it out of the vaporizer unit. At all times after the droplet is ejected from the broth, it is constantly losing mass to the vapor medium around it. This can result into a scenario where a droplet is falling back and during the fall it loses enough mass that the buoyancy forces can now carry it out of the vaporizer. An alternative scenario could be when the droplet undergoes complete vaporization.

There are presented here two approaches to understand the fate of a droplet – a) MATLAB™ approach is used to track droplets without any mass transfer to vapor medium (no evaporation) based on the droplet injection velocity and velocity of the surrounding vapor phase, and b) ANSYS™ CFX™ has been used to test the worst case scenario – where a droplet is ejected right underneath an outlet from the vaporizer with the vapor velocity coinciding to be upwards and parallel to the path of the droplet.

The droplet trajectory calculating MATLAB™ code being used in this chapter was developed by Dr. Natalia Kabaliuk (Post-doctorate Fellow, University of Canterbury, Christchurch, NZ).

The aim of this chapter is similar to a proof of concept and shows two different approaches towards resolving the fate of a droplet ejected into the vapor space of a vaporizer. The ANSYS™ CFX™ approach is used here because of current incapability of MATLAB™ code to predict droplet vaporization. In future work, this capability will be included in the code and thus creating a single point solution towards predicting the droplet trajectory in a vaporizer.

6.1 MATLAB™ approach to droplet trajectory prediction

Steps in the MATLAB™ data processing:

- **Extraction of CFD-Post™ data**

The vapor velocity field data is extracted from CFD-Post™ once the simulation is complete. The data is extracted by defining a region in CFD-Post™. This region can be defined as a spherical region or all of the region above a particular plane can be extracted Figure 109. For the current study the spherical region based data has been used.

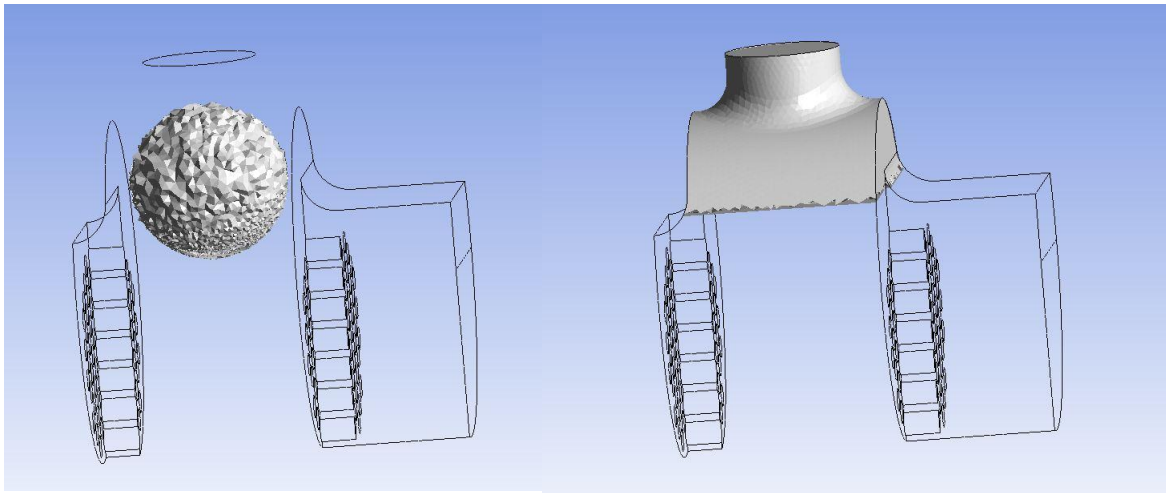

Figure 109 - Region for CFD-Post™ data extraction

- **Domain displacement**

The CFD-Post™ data has both –ve and +ve coordinates but the MATLAB™ code being used is currently meant to be used with all positive coordinates. The domain is transposed to all positive coordinates to comply with this constraint of the code Figure 110.

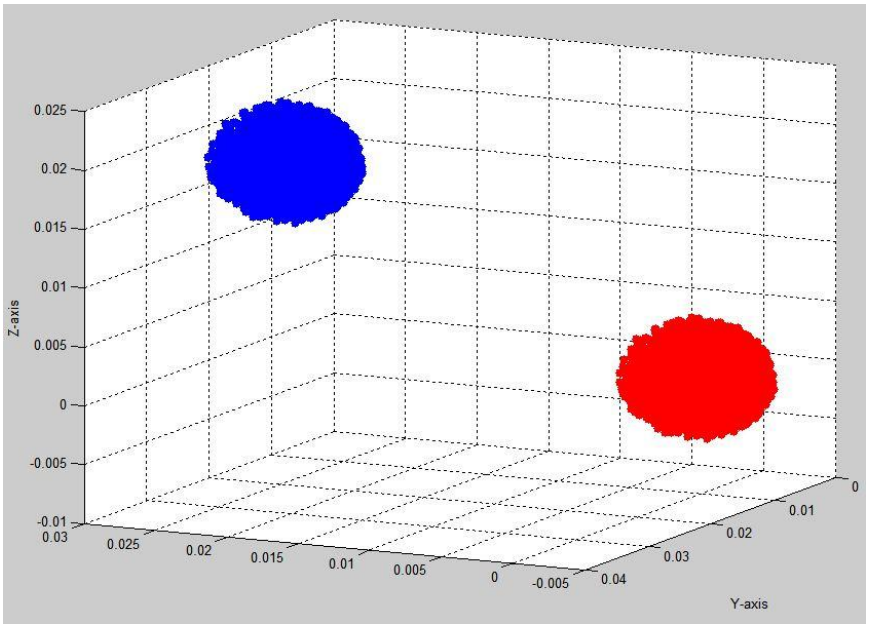

Figure 110 - Domain displacement to all positive coordinates[Red-original, Blue-displaced]

- **MATLAB™ code execution**

The original MATLAB™ code was developed to work with a uniform medium (vapor phase) velocity condition specified at the start. The current MATLAB™ code can be used with both constant and variable conditions for the surrounding vapor field due to constant updating of vapor field's velocity components at each iteration. For variable values of vapor velocity field, the code compares the X, Y & Z coordinates predicted for the droplet to the CFD-Post™ data and provides the required velocity values for the vapor phase at the required coordinates.

The MATLAB™ code uses the Taylor Analogy Break-up model [109] for predicting particle breakup.

Overview of TAB Model [102, 109]:

The TAB model views an oscillating and distorting drop as a spring-mass system and the deformation of the droplet is represented as a one-dimensional harmonic oscillation under the deforming aerodynamic force, restoring surface tension force and damping viscous force [102]. The deformation is calculated as dimensionless distortion:

$$y = \frac{2\Delta d_{min}}{d_o/_2} \qquad 141$$

Δd_{min} describes the deviation of the minor drop diameter (or the one parallel to the direction of the flow or drop relative velocity) from its undisturbed value d_o.

The equation of motion for deformation is:

$$\frac{d^2y}{dt^2} + \frac{4C_d\mu}{\rho d^2}\frac{dy}{dt} + \frac{8C_k\sigma}{\rho d^3}y = \frac{4C_f\rho_a v^2{}_{rel}}{C_b\rho d^2} \quad 142$$

The solution is:

$$y(t) = We_C + e^{-1/t_D}\left\{(y_0 - We_C)\cos\omega t + \frac{1}{\omega}\left(\frac{dy_0}{dt} + \frac{y_0 - We_C}{t_D}\right)\sin\omega t\right\} \quad 143$$

$$where, \qquad We_C = We\frac{C_f}{C_kC_b};\ We = \frac{\rho_a v^2{}_{rel}d}{2\sigma};\ \omega = \sqrt{\frac{8C_k\sigma}{\rho d^3} - \left(\frac{1}{t_D}\right)^2};\ t_D = \frac{\rho d^2}{2C_d\mu}$$

We is the Weber number, ω is a natural frequency of drop oscillations and t_D is the damping time. C_b, C_d, C_f, C_k are model parameters. $C_b = 1/2$ is the scaling coefficient for deforming force non-dimensionalization. $C_d = 5$ is the dynamic coefficient. $C_k = 8$ is the restoring force coefficient and C_f is the aerodynamic force coefficient.

- **CFD-Post™ data analysis**

The CFD post data extracted has a very small volume with diameter = 10 cm as very small geometries are tested in this project. With this small a size, the droplet exits the domain within few iterations. A run with actual CFD-Post™ data is shown in Figure 111.

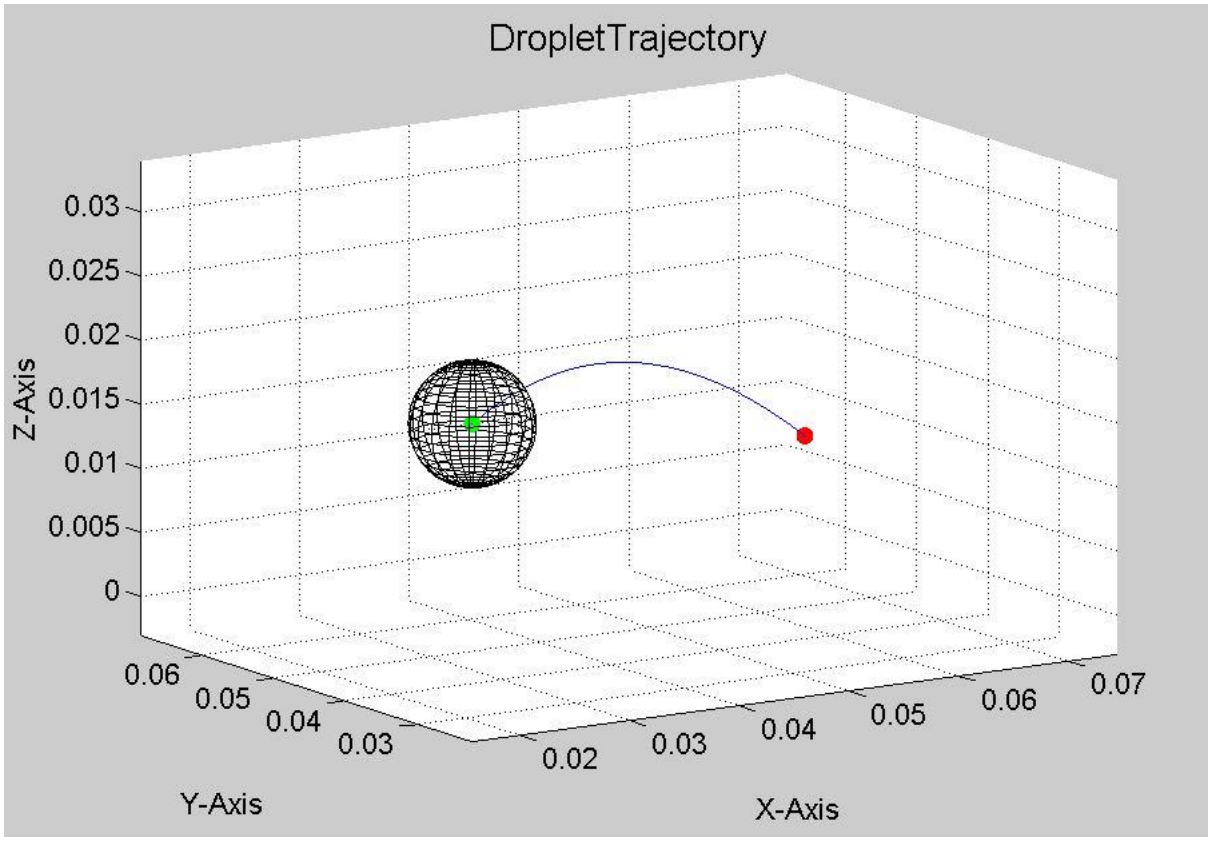

Figure 111 - Droplet trajectory based on actual CFD-Post™ data

- **Using random data as a demonstration for the MATLAB™ code**

Keeping in view the small volume of CFD-Post™ extracted data, a larger spherical (3 meter radius) domain is filled with randomly generated velocity values [-5 m/s to +5 m/s] and the MATLAB™ code is run with this as the vapor velocity field. The droplet is injected at 1.5 m/s velocity at 30^o, 60^o and 30^o angles w.r.t. X, Y and Z axes respectively at the centre of the domain. The droplet trajectory is calculated for a 1.5 second time period.

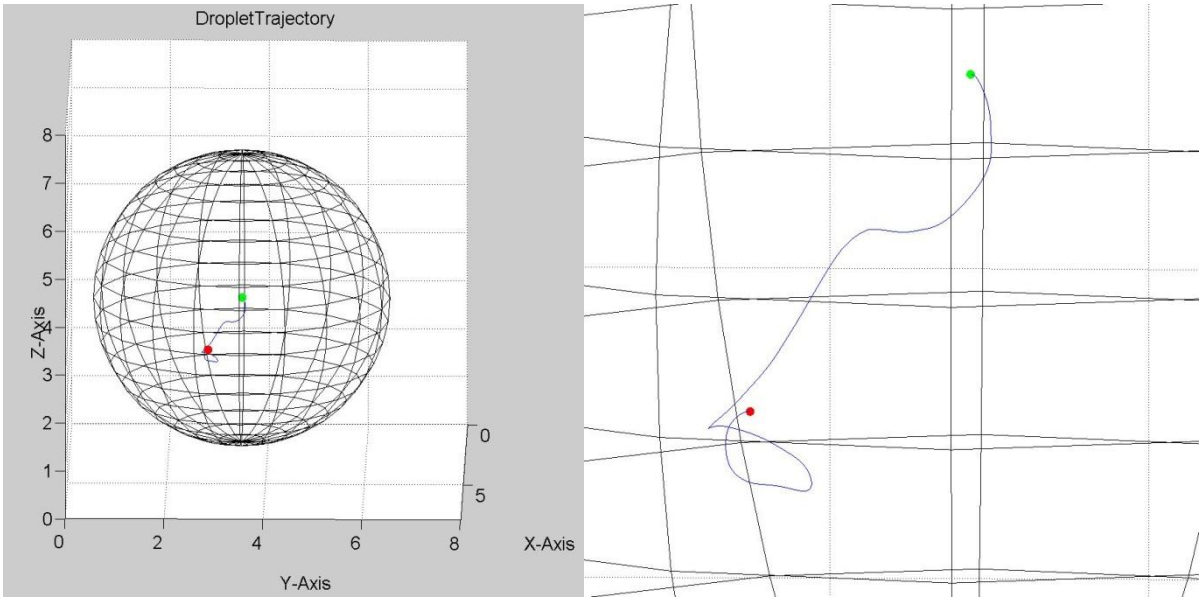

Figure 112 - Droplet trajectory based on variable medium velocity (randomly generated); GREEN DOT -> starting point, RED DOT-> end point

6.2 ANSYS™ CFX™ approach to droplet vaporization

In ANSYS™ CFX™, particle transport modeling is a type of multi-phase simulation that applies Lagrangian approach to tracking the particulates rather than particles being modeled as an extra Eulerian phase. In case a large number of particles are defined, i.e. heavy particulate load, the full particulate phase is modeled by just a sample of individual particles. The tracking is carried out by forming a set of ordinary differential equations in time for each particle consisting of equations for position, velocity, temperature and masses of species [5]. In the simulations carried for this project, one-way coupling is used, i.e. particles feel the influence of the medium but medium is not affected by the particles. It was deemed sufficient for the current study as the particulate load is not heavy for the real world conditions and the main goal of current study is to observe what size droplets can be carried out of the domain and what size droplets either fall back due to gravity or are fully vaporized. ANSYS™ CFX™ has a Liquid Evaporation Model built into the Solver which is used for particles with heat and mass transfer. It is implemented for the current study. The droplets have been analysed with particle break-up activated and de-activated. For cases where the particle break-up is active, the Taylor Analogy Breakup (TAB) model has been chosen out of available options as it has been extensively validated against experimental data. It is observed in the simulations' results that the activation or de-activation of particle break-up has a significant impact on the final results.

The domain has been defined as a 4 m long rectangular tube with structured fully hexahedral meshing having 160,000 elements. Steady state analysis is carried out using $k - \varepsilon$ scalable model. Velocity-pressure coupling was not activated for the model.

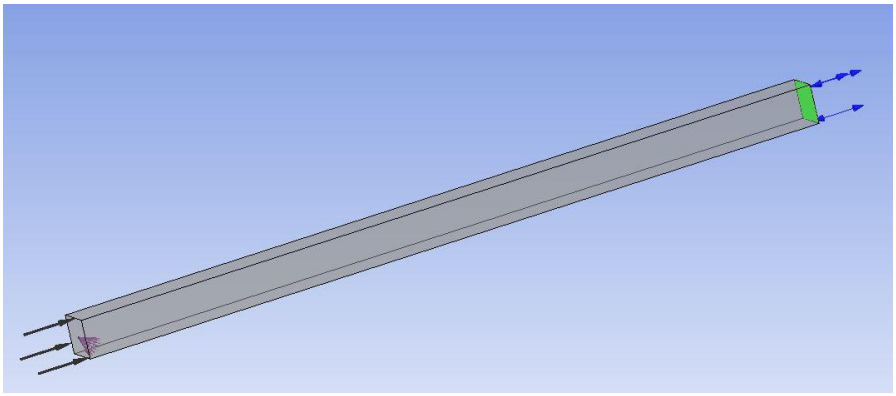

Figure 113 - Domain used for CFD simulation of droplet vaporization

The operating conditions are – a) 20 bar pressure, b) pentane material properties at the operating pressure, c) droplet is injected at 3 degrees of subcooling, and d) vapor phase is at saturation temperature. The vapor field is defined as having velocity in vertically upward direction equal to 0.5 m/s while the droplet is injected to directional orientations at a velocity of 0.1 m/s. The conditions are defined so as the goal of droplet vaporization analysis in ANSYS™ CFX™ is to simulate worst possible scenario i.e. a droplet most likely to survive to enter the superheater, where a droplet is ejected into the vapor space directly below an outlet with vapor velocity field pushing it upwards as well. The two directional orientations of injection for the droplet:

a) Vertical injection
b) Angular injection

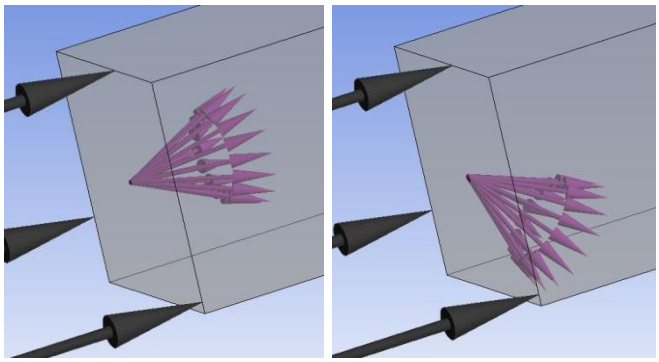

Figure 114 - Different directional orientations of droplet injection

TAB MODEL ON

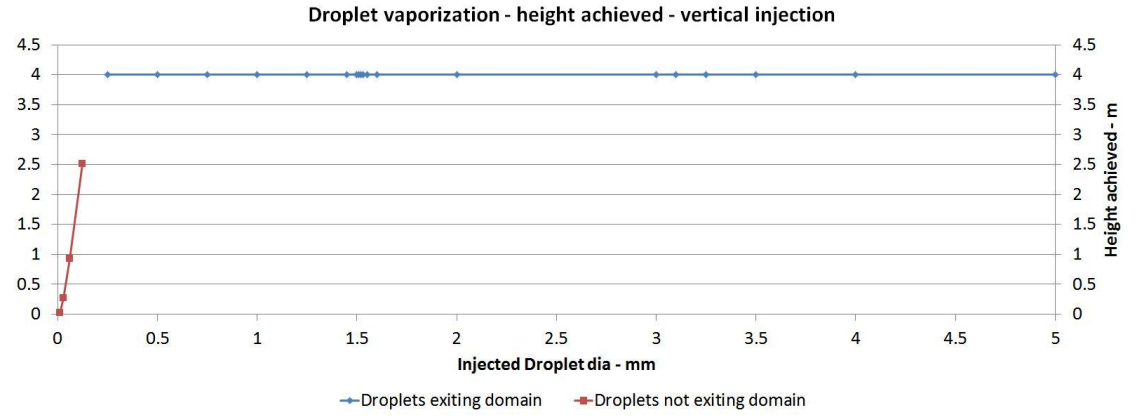

Figure 115 - Maximum height achieved by droplets

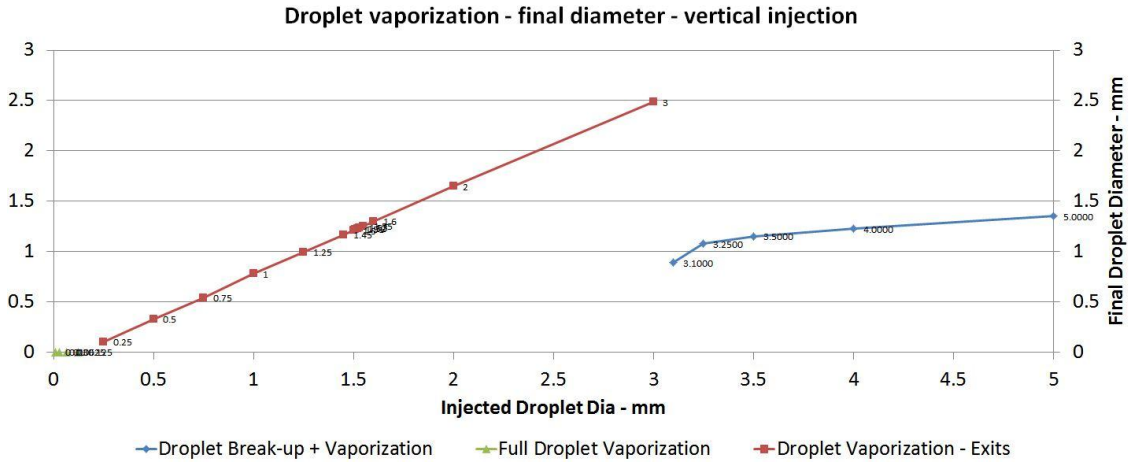

Figure 116 - Final diameter of droplets

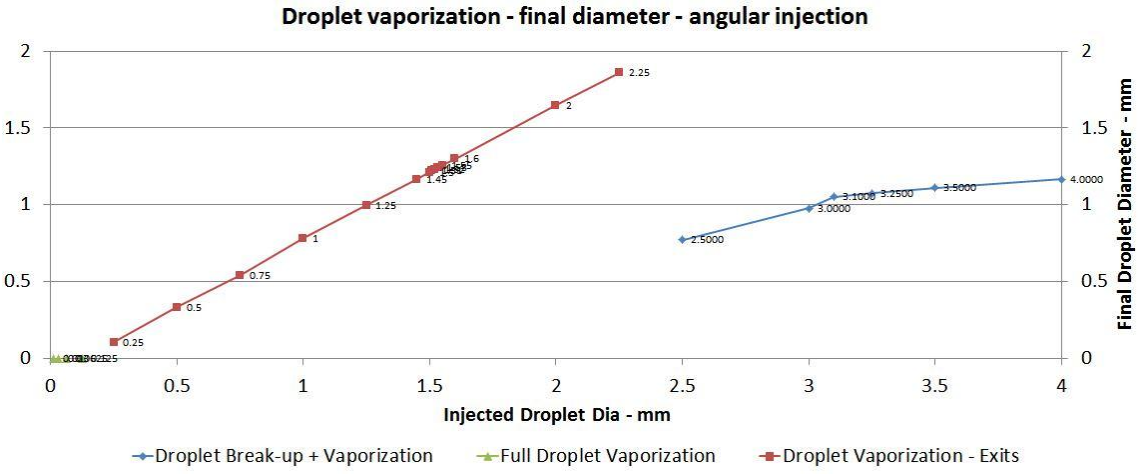

Figure 117 - Final diameter of droplets

Figure 115 shows that all the droplets larger than 0.125 mm are able to cross the entire domain of length 4m. Droplets of size 0.0625 mm survive up to a height of 92.4 cm. Such a form of data is useful in design/selection of demister as discussed at the end of the chapter.

Figure 116 & Figure 117 show the final diameters for injected droplets (in vertical and angular orientations respectively). In case of vertical droplet injection, we see that droplets larger than 3 mm suffer breakup while in case of angular injection of droplets, drops bigger than 2.5 mm suffer breakup. Such a data is useful in knowing the droplet sizes that might exist at different heights from the droplet ejection point. It is beneficial in design/selection of demisters for vaporizers once the distance from vapor space (region above tube bank in a vaporizer) to demister is known as we will have a better of idea droplet sizes that the demister needs to stop while overdesign can be prevented. Overdesign of demister here means that it has been designed to stop droplets smaller than minimum diameter that can reach the demister. Prevention of such overdesign will reduce unnecessary pressure losses in the system.

ANSYS™ CFX™ does not provide data of all the droplets post break-up, but evidence of break-up is clear from the main particle track available in CFD-Post™. The droplets that undergo break-up show a drastic reduction in diameter just after injection whereas the droplets that do not break-up and lose mass only because of vaporization show a steady gradual reduction in diameter.

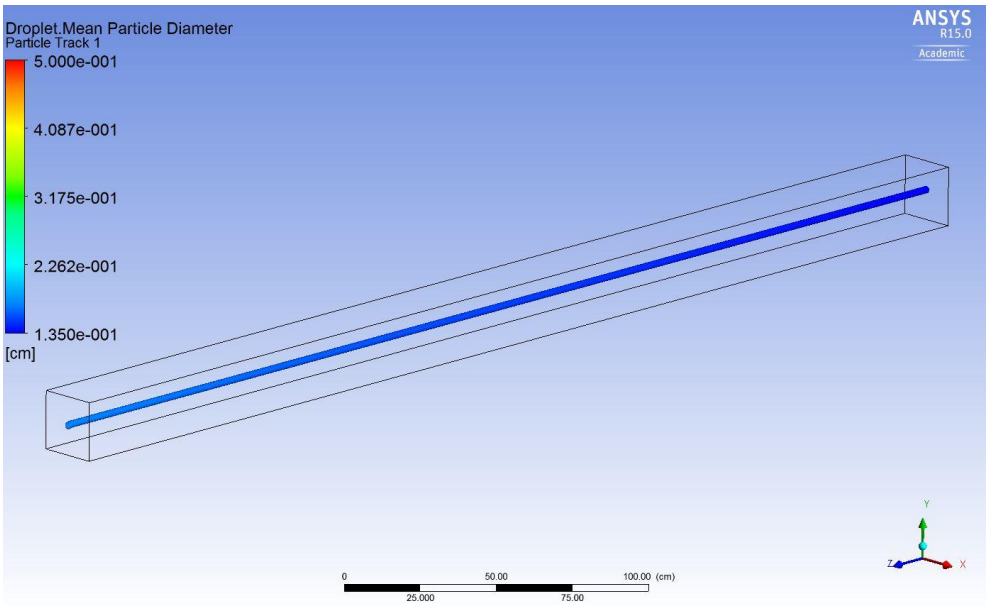

Figure 118 - Droplet suffering break-up - 5mm diameter at injection

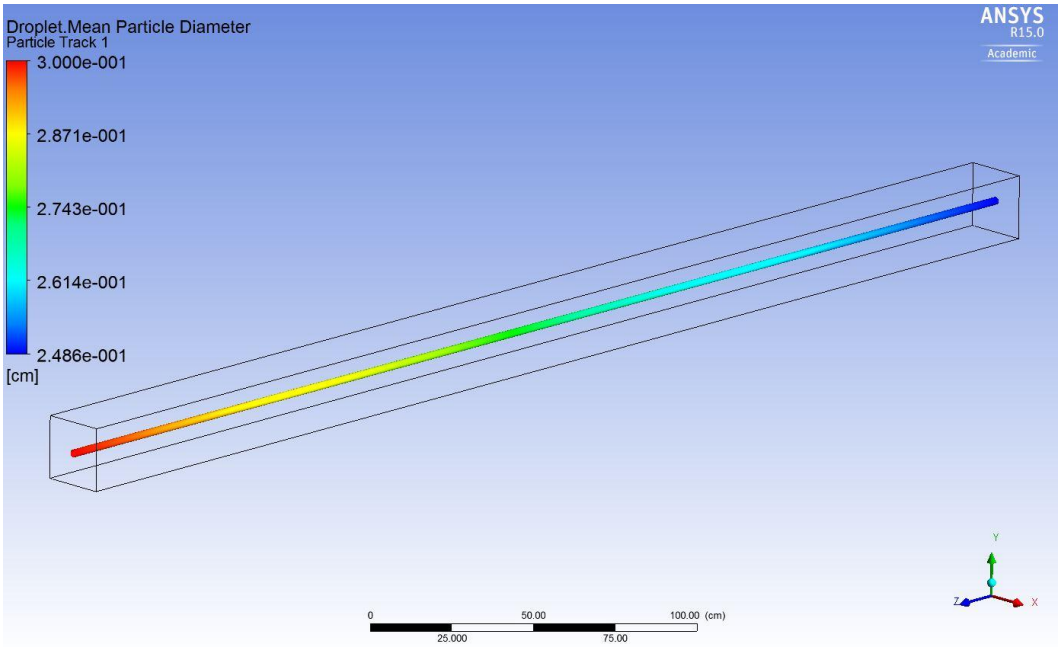

Figure 119 - Droplet losing mass only because of vaporization - 3mm diameter at injection

If the distance between tube banks in the vaporizer and the top of the outlet is assumed to be 1 meter, than droplets of diameter above 0.0625 mm or 62.5 micron will survive the distance if the conditions are similar to the ones used in the simulation.

TAB MODEL OFF

With the particle break-up de-activated, it is noticed that droplets that fall back are much smaller than the droplets that break-up and continue to be pushed upwards when the TAB model is activated. This was expected to be observed. In case of droplets that undergo full vaporization, no change is seen when compared to the case with TAB model activated which is because of the fact that droplets that undergo full vaporization were small enough to not suffer break-up.

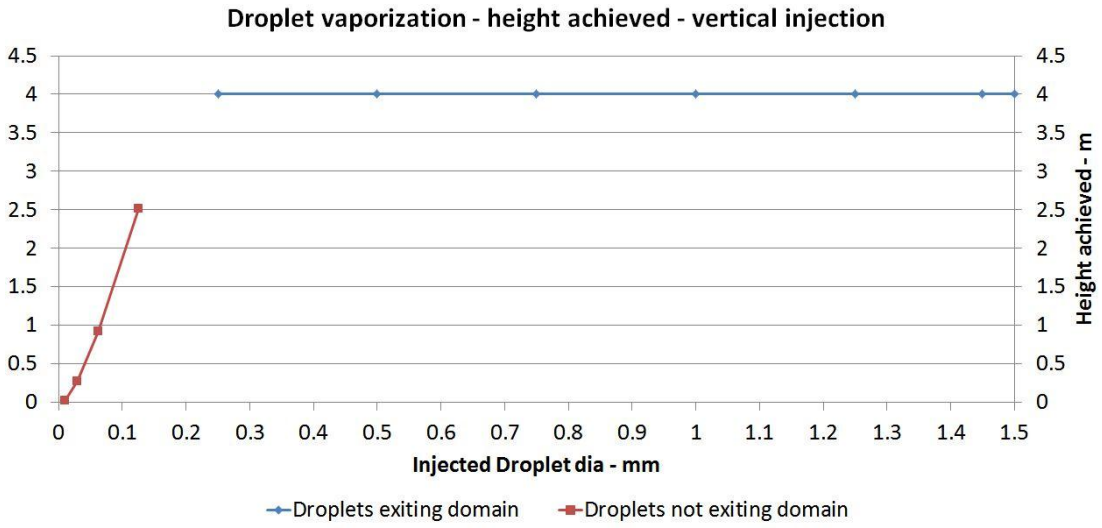

Figure 120 - Maximum height achieved by droplets

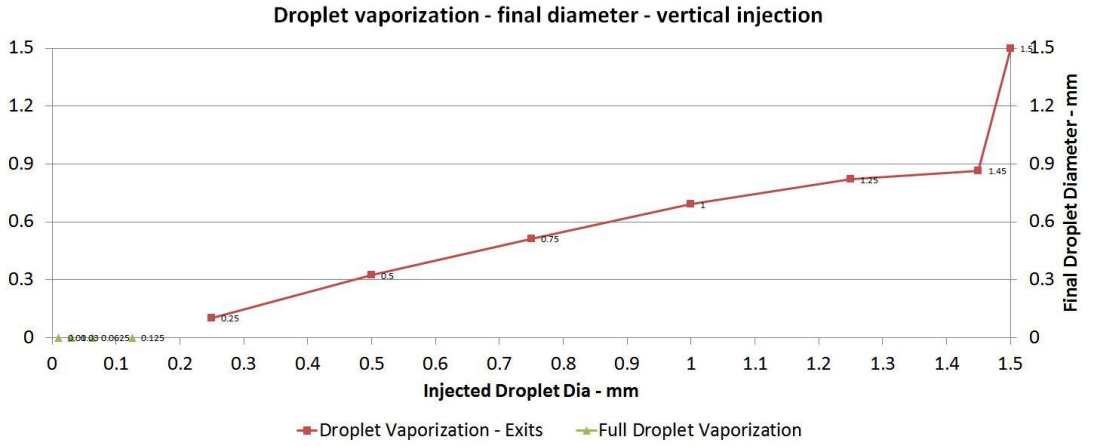

Figure 121 - Final diameter of droplets

Discussion

The ANSYS™ CFX™ simulations carried out to predict droplet diameters that can be carried out of the domain under worst case scenarios are beneficial in knowing the smallest size droplets that can be carried out of the domain, but do not directly tie into the results extracted from CFD analysis of a heat exchanger unlike the MATLAB™ code which uses the CFD-Post™ data directly to predict droplet trajectory. This will be remedied in the future work by making MATLAB™ code capable of calculating loss in mass and diameter of droplet while simultaneously calculating its trajectory. One major constraint is the lack of an atomization model for prediction of droplet sizes that can be ejected from the boiling froth into the vapor space above it. There are available atomization models for jet break-up developed for fuel injection studies but none was found for pool boiling conditions.

The current study using ANSYS™ CFX™ although does not tie directly into the CFD-Post™ data but it provides as useful information about the sizes of droplets that can be carried through. Most of the vaporizer applications use demisters post the vaporizer to eliminate droplet carryover. Demisters are designed to block droplets above a particular size. Demisters are a significant contributor to pressure loss. Such a study, as has been carried out using ANSYS™ CFX™ in this chapter can provide advantages to proper demister design/selection so that they are not causing unnecessary pressure loss due to their design to stop droplets smaller than a size, which cannot survive the distance from vapor space in vaporizer to demister assembly on account of having been completely vaporized

7.0 Conclusion

The current project started with an overarching goal of understanding the boiling process inside a kettle vaporizer with the aim of troubleshooting currently installed units while providing a foundational knowledge base that could be extended in scope to design optimization and even to developing novel heat exchangers. It was later extended to include the CFD analysis of single-phase PHEs, STHEs and helical baffled CMSP-STHEs as well, to demonstrate CFD-based approach as a comprehensive methodology towards the field of HE analysis and troubleshooting. The envisioned scope of the project included conducting a CFD simulation of a full scale pentane vaporizer but the time constraints have limited the scope of the project. The project completes the following tasks:

- A MATLAB™ code for PHEs has been developed and validated against experimental data
- A MATLAB™ code for vaporizer analysis has been developed that can predict thermodynamic conditions of the working fluid at every tube row and validated against real world data from two NZ geothermal power plants
- CFD simulation for single-phase heat exchangers has been completed with validation for STHEs and as a proof-of-concept for PHEs and helical baffled CMSP-STHEs
- CFD simulation for phase-change in single-tube and multi-tube configurations has been completed with validation
- Selection of substitute fluid considering absence of pentane boiling data in multi-tube configurations has been completed
- A preliminary CFD analysis on a geometry representative of full scale vaporizer's repeating structural unit has been performed
- A parametric study of STHE slice geometry with 121 tubes at 5 different inflow rates has been performed
- A MATLAB™ code capable of predicting a droplet's trajectory inside vapor field extracted from CFD-Post™ has been developed albeit vaporization is not factored into the code currently
- Droplet vaporization has been simulated using Lagrangian approach for particle tracking in ANSYS™ CFX™

In conclusion, it can be said that the foundational set-up work of finalizing and validating an approach towards CFD simulation of a full scale vaporizer unit has been completed in this project while a comprehensive CFD-based approach has been presented with validations wherever data was available. The future work for the current project can be classified as – a) requiring computational time with CFD set-up already available – simulation of 3D geometry and mesh dependence studies do not require any new knowledge development but only need more time and HPC facilities, and b) mitigation of constraints with the CFD set-up and MATLAB™ code being used for droplet trajectory calculation.

With regards to assumptions and constraints, this project finishes with constraints on the current CFD set-ups and MATLAB™ codes rather than any major assumptions. The term 'constraint' here means resources and lack of data/knowledge (i.e. HPC hardware, time and new models (present in literature) required to be integrated into current MATLAB™ models and CFD set-ups), while the term 'assumption' refers to any simplifications or physics-based assumptions made in the completed work. The removal of these constraints in future will give the methods developed in this project the capability to act as a complete knowledge base for analysing and troubleshooting heat exchangers used in various process industries whether for single-phase heating or vaporization. The details of constraints and future work that can mitigate these constraints are discussed in Chapter 8.

8.0 Future Work

The current project has been able to develop and validate an approach that forms a strong foundation for further work along the path towards a CFD analysis based troubleshooting, analysis and designing strategy for heat exchangers used in geothermal power plants or in any process industry in general. The project has narrowed down the crucial data requirements from future experiments with multi-tube boiling of hydrocarbons while validation against currently available data has been completed.

Even in absence of any experiments in near future, the current constraints of the CFD modeling approach can be mitigated to a large extent by adopting the mechanistic approaches to bubble dynamics and implementing them in ANSYS™ CFX™ using customization routines.

9.1 Regarding CFD simulations

9.1.1 CFD simulations of scaled down representative geometry

The next step is to carry out CFD analysis of scaled down representative geometry (Figure 95) including mesh dependency analysis. For this study, it is essential to have access to High Performance Computing (HPC) facilities due to the extremely large computation time on even a 16 core desktop PC. This analysis will provide us with the understanding of vapor flow patterns when the vaporizing working fluid is forced to move around the baffles as the current project has been able to analyse only simple bottom-to-top flow in a vaporizer. The understanding of these vapor flow patterns will help in understanding the similarities and differences vis-a-vis the fluid flow simulated from bottom-to-top of the tube-bank in Chapter 5. If enough computational resources are available, the representative geometry can be used with periodic BC at horizontal inlet and outlet so as to simulate the entire vaporizer unit at lowered computational cost. Such a CFD analysis has been performed preliminarily (Figure 91) with a smaller geometry and very few tubes in order to verify that the CFD set-up is working as desired.

9.1.2 Regarding inclusion of mechanistic approach towards bubble dynamics into CFD set-up for boiling simulations

One of the constraints is the empirical modeling of effect of bubble dynamics on the overall flow and heat transfer. This limitation has two components – a) currently bubble break-up

and coalescence cannot be modeled when Wall Boiling model is activated in ANSYS™ CFX™ ([4, 5]), b) It has been observed experimentally that nucleate boiling only occurs at the lowermost tube rows only and not in the upper parts of tube bank where the combined effects of forced liquid convection and sliding bubbles are sufficient to account for the transfer of heat flux out of the tubes [25]. There have been recent articles [see 2.3.5.7 Mechanistic Approach: Bubble Dynamics & Modified Wall Heat Flux Partitioning Model] that layout the mechanism of bubble sliding and its effect on the bubble dynamics and heat transfer. An important part of future work on CFD simulation of vaporizers would be to incorporate these into the model set-up as user-defined routines. It is thought that this would result in better matching of the CFD results to real-world vaporizers. Although, to test this, there is need for a test-rig to validate and tube the CFD model set-up.

9.2 Regarding multi-tube CFD simulations set-up

There are some steps required to tune the CFD simulations further:

- The bubble and drop diameters in the Blended Drag CEL are fixed at the moment. This needs to be rectified in future if some experimental data is available for it, or a detailed mathematical modeling is carried out.
- The R113 has been defined as a constant property fluid. This needs to be changed so that the thermophysical properties are temperature- or pressure- dependent.
- Integration into CFD set-up and testing of mechanistic approach to bubble dynamics as discussed in 2.3.5.7 Mechanistic Approach: Bubble Dynamics & Modified Wall Heat Flux Partitioning Model.
- During dry-out of top tube rows when the in-flow rate in low enough to allow it, it was seen that the ANSYS™ CFX-Solver™ crashes. It is because of the fact that the Wall Boiling Model built into the Solver divides the heat flux coming from the heated surface into 3 components – liquid convection heat flux, heat flux being used as latent heat for bubble departure area and quenching heat flux under default formulations. It was learned in discussions with Dr. David Fletcher that this can be modified into a 4-way partition with the fourth component being transfer of heat flux to vapor phase. It was not included into the current scope of the project due to time constraints. But it will be included into the future work on the project to enhance the capabilities of CFD set-up.

9.3 Regarding MATLAB™ code used for droplet trajectory prediction

The current MATLAB™ code is unable to calculate droplet vaporization as it moves through the vapor field. Due to this limitation, the worst case scenario for droplet ejection into the vapor space in the vaporizer is simulated with ANSYS CFX™. In the future, a droplet vaporization algorithm will be integrated into the MATLAB™ code itself, so that a complete picture of droplet trajectory would be available.

9.4 Regarding future experiments -> Preliminary design of test rig

The most significant limitation during the project was the non-availability of detailed experimental data for boiling of pentane in multi-tube configuration. To overcome this limitation a preliminary design of a test-rig has been developed [see Figure 122]. It could not be realized due to financial constraints around the project.

The design of the test-rig must ensure a measurement of local heat transfer coefficient, which is possible by recording and mapping the working fluid and hot fluid temperature gradient [139]. This requires placement of thermocouples at various positions inside the HE being used for experiments. This customization of the heat exchanger is both complicated and costly and puts a restraint on the use of different heat exchanger geometries. The proposed test rig will initially have instrumentation to vary the inlet conditions in terms of temperature, pressure and mass flow rate, and to measure and record inlet and outlet conditions. Further down the line it can be upgraded so to be able to provide us with the information about the void fraction values. There are a few techniques available to measure the void fraction values: a) Gamma densitometer, b) Resistance void probe, c) Optical probe, d) Laser two phase detection and e) High speed photography.

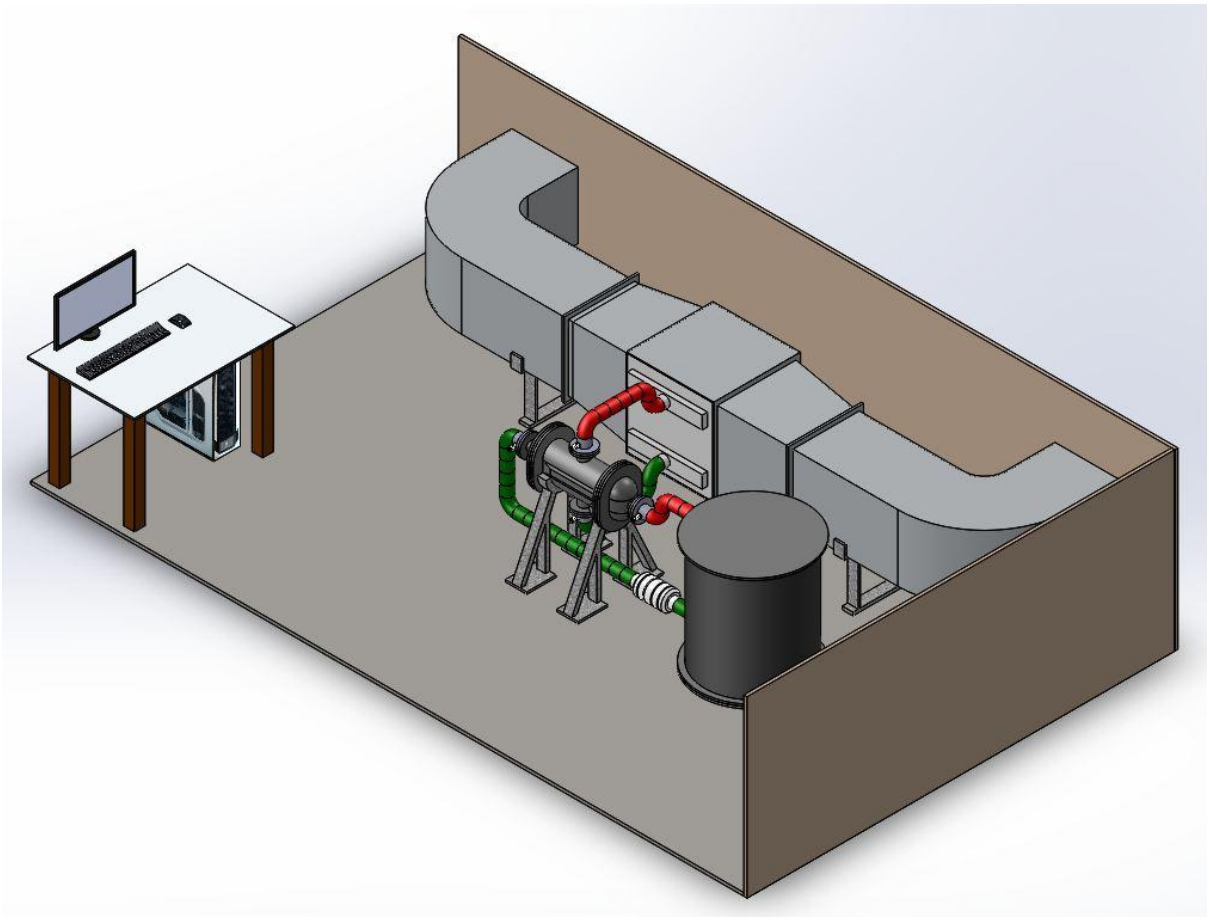

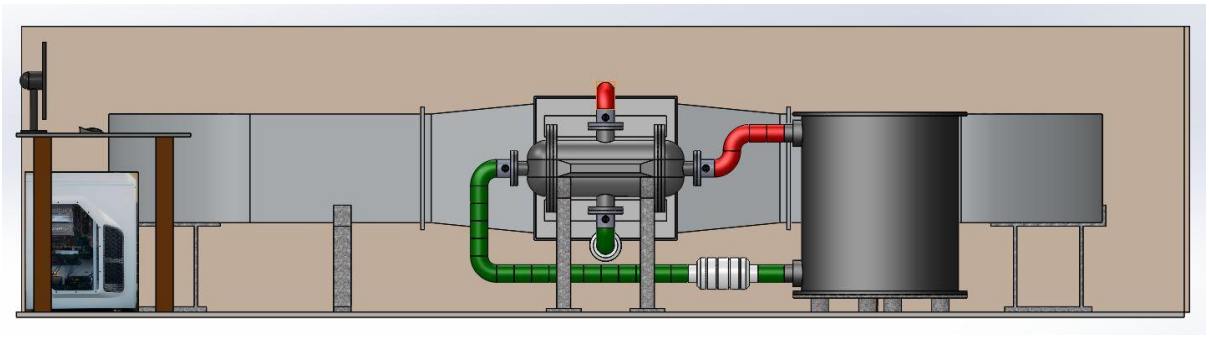

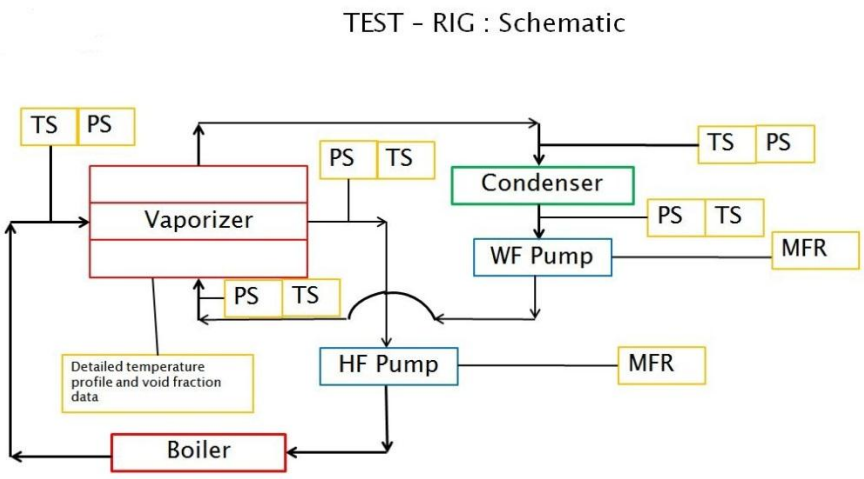

Figure 122 - Preliminary test rig design and schematic

The heat exchanger design, and FEA analysis for stress, for the test rig are shown in Figure 123.

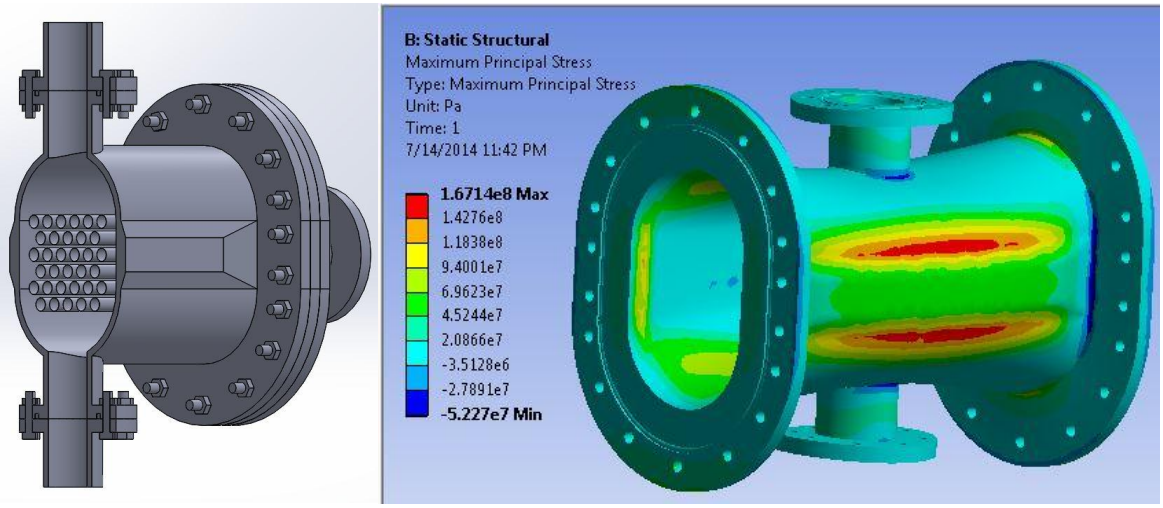

Figure 123 - Test-rig vaporizer design and pressure testing (FEA analysis) results

Appendix 1: HE Standards & Codes

The manufacturing of Heat Exchangers is subject to standards and codes that are specified by various organisations and associations, and these standards become legislation and have the force of law once they are adopted by legal and governmental authorities and incorporated into the contract.

Need for Standards and Codes:

Heat exchangers are high pressure mechanical equipment and have people working in close proximity. In the earlier days, HEs were manufactured by a lot of companies each having their own design theory, often an incomplete one. Any flaws in the design and manufacturing of the HE can cause potentially serious damage and loss of human life and so it was decided that some standards and codes must be developed that every manufacturer must adhere to be allowed to sell its product in the market that has adopted the standards and codes. In the 19th century, there were literally thousands of boiler explosions in the US and Europe, some of which resulted in a heavy toll on human life [2]. Undoubtedly, one of the most important failures that proved the need for Boiler Laws was the boiler explosion that occurred at the Grover Shoe Factory in Brockton, Massachusetts on March 10, 1905. That incident resulted in 58 deaths and 117 injuries and completely levelled the factory (Figure 124 & Figure 125 [45]). This catastrophe brought attention to the need to protect the public against such accidents with pressure-retaining equipment [2]. The standards and codes are updated from time to time to keep abreast of changing technology and also newer working conditions. The adopted standards and codes have the power of legislation behind them and are mandatory to be followed. The first Boiler and Pressure Vessel Code (B&PVC, 1914 Edition) was published in 1915.

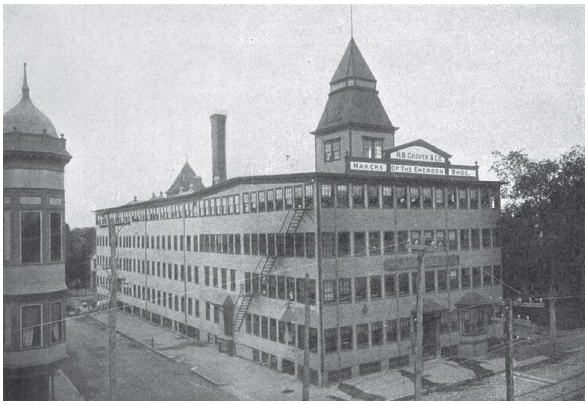

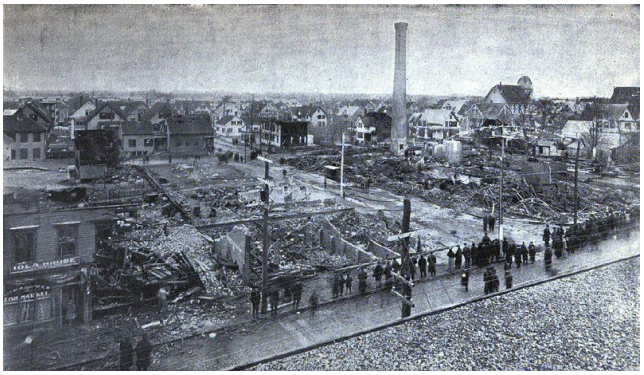

Figure 124- Grover Shoe Factory, before explosion, after explosion

Figure 125- Boiler lodged into one of the adjacent houses

STANDARDS & CODES:

- **TEMA**

It is the Tubular Exchanger Manufacturers' Association, Inc., a trade association of leading manufacturers of shell and tube heat exchangers. It covers 10 sections [143]:

1. Nomenclature (Figure 9) – the first letter describes the front header type, the second letter tells about the shell type and the third letter describes the rear header type.
2. Fabrication Tolerances
3. General Fabrication and Performance Information
4. Installation, Operation and Maintenance
5. Mechanical Standards TEMA Class RCB Heat Exchangers (Class R – for severe requirements of petroleum processing and usually most large scale processing applications, Class C – for general commercial application, Class B – for chemical process service)
6. Flow Induced Vibration

7. Thermal Relations (includes fouling and charts of the configuration correction factor on the Logarithmic Mean Temperature Difference)
8. Physical Properties of Fluids
9. General Information (e.g. dimensions of pipe, tubing, fittings and flanges, pressure-temperature ratings, conversion factors, etc.)
10. Recommended Good Practice (to extend the standard to sizes and conditions not covered by the current standards)

- **HEI**

Heat Exchange Institute, Ohio, USA is another standards development organisation. HEI Standards combine present industry standards, typical purchaser requirements, and manufacturers' experience in outlining the important design criteria for power plant heat exchangers. Topics pertinent to power plant heat exchanger include:

1. Materials of construction
2. Tube-to-tubesheet welds
3. Temperature efficiency curves
4. Typical shell requirements
5. Fouling and cleanliness factor
6. Expansion joints

Information is also provided on tube side pressure loss, cathodic protection, and SI unit tolerances, SI and MKH specification sheets, table of thermal conductivity, and heat exchanger troubleshooting guide is also included.

- **API**

American Petroleum Institute also develops standards for heat exchange equipment design, manufacture, maintenance and application. The API – 660 standards is specifically for Shell and Tube Heat Exchangers (STHEs). It caters to several aspects of STHEs [138]:

1. Guidelines for the mechanical design
2. Material selection
3. Fabrication
4. Inspection

5. Testing
6. Preparation for shipment of shell-and-tube heat exchangers for the petroleum, petrochemical and natural gas industries.

This API standard is applicable to heaters, condensers, coolers and re-boilers, but not applicable to vacuum-operated steam surface condensers and feed-water heaters.

- **ASME**

American Society of Mechanical Engineers' code is the most commonly used code for heat exchangers and is in 12 sections [8]. It is a standard written to provide rules for the design, fabrication and inspection of boilers and pressure vessels. Currently, all provinces of Canada and 49 of the 50 United States have adopted, by law, various Sections of the Boiler and Pressure Vessel Code. Furthermore, the B&PVC is international. Over 25 per cent of the companies accredited by the ASME Codes and Standards to manufacture pressure parts in accordance with various Sections of the B&PVC are located outside of the United States and Canada [2].

The code covers areas of material selection, design & construction, reference standards for design and selection of components such as flanges, nozzles, pipes, sockets etc., and also non-destructive testing and final inspection.

- **BS 5500**

It is also known as British Master Pressure Vessel Standard.

- **ISO (International Standards Organisation)**

It has many standards catering to different areas of heat exchanger manufacture, maintenance and application.

1. ISO 1129:1980 – Steel tubes for boilers, superheaters, and heat exchangers: Dimensions, tolerances and conventional masses per unit length.
2. ISO 6758:1980 – Welded steel tubes for heat exchangers
3. ISO 6759:1980 – Seamless steel tubes for heat exchangers

4. ISO 12211:2012 – Petroleum, petrochemical and natural gas industries -- Spiral plate heat exchangers
5. ISO 12212:2012 – Petroleum, petrochemical and natural gas industries -- Hairpin-type heat exchangers
6. ISO 13706:2011 – Petroleum, petrochemical and natural gas industries -- Air-cooled heat exchangers
7. ISO 15547-1:2005 – Petroleum, petrochemical and natural gas industries -- Plate-type heat exchangers -- Part 1: Plate-and-frame heat exchangers
8. ISO 15547-2:2005 – Petroleum, petrochemical and natural gas industries -- Plate-type heat exchangers -- Part 2: Brazed aluminium plate-fin heat exchangers
9. ISO 16528-1:2007 – Boilers and pressure vessels -- Part 1: Performance requirements
10. ISO 16528-2:2007 – Boilers and pressure vessels -- Part 2: Procedures for fulfilling the requirements of ISO 16528-1
11. ISO/CD 16812 – 4Petroleum, petrochemical and natural gas industries -- Shell-and-tube heat exchangers
12. ISO 16812:2007 – Petroleum, petrochemical and natural gas industries -- Shell-and-tube heat exchangers

DESIGN, CONSTRUCTION AND MAINTENANCE CODES FOR HEAT EXCHANGERS, GEOGRAPHIC DISTRIBUTION:

AREA	**CODE**	**Issuing Authority**
US	ASME Boiler & Pressure Vessel Code	ASME
UK	BS 1515 – Fusion welded pressure vessels BS 5500 – Unfired fusion welded pressure vessels	British Standard Institute
Germany	AD Merblatter	Arbitsgemeinschaft Druchbehalter
Italy	ANCC	Associazione Nationale Per II Controllo Peula Combustione
Netherlands	Regeis Voor Toestellen	Dienst voor het Stoomvezen
Sweden	Tryckkarls Kommissionen	Swedish Pressure Vessel Commission
Australia & NZ	AS/NZS 1200: SAA Boiler Code	Standards Association of Australia

	AS 1210: Unfired Pressure Vessel	
Belgium	IBN Construction Code for Pressure Vessels	Belgian Standards Institute
Japan	MITI Code	Ministry of International Trade and Industry
France	SNCT Construction Code for Unfired Pressure Vessels	Syndicat National de Chaudronnerie et de la Tuyauterie Industrielle

How can a HE manufacturer get the approval for stamping his products with any of the Standards?

- A manufacturer obtains permission to use one of the stamps through the required Standards Organization's conformity assessment process.
- The manufacturer's plant infrastructure, quality control system and the capability to implement all the required regulations is thoroughly reviewed by the Standards Organization's inspection team.
- If the manufacturer meets the Standard Organization's requirements and can demonstrate the successful implementation of the program for some stipulated probationary period, then the manufacturer's facilities are accredited by the Standard Organization.
- The manufacturer may then certify that the product meets the Standard Organization's standards and criteria, and can stamp his products with the Standard Organization's provided stamps. This entire process is a paid process with the costs being borne by the manufacturer.

Note:

The detailed ASME certification procedure for getting approval is present in Appendix 2.

Appendix 2: ASME Certification Procedure

1. The "Applicant" (Manufacturer) sends an e-mail/telefax/letter to the ASME Accreditation Department / National Board (NB) to request original "Application Forms" or applies online via "CA Connect" (e-mail: ca@asme.org / ASME Fax No: 001 212 591 8599 / NB: 001 614 847 1828) or download it from:
    - http://www.asme.org/kb/standards/certification---accreditation/product-certification/boiler---pressure-vessel-certification/application-process-and-forms
    - http://www.nationalboard.org/SiteDocuments/Registration/nb211.pdf
    - https://login.asme.org/caconnect/home.cfm
2. Signing of an Inspection Service Agreement between the AIA (OneCIS Insurance Company represented by ONE/TÜV/BV) and the "Applicant"
3. Completion of the "Application Forms" indicating the type / scope of certification and stamps applied for and the "AIA" (Authorized Inspection Agency) selected and contracted (= OneBeacon America Insurance Company / OneCIS)
4. The completed "Application forms" (copy to AIA) are returned to the ASME Accreditation Department / National Board by air courier / e-mail or online application via "CA Connect".
    - ca@asme.org / information@nationalboard.org
    - https://login.asme.org/caconnect/home.cfm
5. Procurement of ASME Code Books, as required per type of certification applied for, with ASME / NB directly
6. ASME notifies the AIA contracted to confirm to ASME that an Inspection Service Agreement has been signed with the "Applicant"
7. The AIA and the "Applicant" establish a Time Schedule for all action to be taken to prepare the Joint Review
8. Scheduling of the Joint Review date with ASME

9. Preparation of the Joint Review:
    - preparation of the Quality Manual
    - preparation of a representative component or component part as demonstration item
    - preparation of the Welding Procedure Specification (WPS), Procedure Qualification Record (PQR), Welding personnel (WPQ / WOPQ)
    - preparation of the drawing and the design calculation
    - preparation of work procedures (e.g. for the hydrostatic test, heat treatment, handling of welding filler material, calibration, NDE)
    - demonstration (qualification) of NDE procedures to the AI (Authorized Inspector)
    - qualification of NDE personnel
    - material purchasing
    - preparation of Traveller (Fabrication/Testing/Inspection Sequence Plan)
    - preparation of the Manufacturers Data Report (MDR)
10. Implementation of the above-mentioned quality program by the "Applicant"
11. Pre-Joint Review to verify the implementation of the quality program performed by the AI and the AIS approx. 4 weeks before the Joint Review
12. Joint Review with the AIA and ASME
13. ASME issues the certificate(s) and the ASME Certification Mark to the "Applicant"
14. The "Applicant" applies to the National Board for the "Certificate of Authorisation for Registration" and the NB-Stamp. This certificate is required to register components built and stamped in compliance with the ASME Code. The registration fee is depending on the size of each item.
15. Receipt of the "Certificate of Authorisation for Registration" and the NB stamp.
16. Fees:

US $	10,000.00	Advance payment for Joint Review (This is balanced with	ASME

		actual costs after the Joint Review)	
US $	Approx. 4,400.00	for Code books and binders	ASME
US $	2,820.00	per ASME certificate (For "H" or "UM":940 US $)	ASME
US $	280.00	per ASME Certification Mark	ASME
US $	Approx. 20.00	bank handling fee	ASME
US $	Free of charge	for Certificate of Authorisation for Registration and NB-stamp	National Board
US $	Approx. 500.00	for NB Review (when the Review is conducted in conjunction with an ASME Joint Review)	National Board
US $	630.00	NB Certificate fee ("R"-stamp or "VR"-stamp or "NR"-stamp)	National Board
US $	60.00	per NB stamp ("R"-stamp or "VR"-stamp or "NR"-stamp)	National Board
US $	Hard Copy 265.00	for National Board Inspection Code (NBIC) ANSI/NB-23 (electronic version on CD or Flash drive: 265 US $)	National Board

Note: Certificates are valid for three years only whereas the Code Books are issued every 2 years.

The construction code for shell and tube heat exchangers is ASME Code Section VIII, and it covers the minimum requirements for design, materials, fabrication, inspection, testing, and preparation for initial delivery. After the 2003 addenda of ASME Code Section VIII Div. 1, the design of the shell and tube needs to be done based on Subsection C, in UHX part. And design base TEMA, or any similar code and standards is not allowed. [8]

Inspection and Test Plan: [10]

The working process starts with an agreement between the purchaser and manufacturer. The manufacturer provides the Proforma Invoice (PI) to the purchaser, which explains the equipment specification and related price.

Then the purchaser issues the Purchase Order (PO), which confirms the proforma invoice. Before the start of manufacturing, the purchaser must provide an equipment inspection and a test plan (ITP) to the manufacturer.

The ITP identifies all inspection points for the purchaser's inspector. Then the manufacturer needs to prepare the project quality control plan based on this inspection and test plan.

The manufacturer notifies the purchaser's inspector in advance to attend at the factory for witnessing the inspections and tests.

The communication and coordination channel between the manufacturer, purchaser inspector and purchaser are agreed to in the Pre-inspection meeting (PIM).

Based on the international practice, the manufacturer sends a notification to the purchaser, and the purchaser reviews the notification, and after approval sends it to the inspector.

Then the inspector will go to the manufacturer's shop to witness the test or inspection.

The purchaser's inspector will send the inspection visit report to the purchaser.

The Purchaser can assign its own inspector, which is its direct employee or hire a third party inspection agency to carry out the inspection.

The ITP have a tabular format and the content extracted from the construction code. In each row of the table, there is a quality control and inspection requirement and this determines which party is responsible for control and inspection.

There are three parties in the ITP, the Manufacturer, the Third Party Inspector (TPI) and the Client or purchaser. Normally, the table accommodates 3 sections as following:

- Before Manufacturing
- During Manufacturing
- Final Inspection

The before Manufacturing section consists of the Pre-Inspection Meeting (PIM) and review of the quality control documents that need to be approved before start of manufacturing.

There are 3 or 4 important terminologies in the ITP that determines the responsibility of each party. These are:

Hold point (H): Hold on the production till TPI Inspector performs inspection and supervises the required test. In general, attendance to the PIM meeting, raw material inspection and

identification, Post Weld Heat Treatment Review, Hydrostatic Test, Performance Test, Run-Out Test and Final Inspection are Hold points. Normally, manufactures shall notify the TPI Inspector 7 working days in advance.

Witness Point (W): The manufacturer shall notify the client and TPI Inspector, but there is no hold on the production. The client can waive this inspection based on its discretion and inform the TPI Inspector.

Spot Witness (SW): for items with spot witness, the manufacturer shall notify the TPI inspector as fulfilling the monitoring. For example one random visit for all of the UT Tests or one or two visits for whole surface preparation work for painting.

Review (R): Review means Review document, which includes the review of quality control records, test reports, etc. When the TPI Inspector makes a visit for a hold or witness point, the inspector can review the related documents.

Inspection and Test Plan for S&T HEs (Main Points): [63]

- All plates need to be identified against mill test certificates at the Vendor`s works before commencement of fabrication.
- Mill inspection of materials.
- Ensuring that welding procedure and welders are qualified before commencement of fabrication.
- Checking fit-up and witness chipping-back of welded seams.
- Wherever applicable, selecting spots for radiography.
- If specified witnessing any crack detection, hardness checks, ultrasonic tests etc. Which are specified in drawing, specification, data sheet etc.
- Reviewing of radiographs (spot check)
- Witnessing all hydrostatic tests on shell and tube sides.
- Complete dimensional checking for stacked units. This is to be carried out in the full assembly stage.
- Checking that all material test certificates and where applicable, heat treatment charts are in order. Ensure that Vendor is familiar with the requirements regarding data books and see that the documentation is submitted without any delay.

- Witnessing any further test required by purchaser

THIRD PARTY INSPECTION OF S&T HEs: [64]

All shell and tube heat exchanger inspection and testing is done against the approved drawings, purchase order specifications, purchasers or company standards, and within the practices and rules of the country, state or province and any government decrees, laws, ordinance or regulation as may apply.

The applicable codes and specifications for a shell and tube heat exchanger that is under the construction process are:

- Design code
- Purchase order specification
- Purchaser's standards
- Approved drawings

And the applicable codes and standard are:

- ASME VIII Division 1 or 2
- ASME V
- ASME IX

The applicable codes and standard may be based other international standards such as BS 5500, etc. the provided method is general and is useful even if the design code is different from ASME Code.

Required Documents for Third Party Review:

The list of documents normally is agreed upon in the Pre-Inspection meeting, which is held several weeks before the actual commencement of the inspection work. The parties that participate in this meeting are the manufacturer, purchaser and third party inspection agency representatives. The following is the list of documents which are normally agreed to be presented to the inspector:

- Shell and Tube Heat Exchanger Manufacture Quality Control Plan
- Shell and Tube Heat Exchanger Inspection and Test Plan
- Shell and Tube Heat Exchanger Data Sheet
- Shell and Tube Heat Exchanger Approved Drawings
- Shell and Tube Heat Exchanger Strength Calculation Sheets

- Shell and Tube Heat Exchanger Material Test Reports
- Shell and Tube Heat Exchanger Welding Specification Procedures (WPS) and Procedure Qualification Records(PQR)
- Shell and Tube Heat Exchanger Welding Map
- Shell and Tube Heat Exchanger Welders Qualifications Reports
- Shell and Tube Heat Exchanger NDE procedures (Radiography, Ultrasonic, Magnetic Particle, Dye Penetration, etc.)
- Shell and Tube Heat Exchanger NDE Personnel qualifications Reports
- Shell and Tube Heat Exchanger Heat Treatment Procedure
- Shell and Tube Heat Exchanger Calibration Certificates for Test Equipment
- Hydrostatic Testing Procedure and Water Quality Document
- Shell and Tube Heat Exchanger Preparation and Painting Procedure
- Shell and Tube Heat Exchanger Preservation, Packing and Shipping Procedure
- Shell and Tube Heat Exchanger Packing List

Material Inspection:

If the purchase order has mandated the MTR to be provided for all components, such as nozzle pipes, fittings, etc., then the manufacturer needs to provide them along with other documents to the Third Party Inspector. The original or authenticated copies of mill certificates for plates normally are available at the manufacturer's premises. The third party inspector examines these certificates for compliance with specifications, and where appropriate, drawings.

The review includes checks on:

- Certificate No.
- Heat or cast No.
- Chemical composition.
- Mechanical properties.
- Heat treated condition.
- NDE applied and results.

Then the inspector witnesses the plate material identification on the certificates against the plate marking. It is also necessary to check the identification with the shell and tube heat exchanger drawing datasheet, material list and other specifications as appropriate. The

transfer identification to cut off plates also is checked. Visual inspections for surface finish and probable defects are done and dimensional compliance with specification also needs to be controlled. For more detail about shell and tube heat exchanger raw material inspection, you may review the Pressure Vessel Dimension Inspection article.

When the third party inspector carries out the material inspection, then provides the inspection visit report (IVR), the report contains the following items:

- Confirmation of satisfactory document review
- Record of the endorsement of certification reviewed/witnessed
- Record of all non-conformities
- Record of any tests witnessed and the result

Fabrication:

When the shell and tube heat exchanger raw material inspection is carried out, and the results were satisfactory or non-conformities were closed by remedial action, then the shell and tube heat exchanger manufacturer will start fabrication.

The third party inspector checks the following points on the shell and tube heat exchanger based on the inspection and test plan (ITP), which has already been agreed upon between the purchaser and the shell and tube heat exchanger manufacturer. The inspection scope is determined in the ITP. Some purchasers prefer to have stringent controls and assign the TPI for more “hold or witness points” for inspection and test activities, and some others prefer less “hold or witness points” and assign the TPI much more work in the “review document.”

This depends in the inspection budget, which purchasers assign for inspection. Much more inspection will have a much larger cost and less risk, and conversely, less inspection will have less cost but more risks.

Preparation for Welding:

The third party inspector carries out the visual and dimensional check to ensure compliance with WPS and other specifications. Where specified, weld bevels are examined by the required code method after grinding/machining. It is necessary that the edges and weld bevels are clean, dry and free from surface defects, laminations, cracks, voids, notches, etc. They are causes for rejection unless suitable/satisfactory remedial action can be taken. Weld repairs are carried out in accordance with the code requirements and approved by the client before welding proceeds and serious or excessive defects normally are reported.

Fit-Up Inspection:

Shapes and dimensions are checked in accordance with the approved WPS and drawing. Tack welds are produced using the applicable WPS conditions, and it is necessary to be visually free from defects. Magnetic Testing (MT) or Penetration Testing (PT) may be performed in accordance with the code requirement.

Monitoring of Weld Conditions:

The third party inspector controls preheat heat temperature and method, inter-pass temperatures, weld material control, welder and process qualifications for conformity to the code requirements.

Back Gouging Inspection:

The third party inspector controls the shape and dimensions of the back gouged groove for conformity to the WPS requirement. It is necessary that the visual appearance is clean and free from defects. NDE examination is done in accordance with the code requirement.

Inspection of Completed Weld:

After completion of all welding and grinding operations, a visual examination confirms there are no harmful defects such as cracks, lack of fusion, surface porosity or exposed slag inclusions, incomplete penetration, incorrect profile of the weld, lack of leg length and overlap. Temporary attachments are removed, ground smooth, and the areas are checked for defects by MP or PT for defects.

Non-Destructive Examination:

NDE is performed by qualified personnel by the approved techniques. The techniques available are dependent on the vessel classification and the materials used.

Weld Repair:

The shell and tube heat exchanger weld repairs are completed using an approved WPS method and retested accordingly. It is necessary that all repairs are approved before any post weld heat treatment is carried out.

Post-Weld Heat Treatment:

The third party inspector reviews the post weld heat treatment record of the temperature and time in accordance with the approved code/procedure. The results of hardness tests are reviewed in accordance with the code requirements.

Mock-up Test of Tube to Tube-sheet Weld:

Mock-up test is made when required by purchase order or contract. Identification, visual appearance and dimensions, weld control, PT, section of weld, Macro-observation, hardness check of weld metal and heat affected zone are checked as required.

Visual and Dimensional Inspection of Tubes, Tube Bundle and Shell:

The third party inspector carries out following controls:

- Tubes after bending for thinning particularly on the back of bends.
- Tube sheet and baffle plate, including tube hole, heads, flanges, tubes, flange facing finish.
- Channel, shell, floating head, cover, tube bundle assembly.
- Template check of shell is performed in accordance with the applicable specifications as required. Size and construction of template are to be checked, and the template pass smoothly, without binding through the full length of the shell.
- Direction and orientation of nozzle, impingement baffles, lugs and external, internal fittings are checked.
- Out of roundness, diameters, length, wall thickness, straightness of shell are checked.
- Expansion ratio of tube ends is checked. Tubes to be checked for thinning after expansion.
- U-tubes are formed from a single length having no circumferential welds, and flattening need not exceed 10% of the nominal OD of tube.
- Tube sheet flatness on gasket contact surface is checked as required.

Tube Bundle Insertion:

Tube bundle insertion is checked as required. Cleanliness, insertion without binding, contact of tube sheet and shell flange and gasket used need to be confirmed.

Pneumatic Test:

The third party inspector witnesses the low pressure pneumatic test for nozzle reinforcing pads, support saddles or other attachments when specified by approved low pressure pneumatic test procedure using soapy water as the indicating medium. A minimum of 1 gauge with correct working ranges as described by the code is used.

Hydrostatic Testing:

The third party inspector controls the following items for Hydro-static Testing:

- Calibration status and correct working ranges of gauges. A minimum of 2 pressure gauges are attached to item under test.
- Adequate provision for venting of high points and draining are provided.
- Test pressure is applied as directed by procedure or code until test limiting pressure is reached. During hold period, a methodical check for leaks is conducted.
- Test pressures, metal and water temperatures are recorded.
- Water quality is as specified.

Special requirements of the purchaser's specification for deflection or strain gauges or pressure/time/temperature recordings is examined by the inspector and records verified.

Note: If the third party inspector is not in the hold or witness point in the ITP for any of the above inspection stage(s), then he/she will review the shell and tube heat exchanger manufacturer quality control report in his/her coming visit or on the final inspection day.

Final Inspection:

After hydro-static testing, the vessel is thoroughly drained and dried out by approved methods. All internal fittings, attachments, coatings or other requirements need to be completed. The specified post hydrostatic test NDE needs to be completed and the vessel closed. All shell and tube heat exchangers are checked for cleanliness and dryness by an approved method. The third party inspector rechecks the nozzle, saddle and bracket locations and orientations against the assembly drawings.

Name Plate Checking:

The content of the marking is checked in accordance with approved drawing and specifications by the third party inspector. Name plate need to be mounted on bracket welded to shell at the height specified.

Painting and Coating:

Surface preparation for painting is checked for the following points, according to specification by the third party inspector:

- Cleaning method (Blast or scraping and wire brushing)

- Preparation grades
- Freedom from weld spatter, blow-holes and other defects
- Dry film thickness is checked according to specification

Surface condition needs to be free from pin-holes, runs damage and other discontinuity.

Spares and Accessories:

The third party inspector controls spares, tools and accessories and makes visual and dimensional inspection for materials, workmanship and quantity according to the purchase order specification and packing list. The marking and/or tag is checked for identification.

Reporting:

The third party inspector provides an Inspection Visit Report (IVR) after each visit, as well as a final report summarizing the activities carried out during the shell and tube heat exchanger production in accordance with the contract requirements and circulated within the time limits specified in the contract.

The report is in the format required by the client and clearly indicates final acceptance or rejection of the shell and tube heat exchanger.

Release Note:

When required by the contract or purchase order, a release note is issued by the third party inspection agency and given to the manufacturer when the shell and tube heat exchangers have been accepted.

Packing, Marking and Shipping:

The following points are checked by the third party inspector:-

- Cleanliness and dryness of Shell and Tube Heat Exchangers
- Rust prevention for all machined surfaces
- Protection for cover for all opening and protruding parts
- Packing style and suitably for overseas transportation
- Shipping marks and other markings and notification of welding procedures, etc.
- Where nitrogen purge is specified the gas pressure is checked and the presence of warning notices checked.

Final Book (Dossier):

The following final documents are reviewed and signed off by the third party inspector – As built, drawings if required, Manufacturer's data reports, Material certificate or certified mill test reports for all pressure parts, Material list or map, Welder record for each seam or map, Heat treatment records (Temperature-time record chart during PWHT), Dimensional record, NDE records, Production test record/mock test record, Alloy verification records, (if required), Hydrostatic test record, Pneumatic test record, Hardness test record, Post weld heat treatment NDE, if specified, Name plate or other marks, Packing list and Spare parts and tool list.

Appendix 3: Bulk Bubble Diameter Modeling CEL

CALCULATING BULK BUBBLE DIAMETER

#The formula will give bubble diameter in "mm"

#SET OF PARAMETERS -as mentioned in Paper - Koncar Krepper Egorov 2007 - without using the ABS function

diaref1c=0.15[mm]

diaref2c=7[mm]

tempref1c=13.5[K]

tempref2c=-5[K]

########Tanh Method

temprefmeanc=0.5*(tempref1c+tempref2c)

temprefscale=4[K]

tempsub=SaturTemp-water.T

TanhArgum=(tempsub-temprefmeanc)/temprefscale

TanhBlend=1.0/(1.0+exp(TanhArgum))

DBulkTanh=TanhBlend*(diaref2c-diaref1c)+diaref1c

Appendix 4: Bubble Departure Diameter Modeling CEL

CALCULATING BUBBLE DEPARTURE DIAMETER BY COMBINING UNAL AND TOLUBINSKI-KOSTANCHUK MODELS AS PER CHENG-LI-WANG PAPER-suffix is: clw

UNAL MODEL IS TAKEN FROM CHENG-LI-WANG PAPER

a = 1

velref=0.61 [m s^-1]

velbulk=volumeAve(vel)@Fluid

#vellocal: local liquid velocity temperature at the first near-wall computational cell

vellocalwater=ave(water.vel)@heated

vellocal=areaAve(vel)@heated

vellocal comes out to be smaller than the bulk velocity

#b = (vellocal/velref)^0.47

b = (velbulk/velref)^0.47

phi = max(a,b)

bvalclw = ((deltaTsubinlet)/(2*(1-(rhovap/rholiq))))

cvalclw=(((Hlv*muliq)*((cpliq/(0.013*Hlv*((Prliq)^1.7)))^3))/((sigma/((rholiq-rhovap)*gacc))^(1/2)))#/(1[kg s^-3 K^-3 m^-1])# MADE DIMENSIONLESS

NOTE: To keep the value of "avalclw" positive, the value of deltaTsub must be < (fluxwall/honephase). We need to put in a safeguard for this.

Tsubsafeaval=((fluxwall/1[W m^-2])-100)/(honephase/1[W m^-2 K^-1])

deltaTsubsafeaval=if(deltaTsub<Tsubsafeaval,deltaTsub,Tsubsafeaval)

avalclw=(((((fluxwall-honephase*(deltaTsubsafeaval*1[K])))^(1/3))*lambdaliq)/(2*(cvalclw^(1/3))*Hlv*rhovap*((

(pi*lambdaliq)/(rholiq*cpliq))^0.5)))*(((lambdawall*rhowall*cpwall)/(lambdaliq*rholiq*cpliq))^0.5))/(1[m s^-0.5])

MADE DIMENSIONLESS

honephase is single phase heat transfer coefficient

dbwclw is the bubble departure diameter at inlet as per UNAL's correlation

dbwclw=((2.42*10^(-5)*(pressure^0.709)*avalclw)/((bvalclw*phi)^0.5))*(1[m]) # AS PER CHENG LI WANG PAPER

Using the above obtained bubble departure diameter to calculate the value of C_bw to use in Tolubinksi-Kostanchuk formula

The usual value of Cbw is taken as 0.6mm or 0.0006m

Cbwclwcalc=(dbwclw/(exp((-deltaTsubinlet)/(Tconstt))))#/(1[kg^0.333 s^-2 K^-1])

Cbwclw=0.00015[m]

bubblecalcclw=Cbwclw*(exp((-deltaTsublocal)/(Tconstt)))

bubblecalcclw2=Cbwclw*(exp((-deltaTsub)/(Tconstt)))

bubbledepdiaclw=min(bubblemin,bubblecalcclw)

bubbledepdiaclw2=min(bubblemin,bubblecalcclw2)

References

1) **Abhilas Swain, Mihir Kumar Das.** 2013. "A review on saturated boiling of liquids on tube bundles." *Heat Mass Transfer*, DOI 10.1007/s00231-013-1257-1.

2) **Accidents, Boiler.** "https://www.asme.org/engineering-topics/articles/boilers/the-history-of-asmes-boiler-and-pressure, Accessed on 19 Aug, 2013."

3) **Adrian Bejan, Allan D. Krauss.** 2003. "Heat Transfer Handbook."

4) **ANSYS.** October 2012. "ANSYS CFX-Solver Modelling Guide." *ANSYS*, Release 14.5.

5) **ANSYS.** October 2012. "ANSYS CFX-Solver Theory Guide." *ANSYS*, Release 14.5.

6) **ANSYS.** October 2012. "ANSYS FLUENT Theory Guide." *ANSYS*, Release 14.5.

7) **ANSYS.** October 2012. "ANSYS FLUENT User's Guide." *ANSYS*, Release 14.5.

8) **ASME.** "https://www.asme.org/getmedia/1adfc3df-7dab-44bf-a078-8b1c7d60bf0d/ASME_BPVC_2013-Brochure.aspx, Accessed: 30 Sept 2015."

9) **ATLAS, VDI HEAT.** 2010. "G7 Heat Transfer in Cross-flow Around Single Rows of Tubes and Through Tube Bundles." *Springer*.

10) **B. Peng, Q. W. Wang, C. Zhang, G. N. Xie, L. Q. Quo, Q. Y. Chen, M. Zeng.** "An experimental study of Shell and Tube Heat exchangers with continuous helical baffles." *Journal of Heat Transfer*, 129(October 2007), 1425-31.

11) **B.B. Mikic, W.M. Rohsenow.** 1969. "A new correlation of pool boiling data including the effect of heating surface characteristics." *Journal of Heat Transfer*, 9(245-250).

12) **B.M. Burnside, K.M. Miller, D.A. McNeil, T. Bruce.** 2001. "Heat Transfer Coefficient Distributions in an Experimental Kettle Reboiler Thin Slice." *Institution of Chemical Engineers*, 79(May 2001), 445-52.

13) **B.M. Burnside, N.F. Shire.** 2005. "Heat Transfer in Flow Boiling over a Bundle of Horizontal Tubes." *Chemical Engineering Research and Design*, 83(May, 2005), 527-238.

14) **Bertani, Ruggero.** 2015. "Geothermal Power Generation in the World 2010-2014 Update Report." *Proceedings World Geothermal Congress 2015, Melbourne, Australia, 19-25 April 2015*.

15) **Bestion, D.** 2014. "The difficult challenge of a two-phase CFD modelling for all flow regimes." *Nuclear Engineering and Design*, http://dx.doi.org/10.1016/j.nucengdes.2014.04.006(2014).

16) **Bestion, D.** 2012. "Applicability of two-phase CFD to nuclear reactor thermohydraulics and elaboration of Best Practice Guidelines." *Nuclear Engineering and Design*, 253(2012), 311-21.

17) **Bostjan Koncar, Eckhard Krepper.** 2008. "CFD simulation of convective flow boiling of refrigerant in a vertical annulus." *Nuclear Engineering and Design*, 238(2008), 693-706.

18) **Bostjan Koncar, Ivo Kljenak, Borut Mavko.** 2004. "Modeling of local two phase flow parameters in upward subcooled flow boiling at low pressure." *International Journal of Heat and Mass Transfer*, 47(2004), 1499-513.

19) **Bostjan Koncar, Marko Matkovic.** 2012. "Simulation of turbulent boiling flow in a vertical rectangular channel with one heated wall." *Nuclear Engineering and Design*, 245(2012), 131-39.

20) **C. Y. Han, P. Griffith.** 1965. "The mechanism of heat transfer in nucleate pool boiling - I." *International Journal of Heat Mass Transfer*, Vol. 8(1965), 887-904.

21) **C.Y. Han, P. Griffith.** 1965. "The mechanism of heat transfer in nucleate pool boiling - II." *International Journal of Heat Mass Transfer*, 905-914.

22) **Chen, T.** 2013. "An experimental investigation of nucleate boiling heat transfer from an enhanced cylindrical surface." *Applied Thermal Engineering*, 59(2013), 355-61.

23) **Chen, T.** 2012. "Water-heated Pool Boiling of Different Refrigerants on the Outside Surface of a Smooth Horizontal Tube." *Journal of Heat Transfer*, 134(February 2012).

24) **Cooper, M.G.** 1989. "Flow boiling - the 'apparently nucleate' regime." *International Journal of Heat Mass Transfer*, Vol. 32(No. 3), 459-64.

25) **Cornwell, Keith.** 1990. "The influence of bubbly flow on boiling from a tube in the bundle." *International Journal of Heat and Mass Transfer*, 33(12), 2579-84.

26) **Crowe, Clayton T.** 2006. "Multiphase Flow Handbook." *CRC Taylor and Francis Group*.

27) **D. Dovic, B. Palm, S. Svaic.** 2009. "Generalized correlations for predicting heat transfer and pressure drop in plate heat exchanger channels of arbitrary geometry." *International Journal of Heat and Mass Transfer*, 52(2009), 4553-63.

28) **D. Gorenflo, P. Sokol, S. Caplanis.** 1990. "Pool boiling heat transfer from single plain tubes to various hydrocarbons." *International Journal of Refrigeration*, 13(September 1990), 286-92.

29) **D. Jung, Y. Kim, Y. Ko, K. Song.** 2003. "Nucleate boiling heat transfer coefficients of pure halogenated refrigerants." *International Journal of Refrigeration*, Vol. 26, Issue 2, 240-48.

30) **D.S. Schrage, J. T. Hsu, M.K. Jensen.** 1988. "Two-phase pressure drop in vertical crossflow across horizontal tube bundle." *American Institute of Chemical Engineers (AIChE)*, Vol. 34, No. 1(January 1988), 107-15.

31) **Damir Dovic, Srecko Svaic.** "Influence of Chevron Plates Geometry on Performance of Plate Heat Exchangers." *Technical Gazette 14, 2007; ISSN: 1330-3651*, 37-45.

32) **David A. McNeil, Azmahani Sadikin, Khalid H. Bamardouf.** 2012. "A Mechanistic Analysis of Shell-side Two-phase flow in an Idealised in-line Tube Bundle." *International Journal of Multiphase Flow*, 45(May 2012), 53-69.

33) **Dieter Gorenflo, David Kenning.** 2010. "Pool Boiling." *VDI Heat Atlas*, 2010(2010), 757-92.

34) **Dieter Gorenflo, Stephan Kotthoff.** 2008. "Pool Boiling Heat Transfer to Hydrocarbons and Ammonia: A state-of-the-art Review." *International Journal of Refrigeration*, 31(2008), 573-602.

35) **DiPippo, Ronald.** 2012. "Geothermal Power Plants: Principles, Applications, Case Studies and Environmental Impact." *Elsevier*, Third Edition.

36) **E. van Rooyen, J.R. Thome.** 2012. "Pool boiling data and prediction method for enhanced boiling tubes with R-134a, R-236fa and R-1234ze(E)." *International Journal of Refrigeration*, 36(2013), 447-55.

37) **Eckhard Krepper, Bostjan Koncar, Yury Egorov.** 2007. "CFD Modeling of subcooled boiling - Concept, Validation and Application to fuel assembly design." *Nuclear Engineering and Design*, 237, 716-31.

38) **Eckhard Krepper, Roland Rzehak.** 2011. "CFD for subcooled flow boiling - Simulation of DEBORA Experiments." *Nuclear Engineering and Design*, 241(2011), 3851-66.

39) **Eckhard Krepper, Roland Rzehak, Conxita Lifante, Thomas Frank.** 2013. "CFD for subcooled flow boiling: Coupling wall boiling and population balance models." *Nuclear Engineering and Design*, 255(2013), 330-46.

40) **Ender Ozden, Ilker Tari.** 2010. "Shell side CFD analysis of small shell and tube heat exchanger." *Energy Conversion and Management*, 51, 1004-14.

41) **Erfeng Chen, Yanzhong Li, Xianghua Cheng.** 2009. "CFD simulation of upward subcooled boiling flow of refrigerant-113 using two-fluid model." *Applied Thermal Engineering*, 29(2009), 2508-17.

42) **Erfeng Chen, Yanzhong Li, Xianghua Cheng, Lei Wang.** 2009. "Modeling of low-pressure subcooled boiling flow of water via homogeneous MUSIG approach." *Nuclear Engineering and Design*, 239(2009), 1733-43.

43) **F.D. Moore, R.B. Mesler.** 1961. "The measurement of rapid surface temperature fluctuations during nucleate boiling of water." *American Institute of Chemical Engineers (AIChE)*, Vol. 7(620-624).

44) **F.H. Rahman, J.G. Gebbie, M.K. Jensen.** 1996. "An Interfacial Friction Correlation for Shell-side Two-phase Cross-flow past Horizontal in-line and Staggered Tube Bundles." *International Journal of Multiphase Flow*, 22(1996), 753-66.

45) **Factory, Grover Shoe.** "http://en.wikipedia.org/wiki/File:Grover_Shoe_Factory_before.jpg, http://en.wikipedia.org/wiki/File:Grover_Shoe_site_after.jpg, http://en.wikipedia.org/wiki/File:Grover_shoe_disaster_boiler.jpg, Accessed on 22 Aug, 2013."

46) **Franz Ramstorfer, Helfried Steiner, Gunter Brenn.** 2008. "Modeling of the microconvective contribution to wall heat transfer in subcooled boiling flow." *International Journal of Heat and Mass Transfer*, 51(2008), 4069-82.

47) **G.H. Yeoh, J.Y.Tu.** 2006. "Numerical modeling of bubbly flows with and without heat and mass transfer." *Applied Mathematical Modeling*, 30(2006), 1067-95.

48) **G.H. Yeoh, Mark K.M. Ho, S.C.P. Cheung, J.Y.Tu.** 2008. "Fundamental consideration of wall heat partition of vertical subcooled boiling flows." *International Journal Heat and Mass Transfer*, 51(2008), 3840-53.

49) **G.H. Yeoh, S. Vahaji, S.C.P. Cheung, J.Y.Tu.** 2014. "Modeling of subcooled flow boiling in vertical channels at low pressures - Part II: Evaluation of mechanistic approach." *International Journal Heat and Mass Transfer*, 75(2014), 754-68.

50) **G.P. Xu, C.P. Tso, K.W. Tou.** 1998. "Hydrodynamics of two-phase flow in vertical up and down-flow across a horizontal tube bundle." *International Journal of Multiphase Flow*, 24(1998), 1317-42.

51) **G.R. Noghrekar, M. Kawaji, A.M.C. Chan.** 1998. "Investigation of two-phase flow regimes in tube bundles under cross-flow conditions." *International Journal of Multiphase Flow*, 25(1999), 857-74.

52) **Gh.S. Jahanmir, F. Farhadi.** 2012. "Twisted bundle heat exchangers performance evaluation by CFD." *International Communications in Heat and Mass Transfer*, 39(2012), 1654-60.

53) **Gherhardt Ribatski, John R. Thome.** 2004. "Dynamics of two-phase flow across horizontal tube bundles - A review." *Proceedings of the 10th Brazilian Congress of Thermal Sciences and Engineering - ENCIT 2004*.

54) **Gherhardt Ribatski, Jose M. Saiz Jabardo.** 2003. "Experimental study of nucleate boiling of halocarbon refrigerants on cylindrical surfaces." *International Journal of Heat and Mass Transfer*, 46(2003), 4439-51.

55) **Gherhardt Ribatski, Jose M. Saiz Jabardo, Evandro Fockink da Silva.** 2008. "Modeling and experimental study of nucleate boiling on a vertical array of horizontal plain tubes." *Experimental Thermal and Fluid Science*, 32(2008), 1530-37.

56) **Gregory Nellis, Sanford Klein.** 2009. "Heat Transfer - Nellis & Klein." *Cambridge University Press*, 2009.

57) **H. Anglart, O. Nylund.** 1996. "CFD application to prediction of void distribution in two-phase bubbly flows in rod bundles." *Nuclear Engineering and Design*, 163(1996), 81-98.

58) **H. Anglart, O. Nylund, N. Kurul, M.Z. Podowski.** 1997. "CFD prediction of flow and phase distribution in fuel assemblies and spacers." *Nuclear Engineering and Design*, 177(1-3), 215-28.

59) **H.K. Forster, N. Zuber.** 1955. "Dynamics of vapor bubbles and boiling heat transfer." *AIChE J.*, Vol. 1, No. 4(1955), 531-39.

60) **Hewitt, G.F.** 1998. "Chapter-15." *Handbook of Heat Transfer (Third Edition), McGraw Hill*.

61) **Hewitt, G.F.** 1998. "Chapter 15." *Handbook of Heat Transfer (Third Edition), McGraw Hill*.

62) **http://www.thermopedia.com/content/590/.** Accessed on 04 Feb 2016. "Boiling Number."

63) **Inspection.** "http://www.inspection-for-industry.com/inspection-and-test-plan-for-shell-and-tube-heat-exchanger.html, Accessed on 05 Sept, 2013."

64) **Inspection, Third-party.** "http://www.inspection-for-industry.com/third-party-inspection-for-shell-and-tube-heat-exchanger.html, Accessed on 06 Sept, 2013."

65) **J. Darabi, M.M. Ohadi, M.A. Fanni, S.V. Dessiatoun, M.A. Kedzierski.** 1999. "Effect of heating boundary conditions on Pool Boiling experiments." *HVAC&R Research*, Vol. 5, No. 4(October 1999).

66) **J. F. Klausner, R. Mei, D. M. Bernhard, L. Z. Zeng.** 1993. "Vapor bubble departure in forced convection boiling." *International Journal Heat and Mass Transfer*, Vol. 36, No. 3(1993), 651-62.

67) **J. J. Wei, B. Yu, H. S. Wang.** 2003. "Heat transfer mechanisms in vapor mushroom region of saturated nucleate pool boiling." *International Journal of Heat and Fluid Flow*, 24(2003), 210-22.

68) **J. S. Jayakumar, S. M. Mahajani, J. C. Mandal, P. K. Vijayan, Rohidas Bhoi.** 2008. "Experimental and CFD Estimation of Heat Transfer in Helically Coiled Heat Exchangers." *Chemical Engineering Research and Design*, 86, 221-32.

69) **J. Y. Tu, G. H. Yeoh.** 2003. "Development of a Numerical Model for Subcooled Boiling Flow." *Third International Conference on CFD in the Minerals and Process Industries, CSIRO, Melbourne, Australia, 10-12 December, 2003*, 559-68.

70) **J. Y. Tu, G. H. Yeoh.** 2002. "On numerical modeling of low-pressure subcooled boiling flows." *International Journal of Heat and Mass Transfer*, 45(2002), 1197-209.

71) **J.G. Myers, V.K. Yerrsmilli, S.W. Hussey, G.F. Yee. Jungho Kim.** 2005. "Time and space resolved wall temperature and heat flux measurements during nucleate boiling with constant heat flux boundary condition." *International Journal of Heat Mass Transfer*, Vol.48, 2429-42.

72) **J.R. Thome, D.M. Robinson.** 2006. "Prediction of local bundle boiling heat transfer coefficients: Pure refrigerant boiling on plain, low fin, and Turbo-BII Tube bundles." *Heat Transfer Engineering*, Vol. 27, No. 10(2006), 20-29.

73) **James G. Gebbie, Michael K. Jensen.** 1997. "Void Fraction Distributions in a Kettle Reboiler." *Experimental Thermal and Fluid Science*, 14(1997), 297-311.

74) **Janusz T. Cieslinski, Artur Fiuk.** 2013. "Heat transfer characteristics of a two-phase thermosyphon heat exchanger." *Applied Thermal Engineering*, 51(2013), 112-18.

75) **Jeongbae Kim, Byung Do Oh, Moo Hwan Kim.** 2006. "Experimental study of pool temperature effects on nucleate pool boiling." *International Journal of Multiphase Flow*, 32(2006), 208-31.

76) **Jian-Fei Zhang, Ya-Ling He, Wen-Quan Tao.** 2009. "3D numerical simulation on shell-and-tube heat exchangers with middle-overlapped helical baffles - Part 1: Numerical model and results of whole heat exchanger with middle overlapped helical baffles." *International Journal of Heat and Mass Transfer*, 52(2009), 5371-80.

77) **Jian-Feng Yang, Min Zeng, Qiu-Wang Wang.** 2014. "Effects of sealing strips on shell-side flow and heat transfer performance of a heat exchanger with helical baffles." *Applied Thermal Engineering*, 64(2014), 117-28.

78) **Jian Fei Zhang, Ya-Ling He, Wen-Quan Tao.** 2009. "3D numerical simulation on shell-and-tube heat exchangers with middle-overlapped helical baffles and continuous baffles - Part2: Simulation results of perioddic model and comparison between continuous and non-continuous helical baffles." *International Journal of Heat and Mass Transfer*, 52(5381-5389).

79) **Jie Yang, Lei Ma, Jessica Bock, Anthony M. Jacobi, Wei Liu.** 2014. "A comparison of four numerical modeling approaches for enhanced shell and tube heat exchangers with experimental validation." *Applied Thermal Engineering*, 65, 369-83.

80) **John G. Collier, John R. Thome.** 1994. "Convective Boiling and Condensation (Third Edition)." *Oxford Science Publications*.

81) **Jose M. Saiz Jabardo, Gherhardt Ribatski, Elvio Stelute.** 2009. "Roughness and surface material effects on nucleate boilinig heat transfer from cylindrical surfaces to refrigerants R-134a and R-123." *Experimental Thermal and Fluid Science*, 33(2009), 579-90.

82) **K. Stephan, M. Abdelsalam.** 1980. "Heat transfer correlations for Natural Convection Boiling." *International Journal of Heat and Mass Transfer*, 23(1980), 73-87.

83) **Kang, Myeong-Gie.** 2000. "Effect of surface roughness on pool boiling heat transfer." *International Journal of Heat and Mass Transfer*, 43(2000), 4073-85.

84) **Kedzierski, Mark A.** 1995. "Calorimetric and Visual Measurements of R-123 Pool Boiling on Four Enhanced Surfaces." *Prepared for U.S. Department of Energy, NISTIR 5732*, 59.

85) **Keith Cornwell, J. G. Einarsson.** 1983. "Peripheral variation of heat transfer under pool boiling on tubes." *International Journal of Heat and Fluid Flow*, Vol. 4, No. 3(September 1983), 141-44.

86) **Keith Cornwell, S. D. Houston.** 1994. "Nucleate pool boiling on horizontal tubes: a convection based correlation." *International Journal of Heat and Mass Transfer*, 37(1994), 303-09.

87) **Kim, Jungho.** 2009. "Review of nucleate pool boiling heat transfer mechanisms." *International Journal of Multiphase Flow*, 35(2009), 1067-76.

88) **Kutateladze, S. S.** 1979. "Boiling and bubbling heat transfer under free convection of liquid." *International Journal Heat and Mass Transfer*, Vol. 22(1979), 281-99.

89) **L. Aprin, P. Mercier, L. Tadrist.** 2007. "Experimental analysis of local void fractions measurements for boiling hydrocarbons in complex geometries." *International Journal of Multiphase Flow*, 33(2007), 371-93.

90) **L. Aprin, P. Mercier, L. Tadrist.** 2011. "Local heat transfer coefficient for boiling of hydrocarbons in complex geometries: A new approach for heat transfer prediction in staggered tube bundle." *International Journal of Heat and Mass Transfer*, 54(2011), 4203-19.

91) **L. Z. Zeng, J. F. Klausner, D. M. Bernhard, R. Mei.** 1993. "A unified model for the prediction of bubble detachment diameters in boiling systems - I: Pool Boiling." *International Journal Heat and Mass Transfer*, Vol. 36, No. 9(1993), 2261-70.

92) **L. Z. Zeng, J. F. Klausner, D. M. Bernhard, R. Mei** 1993. "A unified model for prediction of bubble detachment diameters in boiling systems - 2. Flow Boiling " *International Journal of Heat and Mass Transfer*, 36, No. 9(1993), 2271-79.

93) **Leiner, W.** 1994. "Heat transfer by nucleate pool boiling - general correlation based on thermodynamic similarity." *International Journal of Heat Mass Transfer*, Vol. 37, No.5, 763-69.

94) **Luke, A.** 1997. "Pool boiling heat transfer from horizontal tubes with different surface roughness." *International Journal of Refrigeration*, Vol. 20, No. 8(1997), 561-74.

95) **M. K. Jensen, M. J. Reinke, J. T. Hsu.** 1989. "The influence of tube bundle geometry on cross-flow boiling heat transfer and pressure drop." *Experimental Thermal and Fluid Science*, 2(1989), 465-76.

96) **M. Karas, D. Zajac, R. Ulbrich.** 2012. "Heat and flow characteristics of two-phase gas-liquid mixture flow over tube bundle using electrochemical and DPIV methods." *20th International Congress of Chemical and Process Engineering (CHISA - 2012), Prague, Czech Republic.*

97) **M.G. Cooper, A.J.P. Lloyd.** 1969. "The microlayer in nucleate pool boiling." *International Journal of Heat Mass Transfer*, Vol. 12(1969), 895-913.

98) **M.K. Dobson, J.C. Chato.** 1998. "Condensation in smooth horizontal tubes." *Journal of Heat Transfer*, Vol. 120(February 1998), 193-213.

99) **M.W. Browne , P.K. Bansal.** 1999. "Heat Transfer Characteristics of Boiling Phenomenon in Flooded Refrigerant Evaporators." *Applied Thermal Engineering*, 19(1999), 595-624.

100) **Mamoru Ishii, Takashi Hibiki.** 2011. "Thermo Fluid Dynamics of Two-Phase Flow, Second Edition." *Springer*.

101) **Muhammad Mahmood Aslam Bhutta, Nasir Hayat, Muhammad Hassan Bashir, Ahmed Rais Khan, Kanwar Naveed Ahmed, Sarfaraz Khan.** 2012. "CFD Applications in various heat exchangers design: A review." *Applied Thermal Engineering*, 32(2012), 1-12.

102) **N. Kabaliuk, M.C. Jermy, E. Williams, T.L. Laber, M.C. Taylor.** 2014. "Experimental validation of a numerical model for predicting the trajectory of blood drops in typical crime scene conditions, including droplet deformation and breakup, with a study of the effect of indoor air currents and wind on spatter drop trajectories." *Forensic Science International*, Vol. 245, 107-20.

103) **O. Zeitoun, M. Shoukri.** 1996. "Axial void fraction profile in low pressure subcooled flow boiling." *International Journal of Heat and Mass Transfer*, Vol. 40, No. 4(1997), 867-69.

104) **O. Zeitoun, M. Shoukri.** 1996. "Bubble Behavior and Mean Diameter in Subcooled Flow Boiling." *Journal of Heat Transfer*, Vol. 118(February 1996), 110-16.

105) **P. Stephan, J. Hammer.** 1994. "A new model for nucleate boiling heat transfer." *Warme-und Stoffubertragung 30 (1994) 119-125, Springer-Verlag 1994*.

106) **P.A. Feenstra, D.S. Weaver, R.L. Judd.** 2000. "An Improved Void Fraction Model for Two-phase Cross-flow in Horizontal Tube Bundles." *International Journal of Multiphase Flow*, 26(2000), 1851-73.

107) **Palen, J W.** 1992. ""Thermal Design of Shell-and-Tube Reboilers"." *Hemisphere Handbook of Heat Exchanger Design, Section 3.6.2, Begell House, New York - 1992*.

108) **Peter Hubner, Wolfgang Kunstler.** 1997. "Pool boiling heat transfer at finned tubes: influence of surface roughness and shape of fins." *International Journal of Refrigeration*, Vol. 20, No. 8(1997), 575-82.

109) **Peter J. O' Rourke, Anthony A. Amsden.** 1987. "The TAB Method for Numerical calculation of spray droplet breakup." *1987 International Fuels and Lubricants Meeting and Exposition, Toronto Hilton Hotel, Toronto, Ontario, November 2-5, 1987*.

110) **Plant, ORMAT Air-cooled Binary Geothermal Power.** "http://www.ormatfunding.com/our_business/technology, Accessed on 30 Jan, 2016."

111) **Q. W. Dong, Y. Q. Wang, M. S. Liu.** 2008. "Numerical and experimental investigation of shellside characteristics for RODbaffle heat exchanger." *Applied Thermal Engineering*, 28(2008), 651-60.

112) **Qiuwang Wang, Qiuyang Chen, Guidong Chen, Min Zeng.** 2009. "Numerical investigation on combined multiple shell-pass shell-and-tube heat exchanger with continuous helical baffles." *International Journal of Heat and Mass Transfer*, 52(2009), 1214-22.

113) **R Dowlati, M Kawaji, A.M.C. Chan.** 1990. "Pitch-to-Diameter effect on two phase flow across an inline tube bundle." *American Institute of Chemical Engineers (AIChE)*, Vol. 36, No. 5(May 1990), 765-72.

114) **R Dowlati, M. Kawaji, A.M.C. Chan.** 1992. "Hydrodynamics of two-phase flow across horizontal in-line and staggered rod bundles." *Journal of Fluids Engineering, Transactions of ASME,*, Vol. 114(Sept. 1992), 450-56.

115) **R Dowlati, M. Kawaji, A.M.C. Chan.** 1996. "Two-phase Crossflow and Boiling Heat Transfer in Horizontal Tube Bundles." *Journal of Heat Transfer*, 118(February 1996), 124-31.

116) **R. Dowlati, M. Kawaji, A.M.C. Chan.** 1996. "Two-phase Crossflow and Boiling Heat Transfer in Horizontal Tube Bundles." *Journal of Heat Transfer*, 118(February 1996), 124-31.

117) **R. L. Judd, K. S. Hwang.** 1976. "A Comprehensive Model for Nucleate Pool Boiling Heat Transfer including Microlayer Evaporation." *Journal of Heat Transfer,* (November 1976), 623-29.

118) **R. Roser, B. Thonon, P. Mercier.** 1999. "Experimental Investigations on boiling of n-pentane across a horizontal tube bundle: two phase flow and heat transfer characteristics." *International Journal of Refrigeration*, 22(1999), 536-47.

119) **R.C. Hendricks, R.R. Sharp.** 1964. "Initiation of cooling due to bubble growth on a heating surface." *NASA TN D2290*.

120) **R.K. Shah, D.P. Sekulic.** 1998. "Chapter 17." *Handbook of Heat Transfer (Third Edition), McGraw Hill*.

121) **R.K. Shah, D.P. Sekulic.** 2003. "Fundamentals of Heat Exchanger Design."

122) **R.P. Roy, S. Kang, J.A. Zarate, A. Laporta.** 2002. "Turbulent Subcooled Boiling Flow - Experiments and Simulations." *Journal of Heat Transfer*, Vol. 124(February 2002), 73-93.

123) **R.W. Lockhart, R.C. Martinelli.** 1949. "Proposed correlation of data for isothermal two-phase, two-component flow in pipes." *Chemical Engineering Progress*, Vol. 45, No. 1(January 1949), 39-48.

124) **Rachna Vidhi, D Yogi Goswami, Elias Stefanakos.** 2014. "Supercritical Rankine Cycle coupled with ground cooling for low temperature power generation." *Energy Procedia 57 (2014) 524-532*.

125) **Roh, Heui-Seol.** 2013. "Heat Transfer Mechanisms in Pool Boiling." *International Journal of Heat and Mass Transfer*, 68(2014), 332-42.

126) **Rohsenow, W.M.** 1951. "A Method of Correlating Heat Transfer Data for Surface Boiling of Liquids." *Technical Report No. 5, Massachusetts Institute of Technology, Division of Industrial Cooperation, Cambridge 39, Massachusetts*.

127) **S. A. Alavi Fazel, S. Roumana.** "Pool Boiling Heat Transfer to Pure Liquids." *Continuum Mechanics, Fluid, Heat*, 211-16.

128) **S. B. Memory, N. Akcasayar, H. Eraydin, P.J. Marto.** 1995. "Nucleate pool boiling of R-114 and R114-oil mixtures from smooth and enhanced surfaces - II: Tube bundles." *International Journal of Heat and Mass Transfer*, Vol. 38, No. 8(1995), 1363-76.

129) **S. Freund, S. Kabelac.** 2010. "Investigation of local heat transfer coefficients in plate heat exchangers with temperature oscillation IR thermography and CFD." *International Journal of Heat and Mass Transfer*, 53(2010), 3764-81.

130) **S. S. Pawar, Vivek K. Sunnapwar.** 2014. "Experimental and CFD Investigation of Convective Heat Transfer in Helically Coiled Tube Heat Exchanger." *Chemical Engineering Research and Design*, "Article In Press".

131) **S.B. Memory, D.C. Sugiyama, P.J. Marto.** 1995. "Nucleate Pool Boiling of r-114 and R-114/Oil mixtures from smooth and enhanced tubes - I. Single Tubes." *International Journal of Heat Mass Transfer*, Vol. 38, No. 8(1995), 1347-61.

132) **S.C.P. Cheung, S. Vahaji, G.H. Yeoh, J.Y. Tu.** 2014. "Modeling subcooled flow boiling in vertical channles at low pressures - Part I: Assessment of empirical correlations." *International Journal of Heat and Mass Transfer*, 75(2014), 736-53.

133) **S.M. McManus, P.J. Marto, X. Wanniarachchi.** 1986. "An evaluation of enhanced heat transfer tubing for use in R114 chillers." *ASME Heat Transfer Air Cond. Refrig. Equip. HTD 65*, 222-30.

134) **S.W. Churchill, M. Bernstein.** 1977. "A correlating equation for forced convection from gases and liquids to a circular cylinder in cross-flow." *Journal of Heat Transfer*, Vol. 99(May 1977), 300-06.

135) **Saeed Moghaddam, Ken Kiger.** 2009. "Physical mechanisms of heat transfer during single bubble nucleate boiling of FC-72 under saturation conditions - I: Experimental Investigation, II: Theoretical Analysis." *International Journal of Heat and Mass Transfer*, 52(2009), 1284-94,95-303.

136) **Sergio Pereira Rocha, Olivier Kannengieser, Elaine Maria Carduso, Julio Cesar Passos.** 2013. "Nucleate pool boiling of R-134a on plain and micro-finned tubes." *International Journal of Refrigeration*, 36(2013), 456-64.

137) **Simin Wang, Jian Wen, Huizhu Yang, Yulan Xue, Hanfei Tuo.** 2014. "Experimental investigation on heat transfer enhnacement of a heat exchanger with helical baffles through blockage of traingle lekage zones." *Applied Thermal Engineering*, 67(2014), 122-30.

138) **Standards, API.** "http://www.enggcyclopedia.com/2011/09/api-standards-heat-exchangers, Accessed on 20 Aug, 2013."

139) **Steven Eckels, Evraam Gorgy.** 2012. "Local heat transfer coefficient for pool boiling of R-134a and R-123 on smooth and enhanced tubes." *International Journal of Heat and Mass Transfer*, 55(2012), 3021-28.

140) **T. H. Hwang, S. C. Yao.** 1986. "Crossflow Boiling Heat Transfer in Tube Bundles." *International Comm. Heat Mass Transfer*, 13(1986), 493-502.

141) **T. H. Hwang, S. C. Yao.** 1986. "Forced convective boiling in horizontal tube bundles." *International Journal of Heat Mass Transfer*, 29, No. 5(1986), 785-95.

142) **T. H. Lee, G. C. Park, D. J. Lee.** 2002. "Local flow characteristics of subcooled boilinig flow of water in vertical concentric annulus." *International Journal of Multiphase Flow*, 28(2002), 1351-68.

143) **TEMA.** "http://www.thermopedia.com/content/1182/, Accessed on 14 Aug, 2013."

144) **Thome, John R.** 2009. "Engineering Data Book III." *Wolverine Tube INC.*

145) **Thome, John R.** 2009. "Boiling Heat Transfer on External Surfaces." *Wolverine Engineering Databook - III*.

146) **Thome, John R.** 2009. "Wolverine Engineering Databook III."

147) **Thulukkanam, Kuppan.** 2013. "Heat Exchanger Design Handbook, Second Edition." *CRC Press*.

148) **W.L. Haberman, R.K. Morton.** 1953. "An experimental investigation of the drag and shape of air bubbles rising in various liquids." *Armed Services Technical Information Agency, Document Service Center, Dayton, Ohio*, September 1953.

149) **Xiang-hui Tan, Dong-sheng Zhu, Guo-yan Zhou, Li-ding Zeng.** 2013. "Heat transfer and pressure drop performance of twisted oval tube heat exchanger." *Applied Thermal Engineering*, 50(2013), 374-83.

150) **Yadigaroglu, G.** 2014. "CMFD and the critical-heat-flux grand challenge in nuclear thermal-hydraulics - A letter to the editor of this special issue." *International Journal of Multiphase Flow*, In Press(2014).

151) **Yong-Gang Lei, Ya-Ying He, Pan Chu, Rui Li.** 2008. "Design and optmization of heat exchnagers with helical baffles." *Chemical Engineering Science*, 63(2008), 4386-95.

152) **Yong-Gang Lei, Ya-Ying He, Rui Li, Ya-Fu Gao.** 2008. "Effects of baffle inclination angle on flow and heat transfer of a heat exchanger with helical baffles." *Chemical Engineering and Processing*, 47(2008), 2336-45.

153) **Zeljko R. Simovic, Sanja Ocokoljic, Vladimir D. Stevanovic.** 2006. "Interfacial Friction Correlations for the Two-phase flow across tube bundle." *International Journal of Multiphase Flow*, 33(2007), 217-26.

154) **Zhengguo Zhang, Dabin Ma, Xiaoming Fang, Xuenong Gao.** 2008. "Experimental and numerical heat transfer in a helical baffled heat exchanger combined with one three-dimensional finned tube." *Chemical Engineering and Processing*, 47(2008), 1738-43.